Theory of the Optical Properties of III-V Semiconductor Quantum Wells

A Thesis
Submitted To The
Faculty Of Engineering
Of The University Of Glasgow
For The Degree Of
Doctor Of Philosophy
By

Alistair Thomas Meney BSc, MSc

Acknowledgements

I would like to thank all those who have expressed interest in my work, in particular Dr. Chris R. Chatwin, Professor Richard M. DeLaRue and my supervisor Dr. John M. Arnold. I am also grateful to Chris Chatwin and Rupert Young for many useful and interesting discussions.

Computing facilities were provided by the University Computing Service and the Department of Mechanical Engineering, University of Glasgow. I would like to express my gratitude to Professor Brian Scott, Department of Mechanical Engineering, University of Glasgow, for the provision of both computing and word-processing facilities. The production of this thesis, and all publications arising from my work, were only made possible by the provision of these facilities.

Part of this research was supported by a quota award from the Science and Engineering Research Council (UK).

Contents

Abstract

The aim of this project is to investigate the electronic and optical properties of III-V semiconductor quantum wells, specifically those based on the GaAs-AlGaAs system. Both the linear and non-linear optical properties of these systems are considered.

A theoretical model for the refractive index in GaAs-AlGaAs quantum well structures for optical frequencies close in energy to the fundamental band gap has been constructed, and is based on knowledge of the electronic band structure. This model includes the Γ valley states, and also allows for inclusion of the electronic states at the X and L points. The ground state and excited state excitons have also been explicitly included within the theoretical model. The exciton model which is employed in this thesis takes into account the Coulomb coupling between different exciton states. In addition, the effects of band filling and screening have both been incorporated, allowing the intensity-dependent index of refraction to be obtained. Calculations are presented for a range of material compositions and quantum well structures, including both single and double quantum wells.

The results obtained for the index of refraction are therefore more complete and accurate than any previous published calculations. It is expected that the results presented here can be used directly in the design of refractive-based optoelectronic devices.

1 Introduction

Historical introduction

During the past two decades, the semiconductor laser (also known as the diode laser) has been the subject of much development. This has led to recent advances in the field of semiconductor integrated optoelectronics, based on the production of elementary devices such as semiconductor lasers and photodetectors. The semiconductor laser has become a key component in this field, due to its excellent operating characteristics, which include high efficiency, high-speed modulation properties and reliability.

Originally, due to the large lasing threshold, the gallium arsenide (GaAs) homojunction laser[1] was operated in pulsed mode only. The possibility of transverse mode control[2] and high-speed modulation[3,4] soon became obvious and continuous (CW) operation at room temperature of GaAs-AlGaAs heterojunction lasers[5-7] was soon realised, leading to substantial development. Longer

wavelength operation, for possible optical fibre communications, was made possible by the development of GaInAsP-InP heterojunction laser diodes[8-10], operating in the wavelength range of 1.2μm to 1.6μm.

Also, during this period, fabrication of artificial microstructures has been made possible due to the development of novel semiconductor technologies such as molecular beam epitaxy[11] (MBE) and metal-organic-chemical-vapour deposition[12] (MOCVD). These techniques have led to the introduction of devices with physical dimensions comparable to interatomic distances. Research on semiconductor superlattices was initiated following a proposal by Esaki and Tsu[13,14] for a one-dimensional potential structure to be fabricated with epitaxy of alternating ultrathin layers. This is shown schematically in Figure 1.1. Two possible types of these structures, doping-superlattices and compositional-superlattices are illustrated in Figure 1.2.

Within these devices "quantum size" phenomena become important, since the characteristic dimensions of superlattice period or quantum well width are reduced to less than the electron mean free path and the entire electron system enters a quantum regime of reduced dimensionality. The quantum well laser[15,16] which exploits the electronic properties of a quasi two-dimensional system, is of interest due to its reduced threshold current and high temperature operation. One of the most important parameters in quantum well optoelectronic devices is the index of refraction, which is studied in this thesis. Knowledge of the dispersion of the index of refraction is of significant importance in the design of optoelectronic devices.

Layout of thesis

In Chapter 2, many of the basic physical properties of bulk GaAs and AlGaAs are presented. This is not intended to be exhaustive, but to offer sufficient background material for later use.

The electronic dispersion in quasi two-dimensional systems is of fundamental importance in this work. Before discussing this in some detail in Chapter 4, the basic fundamentals of band theory in bulk systems are given in Chapter 3. Again, this is not exhaustive, but presents the fundamentals required for the calculations in Chapter 4.

The successful calculation of quantum well electronic dispersion allows accurate determination of physical properties and observables. In Chapter 5, we concentrate on the optical absorption spectrum in the vicinity of the fundamental band gap. The linear absorption spectrum is obtained directly from the imaginary part of the dielectric response function. Since this is used to obtain the index of refraction it is necessary to obtain the dielectric function as accurately as possible. At frequencies close to the fundamental band gap, exciton effects are extremely important, even at room temperature,[17] in GaAs-$Al_xGa_{1-x}As$ quantum wells. The theoretical model employed to obtain the

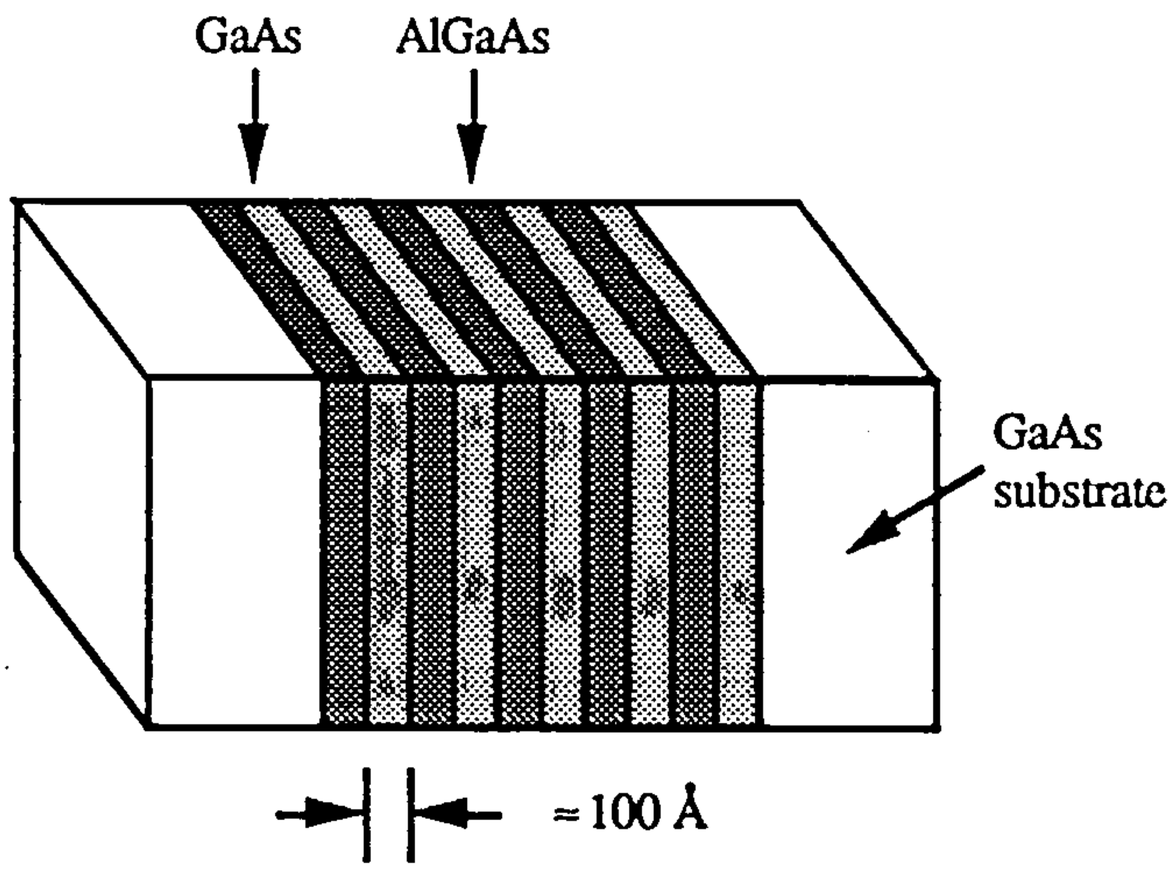

Figure 1.1 *Schematic illustration of a GaAs-AlGaAs multiple quantum well (MQW) or superlattice. The lighter coloured layers are GaAs, sandwiched between layers of AlGaAs. The well thickness of 100Å is typical.*

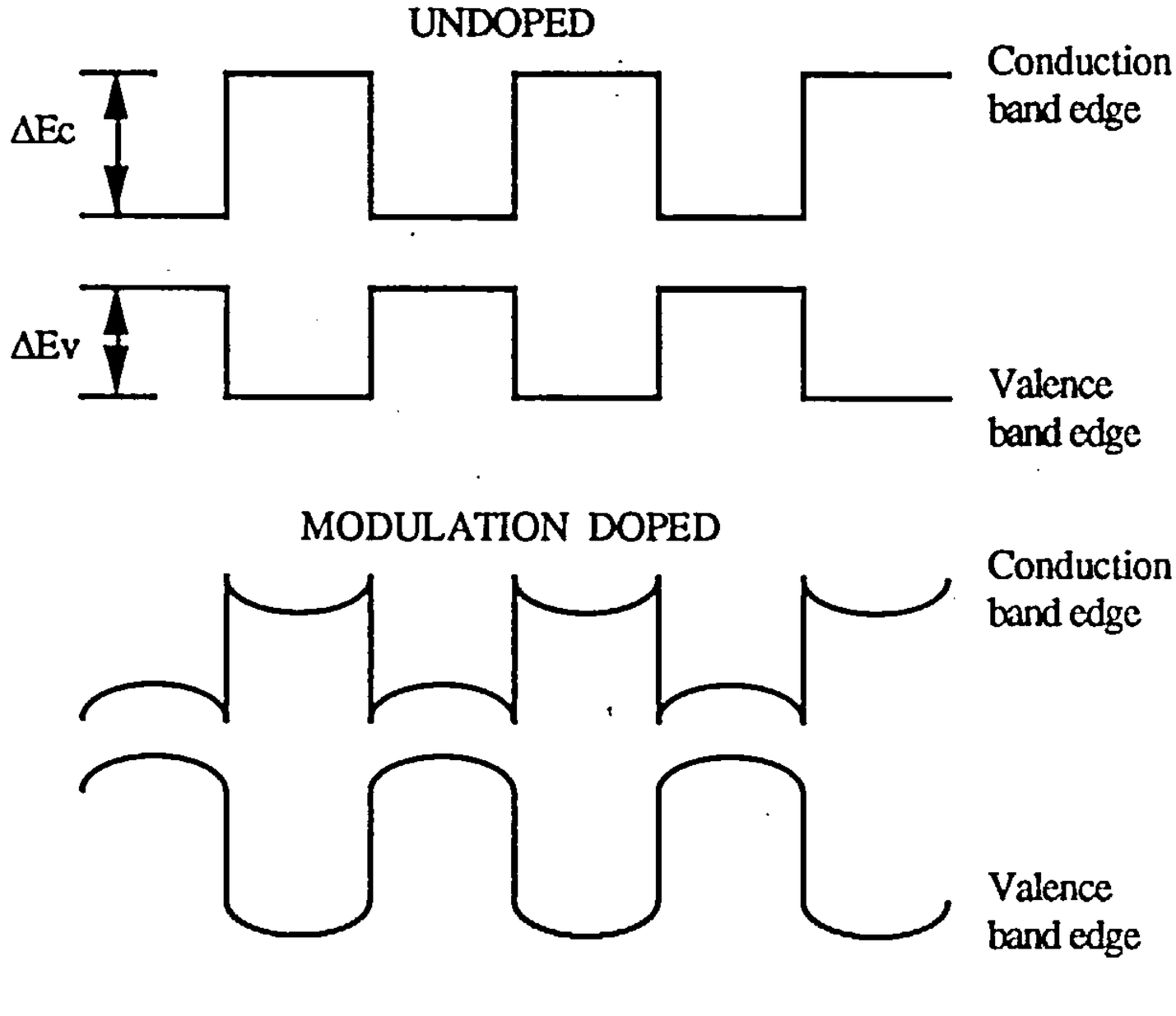

Figure 1.2 *Schematic illustration of the conduction band edge and valence band edge potential profiles in an undoped compositional superlattice (top) and a modulation (periodic) doped superlattice (bottom). The top figure represents the idealised situation of perfect interfaces.*

exciton wave functions is presented in Appendix B, to maintain separation from the main body of the text. Many-body effects are also important and lead to a screened dielectric function. These have a significant effect on the exciton wave functions and are included in Chapter 5. A self-consistent Hartree scheme is used throughout, both in the case of doping and in the case of a free-carrier plasma generated by optical absorption.

Chapter 6 concentrates solely on the index of refraction in quantum well structures. The calculations draw heavily on the results of the two preceding Chapters. This gives the necessary electronic band structure and the calculated dielectric function, including excitons, which are used to obtain the index of refraction. The effects of both material parameters and structure-dependence on the index of refraction are examined. The effects of external perturbations on the refractive index are also considered in detail. Also of importance is the reduction in the refractive index due to the effects of saturation. Calculation of the intensity-dependent index of refraction are therefore also presented in this Chapter.

For convenience we have included several Appendices. This allows each Appendix to deal separately with an important theoretical subject and derivation, without losing coherence and brevity within the main text of the thesis. In particular, as mentioned above, the model used to obtain the exciton wave functions is presented in Appendix B. This theory couples together several exciton states to form a variational basis set. In addition we find that only those excitons which are coupled by the Coulomb interaction need be included in the basis set. This not only allows accurate calculation of the exciton binding energies and oscillator strengths, but also takes into account the proper physics of the problem.

Accurate knowledge of the refractive index is important for optoelectronic device modelling. It is necessary to obtain the refractive index spectrum as accurately and conveniently as possible. The material presented in this thesis is therefore intended to provide the necessary theoretical background to accomplish this task. It is hoped that it will be readily accessible to all requiring to make use of the theory and results contained herein.

The results of the research leading to the production of this thesis has successfully led to several publications. A list of these publications is included at the end of the thesis.

References

1 M.I. NATHAN, W.P. DUMKE, G. BURNS, F.H. DILL and G. LASHER, Applied Physics Letters **1**, 62 (1962)

2 J.C. DYMENT, Applied Physics Letters **10**, 84 (1967)

3 B.S. GOLDSTEIN and R.M. WEIGAND, Proceedings of the IEEE **53**, 195 (1965)

4 J. TAKAMIYA, F. KITISAWA and J.I. NISHIZAWA, Proceedings of the IEEE **56**, 135 (1968)

5 H. KROEMER, Proceedings of the IEEE **51**, 1782 (1963)

6 Zh.I. ALFEROV, V.M. ANDREEV, E.L. PORTNOI and M.K. TRUKAN, Soviet Physics Semiconductors **3**, 1107 (1970)

7 I. HAYASHI, M.B. PANISH, P.W. FOY and A. SUMSKI, Applied Physics Letters **17**, 109 (1970)

8 K. OE and K. SUGIYAMA, Japanese Journal of Applied Physics **15**, 740 (1976)

9 T. YAMAMOTO, K. SAKAI, S. AKIBA and Y. SUEMATSU, Electronic Letters **13**, 142 (1977)

10 K. OE, S. ANDO and K. SUGIYAMA, Japanese Journal of Applied Physics **16**, 1273 (1977)

11 R.D. DUPUIS and P.D. DAPKUS, Applied Physics Letters **34**, 262 (1979)

12 A.Y. CHO, R.W. DIXON, H.C. CASEY and R.L. HARTMANN, Applied Physics Letters **28**, 501 (1976)

13 L. ESAKI and R. TSU, IBM Research Note RC-2418 (1969)

14 L. ESAKI and R. TSU, IBM Journal of Research and Development 61 (1970)

15 N. HOLONYAK, R.M. KOLBAS, R.D. DUPUIS and P.D. DAPKUS, IEEE Journal of Quantum Electronics **QE-16**, 170 (1980)

16 W.T. TSANG, Applied Physics Letters **40**, 217 (1982)

17 D.S. CHEMLA, D.A.B. MILLER, P.W. SMITH, A.C. GOSSARD and W. WEIGMANN, IEEE Journal of Quantum Electronics **QE-20**, 265 (1984)

MISSING

PAGE/PAGES

HAS NO

CONTENT

2 Physical Properties of Bulk Gallium Arsenide and Aluminium Gallium Arsenide

Introduction

The aim of this chapter is to briefly review some of the major physical properties of the binary semiconductor Gallium Arsenide (GaAs) and the ternary alloy semiconductor Aluminium Gallium Arsenide ($Al_xGa_{1-x}As$, where x indicates the fraction of Gallium atoms replaced by Aluminium atoms).

Since the symmetry properties of the zone-centre electronic states are similar to those of the full crystal point group, it is useful to consider the basic crystal properties in both real space and reciprocal space. Various methods of calculating the electronic energy dispersion will be discussed in the next chapter.

Crystal structure

Gallium Arsenide was first produced in the 1920s and is known to have the zincblende (cubic=sphalerite) lattice. This has face-centred cubic (fcc) symmetry and a basis of one GaAs molecule, with one atomic species at (000) and the other at $(\frac{1}{4}\frac{1}{4}\frac{1}{4})$ of the nonprimitive fcc unit cube.

The Ga atoms and the As atoms thus separately form overlapping fcc sublattices. The conventional unit cube (see Figure 2.1) has a side length of 5.653Å, at 300K. The volume of this unit cell is $1.807\text{x}10^{-22}\text{cm}^{-3}$ and is four times the volume of a primitive cell. The lattice constant of $Al_xGa_{1-x}As$ is obtained by linear interpolation between the lattice constants of GaAs (x=0) and AlAs (x=1). This gives

$$a(Al_xGa_{1-x}As) = (5.653 + 0.007x)\ \text{Å} . \qquad (2.1)$$

Crystal cleavage occurs most easily on {110} family planes, followed by {111} and then between (111) and (011). In the particular case of {111} planes, the cleaved terminator plane contains only one species of atom. This is either a Gallium (111A) plane, or an Arsenic (111B) plane and both have different chemical properties.

The dispersion of electronic states and lattice vibrations is described in the coordinate system of reciprocal space. The first Brillouin zone (body-centred cubic) for GaAs is shown in Figure 2.2. This represents a truncated octahedron and lies within a cube of side length $(4\pi/a) = 2.2\text{x}10^{10}\text{m}^{-1}$. In Figure 2.2, the most important special points (i.e. points of highest symmetry) and special lines are indicated. The location of these points within the Brillouin zone and the distances between them are given in Table 2.1.

The dependence of physical parameters in III-V compounds of type $A^{III}_xB^{III}_{1-x}C^{V}$, on the compositional value x is usually given by the formula, for some parameter α

$$\alpha(x) = a + bx + cx^2 , \qquad (2.2)$$

with $a = \alpha(0)$, $b + c = \alpha(1) - \alpha(0)$. The bowing parameter c indicates the deviation from linear dependence. For $Al_xGa_{1-x}As$, with $x<0.4$, it is found that a linear relation of the form

$$\alpha(x) = a + bx , \qquad (2.3)$$

is sufficiently accurate for many physical properties (e.g. lattice and band structure parameters).

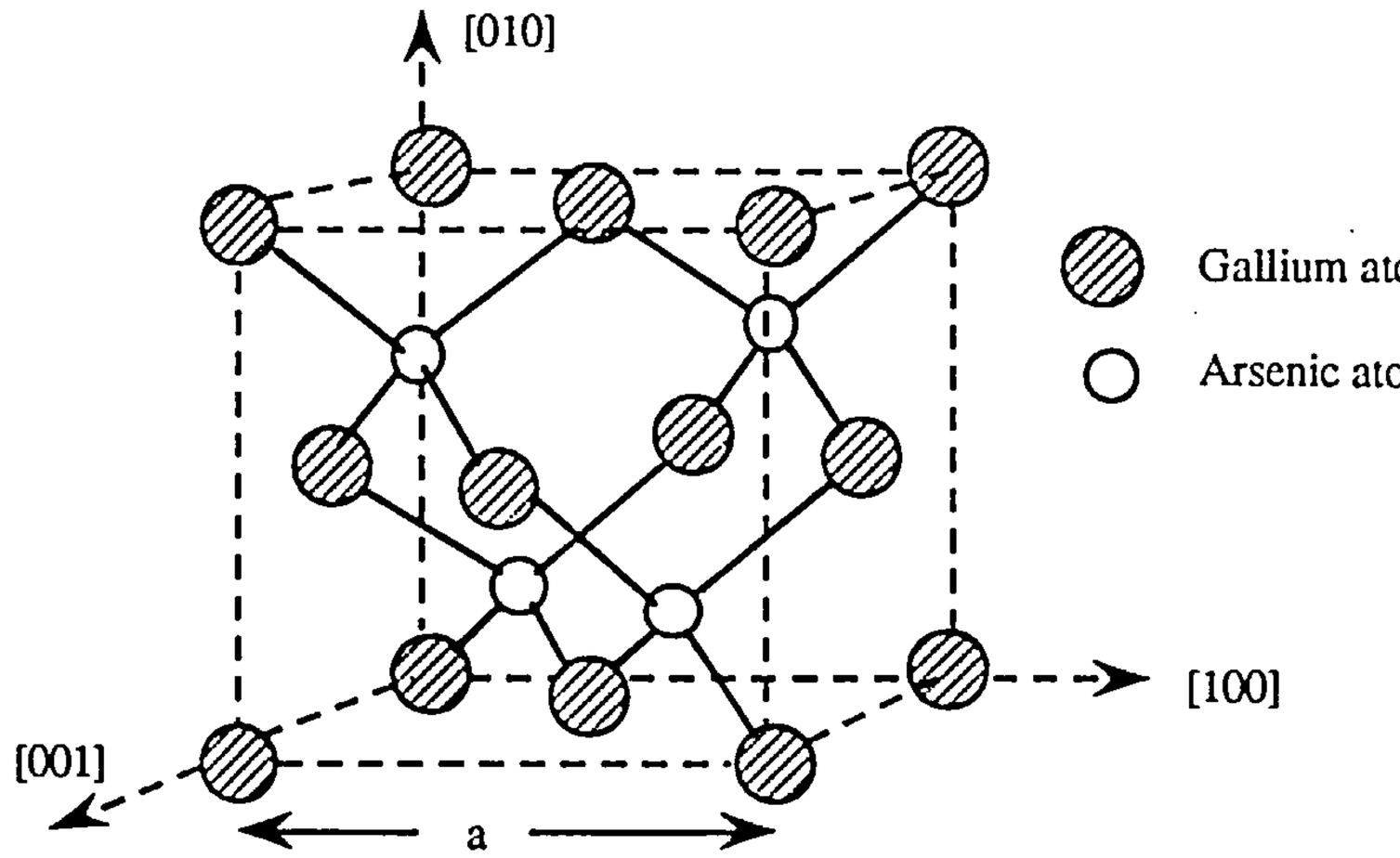

Figure 2.1 *Conventional unit cube for GaAs, with a volume four times that of a primitive cell. The bonds from any one atom are separated by the tetrahedral bond angle* $\cos^{-1}(-1/3) = 109.47^{o}$.

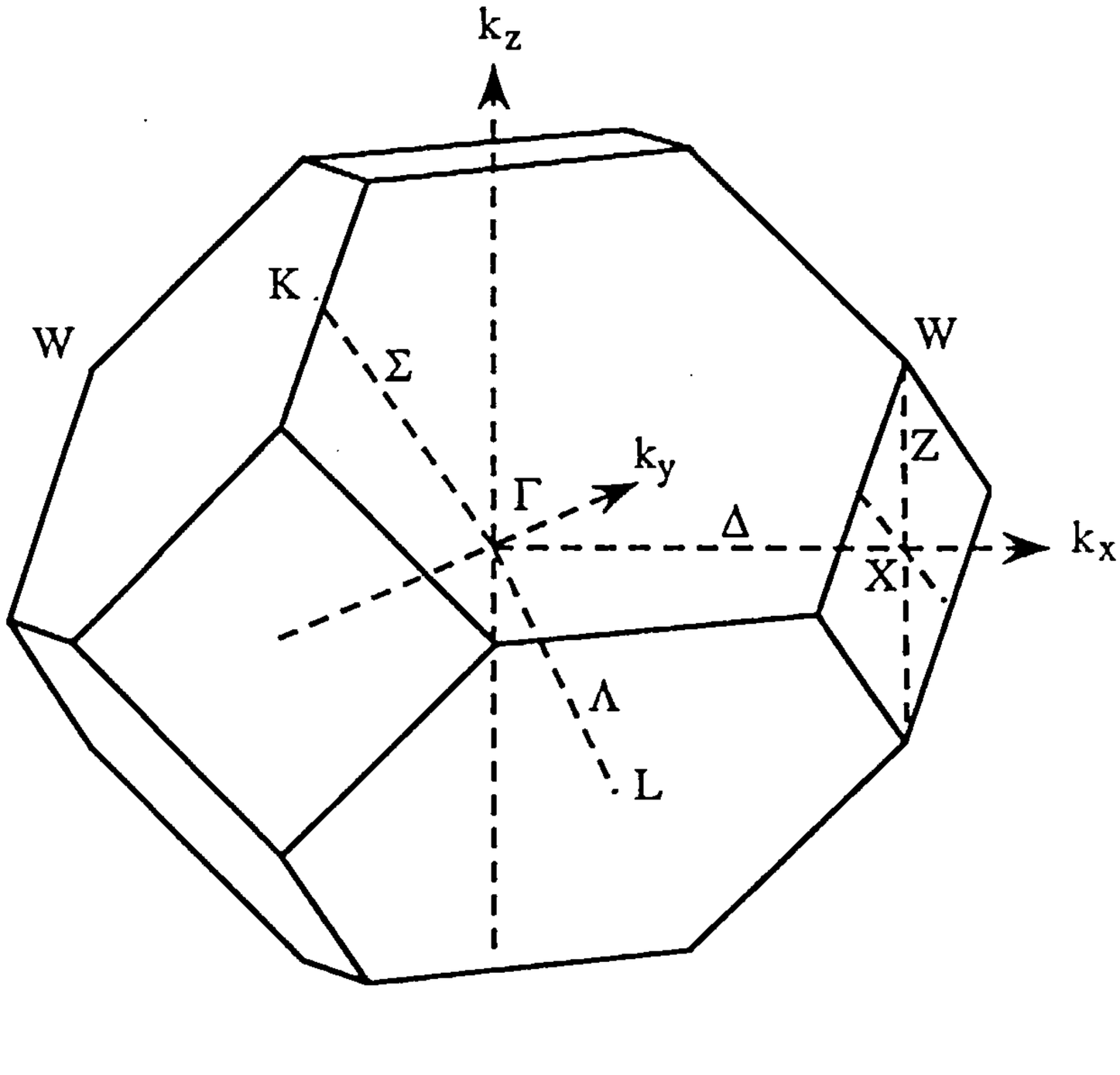

Figure 2.2 *The body-centred cubic first Brillouin zone of GaAs. This has the same symmetry properties as the direct space fcc lattice. Special points and lines are indicated, along with the direction of each wavevector component.*

Point	Location	Distance		
Γ	0 0 0			
X	1 0 0	|ΓX|	=	1
W	$1\ \frac{1}{2}\ 0$	|ΓW|	=	$\sqrt{5/4}$
U	$1\ \frac{1}{4}\ \frac{1}{4}$	|UX|	=	$\sqrt{1/8}$
		|UW|	=	$\sqrt{1/8}$
		|ΓU|	=	$\sqrt{9/8}$
L	$\frac{1}{2}\ \frac{1}{2}\ \frac{1}{2}$	|ΓL|	=	$\sqrt{3/4}$
K	$0\ \frac{3}{4}\ \frac{3}{4}$	|ΓK|	=	$\sqrt{9/8}$
		|LK|	=	$\sqrt{3/8}$
R	$0\ \bar{1}\ 1$	|ΓR|	=	$\sqrt{2}$

Table 2.1 *Locations of special points within the first Brillouin zone (relative to the zone centre at Γ) and the distance between them, in units of* $(2\pi/a) = 1.11 \times 10^{10} m^{-1}$.

Crystal bonding

In both elemental semiconductors (e.g. Silicon, Germanium) and alloy semiconductors, the binding is primarily covalent and each of the atoms has four nearest neighbours. The alloy zincblende structure displays the sp^3 hybrid bond orbitals which form tetrahedral bonds to the four nearest neighbour atoms. This is illustrated in Figure 2.1. To understand bond hybridisation, consider a Beryllium atom with the electronic configuration $1s^2 2s^2$. The ground state contains no unpaired electrons and a covalent bond is not expected. However, the low-lying excited state $1s^2 2s^1 2p_y^1$ has two unpaired electrons. The unpaired s- and p-orbitals can form two hybrid orbitals

$$\phi_1 = \frac{1}{\sqrt{2}}(s + p), \qquad \phi_2 = \frac{1}{\sqrt{2}}(s - p). \tag{2.4}$$

These can overlap and form a covalent bond with two atoms. The 'promotional' energy required to form these orbitals from the $1s^2 2s^2$ ground state is offset by the overlap energy obtained by bond formation. This type of hybridisation is called an sp hybrid. The sp^3 hybrid bond orbitals of tetrahedrally bonded semiconductors are due to the same basic mechanism but are rather more complex. In this case, the four hybrid functions which can be formed from the normalised s-wave

function and p_x, p_y, p_z normalised p-wave functions are

$$\phi_1 = \frac{1}{2}(s + p_x + p_y + p_z) \qquad \phi_2 = \frac{1}{2}(s - p_x - p_y + p_z)$$
$$\phi_3 = \frac{1}{2}(s + p_x - p_y - p_z) \qquad \phi_4 = \frac{1}{2}(s - p_x + p_y - p_z)\ . \qquad (2.5)$$

In the zincblende structure there are two atoms in each primitive cell and eight valence electrons. The Pauli exclusion principle allows two electrons per atom per electron band and therefore four valence bands are required in order to accommodate all the valence electrons. At T = 0K, an ideal semiconductor has completely filled valence bands. All the additional states into which an electron may be put comprise the conduction bands.

Energy gaps and effective masses

In this work, the principal electron bands of interest are the highest three valence bands and the lowest conduction bands. These are labelled according to the irreducible representations of the crystal point group (T_d or $\bar{4}3m$ for zincblende lattices). The three representations of the double group (compatible with electron spin) are known as Γ_6, Γ_7 and Γ_8 (using the Bethe[5] notation), at the zone centre Γ (k = 0).

Table 2.2 *Direct and indirect energy gaps in GaAs and $Al_xGa_{1-x}As$*

	Energy gap	representations	GaAs	$Al_xGa_{1-x}As$
T = 4K	E_o (eV) [6]	$\Gamma_6^c - \Gamma_8^v$	1.519	1.519 + 1.34x
	Δ_o (eV) [7]	$\Gamma_8^v - \Gamma_7^v$	0.34	0.34 - 0.06x
	E'_o (eV)	$\Gamma_7^c - \Gamma_8^v$	4.488	4.488 + 0.01x
	Δ'_o (eV)	$\Gamma_8^c - \Gamma_7^c$	0.171	0.171 - 0.04x
T = 300K	E_o (eV) [8]	$\Gamma_6^c - \Gamma_8^v$	1.425	$1.425 + 1.155x + 0.37x^2$
	Δ_o (eV) [9]	$\Gamma_8^v - \Gamma_7^v$	0.34	0.34 - 0.04x
	E'_o (eV)	$\Gamma_7^c - \Gamma_8^v$	4.44	4.44 + 0.1x
	Δ'_o (eV)	$\Gamma_8^c - \Gamma_7^c$	0.19	0.19 - 0.04x
T = 300K	$E_g(L)$	$L_6^c - \Gamma_8^v$	1.734	$1.734 + 0.574x + 0.055x^2$
	$E_g(X)$	$X_6^c - \Gamma_8^v$	1.911	$1.911 + 0.005x + 0.245x^2$

Considering first the point Γ (k=0), the lowest conduction band is Γ_6, the highest valence bands (heavy- and light-hole bands) are Γ_8 and the spin-orbit split-off band is Γ_7. The latter is reduced in energy due to the spin-orbit interaction. The next highest conduction bands are the Γ_7^c and Γ_8^c p-antibonding conduction bands.

The experimental values of the direct and indirect energy gaps are given in Table 2.2. The values given for $Al_xGa_{1-x}As$ are for $x \leq 0.45$. For larger values of x, the smallest energy gap is the indirect gap $E_g(x)$. The temperature dependence of the direct gap E_o in GaAs can be given in the numerical form[10]

$$E_o = 1.519 - 5.405\text{x}10^{-4}\left(\frac{T^2}{T+204}\right) \text{eV}, \tag{2.6}$$

where T is the temperature in Kelvins.

The effective mass is strongly connected with carrier mobility and is one of the most important device parameters. There are, however, several definitions of effective mass and it must be made clear the definition used here. One definition, the *optical* or *slope* effective mass is important when considering such phenomena as magnetic susceptibility or Faraday rotation. This is defined as

$$m_{opt} = \hbar k\left(\frac{\partial E}{\partial k}\right)^{-1} . \tag{2.7}$$

The other definition, used in the present work, is the band curvature effective mass defined as

$$m^* = \hbar^2\left(\frac{\partial^2 E}{\partial k^2}\right)^{-1} . \tag{2.8}$$

This definition includes the free electron mass $m_o = 9.11\text{x}10^{-31}$ kg. Removing this factor leads to

Table 2.3 *Zone centre effective masses in GaAs and $Al_xGa_{1-x}As$*

		GaAs	$Al_xGa_{1-x}As$
m_c [11]	Γ_6^c	0.067	0.067 + 0.083x
m_{hh} [12]	Γ_8^v	0.45	0.45 + 0.31x
m_{lh}	Γ_8^v	0.082	0.082 + 0.068x
m_{so}	Γ_7^v	0.15	0.15 + 0.09x

the definition of effective mass used throughout this thesis

$$m_n \left(\equiv \frac{m_n^*}{m_o} \right) = \frac{\hbar^2}{m_o} \left(\frac{\partial^2 E_n}{\partial k^2} \right)^{-1} , \qquad (2.9)$$

for an electron in band n.

This definition is obtained by considering the group velocity of an electron wave packet, centred at wavevector **k**. Given that $E = \hbar\omega$ and $v_g = (d\omega/dk)$, then

$$v_g = \frac{1}{\hbar} \frac{\partial E}{\partial k} , \quad \text{and} \quad \frac{dv_g}{dt} = \frac{1}{\hbar} \frac{\partial^2 E}{\partial k^2} \frac{\partial k}{\partial t} . \qquad (2.10)$$

An external field, applied for a time δt, will do an amount of work on an electron of charge -e given by

$$\delta E = -eEv_g(\delta t) = \frac{\partial E}{\partial k}(\delta k) . \qquad (2.11)$$

Since $\delta E = (\partial E/\partial k)\delta k = \hbar v_g \delta k$, then

$$\frac{d(\hbar k)}{dt} = -eE . \qquad (2.12)$$

Table 2.4 *Density of states effective masses and conductivity effective masses for the L valley and X valley conduction band minima, calculated from equations (2.15) and (2.16).*

minimum	effective mass	GaAs	$Al_xGa_{1-x}As$
L_6^c	m_l	1.9 [13]	——
	m_t	0.075 [14]	——
	m_L^{DOS}	0.56	0.56 + 0.1x
	m_L^c	0.11	0.11 + 0.03x
X_6^c	m_l	1.3 [15]	——
	m_t	0.23 [16]	——
	m_X^{DOS}	0.85	0.85 - 0.14x
	m_X^c	0.32	0.32 - 0.06x

From equation (2.10),

$$\frac{dv_g}{dt} = \frac{1}{\hbar^2}\frac{\partial^2 E}{\partial k^2}(-eE) \ . \tag{2.13}$$

Comparing this with Newton's law (a = F/m) gives

$$\frac{1}{m^*} \equiv \frac{1}{\hbar^2}\frac{\partial^2 E}{\partial k^2} \ .$$

Since the energy surfaces are not constrained to be spherical, the effective mass is replaced by an effective mass tensor, given by

$$\left(\frac{1}{m_n}\right)_{ij} = \frac{m_o}{\hbar^2}\left(\frac{\partial^2 E_n}{\partial k_i \partial k_j}\right) . \tag{2.14}$$

The experimental values quoted in Table 2.3 are all intended to be spherically-averaged values, which are most commonly used in device calculations. The values quoted are for **k** = 0. The density of states mass is obtained at each conduction band minimum (Γ, X or L) as

$$m_\alpha^{DOS} = N_\alpha^{2/3} m_{t_\alpha}^{2/3} m_{l_\alpha}^{1/3} \ , \tag{2.15}$$

where N_α is the number of equivalent minima at α, m_t and m_l are the transverse and longitudinal components of the effective mass. $N_L = 4$ and $N_X = 3$. The conductivity effective mass at each minimum is obtained from

$$\frac{1}{m_\alpha^c} = \frac{1}{3}\left(\frac{2}{m_t^\alpha} + \frac{1}{m_l^\alpha}\right) . \tag{2.16}$$

These values are given in Table 2.4.

Density of states

The density of states (DOS) function g(E) is an extremely important and useful parameter. It represents the number of allowed electron states per spin, per unit of energy, per unit of volume in a particular band at energy E in the interval (E, E+dE). For an arbitrary number of dimensions this is

given by

$$g_i(E)\,dE = \sum_{\text{spin}}\sum_{\alpha}\int \frac{dk}{(2\pi)^i}\,, \tag{2.17}$$

where α represents degenerate band minima and *i* is the number of dimensions. The quantity dk is the differential length (1D), area (2D) or volume (3D) for a surface of constant energy. The DOS function is therefore obtained by taking the derivative of equation (2.17) with respect to energy E. Since analytical forms for E(**k**) do not in general exist, a useful general expression for the DOS is

$$g_i(E)\,dE = \sum_{\text{spin}}\sum_{\alpha}\int \frac{1}{(2\pi)^i}\,\frac{dS}{|\nabla_k E|}\,, \tag{2.18}$$

where dS is the differential surface area of constant energy in 3D, or a differential length for 2D systems. Near a band minimum and if a parabolic approximation to E(**k**) is sufficiently accurate, then the density of states per spin takes the simple form

$$\text{1D} \quad g(E) = \frac{1}{2\pi}\left(\frac{2m^*}{\hbar^2}\right)^{1/2}\frac{1}{\sqrt{E}}$$

$$\text{2D} \quad g(E) = \frac{1}{2\pi}\left(\frac{2m^*}{\hbar^2}\right)$$

$$\text{3D} \quad g(E) = \left(\frac{1}{2\pi}\right)^2\left(\frac{2m^*}{\hbar^2}\right)^{3/2}\sqrt{E}\,, \tag{2.19}$$

where the energy E is measured with respect to the band edge minimum.

The joint density of states, essentially the number of pairs of electron states separated by a given energy interval E is extremely important when considering optical transitions and the dielectric function. This can be simply defined as

$$\rho_J(E) = \sum_{m}\sum_{n\neq m}\sum_{k}\delta(E - E_{mk} - E_{nk})\,, \tag{2.20}$$

where the sum extends over the entire Brillouin zone.

In general equations (2.20) and (2.18) must be solved numerically. In this work, this is obtained from the calculated band structure of each system under consideration. Note that the joint density of states can be expressed in a form analogous to equation (2.18) as

$$g_i(E) = \sum_{\text{spin}}\sum_{\alpha}\int \frac{1}{(2\pi)^i}\,\frac{dS}{|\nabla_k E_m - \nabla_k E_n|}\,. \tag{2.21}$$

Lattice vibrations: phonons

The vibrational spectrum of GaAs extends to 7×10^{12}Hz for acoustic modes and 9×10^{12}Hz for optical (intramolecular) modes. The two branches are a consequence of the two-atom primitive basis of GaAs. For n atoms per primitive unit cell, there are 3n branches of lattice vibrations. Each triple of values corresponds to one *longitudinal* and two *transverse* branches. Three acoustic branches are given by $\omega \rightarrow 0$ as $\mathbf{q} \rightarrow 0$. The remaining 3(n-1) optical branches have non-zero energy at $\mathbf{q} = 0$. The phonons belonging to these branches are labelled as LA-, TA-, LO- and TO-phonons.

Most experimental results for ν-q phonon dispersion curves are obtained using inelastic neutron scattering[17]. The phonon frequencies and energies for some important symmetry points in q-space are given in Table 2.5.

In polar semiconductors coupling between the electrons and the LO phonons can become so strong that a new quasi-particle, the polaron, can be useful. In these semiconductors, measurements of the electron effective mass actually yield the polaronic mass m^{**}. This can be related to the *bare*

Table 2.5 *Phonon frequencies and energies in GaAs at high symmetry locations within the Brillouin zone.*

Reciprocal space location	Mode character	ν (10^{12} Hz)	$h\nu$ (meV)
Γ (q = 000)	LO	8.55	35.4
	TO	8.02	33.2
X (q = 100)	TO	7.56	31.3
	LO	7.22	29.9
L ($q = \frac{1}{2}\frac{1}{2}\frac{1}{2}$)	TO	7.84	32.4
	LO	7.15	29.6
	LA	6.26	25.9
	TA	1.86	7.7
K ($q = 0\ \frac{3}{4}\ \frac{3}{4}$)	$TO_{\parallel}$	7.9	32.7
	$TO_{\perp}$	7.51	31.1
	LO	6.44	26.6
	LA	5.65	23.4
	$TA_{\parallel}$	3.48	14.4
	$TA_{\perp}$	2.38	9.58

mass m^* by[18]

$$m^{**} = \frac{1 - 0.0008\alpha^2}{1 - (\alpha/6) + 0.0034\alpha^2} m^* , \qquad (2.22)$$

where α is the Fröhlich coupling parameter

$$\alpha = \left(\frac{e^2}{8\pi\varepsilon_o \hbar\, \omega_{LO}}\right)\left(\frac{2m\omega_{LO}}{\hbar^2}\right)^{1/2}\left[\frac{1}{\varepsilon(\infty)} - \frac{1}{\varepsilon(0)}\right] . \qquad (2.23)$$

The variation in the LO- and TO-phonon energies in $Al_xGa_{1-x}As$ with x, for x<0.4, can be expressed as[19]

$$\begin{aligned} \hbar\omega_{LO}\ (\text{meV}) &= 36.25 - 6.55x + 1.79x^2 \\ \hbar\omega_{TO}\ (\text{meV}) &= 33.29 - 0.64x - 1.16x^2 . \end{aligned} \qquad (2.24)$$

Dielectric and optical properties

Much research has been done on the optical properties of bulk GaAs and $Al_xGa_{1-x}As$ and there exist numerous research papers and an extensive review literature. The basic terminology used in this thesis is briefly outlined. Given that ε is the complex dielectric permittivity at frequency ω, then the dimensionless dielectric constant is

$$\frac{\varepsilon}{\varepsilon_o} \equiv \varepsilon_r = \varepsilon_1 - i\,\varepsilon_2 . \qquad (2.25)$$

The real and imaginary parts can each be a function of frequency. The complex index of refraction n^* may be defined as

$$n^* \equiv \varepsilon^{1/2} = n - ik , \qquad (2.26)$$

with the real refractive index n and the extinction coefficient k as components. It follows that

$$\begin{aligned} \varepsilon_1 &= n^2 - k^2 , \\ \varepsilon_2 &= 2nk , \end{aligned} \qquad (2.27$$

and further that

$$n = \frac{1}{\sqrt{2}}\left[(\varepsilon_1^2 + \varepsilon_2^2)^{1/2} + \varepsilon_1\right]^{1/2},$$

$$k = \frac{1}{\sqrt{2}}\left[(\varepsilon_1^2 + \varepsilon_2^2)^{1/2} - \varepsilon_1\right]^{1/2}. \qquad (2.28)$$

The optical response can therefore be described by (ε_1,ε_2) or by (n,k). Many optical phenomena may be observed and measured with great accuracy by using modulation and derivative methods. A detailed account of these methods and useful experimental information, has been given by Cardona.[20] The modulation-type optical experiments reported for GaAs include: wavelength modulated reflectance[21], piezoabsorption[22], piezoreflectance[23], thermoreflectance[24], electroabsorption[25], electroreflectance[13,14,26-29] and piezo-electroreflectance.[30] The determination of the ordering and spacings of the GaAs valence and conduction bands has been greatly aided by the use of modulated electric field and/or uniaxial stress techniques.

The low frequency dielectric constant

The static (low frequency) dielectric constant $\varepsilon(0)$ is normally measured for frequencies between dc and millimetre wave regions (around 10^{11}Hz). This constant is most commonly used to consider long range Coulomb interactions (i.e. excitons), and is therefore considered as a crystal screening parameter. The contributions to $\varepsilon(0)$ arise from both electronic motion and ionic motion. At high frequencies the ions are too heavy to follow an applied field and only the electron motion contributes. For polar semiconductors however, the coupling of electrons and phonons leads to an indirect contribution to $\varepsilon(0)$ from the ionic lattice at higher frequencies. The temperature dependence of $\varepsilon(0)$ can be given by[31]

$$\varepsilon(0)(T) = 12.4(1 + 1.2\text{x}10^{-4}T), \qquad (2.29)$$

where T is in Kelvins. This value is used for modelling ionisation energies and the Bohr radius for a shallow impurity. The criterion for use of $\varepsilon(0)$ is that the Bohr orbital frequency be small compared to ν_{TO}. For tightly bound excitons and deep level impurities, the high orbital frequencies require that $\varepsilon(\infty)$ be used instead. Equation (2.29) is based on the results of several experimental investigations. The room temperature value of $\varepsilon(0)$ of 12.85 will be used in this thesis.

The high frequency dielectric constant

For frequencies below the fundamental energy gap E_o, but above the infra-red, the high frequency dielectric constant $\varepsilon(\infty)$ should be used. For negligible absorption, well below the fundamental gap,

the index of refraction is obtained as

$$n_\infty \equiv \sqrt{\varepsilon(\infty)} = 3.255(1 + 4.5\text{x}10^{-5}T) \ . \tag{2.30}$$

This value is obtained from the experimental investigations by Hambleton[32], Seraphin[33] and Sell.[34] The results of these authors may be combined to give the room temperature dispersion of n, at frequencies approaching the fundamental absorption edge at E_o. This gives

$$n(\nu) \equiv \sqrt{\varepsilon} = \left\{7.10 + \frac{3.78}{1 - 0.18(h\nu)^2}\right\}^{1/2} , \tag{2.31}$$

where ν is the incident photon energy, in electron-Volts. Accurate knowledge of $n(\nu)$ for photon energies in the vicinity of the fundamental absorption edge is required to model such optoelectronic devices as waveguides, LEDs and diode lasers. The nonparabolic band structure and presence of exciton states makes microscopic calculations of n rather difficult. In bulk GaAs equation (2.31) is fairly accurate for energies below E_o and indeed accounts reliably for the index of refraction to energies just below the absorption threshold. The temperature dependence can be included from the data of Marple[35] which gives a linear progression of n_∞ with temperature as

$$\frac{1}{n_\infty}\frac{dn_\infty}{dT} = 4.5\times 10^{-5}\left(\text{K}^{-1}\right), \tag{2.32}$$

which gives the temperature dependence of the high frequency dielectric constant as

$$\varepsilon(\infty) = 10.60(1 + 9.0\text{x}10^{-5}T) \ . \tag{2.33}$$

An attempt to model the temperature dependence of n_∞ was made by Yu and Cardona[36], for both diamond and zincblende semiconductors, using the 'Penn' model[37] with a Penn gap of 4.9eV for GaAs. This gives

$$\frac{1}{n_\infty}\frac{dn_\infty}{dT} = 5.4\times 10^{-5}\left(\text{K}^{-1}\right), \tag{2.34}$$

which agrees rather well with equation (2.32) despite the rather crude theory used.

References

1 V.M. GOLDSCHMIDT, Transactions of the Faraday Society **25**, 253 (1929)

2 C.M. DRISCOLL in: *Gallium Arsenide and Related Compounds*, Vol **24** (IOP, London)

3 W.B. PEARSON, *A Handbook of Lattice Spacings and Structure of Metals and Alloys* (Pergamon Press, 1967)

4 A.N. GORYUNOVA in: *The Chemistry of Diamond-like Semiconductors*, ed. by J.C. Anderson (MIT Press, 1965)

5 H. BETHE, Annalen der Physik **3**, 135 (1929)

6 B. LAMBERT, J. CAULET, A. REGRENY, M. BAUDET, B. DEVEAUD and A CHARETTE, Semiconductor Science and Technology **2**, 491 (1987)

7 all other T=4K energy gaps and indirect energy gaps are from: *Numerical Data and Functional Relationships in Science and Technology*, Vol **17** of Landolt-Börnstein, ed. by O. MADELUNG (Springer, Berlin, 1982)

8 H.J. LEE, L.Y. JURAVEL and J.C. WOOLLEY, Physical Review **B21**, 659 (1980)

9 all other T=300K direct energy gaps from: S. ADACHI, Journal of Applied Physics **58**, R1 (1985)

10 C.D. THURMOND, Journal of the Electrochemical Society **122**, 1133 (1975)

11 H.C. CASEY and M.B. PANISH, *Heterostructure Lasers* (Academic Press, New York, 1978)

12 all valence band mases from Reference 7

13 D.E. ASPNES, Physical Review **b14**, 5331 (1976)

14 D.E. ASPNES and A.A. STUDNA, Physical Review **B7**, 4605 (1973)

15 E.M. CONWELL and M.O. VASSELL, Physical Review **166**, 797 (1968)

16 F.H. POLLAK, C.W. HIGGINBOTHAM, P. FISCHER and G. KUHN, Physica Status Solidi **b49**, K167 (1972)

17 J.L.T. WAUGH and G. DOLLING, Physical Review **132**, 2410 (1963)

18 D.C. LANGRETH, Physical Review **159**, 717 (1967)

19 O.K. KIM and W.G. SPITZ, Journal of Applied Physics **50**, 4362 (1979)

20 M. CARDONA, *Modulation Spectroscopy* (Academic Press, New York, 1969)

21 R.R.L. ZUCCA, J.P. WALTER, Y.R. SHEN and M.L. COHEN, Solid State Communications **8**, 627 (1970)

22 I. BALSLEV, Physical Review **177**, 1173 (1969)

23 I. BALSLEV, Solid State Communications **5**, 315 (1967)

24 E. MATATAGUI, A.G. THOMPSON and M. CARDONA, Physical Review **176**, 950 (1968)

25 T.S. MOSS, Journal of Applied Physics **32**, 2136 (1961)

26 B.O. SERAPHIN, Journal of Applied Physics **37**, 721 (1966)

27 M. CARDONA, K.L. SHAKLEE and F.H. POLLAK, Physical Review **154**, 696 (1967)

28 T. NISHINO, M. OKUYAMA and Y. HAMAKAWA, Journal of Physics and Chemistry of Solids **30**, 2671 (1969)

29 D.E. ASPNES, C.G. OLSON and D.W. LYNCH, Physical Review **B12**, 2527 (1975)

30 F.H. POLLAK and M. CARDONA, Physical Review **172**, 816 (1968)

31 J.S. BLAKEMORE, Journal of Applied Physics **53**, R123 (1982)

32 K.G. HAMILTON, C. HILSUM and B.R. HOLEMAN, Proceedings of the Physical Society of London **7**, 1147 (1961)

33 B.O. SERAPHIN and H.E. BENNETT in: *Semiconductors and Semimetals*, Vol 10, ed. by R.K. WILLARDSON and A.C. BEER (Academic Press, New York, 1975)

34 D.D. SELL, H.C. CASEY and K.W. WECHT, Journal of Applied Physics **45**, 2650 (1974)

35 D.T.F. MARPLE, Journal of Applied Physics **35**, 1241 (1964)

36 P.Y. YU and M. CARDONA, Physical Review **B2**, 3193 (1970)

37 D.R. PENN, Physical Review **128**; 2093 (1962)

MISSING

PAGE/PAGES

HAS NO

CONTENT

3 Energy Band Structure in Bulk Semiconductors

Introduction

In this chapter, several methods of calculating the energy bands of bulk semiconductors are discussed. The most useful of these for the purpose of obtaining the electronic dispersion in two-dimensional systems is the multiband effective mass theory, based on the **k·p** method. In addition to the usual **k·p** interaction, extra kinetic terms derived from the invariance of the Hamiltonian (mainly from the work of Bir and Pikus[1], Hensel & Suzuki[2] and others[3-5]) result in an 'extended' **k·p** matrix which is more accurate away from the centre of expansion (in terms of perturbation theory).

It will be shown later that there are difficulties in applying a non-perturbational **k·p** matrix in the case of two-dimensional systems. All methods available for the calculation of crystalline electronic states include individual approximation and each has its own particular difficulties. It is generally simpler to consider the implications of the crystal symmetry, rather than the actual precise

details of a crystal potential. Semi-empirical schemes, employing known experimental quantities, are particularly appealing.

The large number of interacting particles which together comprise a crystal, forbids analytical solutions. The basic Hamiltonian of all particles can be described as

$$H_T = T_e + T_N + V_{ee} + V_{eN} + V_{NN} , \tag{3.1}$$

where T_e and T_N are kinetic energies of electrons and nuclei and V_{ee}, V_{eN} and V_{NN} represent the appropriate inter-particle interactions.

The strongest interaction, namely electromagnetic, leads to an expression for the Hamiltonian based on Coulomb forces:

$$H_T = -\sum_i \frac{\hbar^2}{2m}\nabla_i^2 - \sum_I \frac{\hbar^2}{2m_I}\nabla_I^2 + \sum_{i<j} \frac{e^2}{|r_i - r_j|} - \sum_{I,i} \frac{Z_I e^2}{|R_I - r_i|} + \sum_{I<J} \frac{Z_I Z_J e^2}{|R_I - R_J|} , \tag{3.2}$$

where i,j (I,J) refer to the electrons (nuclei), and Z is the nuclear charge.

So far, spin-spin interactions have been neglected and the kinetic energy has been assumed to be non-relativistic. The energy eigenvalues are determined by the Schrödinger equation

$$H_T \Psi(\mathbf{R},\mathbf{r}) = E\Psi(\mathbf{R},\mathbf{r}) , \tag{3.3}$$

where $\mathbf{R}(\mathbf{r})$ represents the spatial and spin coordinates of the nuclei (electrons). To make equation (3.3) tractable, several approximations are required.

(i) Adiabatic approximation

The vastly different masses of the electrons and nuclei leads to the Born-Oppenheimer approximation[6], which splits equation (3.3) into two separate (but interdependent) eigenvalue problems. The electron Hamiltonian is given by

$$H_e = T_e + V_{ee} + V_{eN} , \tag{3.4}$$

or by

$$H_e = -\sum_i \frac{\hbar^2}{2m}\nabla_i^2 + \sum_{i<j} \frac{e^2}{|r_i - r_j|} - \sum_{I,i} \frac{Z_I e^2}{|R_I - r_i|} . \tag{3.5}$$

This gives the electron eigenvalue problem for a specified nuclear spatial configuration, which is written as

$$(T_e + V_{ee} + V_{eN})\Phi_n(\mathbf{R},\mathbf{r}) = E_n(\mathbf{r})\Phi_n(\mathbf{R},\mathbf{r}) , \qquad - \qquad (3.6)$$

where n is the set of electron quantum numbers (at coordinate **r**).

The adiabatic approximation states that the electrons will adjust to a change in nuclear coordinates adiabatically and also demands that $E_n(\mathbf{R})$ and $\Phi_n(\mathbf{R},\mathbf{r})$ are functions of **R** in a smooth and continuous way. The 'separated' wave function is then

$$\Phi_{n,m}(\mathbf{R},\mathbf{r}) = \chi_{n,m}(\mathbf{R})\Psi_n(\mathbf{R},\mathbf{r}) , \qquad (3.7)$$

where the **r**-dependence is limited to Ψ_n and m indicates the quantum numbers for nuclei at coordinates **R**. Equations (3.1) and (3.3) then lead to

$$(T_e + T_N + V_{ee} + V_{eN} + V_{NN})\chi_{n,m}(\mathbf{R})\Psi_n(\mathbf{R},\mathbf{r}) = E_{n,m}\,\chi_{n,m}(\mathbf{R})\Psi_n(\mathbf{R},\mathbf{r}) . \qquad (3.8)$$

To obtain T_N, it is necessary to consider the quantity $\nabla_R^2[\chi_{n,m}(\mathbf{R})\Psi_n(\mathbf{R},\mathbf{r})]$. This is

$$\nabla_R^2[\chi_{n,m}(\mathbf{R})\Psi_n(\mathbf{R},\mathbf{r})] = \Psi_n(\mathbf{R},\mathbf{r})\nabla_R^2\chi_{n,m}(\mathbf{R}) + 2\nabla_R\Psi_n(\mathbf{R},\mathbf{r})\bullet\nabla_R\chi_{n,m}(\mathbf{R}) + \chi_{n,m}(\mathbf{R})\nabla_R^2\Psi_n(\mathbf{R},\mathbf{r}) . \qquad (3.9)$$

The smooth dependence of $\Psi_n(\mathbf{R},\mathbf{r})$ on **R**, leads to the assumed dominance of the first term on the right hand side of equation (3.9). The nuclear kinetic operator is simplified to

$$T_N[\chi_{n,m}(\mathbf{R})\Psi_n(\mathbf{R},\mathbf{r})] \sim \Psi_n(\mathbf{R},\mathbf{r})T_N\chi_{n,m}(\mathbf{R}) . \qquad (3.10)$$

From equations (3.6), (3.10) and (3.8), the fundamental equations of the adiabatic approximation are then

$$[T_N + V_{NN} + E_n(\mathbf{R})]\chi_{n,m}(\mathbf{R}) = E_{n,m}\chi_{n,m}(\mathbf{R}) , \qquad (3.11)$$

along with equation (3.6).

Equation (3.6) gives the electronic energies $E_n(\mathbf{R})$ for a given nuclear configuration **R**. These solutions are then potentials in equation (3.11). This leads to separate (although interdependent)

calculation of the electronic and nuclear energy eigenvalues (lattice vibrational states). To go beyond this approximation and explicitly include the electron-lattice interaction, it is necessary to retain the discarded terms from equation (3.9). However, for a reasonable description of the electronic states, equation (3.6) is used and the nuclei are taken as being in their equilibrium positions (lattice sites).

(ii) One-electron approximation

In order to tackle equation (3.6), an intractable many-body problem, a useful starting point is that of the one-electron approximation[7]. The crystal electron states are represented by a determinantal wavefunction, composed of anti-symmetrised products of one-electron wavefunctions. Variational principles show that the best one-electron wavefunctions, written as a determinantal function, satisfy

$$H_{\mathrm{HF}}\psi_n(\mathbf{r}) = E_n\psi_n(\mathbf{r}) , \tag{3.12a}$$

with

$$H_{\mathrm{HF}} = -\frac{\hbar^2}{2m} - \sum_{\mathrm{I}}\frac{Z_{\mathrm{I}}e^2}{|\mathbf{r}-\mathbf{R}_{\mathrm{I}}|} + V_{\mathrm{coul}} + V_{\mathrm{exch}} , \tag{3.12b}$$

$$V_{\mathrm{coul}}(\mathbf{r}) = e^2\sum_{\mathrm{j}}\int\frac{|\psi_{\mathrm{j}}(\mathbf{r})|^2}{|\mathbf{r}-\mathbf{r}_1|}d\mathbf{r}_1 , \tag{3.12c}$$

and

$$V_{\mathrm{exch}}\psi_n(\mathbf{r}) = -e^2\sum_{\mathrm{j}}\psi_{\mathrm{j}}(\mathbf{r})\int\frac{\psi_{\mathrm{j}}^*(\mathbf{r}_1)\psi_n(\mathbf{r}_1)}{|\mathbf{r}-\mathbf{r}_1|}d\mathbf{r}_1 , \tag{3.12d}$$

and summation over spin is implied.

H_{HF} is the 'Hartree-Fock' Hamiltonian. The Coulomb term is local, but the exchange potential is non-local (i.e. is an integral operator over spatial coordinates). Slater[8] suggested an approximate local exchange term to simplify calculation. Replacing equation (3.6) with equation (3.12) may in certain calculations result in poor approximation. In particular, concerning the ground state energy of atoms and free electron gas, screening effects on the exchange term (higher order corrections) must of necessity be included. In crystals, screening the exchange term[8] by a dielectric function (all other terms remaining unaltered) would better the approximation.

(iii) The band approximation

Equation (3.12) so far still presents considerable mathematical difficulty (ignoring even the numerical work involved). The band approximation is basically an assumption of a known crystal potential, such that

$$\left[-\frac{\hbar^2\nabla^2}{2m} + V(\mathbf{r})\right]\psi_n(\mathbf{k},\mathbf{r}) = E_n(\mathbf{k})\psi_n(\mathbf{k},\mathbf{r}) , \qquad (3.13)$$

where V(**r**) is invariant under all the symmetry operations of the crystal space group. The usual initial assumption is a sum of atomic-like potentials based on free atom calculations. The electronic states are largely dependent on the symmetry properties of the crystal potential and not the fine detail in its structure and for this the band approximation will be good. Obtaining accurate values of physical quantities strongly dependent on the crystal potential would not be a reasonable goal in this case.

Self-consistent calculations can improve this aspect considerably. Several well-known methods are then readily available. These comprise the tight-binding method, orthogonalised plane wave (OPW) method and the pseudopotential formulation. These methods expand the crystal potential in a complete set of Bloch type functions and obtain coefficients of the expansion such that the energy eigenvalues satisfy the Schrödinger equation.

The cellular method, augmented plane wave method and Green's function method expand the crystal states in a complete set of solutions of the Schrödinger equation within a unit cell. Appropriate boundary conditions then determine the coefficients of the expansion.

Semi-empirical approaches, making use of experimental data to determine known quantities from the band calculation are also effective. Two such methods are the quantum defect method and the semi-empirical pseudopotential approach.

More important to the present work is the **k·p** interpolation method, which uses knowledge of the band structure at one or more values of **k** to obtain the band structure throughout the Brillouin zone. Several of these methods will be briefly discussed below. The **k·p** method will be discussed in detail and relativistic effects included where necessary.

The tight binding method

This was originally suggested by Bloch[9] in 1928. Suppose that $\phi(\mathbf{r})$ is the eigenstate for an isolated atom, with eigenvalue E_o and that it is normalised and non-degenerate. The basic assumption is that the overlap of this state $\phi(\mathbf{r})$ with its neighbours is small and that the extra potential energy seen by

the electrons in the crystal is small in comparison to the atomic potential. The Hamiltonian is then

$$H = H_{\text{atom}} + H_{\text{crystal}} , \tag{3.14}$$

and $\phi(\mathbf{r})$ is an eigenstate of H_{atom}, with eigenvalue E_o. H_{crystal} is often taken as a perturbation.

If the atoms lie on lattice sites τ_m, then for an electron near $\tau_m = 0$, the eigenfunction is approximately $\phi(\mathbf{r})$. At site τ_m, the eigenfunction is approximately $\phi(\mathbf{r}-\tau_m)$. A wavefunction for a single electron in the whole crystal is therefore

$$\psi_k(\mathbf{r}) = \sum_m C_{km}\phi(\mathbf{r}-\tau_m) . \tag{3.15}$$

For a Bloch form

$$C_{km} = \frac{1}{\sqrt{N}} e^{i\mathbf{k}\cdot\tau_m} , \tag{3.16}$$

and the wavefunction is

$$\psi_k(\mathbf{r}) = \frac{1}{\sqrt{N}} \sum_{\tau_m} e^{i\mathbf{k}\cdot\tau_m}\phi(\mathbf{r}-\tau_m) . \tag{3.17}$$

The use of atomic wavefunctions means that the total wavefunction is a linear combination of atomic orbitals (LCAO). Since H_{crystal} is a perturbation, the energy shift for the wavefunction (i.e. the shift when going to an LCAO wavefunction) is

$$< \psi_k(\mathbf{r}) | H_{\text{crystal}} | \psi_k(\mathbf{r}) > = \frac{1}{N} \sum_m \sum_j e^{i\mathbf{k}\cdot(\tau_m-\tau_j)} \int \psi_j^* H_{\text{crystal}} \psi_m \, d\mathbf{r} , \tag{3.18}$$

where $\psi_m \equiv \psi(\mathbf{r}-\tau_m)$. Keeping only terms with j = m and with j,m nearest neighbours (the tight-binding approximation) gives

$$E_k = E_o - \alpha - \gamma \sum_m e^{i\mathbf{k}\cdot(\tau_m-\tau_j)} , \tag{3.19a}$$

$$\alpha \equiv - < \psi_m | H_{\text{crystal}} | \psi_m > , \tag{3.19b}$$

$$\gamma \equiv - < \psi_k | H_{\text{crystal}} | \psi_m > , \tag{3.19c}$$

and the sum is over nearest neighbours. The sum over lattice points cancels the factor N^{-1} in

equation (3.18).

For a simple cubic lattice, the sum over nearest neighbours involves

$$\tau_m - \tau_j = (\pm a,0,0)\ ;\ (0,\pm a,0)\ ;\ (0,0,\pm a)\ , \qquad (3.20)$$

where a is the lattice constant. It is straightforward to obtain E vs. **k** as

$$E(\mathbf{k}) = E_o - \alpha - 2\gamma\left(\cos k_x a + \cos k_y a + \cos k_z a\right)\ . \qquad (3.21)$$

Obviously the minimum, -6γ occurs at k = 0 and the maximum, +6γ at $\pm\frac{\pi}{a}$ in each direction, in terms of the **k**-dependence only. For small k,

$$E(\mathbf{k}) \approx E_o - \alpha - 6\gamma + \gamma \mathbf{k}^2 a^2\ , \qquad (3.22)$$

which gives spherical energy surfaces near k = 0 and an effective mass of $m^* = \hbar^2/(2\gamma a^2)$.

For an fcc lattice, the **k**-dependence is given by

$$E(\mathbf{k}) = -4\gamma\left[\left(\cos\frac{k_y a}{2}\right)\left(\cos\frac{k_z a}{2}\right)+\left(\cos\frac{k_z a}{2}\right)\left(\cos\frac{k_x a}{2}\right)+\left(\cos\frac{k_x a}{2}\right)\left(\cos\frac{k_y a}{2}\right)\right]\ . \qquad (3.23)$$

The tight-binding method as outlined above can only give reliable results for low energy, well-localised states. Excited states extend over many neighbours and have a continuous spectrum above the ionisation energy.

The matrix elements of the form

$$\int |\psi_m(\mathbf{r}-\tau_m)|^2 H_{crystal}\, d^3\mathbf{r}\ ,$$

known as crystal field integrals, depend critically on the tails of the atomic-like potentials and are different from those of free atoms.

One method of improving the approximation is to use different wavefunctions[10] which are not atomic wavefunctions. These could be solutions of the Schrödinger equation for a single atom, but with a non-atomic potential, to allow for the presence of other atoms in the lattice. These potentials would have the symmetry of the lattice and a self-consistent procedure should result in a better approximation.

The pseudopotential method

The pseudopotential method[11] for calculating the energy structure in crystals is based on the fact that conduction and valence states must be orthogonal to the core states. The effect of orthogonality however is used to further the development of approximation or interpolation procedures.

A conduction or valence state $\varphi_v(\mathbf{k},\mathbf{r})$ satisfies the Schrödinger equation

$$\left[\frac{\mathbf{p}^2}{2m} + V(\mathbf{r})\right]\varphi_v(\mathbf{k},\mathbf{r}) = E(\mathbf{k})\,\varphi_v(\mathbf{k},\mathbf{r}) , \tag{3.24}$$

and the orthogonality condition

$$< \varphi_c \mid \varphi_v > = 0 , \tag{3.25}$$

where φ_c is a core state.

It is possible to write φ_v as

$$\psi(\mathbf{k},\mathbf{r}) = \varphi_v(\mathbf{k},\mathbf{r}) - \sum_c < \varphi_c \mid \varphi_v > \varphi_c . \tag{3.26}$$

Schrödinger's equation is then given by

$$\left[\frac{\mathbf{p}^2}{2m} + V(\mathbf{r})\right]\varphi_v(\mathbf{k},\mathbf{r}) + \sum_c [E_v(\mathbf{k}) - E_c] < \varphi_c \mid \varphi_v > \varphi_c = E_v(\mathbf{k})\,\varphi_v(\mathbf{k},\mathbf{r}) . \tag{3.27}$$

The eigenvalues of (3.27) and (3.24) are the same and the crystal potential V(r) is replaced by the operator

$$V(r) + \sum_c [E_v(k) - E_c] \mid \varphi_c >< \varphi_c \mid \equiv V_p . \tag{3.28}$$

It is easily verified that the functions $\Phi_v = \phi_v + \sum_c a_c \varphi_c$ also satisfy equation (3.27), and the a_c are arbitrary coefficients. Therefore the pseudopotential equation (3.27) can be written as

$$\left[\frac{\mathbf{p}^2}{2m} + V(\mathbf{r})\right]\varphi_v(\mathbf{k},\mathbf{r}) + \sum_c < \varphi_c \mid \mathbf{A} \mid \varphi_v > \varphi_c = E_v(\mathbf{k})\,\varphi_v(\mathbf{k},\mathbf{r}) , \tag{3.29}$$

where A is an arbitrary operator. The choice of A determines the choice of ϕ_v, but does not alter the

eigenvalues of equation (3.27). Further it is easily shown[12] that

$$< \varphi_c \mid \mathbf{A} \mid \varphi_v > \; = \; \left[E_v(\mathbf{k}) \; - \; E_c\right] < \varphi_c \mid \varphi_v > \; . \qquad (3.30)$$

Equations (3.28), (3.29) and (3.30) are the basic fundamentals of pseudopotential theory. From (3.28), it is clear that orthogonalisation is used to subtract from $V(\mathbf{r})\phi_v$ the part expandable in core states, thus reducing V_p in the core region and giving a smooth pseudopotential. The crystal pseudopotential is usually taken as the sum of spherically symmetric local pseudopotentials centred on atomic sites

$$V_p \; = \; \sum_{\tau_v} \sum_{d_\mu} V_{p,\mu}(\mathbf{r} \; - \; d_\mu \; - \; \tau_v) \; . \qquad (3.31)$$

Diagonalising the pseudopotential Hamiltonian

$$H_p \; = \; -\left(\frac{\hbar^2 \nabla^2}{2m}\right) \; + \; V_p \; , \qquad (3.32)$$

leads to a determinantal equation with matrix elements

$$< W_{k_i} \mid H_p - E \mid W_{k_j} > \; = \; \left(\frac{\hbar^2 k_i^2}{2m} - E\right)\delta_{ij} \; + \; \sum_{d_\mu} e^{-i(h_i - h_j) \bullet d_\mu} V_{p,\mu}\left(h_i - h_j\right) \; , \qquad (3.33)$$

where

$$W_{k_j} \; = \; \frac{1}{\sqrt{NV}} \, e^{i(k \, + \, h_j) \bullet r} \; .$$

The Fourier coefficients $V_{p,\mu}(h_i\text{-}h_j)$ are usually treated as disposable parameters, fitting some experimental data which depends on the electronic band structure, often electroreflectance.

Setting $V(h_i\text{-}h_j)$ to zero for sufficiently large $|h_i\text{-}h_j|$ leads to reasonable small equations. For example the valence and conduction bands of Germanium have been reasonably calculated[13] using only the reciprocal lattice vectors

$$\frac{2\pi}{a}(\pm 1,\pm 1,\pm 1), \quad \frac{2\pi}{a}(\pm 2,\pm 2,0), \quad \frac{2\pi}{a}(\pm 3,\pm 1,\pm 1),$$

for the Fourier components of the pseudopotential and with values of -0.23, 0.0 and 0.06 Rydbergs respectively. This takes $V_p(h) = 0$ for $(a^2h^2)/(4\pi^2) > 11$. By using different local pseudopotentials for different valence electron states (i.e. angular momentum-dependent pseudopotentials) enables

crystal states to be calculated from atomic data of excited valence states. This reduces the simplicity however and assumes that atomic core states are similar to crystal core states, which can reduce the validity of the approximation for small lattice spacing (large atomic overlap).

The **k·p** method

The **k·p** method is an extremely powerful method when used in conjunction with *a priori* methods. Introduced by Bardeen[14] and Seitz[7] it is mainly used as a method of determining the effective masses and crystal wavefunctions near points of high symmetry in **k**-space. It was later extended[15,16] to include the spin-orbit interaction. The method can be used to obtain the band structure throughout the entire Brillouin zone[17], based on *a priori* calculations performed only at $\mathbf{k} = 0$.

Suppose that we know the eigenfunctions $\phi_n(\mathbf{k}_o,\mathbf{r})$ and eigenvalues $E_n(\mathbf{k}_o)$ of the Hamiltonian

$$\left[\frac{\mathbf{p}^2}{2m} + V(\mathbf{r})\right]\phi_n(\mathbf{k}_o,\mathbf{r}) = E_n(\mathbf{k}_o)\phi_n(\mathbf{k}_o,\mathbf{r}) ,$$

at the wavevector $\mathbf{k}_o$. Typically this is the point of highest symmetry, $\mathbf{k}_o = 0$. The Bloch functions $\phi_n(\mathbf{k}_o,\mathbf{r})\exp[i(\mathbf{k}-\mathbf{k}_o)\cdot\mathbf{r}]$ are a suitable set in which to expand the crystal wavefunctions $\phi(\mathbf{k},\mathbf{r})$. This leads to

$$\phi(\mathbf{k},\mathbf{r}) = \sum_n c_n(\mathbf{k}) e^{i(\mathbf{k}-\mathbf{k}_o)\cdot\mathbf{r}} \phi_n(\mathbf{k}_o,\mathbf{r}) . \tag{3.34}$$

An alternative is to expand the periodic part of the wavefunction at **k** in terms of the periodic parts of the Bloch functions at $\mathbf{k}_o$. Applying the variational principle with respect to the coefficients c_n, the eigenvalues E(**k**) and the eigenfunctions (3.34) of the crystal Hamiltonian are solutions of the secular equation

$$\left\| < e^{i(\mathbf{k}-\mathbf{k}_o)\cdot\mathbf{r}}\phi_{n'}(\mathbf{k}_o,\mathbf{r}) \mid H - E \mid e^{i(\mathbf{k}-\mathbf{k}_o)\cdot\mathbf{r}}\phi_n(\mathbf{k}_o,\mathbf{r}) > \right\| = 0 . \tag{3.35}$$

Given that

$$\left[\frac{\mathbf{p}^2}{2m} + V(\mathbf{r})\right] e^{i(\mathbf{k}-\mathbf{k}_o)\cdot\mathbf{r}}\phi_n(\mathbf{k}_o,\mathbf{r}) = e^{i(\mathbf{k}-\mathbf{k}_o)\cdot\mathbf{r}}\left[\frac{\hbar^2}{2m}(\mathbf{k}-\mathbf{k}_o)^2 + \frac{\hbar}{m}(\mathbf{k}-\mathbf{k}_o)\cdot\mathbf{p} + E_n(\mathbf{k}_o)\right]\phi_n(\mathbf{k}_o,\mathbf{r}) \tag{3.36}$$

then equation (3.35) becomes

$$\left\| < \left[\frac{\hbar^2}{2m}(\mathbf{k}-\mathbf{k}_o)^2 + E_n(\mathbf{k}_o) - E\right]\delta_{n'n} + \frac{\hbar}{m}(\mathbf{k}-\mathbf{k}_o)\bullet \mathbf{M}_{n'n}(\mathbf{k}_o) > \right\| = 0\,, \quad (3.37)$$

where

$$\mathbf{M}_{n'n}(\mathbf{k}_o) = \int \phi^*_{n'}(\mathbf{k}_o,\mathbf{r})\,\mathbf{p}\,\phi_n(\mathbf{k}_o,\mathbf{r})\,d\mathbf{r}\,, \quad (3.38)$$

integrated over the normalisation volume of the $\phi_n(\mathbf{k}_o,\mathbf{r})$, which is the crystal volume. Given the eigenvalues and eigenfunctions at $\mathbf{k}_o$, then (3.37) gives these values throughout the entire Brillouin zone. Using the effects of crystal symmetry, the matrix elements (3.38) may be given in terms of relatively few parameters. Use of the commutator $[\mathbf{H},\mathbf{r}] = (i\hbar/m)\mathbf{p}$ and since the $\phi_n(\mathbf{k}_o,\mathbf{r})$ are eigenfunctions of the crystal Hamiltonian, then for $E_n(\mathbf{k}_o) \neq E_{n'}(\mathbf{k}_o)$

$$\mathbf{M}_{n'n}(\mathbf{k}_o) = \frac{m}{ih}\left[E_{n'}(\mathbf{k}_o) - E_n(\mathbf{k}_o)\right]\int \phi^*_{n'}(\mathbf{k}_o,\mathbf{r})\,\mathbf{r}\,\phi_n(\mathbf{k}_o,\mathbf{r})\,d\mathbf{r}\,. \quad (3.39)$$

Since $\phi_{n'}(\mathbf{k}_o,\mathbf{r})$ and $\phi_n(\mathbf{k}_o,\mathbf{r})$ belong to the irreducible representation of the double group at $\mathbf{k}_o$ and $\mathbf{r}$ belongs to the representation of the simple group at $\mathbf{k}_o$, the use of group theory enables the number of parameters needed in equation (3.37) to be greatly reduced and easily obtained from group multiplication tables[18] for the elements

$$< \phi^{(\mathbf{k}_o,\mu)}_{n'} \,|\, \mathbf{r} \,|\, \phi^{(\mathbf{k}_o,\nu)}_{n} > \,, \quad (3.40)$$

where μ,ν label the irreducible representations of the bands n', n.

The accuracy of the results depends on the number of basis states (i.e. bands) included in the expansion (3.34). The parameters used in later chapters will be calculated by considering 14 bands (including spin). Since the calculation of optical properties will require E(k) for many points throughout the Brillouin zone (typically around forty thousand are included in the calculations in this thesis), the advantage in using this method is remarkable.

In the absence of *a priori* calculations, the use of experimental data such as energy gaps and effective masses at some value $\mathbf{k}_o$ can be used to fit values of the matrix elements[19] $\mathbf{M}_{n'n}(\mathbf{k}_o)$. Given that the basis set for expansion is large enough, reliable values of $\mathbf{M}_{n'n}(\mathbf{k})$ may be obtained throughout the entire Brillouin zone, by calculating the eigenvectors of equation (3.37) and using the expansion (3.34). In most cases of interest, it is enough to consider the behaviour of the energy

bands and wavefunctions near high symmetry points in k-space (such as Γ, L and X). At such a point, $\mathbf{k}_o$ say, then for $\mathbf{k} \approx \mathbf{k}_o$, the non-diagonal matrix elements are small and in second order of perturbation theory this gives

$$E_n(\mathbf{k}-\mathbf{k}_o) = E_n(\mathbf{k}_o) + \frac{\hbar^2}{2m}(\mathbf{k}-\mathbf{k}_o)^2 + \frac{\hbar}{m}(\mathbf{k}-\mathbf{k}_o)\bullet\mathbf{M}_{nn}(\mathbf{k}_o) + \frac{\hbar^2}{m^2}\sum_{n'\neq n}\frac{\left|(\mathbf{k}-\mathbf{k}_o)\bullet\mathbf{M}_{n'n}(\mathbf{k}_o)\right|^2}{E_n(\mathbf{k}_o)-E_{n'}(\mathbf{k}_o)} . \tag{3.41}$$

If $\mathbf{k}_o$ is an extremum ($\frac{\partial E}{\partial \mathbf{k}} = 0$) then $\mathbf{M}_{nn}(\mathbf{k}_o) = 0$ and the effective mass in the direction of a principal axis of unit vector $\mathbf{u}$ is given by

$$\frac{1}{m_u^*} = \frac{1}{m} + \frac{2}{m^2}\sum_{n'\neq n}\frac{\left|\mathbf{u}\bullet\mathbf{M}_{n'n}(\mathbf{k}_o)\right|^2}{E_n(\mathbf{k}_o)-E_{n'}(\mathbf{k}_o)} . \tag{3.42}$$

This indicates that interaction with higher (lower) bands tends to increase (decrease) the effective mass. For degenerate or nearly degenerate bands at $\mathbf{k}_o$, equation (3.41) must be replaced by that obtained by diagonalising the appropriate determinant (3.37) at $\mathbf{k}_o$. Details of this straightforward procedure have been described fully by Kane.[20]

Relativistic effects

To include relativistic effects for the motion of an electron in a potential V(r), it is necessary to consider the Dirac equation

$$\left[c\,\alpha\bullet\mathbf{p} + \beta mc^2 + V(\mathbf{r})\right]\phi = W\phi , \tag{3.43}$$

where ϕ is a four-component spinor, $\mathbf{p}$ is the operator $-i\hbar\nabla$, α represents the matrix $\begin{pmatrix} 0 & \sigma \\ \sigma & 0 \end{pmatrix}$, and $\beta = \begin{pmatrix} 1 & 0 \\ 0 & -1 \end{pmatrix}$. The σ are the Pauli spin operator matrices and 1 indicates the 2x2 unit matrix. $W = E + mc^2$ is the total energy (including the rest energy mc^2).

In order to decouple the strong and weak components of the Dirac spinor, it is necessary to apply the Foldy-Wouthuysen transformation.[21] For $\mathbf{p}/(mc) \ll 1$, this gives the wave equation for the upper two-component spinor as

$$\left[\frac{\mathbf{p}^2}{2m} + V(\mathbf{r}) - \frac{\mathbf{p}^4}{8m^3c^2} - \frac{\hbar^2}{4m^2c^2}\nabla V \bullet \nabla + \frac{\hbar}{4m^2c^2}\sigma \bullet (\nabla V \times \mathbf{p})\right]\phi = E\,\phi\,. \qquad (3.44)$$

This is commonly referred to as the Schrödinger-Pauli equation. Three new terms appear in this equation in addition to the non-relativistic terms $\frac{\mathbf{p}^2}{2\mathrm{m}} + \mathrm{V}(\mathbf{r})$.

(i) $$H_v = -\frac{\mathbf{p}^4}{8m^3c^2}\,.$$

This is a relativistic correction to the kinetic energy. Expanding the kinetic energy in powers of p gives:

$$\sqrt{(c^2\mathbf{p}^2 + m^2c^4)} = mc^2 + \frac{\mathbf{p}^2}{2m} - \frac{\mathbf{p}^4}{8m^3c^2} + \ldots$$

(ii) $$H_d = -\frac{\hbar^2}{4m^2c^2}\nabla V \bullet \nabla = \frac{\hbar^2}{8m^2c^2}\nabla^2 V\,.$$

This is a relativistic correction to the potential V(r), and known as the Darwin correction.

(iii) $$H_{so} = \frac{\hbar}{4m^2c^2}\sigma \bullet (\nabla V \times \mathbf{p})\,.$$

This is the spin-orbit coupling which mixes the two components of the Pauli spinor. It originates in the interaction of the electron spin magnetic moment with the magnetic field 'seen' by the electron. Since H_v and H_d do not depend on electron spin, they do not change the symmetry properties of the Hamiltonian. The term H_{so} couples operators in both spin space and ordinary space, reducing the symmetry. The eigenstates of the Schrödinger equation are classified by the irreducible representations of the symmetry group of the Hamiltonian and those of equation (3.44) are classified by the irreducible representations of the corresponding double group. Determining how the states of the simple group split into the states of the double group enables the removal of degeneracy due to the spin-orbit interaction to be determined. Note that the operator H_{so} is invariant only under simultaneous rotations in both spin space and real space. To calculate the spin-orbit interaction in a particular crystal, it is possible to use a simple tight-binding method. Although not generally accurate for the total energy of an electronic state, relativistic effects are only important near the nuclei, where the potential is strong and the kinetic energy is consequently large. If the crystal

potential is taken as the sum of atomic-like spherically-symmetric potentials, the H_{so} term can be written as

$$H_{so} = \frac{\hbar}{4m^2c^2} \sum_{\tau_v} \sum_{d_\mu} \frac{1}{|\mathbf{r}-d_\mu-\tau_v|} \frac{dV_\mu(\mathbf{r}-d_\mu-\tau_v)}{d(\mathbf{r}-d_\mu-\tau_v)} \sigma \bullet \mathbf{l}(\mathbf{r}-d_\mu-\tau_v) \ . \qquad (3.45)$$

If, as before, the wavefunctions are taken as

$$\psi_{\mu\nu}(\mathbf{k},\mathbf{r}) = \frac{1}{\sqrt{N}} \sum_{\tau_\mu} e^{i\mathbf{k}\bullet\tau_v} \phi_{\mu\nu}(\mathbf{r}-d_\mu-\tau_v) \ , \qquad (3.46)$$

where n indicates the quantum numbers (nlms), including the spin quantum number, the simplest matrix elements are of the type

$$< \psi_{\mu' n' l' m' s'} | H_{so} | \psi_{\mu n l m s} > = \delta_{\mu'\mu} \delta_{n'n} \delta_{l'l} < s' | \sigma | s > \bullet < Y_{l'm'} | \mathbf{l} | Y_{lm} > \frac{1}{2\hbar} \xi_{\mu n l} \ , \qquad (3.47)$$

where

$$\xi_{\mu n l} = \frac{\hbar^2}{2m^2c^2} \int_0^\infty r R^2_{\mu n l}(\mathbf{r}) \frac{dV_\mu(\mathbf{r})}{dr} dr \ .$$

The spin matrix elements and angular momentum matrix elements can be immediately evaluated. The properties of the Pauli spin matrices give

$$\begin{aligned}
< u_+ | \sigma | u_+ > \bullet < Y_{lm} | \mathbf{l} | Y_{l'm'} > &= < Y_{lm} | l_z | Y_{l'm'} > \ , \\
< u_- | \sigma | u_- > \bullet < Y_{lm} | \mathbf{l} | Y_{l'm'} > &= - < Y_{lm} | l_z | Y_{l'm'} > \ , \\
< u_+ | \sigma | u_- > \bullet < Y_{lm} | \mathbf{l} | Y_{l'm'} > &= < Y_{lm} | l_x - i l_y | Y_{l'm'} > \ , \\
< u_- | \sigma | u_+ > \bullet < Y_{lm} | \mathbf{l} | Y_{l'm'} > &= < Y_{lm} | l_x + i l_y | Y_{l'm'} > \ .
\end{aligned}$$

and the properties of the angular momentum operators give

$$\begin{aligned}
l_z Y_{lm} &= m\hbar Y_{lm} \ , \\
(l_x + i l_y) Y_{lm} &= [(l-m)(l+m+1)]^{1/2} \hbar Y_{l,m+1} \ , \\
(l_x - i l_y) Y_{lm} &= [(l+m)(l-m+1)]^{1/2} \hbar Y_{l,m-1} \ .
\end{aligned}$$

At high symmetry points of the Brillouin zone, the irreducible representations of the double group may be expressed in terms of the spherical harmonics Y_{lm}. This allows equation (3.47) to be

evaluated in a particularly simple fashion. At Γ the lowest conduction band is described by s-type states and the highest valence bands by p-type states.

k·p band structure of GaAs

To ensure reasonable accuracy, the **k·p** expansion should be performed with as many bands as possible. This depends on the experimental data available concerning the energy gaps and effective masses at the chosen value of $\mathbf{k}_o$ in equation (3.37). Using equation (3.37) and considering only the states Γ_6^c, Γ_{7+8}^v and Γ_{7+8}^c and taking $\mathbf{k}_o = 0$, gives the following **k·p** matrix with the direction of angular momentum quantisation along the z-axis

$$\mathbf{H} = \begin{vmatrix} \mathbf{H}_{c'c'} & \mathbf{H}_{c'c} & \mathbf{H}_{c'v} \\ \mathbf{H}_{cc'} & \mathbf{H}_{cc} & \mathbf{H}_{cv} \\ \mathbf{H}_{vc'} & \mathbf{H}_{vc} & \mathbf{H}_{vv} \end{vmatrix}, \tag{3.48}$$

with solution given by

$$\det | \mathbf{H} - \lambda \mathbf{I} | = 0, \tag{3.49}$$

where **I** represents the 14x14 unit matrix.

In equation (3.48) each submatrix is given by

$$\mathbf{H}_{c'c'} = \begin{vmatrix} E_o' + \Delta_o' + \varepsilon & 0 & 0 & 0 & 0 & 0 \\ 0 & E_o' + \Delta_o' + \varepsilon & 0 & 0 & 0 & 0 \\ 0 & 0 & E_o' + \Delta_o' + \varepsilon & 0 & 0 & 0 \\ 0 & 0 & 0 & E_o' + \Delta_o' + \varepsilon & 0 & 0 \\ 0 & 0 & 0 & 0 & E_o' + \varepsilon & 0 \\ 0 & 0 & 0 & 0 & 0 & E_o' + \varepsilon \end{vmatrix}$$

$$\mathbf{H}_{cc} = \begin{vmatrix} E_o + \varepsilon & 0 \\ 0 & E_o + \varepsilon \end{vmatrix}$$

$$\mathbf{H}_{vv} = \begin{vmatrix} \varepsilon & 0 & 0 & 0 & 0 & 0 \\ 0 & \varepsilon & 0 & 0 & 0 & 0 \\ 0 & 0 & \varepsilon & 0 & 0 & 0 \\ 0 & 0 & 0 & \varepsilon & 0 & 0 \\ 0 & 0 & 0 & 0 & -\Delta_o + \varepsilon & 0 \\ 0 & 0 & 0 & 0 & 0 & -\Delta_o + \varepsilon \end{vmatrix}$$

$$\mathbf{H}_{c'c} = \begin{vmatrix} -\frac{1}{\sqrt{2}}P'k_- & 0 \\ \sqrt{\frac{2}{3}}P'k_z & -\frac{1}{\sqrt{6}}P'k_- \\ \frac{1}{\sqrt{6}}P'k_+ & \sqrt{\frac{2}{3}}P'k_z \\ 0 & \frac{1}{\sqrt{2}}P'k_+ \\ -\frac{1}{\sqrt{3}}P'k_z & -\frac{1}{\sqrt{3}}P'k_- \\ -\frac{1}{\sqrt{3}}P'k_+ & \frac{1}{\sqrt{3}}P'k_z \end{vmatrix}$$

$$\mathbf{H}_{c'v} = \begin{vmatrix} 0 & \frac{i}{\sqrt{3}}Qk_+ & \frac{i}{\sqrt{3}}Qk_z & 0 & -\frac{i}{\sqrt{6}}Qk_+ & -i\sqrt{\frac{2}{3}}Qk_z \\ -\frac{i}{\sqrt{3}}Qk_- & 0 & 0 & \frac{i}{\sqrt{3}}Qk_z & 0 & \frac{i}{\sqrt{2}}Qk_+ \\ -\frac{i}{\sqrt{3}}Qk_z & 0 & 0 & -\frac{i}{\sqrt{3}}Qk_+ & -\frac{i}{\sqrt{2}}Qk_- & 0 \\ 0 & -\frac{i}{\sqrt{3}}Qk_z & \frac{i}{\sqrt{3}}Qk_- & 0 & -i\sqrt{\frac{2}{3}}Qk_z & \frac{i}{\sqrt{6}}Qk_- \\ \frac{i}{\sqrt{6}}Qk_- & 0 & \frac{i}{\sqrt{2}}Qk_+ & i\sqrt{\frac{2}{3}}Qk_z & 0 & 0 \\ i\sqrt{\frac{2}{3}}Qk_z & -\frac{i}{\sqrt{2}}Qk_- & 0 & -\frac{i}{\sqrt{2}}Qk_+ & 0 & 0 \end{vmatrix}$$

$$\mathbf{H}_{cv} = \begin{vmatrix} -\frac{1}{\sqrt{2}}Pk_+ & \sqrt{\frac{2}{3}}Pk_z & \frac{1}{\sqrt{6}}Pk_- & 0 & -\frac{1}{\sqrt{3}}Pk_z & -\frac{1}{\sqrt{3}}Pk_- \\ 0 & -\frac{1}{\sqrt{6}}Pk_+ & \sqrt{\frac{2}{3}}Pk_z & \frac{1}{\sqrt{2}}Pk_- & -\frac{1}{\sqrt{3}}Pk_+ & \frac{1}{\sqrt{3}}Pk_z \end{vmatrix}$$

and

$$\mathbf{H}_{c'c} = \mathbf{H}^*_{cc'}, \qquad \mathbf{H}_{vc'} = \mathbf{H}^*_{c'v}, \qquad \mathbf{H}_{vc} = \mathbf{H}^*_{cv},$$

and where $\varepsilon=(\hbar^2k^2/2m_o)$ and $k_\pm=k_x\pm ik_y$. The zero of energy is taken at the top of the Γ_8 valence band at k=0. The momentum matrix elements are obtained by obtaining a basis for each state at k=0, using standard group multiplication tables[18] and following the convention, adopted by Kane[16] that the matrix elements between the Γ_6 and $\Gamma^v_{7,8}$ states be purely real (this introduces a fixed choice of phase factor in each basis). Note that the group tables in Ref. 18 contain several errors for the group T_d. A correct form of the character table for T_d may be found in Ref. 22. If uncorrected, these errors would lead to an incorrect choice of basis. Although many different bases appear in the literature,[5,23,24] most differ only in the choice of phase factor. However, several others[25,26] do not lead to correct results. The matrix elements in equation (3.48) have the following form

$$\begin{aligned} P &= i\frac{\hbar}{m} < \Gamma^v_{5,x} | p_x | \Gamma_6 > \\ P' &= i\frac{\hbar}{m} < \Gamma^c_{5,x} | p_x | \Gamma_6 > \\ Q &= i\frac{\hbar}{m} < \Gamma^v_{5,x} | p_y | \Gamma^c_{5,z} > , \end{aligned} \tag{3.50}$$

where the single band approximation has been used. This is simply the assumption of similar momentum matrix elements between the states of a given Γ_5 multiplet (i.e. $\Gamma_{7,8}$) and any other state of interest.

The basis used to obtain equation (3.48) is given in Table 3.1. Note that the symmetry group of equation (3.48) is O_h. Since the zinc-blende structure (group T_d or $\bar{4}3m$) lacks inversion symmetry, then equation (3.48) has artificially high symmetry. In GaAs (and AlGaAs) there is in general no degeneracy at a general point **k**. Whether splitting of the eigenvalues occurs can be determined from the structure of the double group reprsentations. The splittings are small or zero along the directions [100] and [111] and largest along the direction [110]. Typically they are less than 0.25meV at any point within the Brillouin zone. This is not apparent from equation (3.48) which contains only a few chosen interactions. Also, the basis in Table 3.1 diagonalises the spin-orbit interaction within any given Γ_5 multiplet - i.e. effect of spin-orbit interaction is seen within the diagonal terms only. However, the spin-orbit interaction couples the Γ_5^c and Γ_5^v states, through the term

$$\Delta^- = \frac{-3i\hbar}{4m_o^2c^2} < \Gamma_{5,x}^v \left| [\nabla V, p]_y \right| \Gamma_{5,z}^c > \ . \tag{3.51}$$

This term is extremely small,[27] around -70meV and can be reliably ignored. Also omitted from equation (3.48) are terms linear in **k**, which split the Γ_8^v bands along [110] and the $\Gamma_5^v(3/2,\pm 3/2)$ bands along [111].

To make the problem as tractable as possible it is convenient to reduce the size of the Hamiltonian as far as possible. The Hamiltonians used in this thesis were obtained using invariant expansion methods by Luttinger and Kohn[28] and by Braun and Rössler.[29] Although involving a group-theoretic analysis the approach is simple to describe. From group multiplication tables it is possible to obtain all non-zero matrix elements connecting the states of interest, in terms of the set of basis functions comprising each representation. This requires that each basis function be in the (J,m_J) angular momentum representation. Terms required are of the form

$$\mathbf{H}_{ij} = \sum_n < \Gamma_i | \Gamma_n | \Gamma_j > \ , \tag{3.52}$$

where Γ_n runs over all representations of the group. For the closest bands, the weighting factors are simply obtained using standard **k·p** perturbation theory.

This is the approach of Braun and Rössler[29] for the conduction band in GaAs. They obtain the lowest conduction band dispersion as

$$E(\mathbf{k}) = \frac{\hbar^2\mathbf{k}^2}{2m^*} + \alpha_o\mathbf{k}^4 + \beta_o\left(k_x^2k_y^2 + k_y^2k_z^2 + k_z^2k_x^2\right) \pm \gamma_o\left[\mathbf{k}^2\left(k_x^2k_y^2 + k_y^2k_z^2 + k_z^2k_x^2\right) - 9k_x^2k_y^2k_z^2\right]^{1/2} . \quad (3.53)$$

The parameters α_o, β_o and γ_o which are obtained in this case from a 14-band $\mathbf{k}\cdot\mathbf{p}$ calculation can therefore be given in terms of the standard band structure parameters. These are the momentum matrix elements and the energy gaps. In Ref. 29 the terms α_o, β_o and γ_o are all given in so-called magnetic units, since the purpose of that paper was to investigate magneto-optic transitions and the effects of the conduction band nonparabolicity. Since it may prove rather difficult to extricate anything from the equations as given in Ref. 29, we re-write them in full in SI units for convenience.

$$\begin{aligned}
\alpha_o = & -\frac{\hbar^2P^2}{6m}\left(\frac{2}{E_o^2} + \frac{1}{(E_o+\Delta_o)^2}\right)(1 + C' + \gamma_1') \\
& -\frac{\hbar^2P^2}{3m}\left(\frac{1}{E_o^2} + \frac{2}{E_o(E_o+\Delta_o)}\right)\gamma_2' \\
& -\frac{\hbar^2(P')^2}{6m}\left(\frac{2}{(E_o - E_o' - \Delta_o')^2} + \frac{1}{(E_o - E_o')^2}\right)(1 + C') \\
& -\frac{P^4}{9}\left(\frac{2}{E_o^2} + \frac{1}{(E_o+\Delta_o)^2}\right)\left(\frac{2}{E_o} + \frac{1}{E_o+\Delta_0}\right) \\
& -\frac{P^2(P')^2}{9}\left(\frac{2}{E_o^2} + \frac{1}{(E_o+\Delta_o)^2}\right)\left(\frac{2}{E_o - E_o' - \Delta_o'} + \frac{1}{E_o - E_o'}\right) \\
& -\frac{P^2(P')^2}{9}\left(\frac{2}{E_o} + \frac{1}{E_o+\Delta_o}\right)\left(\frac{2}{(E_o - E_o' - \Delta_o')^2} + \frac{1}{(E_o - E_o')^2}\right) \\
& -\frac{(P')^4}{9}\left(\frac{2}{(E_o - E_o' - \Delta_o')^2} + \frac{1}{(E_o - E_o')^2}\right)\left(\frac{2}{E_o - E_o' - \Delta_o'} + \frac{1}{E_o - E_o'}\right) \\
& +\frac{2|PQ|^2}{9}\left(\frac{1}{E_o} - \frac{1}{E_o+\Delta_o}\right)^2\left(\frac{1}{E_o - E_o' - \Delta_o'}\right) \\
& +\frac{2|P'Q|^2}{9}\left(\frac{1}{E_o - E_o' - \Delta_o'} - \frac{1}{E_o - E_o'}\right)\frac{1}{E_o} .
\end{aligned} \quad (3.54)$$

$$\begin{aligned}
\beta_o = & \frac{2\hbar^2P^2}{m}\left(\frac{1}{E_o^2} + \frac{2}{E_o(E_o+\Delta_o)}\right)(\gamma_2' - \gamma_3') \\
& +\frac{4|PQ|^2}{3}\left(\frac{2}{E_o(E_o+\Delta_o)(E_o - E_o' - \Delta_o')} + \frac{1}{E_o^2(E_o - E_o')}\right) \\
& +\frac{4|P'Q|^2}{3}\left(\frac{2}{E_o(E_o - E_o')(E_o - E_o' - \Delta_o')} + \frac{1}{(E_o+\Delta_o)(E_o - E_o' - \Delta_o')^2}\right).
\end{aligned} \quad (3.55)$$

$$\gamma_o = \frac{4|P^3Q|}{3}\frac{1}{E_o^2\sqrt{E_o(E_o'+\Delta_o')}} - \frac{4|PP'Q|}{3}\left(\frac{1}{(E_o+\Delta_o)(E_o-E_o'-\Delta_o')} - \frac{1}{E_o(E_o-E_o')}\right). \quad (3.56)$$

where the energy gaps are as defined in Chapter 2 and C′ is a constant which corrects the zone-centre effective mass due to remote states not explicitly included in the 14x14 Hamiltonian. The γ_i' are modified Luttinger parameters, discussed below. From equation (3.56) we calculate the value of γ_o in GaAs to be approximately $-17\text{x}10^{-24}\text{eVcm}^3$ which is sufficiently small to be safely neglected throughout. Equation (3.53) is the one which will be used to obtain the quantum well conduction subband dispersion in the following Chapter. For the growth direction [001], the term k_z in equation (3.53) is replaced by $-i\partial/\partial z$ to obtain the bound state z-dependent envelope functions, along with the application of suitable boundary conditions and the inclusion of the confinement potential due to the material composition, which is fully described in Appendix C. A similar treatment has been developed for the valence bands by Luttinger and Kohn.[28] However, due to the proximity of the valence bands they have retained in full the couplings obtained from equation (3.52), but subtracted from these terms the effects of bands outside the Γ_8^v manifold. Also, the spin-orbit split-off band is not included in this 4x4 Hamiltonian. For the energies of interest here, this makes little difference to the results. The 4x4 Hamiltonian is then solved, to obtain 4-component wavefunction solutions, each component due to the admixture of each spin component in the total wavefunction. The Hamiltonian is given as

$$\mathbf{H} = -\begin{vmatrix} P+Q & L & M & 0 \\ L^* & P-Q & 0 & M \\ M^* & 0 & P-Q & -L \\ 0 & M^* & -L^* & P+Q \end{vmatrix} \quad (3.57)$$

where

$$P = \frac{1}{2}\gamma_1\left(k_x^2+k_y^2+k_z^2\right)$$

$$Q = \frac{1}{2}\gamma_2\left(k_x^2+k_y^2-2k_z^2\right)$$

$$L = -\sqrt{3}\gamma_3\left(k_y+ik_x\right)k_z$$

$$M = \frac{\sqrt{3}}{2}\gamma_2\left(k_x^2-k_y^2\right)-\sqrt{3}i\gamma_3 k_x k_y\ .$$

Again, in the case of quantum wells, it is necessary to include the confinement potential and for

Representation	$\|J, m_J\rangle$	Basis
Γ_6	$\|\frac{1}{2}, \frac{1}{2}\rangle$	$iS\uparrow$
	$\|\frac{1}{2}, -\frac{1}{2}\rangle$	$iS\downarrow$
Γ_7	$\|\frac{1}{2}, \frac{1}{2}\rangle$	$\frac{1}{\sqrt{3}}\|X+iY\rangle\downarrow + \frac{1}{\sqrt{3}}\|Z\rangle\uparrow$
	$\|\frac{1}{2}, -\frac{1}{2}\rangle$	$\frac{1}{\sqrt{3}}\|X-iY\rangle\uparrow - \frac{1}{\sqrt{3}}\|Z\rangle\downarrow$
Γ_8	$\|\frac{3}{2}, \frac{3}{2}\rangle$	$\frac{1}{\sqrt{2}}\|X+iY\rangle\uparrow$
	$\|\frac{3}{2}, \frac{1}{2}\rangle$	$\frac{1}{\sqrt{6}}\|X+iY\rangle\downarrow - \sqrt{\frac{2}{3}}\|Z\rangle\uparrow$
	$\|\frac{3}{2}, -\frac{1}{2}\rangle$	$-\frac{1}{\sqrt{6}}\|X-iY\rangle\uparrow - \sqrt{\frac{2}{3}}\|Z\rangle\downarrow$
	$\|\frac{3}{2}, -\frac{3}{2}\rangle$	$-\frac{1}{\sqrt{2}}\|X-iY\rangle\downarrow$

Table 3.1 *Basis functions for electron states at Γ (k=0).*

[001]-growth replace the quantum number k_z by the momentum operator $-i\partial/\partial z$. The necessary boundary conditions in this case are also examined in Appendix C.

The γ_i parameters (Luttinger parameters) are related to the inverse zone-centre valence band effective masses. Since we will take the [001] masses as the quantisation masses in the solution of the Luttinger-Kohn Hamiltonian in quantum wells, it is seen that they are obtained from the diagonal elements of the Hamiltonian at $k_x=k_y=0$. This gives

$$\begin{aligned} m_{hh}(001) &= (\gamma_1 - 2\gamma_2)^{-1} \\ m_{lh}(001) &= (\gamma_1 + 2\gamma_2)^{-1} \ . \end{aligned} \tag{3.58}$$

Also the parameter γ_3 is related to the effective masses in the [111] direction, which are obtained as

$$\begin{aligned} m_{hh}(111) &= (\gamma_1 - 2\gamma_3)^{-1} \\ m_{lh}(111) &= (\gamma_1 + 2\gamma_3)^{-1} \ . \end{aligned} \tag{3.59}$$

The modified Luttinger parameters, mentioned above, are simply the Luttinger parameters γ_i, minus the coupling to the other states in the 14x14 Hamiltonian discussed above,which have been included in the Luttinger-Kohn 4x4 Hamiltonian.

Note that the momentum matrix elements do not explicitly appear in these equations. Since

we are considering materials of similar chemical properties we assume that the momentum matrix elements are similar as well and use the GaAs values throughout.

References

1 G.L. BIR and G.E. PIKUS, *Symmetry and Strain-Induced Effects in Semiconductors* (Wiley, New York, 1974)

2 K. SUZUKI and J.C. HENSEL, Physical Review **B9**, 4184 (1974)

3 N.R. OGG, Proceedings of the Physical Society **89**, 431 (1966)

4 H.R. TREBIN, U. RÖSSLER and R. RANVAUD, Physical Review **B20**, 686 (1979)

5 J.M. LUTTINGER, Physical Review **102**, 1030 (1956)

6 M. BORN and J.R. OPPENHEIMER, Annals of Physics **84**, 457 (1927)

7 F. SEITZ, *The Modern Theory of Solids* (McGraw-Hill,1940)

8 J.C. SLATER, Physical Review **81**, 385 (1951)

9 F. BLOCH, Zeitschrift für Physik **52**, 555 (1928)

10 T.L. GILBERT in: *Molecular Orbitals in Chemistry, Physics and Biology*, ed. by P.O. LÖWDIN and B. PULLMAN (Academic Press, 1964)

11 J.C. PHILLIPS and L. KLEINMAN, Physical Review **116**, 287 (1959)

12 F. BASSANI and V. CELLI, Journal of Physics and Chemistry of Solids **20**, 64 (1961)

13 D. BRUST, J.C. PHILLIPS and F. BASSANI, Physical Review Letters **9**, 94 (1962)

14 J. BARDEEN, Journal of Chemistry and Physics **6**, 367 (1938)

15 G. DRESSELHAUS, A.F. KIP and C. KITTEL, Physical Review **98**, 368 (1955)

16 E.O. KANE, Journal of Physics and Chemistry of Solids **1**, 82 (1956)

17 W. BRINKMAN and B. GOODMAN, Physical Review **149**, 597 (1966)

18 see for example: G.F. KOSTER, J.O. DIMMOCK, R.G. WHEELER and H. STATZ, *Properties of The Thirty-Two Point Groups* (MIT Press, 1963)

19 M. CARDONA and F.H. POLLAK, Physical Review **142**, 530 (1966)

20 E.O. KANE, Journal of Physics and Chemistry of Solids **8**, 38 (1959)

21 L.L. FOLDY and S.A. WOUTHUYSEN, Physical Review **78**, 29 (1950)

22 G. DRESSELHAUS, Physical Review **100**, 580 (1955)

23 L.M. ROTH, B. LAX and S. ZWERDLING, Physical Review **114**, 90 (1959)

24 C.R. PIDGEON and R.N. BROWN, Physical Review **146**, 575 (1966)

25 S.H. GROVES, C.R. PIDGEON, A.W. EWALD and R.J. WAGNER, Journal of Physics and Chemistry of Solids **31**, 2031 (1970)

26 R.C. AGGARWAL in: *Semiconductors and Semimetals*, Vol. 9, edited by R.K. WILLARDSON and A.C. BEER (Academic Press, New York, 1972)

27 F.H. POLLAK, C.W. HIGGINBOTHAM and M. CARDONA, Journal of the Physical Society of Japan, Supplement **21**, 20 (1966)

28 J.M. LUTTINGER and W. KOHN, Physical Review **97**, 869 (1955)

29 M. BRAUN and U. RÖSSLER, Journal of Physics **C18**, 3365 (1985)

4 Electronic Structure in GaAs-AlGaAs Quantum Wells

Introduction

To obtain the bound state eigenfunctions and eigenvalues in quantum wells, it is sufficient to extend the theory of the preceding Chapter. The bound state wavefunctions (e.g. in the valence band) can be taken as having the form

$$\Psi_n(\mathbf{k},\mathbf{r}) = \sum_m g_m^\nu(z)\, U_m^\nu(0)\, e^{-i\mathbf{k}_{||}\bullet\rho}, \qquad (4.1)$$

where $U_m^\nu(0)$ are the zone-centre Bloch functions, $k_{||}$ is the in-plane wavevector and $g_m^\nu(z)$ are the envelope functions in the growth (z) direction.

It is assumed that the confinement potential along z, due to the z-dependent composition,

affects mainly the zone centre states at Γ. The effect at other symmetry points (i.e. X or L) will be considered later. If we consider the conduction and valence bands as effectively decoupled (for small wavevectors), the bandstructure may be obtained directly from the Luttinger-Kohn Hamiltonian[1] for the hole subbands, or the effective mass Hamiltonian of Braun and Rössler[2] for the conduction subbands.

The preliminary sections in the present Chapter will calculate the conduction band dispersion and valence band dispersion, respectively, in a single GaAs-AlGaAs quantum well. This will elucidate the method of calculation, which will be used throughout. Extension to different systems, for example multiple quantum wells, symmetric and asymmetric double quantum wells, is completely straightforward and will be considered later. Note that in using this envelope-function approach, it is assumed that the well and barrier materials are restricted to having similar chemical composition. We are connecting similar types of electron states in each region (along the growth axis). The momentum matrix elements elements do not explicitly appear and have been completely subsumed into the effective mass Hamiltonians. If different states in different regions were at fairly close energies, the method would not be expected to give good results. This particular topic, which necessitates different theoretical methods, will be discussed later.

For the bulk of this thesis, the barrier and well materials under consideration will be of such similar chemical properties that the envelope-function method will always be applicable. It is thus expected to give extremely accurate and reliable results.

Band Offsets

It is assumed throughout this thesis that the material mismatch at each interface introduces an effective band gap offset ΔE_g, which for GaAs-AlGaAs, at T=4K can be given as[3] $\Delta E_g = 1.34x$, where x is the aluminium fraction in the barrier material. This means that the alignment of the two different band states in each material must be specified. Experimentally it is verified that the largest offset is seen at the Γ point, where discontinuities in both the conduction band and valence band are seen. In the GaAs-AlGaAs system, for quantum wells, this leads to the GaAs region becoming a potential well for electrons in both the lowest conduction band and valence band.

The height of this well in both bands, which gives the so-called band offset ratio, has been the subject of much experimental investigation. No precise value has been agreed, but recent experimental results[4-6] have all fallen within a small range of values. These give the offset ratio ΔE_c:ΔE_v in the range 55:45 to 65:35. This contradicts the long-held view[8] that 85:15 was the correct offset ratio for the GaAs-AlGaAs system. We choose a value, therefore, which lies mid-way between these limiting values and take the GaAs-AlGaAs band offset to be 60:40 throughout.

Conduction subband dispersion in single quantum wells

To obtain the correct dispersion it is necessary to consider three important aspects of the bulk conduction band structure in GaAs and AlGaAs. These are:

(i) Isotropic nonparabolicity

(ii) Nonisotropic nonparabolicity

(iii) Spin-splitting within each band

Further, to obtain accurate dispersion, including the above, it is necessary to include the effects of the higher p-antibonding conduction band.

Braun and Rössler (Ref. 2) have obtained an accurate expression for the lowest conduction band dispersion to fourth order in **k**. This was obtained by an invariant expansion (cf previous Chapter) of the two-fold lowest conduction band states. The weighting factors were obtained using standard **k·p** perturbation theory.

The conduction band dispersion may then be written as

$$E(\mathbf{k}) = \frac{\hbar^2\mathbf{k}^2}{2m} + \alpha_o\mathbf{k}^4 + \beta_o\left(k_x^2k_y^2 + k_y^2k_z^2 + k_z^2k_x^2\right) \pm\gamma_o\left[k^2\left(k_x^2k_y^2 + k_y^2k_z^2 + k_z^2k_x^2\right) - 9k_x^2k_y^2k_z^2\right]^{\frac{1}{2}} . \quad (4.2)$$

We will choose to ignore the spin-splitting term since it is small (see calculated value in previous Chapter). The values of α_o and β_o are obtained from equations (3.54) and (3.55) as $-2088\text{eV}\text{Å}^4$ and $-2271\ \text{eV}\text{Å}^4$, respectively. The solution of this equation in single quantum wells has been extensively considered by Ekenberg (Ref. 8). Using $k_x = k_{||}\cos\theta$ and $k_y = k_{||}\sin\theta$ then equation (4.2) may be re-written as

$$k_z^4 + \left[\frac{\hbar^2}{2m\alpha_o} + \frac{(2\alpha_o + \beta_o)}{\alpha_o}k_{||}^2\right]k_z^2 + \frac{\hbar^2}{2m\alpha_o}k_{||}^2 + k_{||}^4 + \frac{\beta_o}{\alpha_o}k_x^2k_y^2 - \frac{E}{\alpha_o} = 0 . \quad (4.3)$$

For a perfect heterostructure, with a step-like potential at each interface, then putting $K=k_z$ in the well region and $\lambda=ik_z$ in the barrier, where $E\rightarrow(E-V_o)$ leads to

$$K = \left[A_1 - A_1\left(1 + \frac{B_1}{A_1^2}\right)^{1/2}\right]^{1/2} \quad (4.4a)$$

$$\lambda = \left[A_2\left(1 + \frac{B_2}{A_2^2}\right)^{1/2} - A_2\right]^{1/2} , \quad (4.4b)$$

where

$$A_1 = -\frac{\hbar^2}{4m_1\alpha_{o_1}} - \frac{(2\alpha_{o_1}+\beta_{o_1})}{2\alpha_{o_1}}k_{||}^2 \qquad (4.5a)$$

$$B_1 = \frac{E}{\alpha_{o_1}} - \frac{\hbar^2}{2m_1\alpha_{o_1}}k_{||}^2 - k_{||}^4 - \frac{\beta_{o_1}}{\alpha_{o_1}}k_x^2k_y^2 \qquad (4.5b)$$

$$A_2 = -\frac{\hbar^2}{4m_2\alpha_{o_2}} - \frac{(2\alpha_{o_2}+\beta_{o_2})}{2\alpha_{o_2}}k_{||}^2 \qquad (4.5c)$$

$$B_2 = \frac{(E-V)}{\alpha_{o_2}} - \frac{\hbar^2}{2m_2\alpha_{o_2}}k_{||}^2 - k_{||}^4 - \frac{\beta_{o_2}}{\alpha_{o_2}}k_x^2k_y^2 \,. \qquad (4.5d)$$

The subscript 1 (2) refers to the well (barrier) material. The consideration of boundary conditions is quite lengthy and is given in Appendix C. The solution is simply given here. The appropriate current-conserving boundary conditions lead to a simple transcendental equation for the bound eigenstates given by

$$\tan(KL) = \frac{\frac{\hbar^2\lambda}{2m_2} - 2\alpha_{o_2}\lambda^3}{\frac{\hbar^2K}{2m_1} + 2\alpha_{o_1}K^3}, \qquad (4.6)$$

for the even-parity solutions at $k_{||}=0$ and where the interfaces are at $z=\pm L$. For the odd-parity solutions, tan(KL) is replaced by -cotan(KL).

For the case of non-zero in-plane wavevectors (i.e. $k_{||}\neq 0$) then equation (4.6) is easily generalised to

$$\tan(KL) = \frac{\left[\frac{\hbar^2}{2m_2} + (2\alpha_{o_2}+\beta_{o_2})k_{||}^2\right]\lambda - 2\alpha_{o_2}\lambda^3}{\left[\frac{\hbar^2}{2m_1} + (2\alpha_{o_1}+\beta_{o_1})k_{||}^2\right]K + 2\alpha_{o_1}K^3}\,. \qquad (4.7)$$

The calculated dispersion for 50Å and 100Å quantum wells (with aluminium concentration in the barriers x=0.2) is shown in Figures 4.1 and 4.2. The dotted line in each figure is the result of the simple parabolic model (1-D particle in a box 'textbook' model) with constant effective mass and where no account has been taken of the correct dispersion at $k_{||}=0$. This simple model, although widely used, uses a constant effective mass and completely isotropic parabolic dispersion is therefore

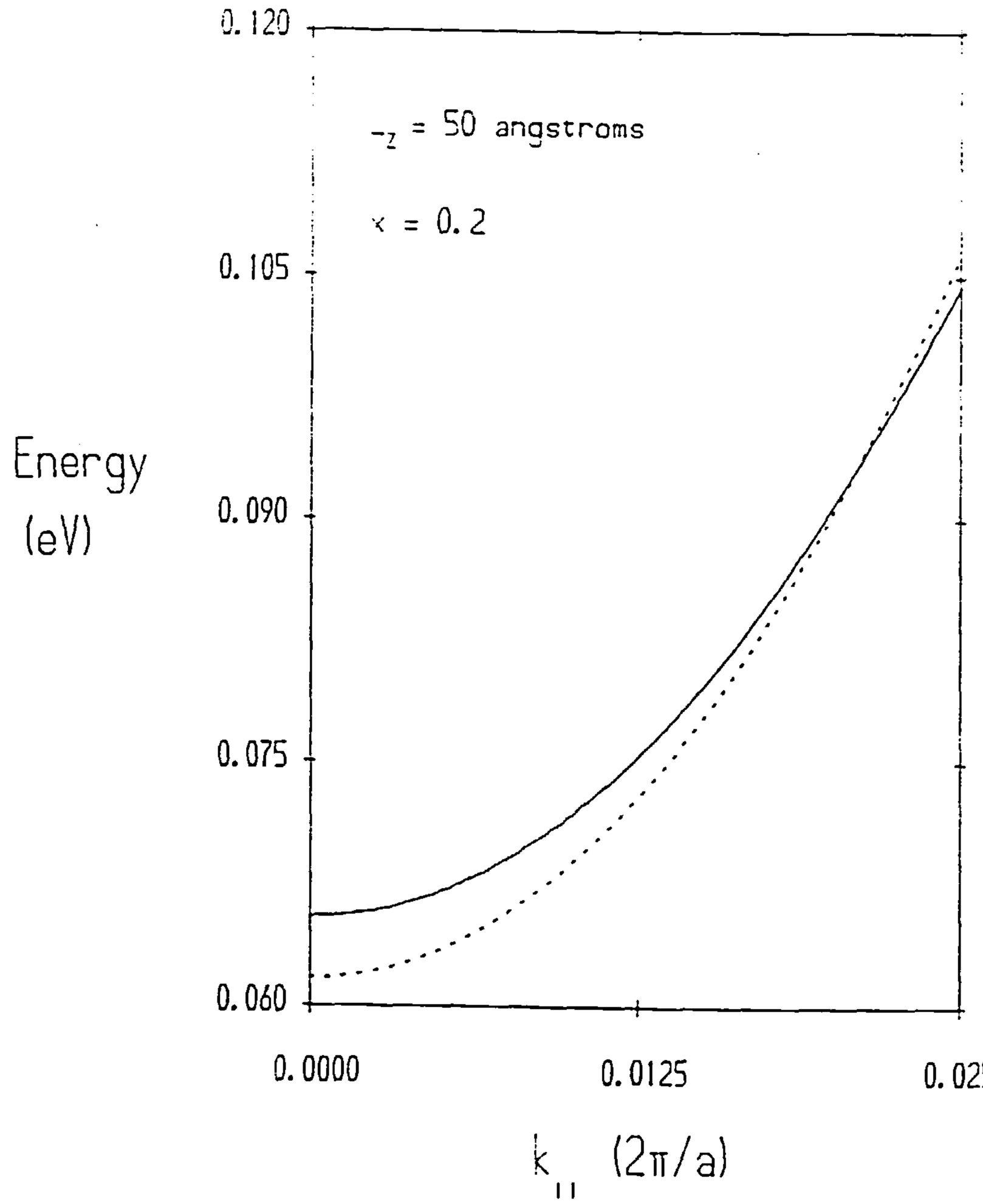

Figure 4.1 *Conduction subband dispersion (n = 1) for a 50Å GaAs-$Al_{0.2}Ga_{0.8}As$ single quantum well with $k_{||} = k_x$. Also shown (dotted curve) is the result of a parabolic approximation to the dispersion. The directions are along [100] to the right and [110] to the left. The energy is measured from the bottom of the conduction band potential well.*

obtained. Note that the confinement energies $E_n(k_{||}=0)$ are not the same. The proper solution shows an increased n=1 subband confinement energy and decreased confinement energy for the n≠1 subbands.

The density-of-states within each subband n is constant in the parabolic model and is given by

$$\rho_n^{2D} = \frac{m_n^*}{\pi\hbar^2}, \tag{4.8}$$

Table 4.1 *Calculated averaged in-plane zone-centre effective masses for conduction subbands n = 1 and n = 2 in GaAs-AlGaAs single quantum wells for several well widths.*

Al in barrier	subband	50Å	100Å	200Å
x = 0.2	CB1	0.0734	0.0697	0.0676
	CB2	—	0.0803	0.0714
x = 0.3	CB1	0.0732	0.0698	0.0677
	CB2	—	0.0811	0.0715

Table 4.2 *Calculated averaged in-plane zone-centre effective masses for valence subbands HH1, LH1 and HH2 in GaAs-AlGaAs single quantum wells for several well widths.*

Al in barrier	subband	50Å	100Å	200Å
x = 0.2	HH1	0.172	0.159	0.154
	LH1	- 1.550	- 0.216	- 0.163
	HH2	0.107	0.0074	0.066
x = 0.3	HH1	0.194	0.181	0.170
	LH1	- 1.970	- 0.284	-0. 163
	HH2	0.124	0.086	0.067

but this is not the case using the more accurate dispersion model. The n=1 and n=2 total density of states is shown for the 100Å well in Figure 4.3. Note that the density of states increases with energy into each subband.

In bulk material, a useful simplified form of the energy dispersion in the lowest conduction band can be expressed as[9]

$$\frac{\hbar^2 k^2}{2m^*} = E(1 + \alpha E) , \tag{4.9}$$

where

$$\alpha = \frac{1}{E_g}\left(1 - \frac{m^*}{m_o}\right)^2 . \tag{4.10}$$

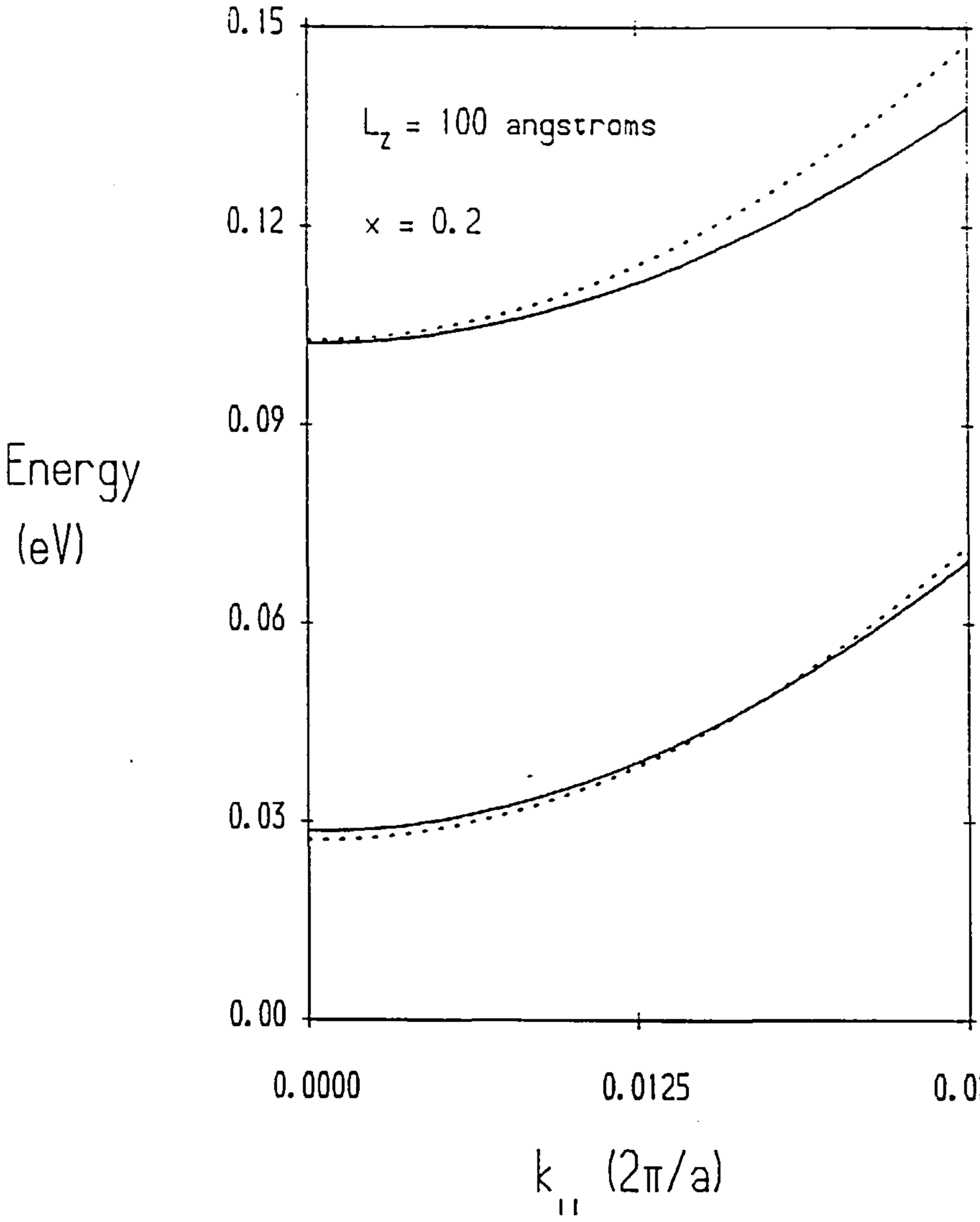

Figure 4.2 *Conduction subband dispersion for a 100Å GaAs-$Al_{0.2}Ga_{0.8}As$ single quantum well, for subbands n = 1 and n = 2 and a parabolic approximation (dotted curves).*

The non-parabolic dispersion given by these equations is similar in trend to that obtained here for the n=1 quantum well subband.

The calculated 2-D density-of-states shown in Figure 4.3 is still step-like, but the effects of the nonparabolicity can be clearly seen. As the energy increases into the conduction band, the band curvature mass increases and the dispersion departs from a parabolic shape. This effect gradually increases the density-of-states deeper into each subband. The results given here were obtained by solving equations (4.3) and (4.4) at every 5^o interval in θ, where θ is defined by

$$k_x = k_{||}\cos\theta$$
$$k_y = k_{||}\sin\theta\,, \qquad (4.11)$$

and $k_{||}$ is the magnitude of the wavevector. The DOS function is calculated by considering which regions in **k**-space are closest to a particular energy, E_i say and summing the numerically obtained DOS from all contributing regions of **k**-space and all contributing subbands. This gives the contribution to $\rho(E)$ as $\rho(E_i)$.

Valence subband dispersion in single quantum wells

To obtain the valence subband dispersion we use the 4x4 Luttinger-Kohn Hamiltonian, given in the previous Chapter. Replacing $\hbar k_z$ by the operator $-i\hbar\partial/\partial z$, the elements of the Hamiltonian now become

$$\begin{aligned} P &= \frac{1}{2}\gamma_1\left(k_x^2+k_y^2\right) - \frac{1}{2}\gamma_1\frac{\partial^2}{\partial z^2} \\ Q &= \frac{1}{2}\gamma_2\left(k_x^2+k_y^2\right) - \gamma_2\frac{\partial^2}{\partial z^2} \\ L &= \sqrt{3}i\gamma_3\left(k_y+ik_x\right)\frac{\partial}{\partial z} \\ M &= \frac{\sqrt{3}}{2}\gamma_2\left(k_x^2-k_y^2\right) - \sqrt{3}i\gamma_3 k_x k_y \,. \end{aligned} \tag{4.12}$$

The correct boundary conditions for the four-component envelope function are discussed in Appendix C. At each interface these require continuity of the envelope function (f_1, f_2, f_3, f_4) and the vector

$$\begin{vmatrix} (\gamma_1-2\gamma_2)\frac{\partial}{\partial z} & \sqrt{3}\gamma_3\left(k_x-ik_y\right) & 0 & 0 \\ \sqrt{3}\gamma_3\left(k_x+ik_y\right) & (\gamma_1+2\gamma_2)\frac{\partial}{\partial z} & 0 & 0 \\ 0 & 0 & (\gamma_1+2\gamma_2)\frac{\partial}{\partial z} & -\sqrt{3}\gamma_3\left(k_x-ik_y\right) \\ 0 & 0 & -\sqrt{3}\gamma_3\left(k_x+ik_y\right) & (\gamma_1-2\gamma_2)\frac{\partial}{\partial z} \end{vmatrix} \begin{vmatrix} f_1 \\ f_2 \\ f_3 \\ f_4 \end{vmatrix} . \tag{4.13}$$

In Figures 4.4 and 4.5 the valence subband dispersion is shown for well widths of 50Å and 100Å respectively. In each case x=0.2 in the barrier material. The subbands have been labelled according to their character at the zone centre, $k_{||} = 0$, where they are decoupled in the Luttinger-Kohn

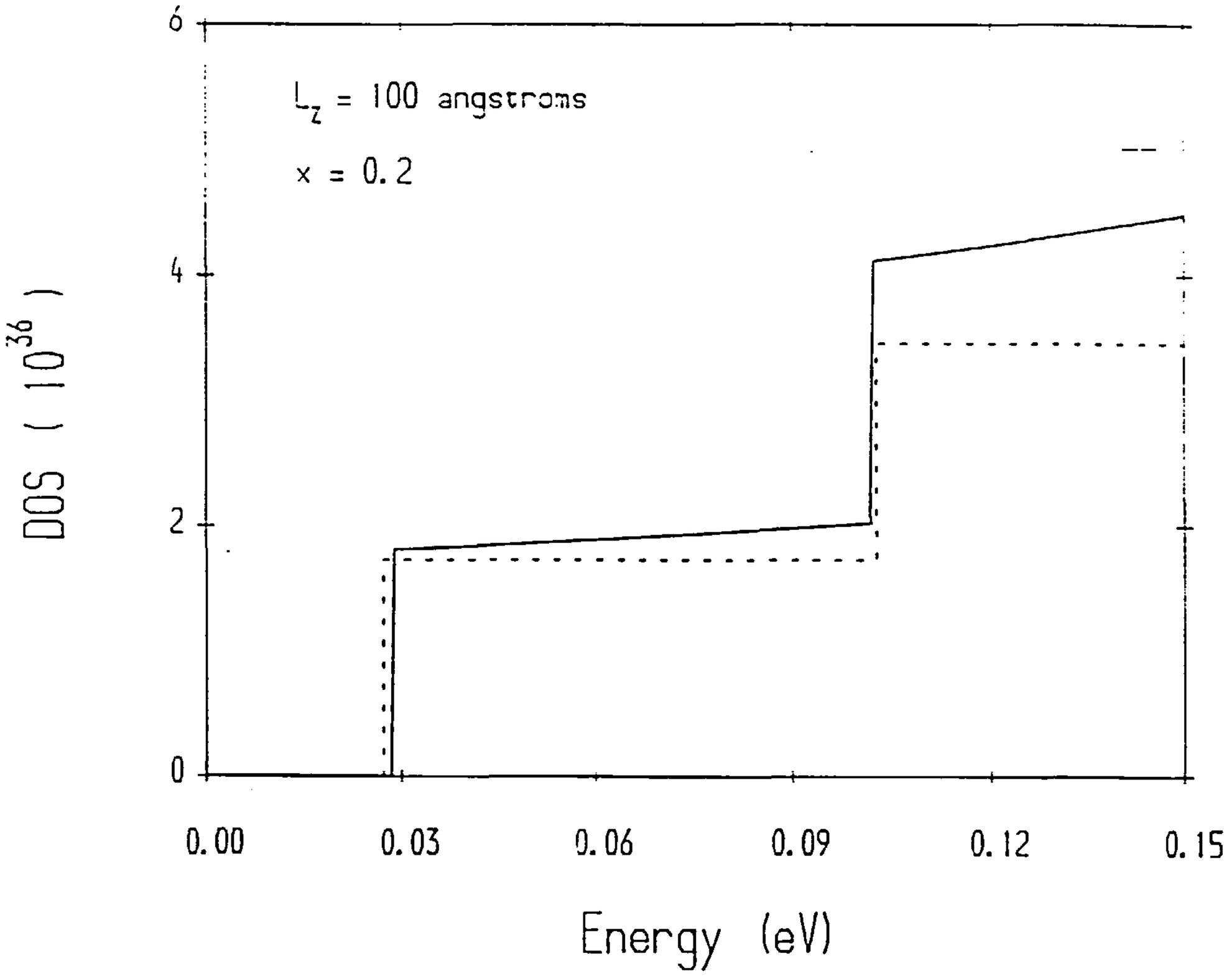

Figure 4.3 *Conduction band 2-D density of states for a 100Å GaAs-$Al_{0.2}Ga_{0.8}As$ single quantum well, for subbands n = 1 and n = 2, and a parabolic approximation (dotted curves).*

4x4 Hamiltonian, and HH denotes Heavy-Hole LH denotes Light-Hole. Note that this description does not apply to the actual in-plane effective masses. The effective masses are now due to the subband mixing at $k_{||} \neq 0$ which arises both from the off-diagonal terms in the Hamiltonian and from the application of the quantum well envelope function boundary conditions. The averaged zone-centre effective masses of the subbands are given in Table 4.2, where the averaging is over the angle θ, defined in equation (4.11). It is clear from these figures that the dispersion is highly nonparabolic. An approximate guide to the trend of the effective masses can be seen from standard second-order perturbation theory. For each subband n, this gives the effective mass as

$$\frac{1}{m_n^*} = (\gamma_1 \pm \gamma_2)^{-1} + \frac{2}{m_o^2} \sum_{n' \neq n} \frac{\left| \sum_i f_i^n |H_{ij}| \sum_j f_j^{n'} \right|^2}{E_n - E_{n'}}, \qquad (4.14)$$

where f_i^n, $f_j^{n'}$ are the four-component envelope functions of bands n, n' respectively and the H_{ij} are

Table 4.3 *Calculated subband confinement energies (meV) in GaAs-AlGaAs single quantum wells for several well widths.*

Al in barrier	subband	50Å	100Å	200Å
x = 0.2	CB1	65.4	28.6	9.9
	CB2	—	102.4	38.4
	HH1	19.0	6.5	1.89
	LH1	40.2	16.8	5.58
	HH2	70.6	25.6	7.55
x = 0.3	CB1	80.9	32.4	10.6
	CB2	—	119.2	41.3
	HH1	20.9	6.7	1.91
	LH1	46.5	17.8	5.62
	HH2	80.4	26.8	7.61

the off-diagonal elements of the Luttinger-Kohn Hamiltonian. Interactions with higher subbands tend to increase the effective mass and interactions with lower subbands tend to decrease the effective mass. The terms $(\gamma_1 \pm \gamma_2)^{-1}$ give the effective masses at $k_{||} = 0$ in the so-called diagonal approximation (this neglects the effect of application of the boundary conditions, essentially ignoring the quantum well structure).

The effective mass values $(\gamma_1 \pm \gamma_2)^{-1}$ are often used to represent the HH1 and LH1 subband effective masses[10-12] when considering the exciton states in quantum wells. From Figures 4.4 and 4.5 it is clear that this is quite incorrect and the actual subband in-plane masses are not given by the above expressions. The values given by $(\gamma_1 \pm \gamma_2)^{-1}$ are 0.115 and 0.206 for the HH1 and LH1 subbands respectively, in the diagonal approximation. The actual calculated in-plane masses (for x=0.2) given in Table 4.2 are 0.172, -1.55 (L_z = 50Å) and 0.194,-0.216 (L_z = 100Å). In the case of the HH1 subband the calculated value is 50% larger and 69% larger than the above approximation for the 50Å and 100Å wells respectively. The situation for the LH1 subband is even worse since the calculated subband dispersion has a different sign of curvature at the zone centre (i.e. negative hole effective mass).

It is essential to point out that the bandgap discontinuity and relative band offsets are extremely important parameters to be input to the calculations of subband structure. As mentioned previously we rely on experimental results for these parameters. State-of-the-art bandstructure calculation methods can hardly be of any help in this instance. Both pseudopotential and *ab initio* methods can not claim accuracy greater than 0.1eV at present. This value, however, is of the same order of magnitude as the valence band offset used here for GaAs-$Al_{0.2}Ga_{0.8}As$ quantum wells. At

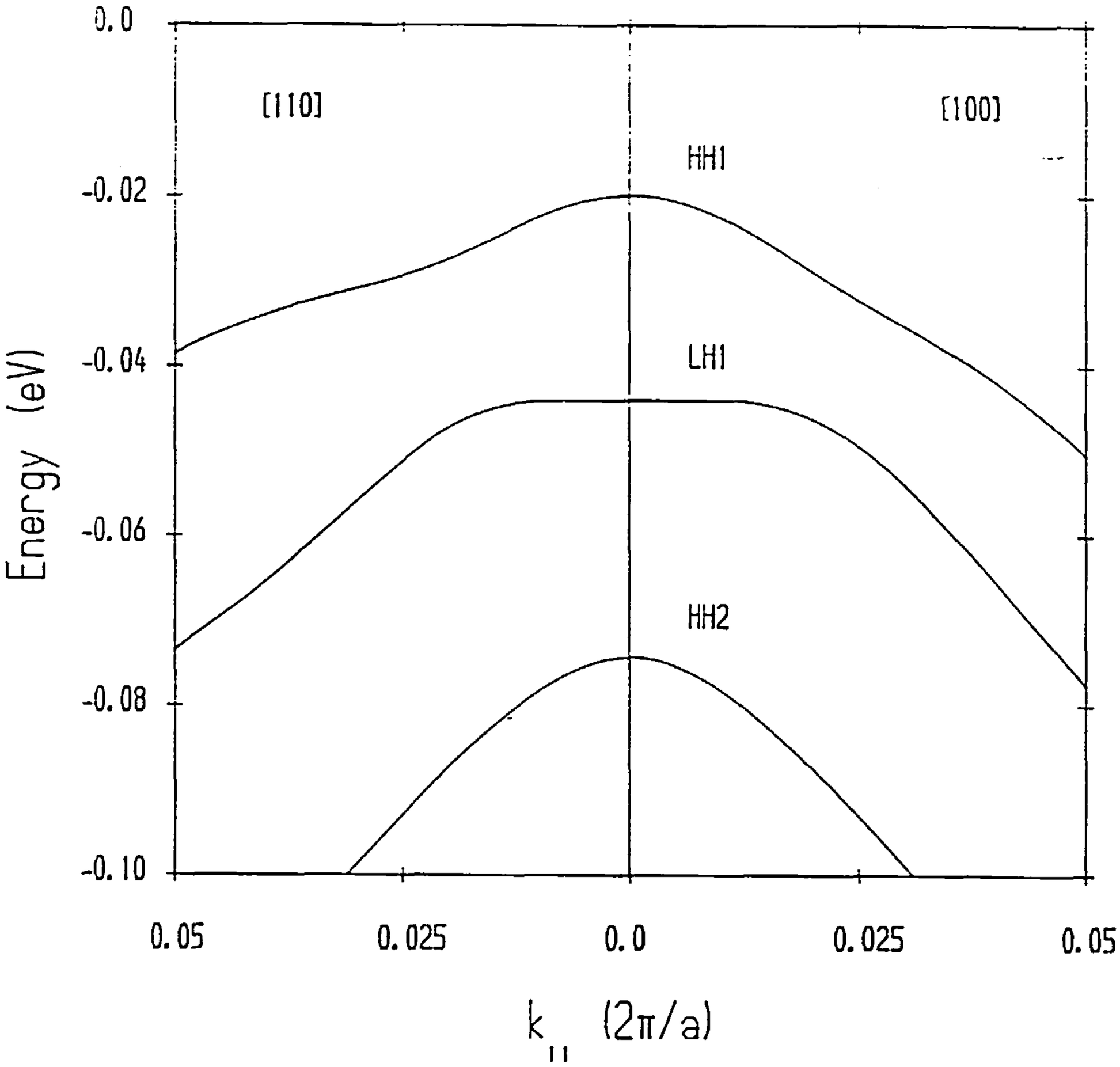

Figure 4.4 *Valence subband dispersion in a 50Å GaAs-$Al_{0.2}Ga_{0.8}As$ single quantum well. The directions are along [100] to the right and [110] to the left. The energy is measured from the bottom of the valence band confinement well. The subband are labelled according to their character at the zone-centre.*

present, therefore, the band offset values used are simply a personal choice made from the range of experimental values published.

The actual subband structures shown in Figures 4.4 and 4.5 are not completely intuitive. This applies especially to the negative effective masses of some subbands at the zone-centre. It is clear, however, that the strong coupling of the wavefunction components and the anti-crossing behaviour of the basis set used, leads to much of the observed in-plane dispersion.

The two directions in these Figures are along <100> and <110>. The results for these directions are fairly similar and it is expected that the so-called axial approximation[13,14] would be reasonable in this case. This approximation neglects the in-plane warping of the subband dispersion,

resulting from a simplified Hamiltonian. The in-plane warping depends on the relative magnitudes of the effective mass parameters γ_2 and γ_3. The axial approximation is simply obtained by neglecting the difference between the values of γ_2 and γ_3 in the M term of the Luttinger-Kohn Hamiltonian. This term then has an average effective mass parameter $\bar{\gamma}$ given by $\bar{\gamma} = \frac{1}{2}(\gamma_2+\gamma_3)$. This neglect of warping in the (k_x,k_y) plane has only a small effect on the dispersion and does not affect the calculation of the $k_{||} = 0$ subband confinement energies.

Subbands which have negative effective mass at the zone-centre typically reach a maximum value in energy at $k_{||} = 2\pi/L_z$ where L_z is the well width. This value of $k_{||}$ is therefore a characteristic value (inverse length) in these structures. The strong subband mixing and the consequent subband nonparabolicity were first predicted theoretically by Nedorezov[15] in the case of an infinitely deep well. The problem in this case can be calculated exactly.

Another simplification widely used is to reduce the 4x4 Hamiltonian to two 2x2 Hamiltonians. This is achieved via a unitary transformation[14,16] which block diagonalises the Hamiltonian. This relies on the artificially high symmetry and the neglect of k-linear terms. The 4x4 block diagonalised Hamiltonian is given by[16]

$$H = \begin{vmatrix} P+Q & R & 0 & 0 \\ R^* & P-Q & 0 & 0 \\ 0 & 0 & P-Q & R \\ 0 & 0 & R^* & P+Q \end{vmatrix}, \tag{4.15}$$

where

$$R = |M| - i\,|L|\,, \tag{4.16}$$

using the notation given earlier for the 4x4 Hamiltonian. The use of this Hamiltonian simplifies the calculations and is computationally slightly more efficient. However, the basis set has also been transformed and the matrix elements between the conduction subbands and the valence subbands now have a different form. This method of solution is only mentioned here for the sake of completeness, the full 4x4 Hamiltonian being used throughout this thesis. Note that in the particular case of asymmetric quantum wells or the application of an external field, the above block-diagonalised form has been shown to be incorrect.[17] In this case all instances of $k_{||}$ in the lower 2x2 block should be replaced by $-k_{||}$. This has not been done in several publications using this method.[18,19] In these cases several of the results quoted are therefore incorrect. The new transformed bases which are given in Refs. 18 and 19 are also incorrect since they were obtained from the point of view of the axial approximation and the neglect of any terms in the 4x4 Hamiltonian containing the factor $\pm(\gamma_2-\gamma_3)$, which was not stated in these References. A correct form is given in Ref. 20.

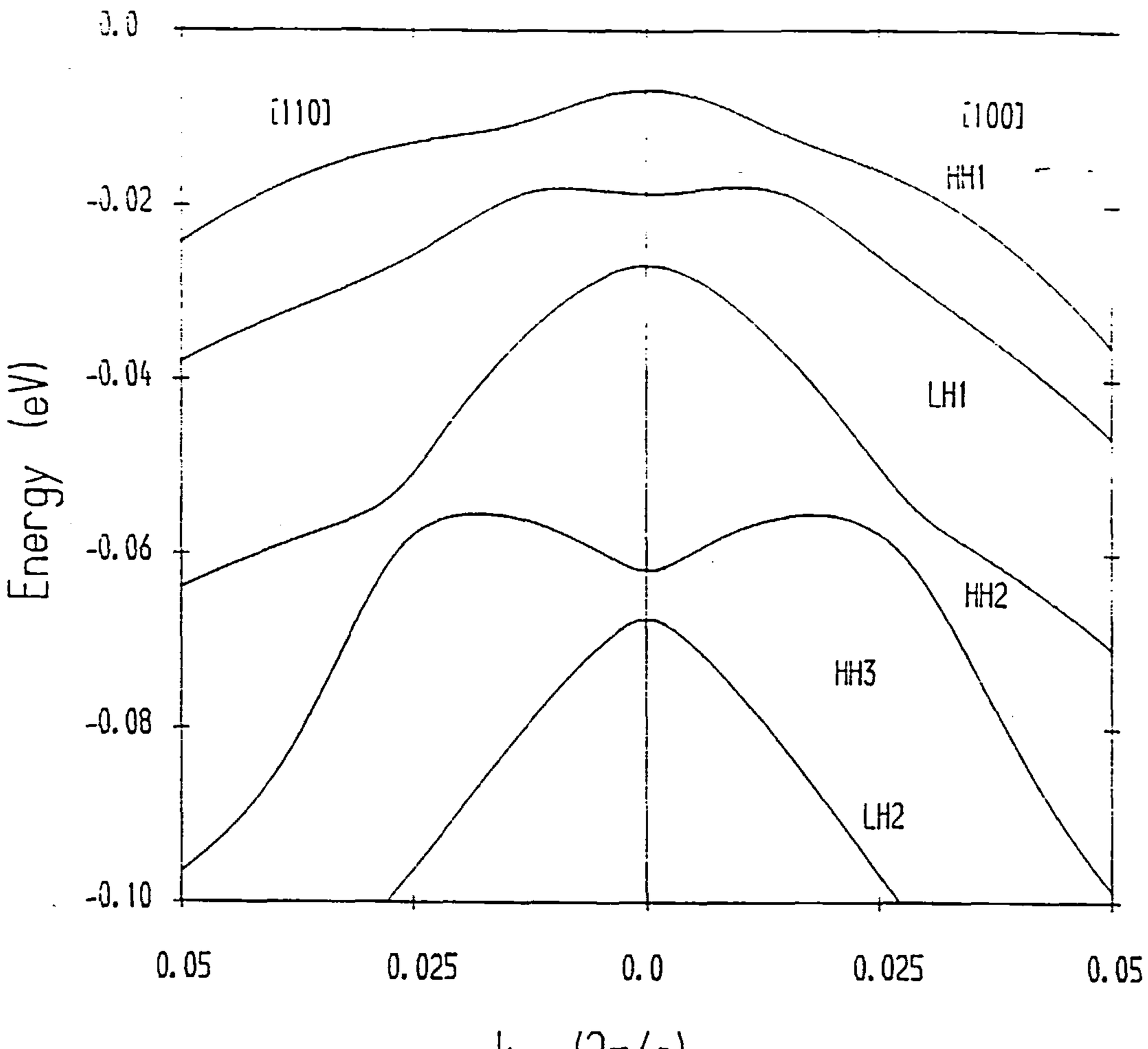

Figure 4.5 *Valence subband dispersion in a 100Å GaAs-$Al_{0.2}Ga_{0.8}As$ single quantum well. The directions are along [100] to the right and [110] to the left. The energy is measured from the bottom of the valence band confinement well. The subband are labelled according to their character at the zone-centre. HH denotes Heavy-Hole, LH denotes Light-Hole.*

The method which we use throughout to solve the matrix equations is the standard finite-difference method. This method is probably the simplest method available and is particularly straightforward to apply. As in the case of the conduction subband dispersion, the subband dispersion is obtained at every five degrees in the in-plane angle θ, defined earlier. The maximum value of the in-plane wavevector chosen was $k_{||} = (0.2\pi/a)$, which represents a distance of ten percent into the Brillouin zone. In calculating the density of states, it is assumed that the gradient $\nabla_k E$ is constant within the small neighbourhood defined by the mesh size in θ and $k_{||}$. By using some five hundred mesh points to sub-divide $k_{||}$ this gives nearly forty thousand points sampled in $k_{||}$-space. By using initial estimates for the bound state envelope functions, the correct solutions are obtained

by simultaneously iterating the finite-difference equations both forwards and backwards. This method is extremely robust and is capable of accommodating an arbitrary potential profile. When considering the effects of an applied electric field, this method will also be applied to the solution of the conduction band Hamiltonian, which could otherwise be considered in terms of Airy functions although not as efficient to solve in terms of the computational time involved.

The results given so far indicate that as the well width increases the number of bound subbands also increases. The energy separation between each subband is seen to decrease with increasing well width. In the case of the conduction subbands, the $n = 1$ subband effective mass is seen to approach the bulk value as the well width increases and at $L_z = 200$Å is only 1.2% larger than the bulk value of 0.0665 for both $x = 0.2$ and $x = 0.3$. This trend is seen in all the conduction subband results in Table 4.1.

The effective masses of the valence subbands also decrease with increasing well width. The only exception here is the LH1 zone-centre effective mass but since this subband has negative effective mass the magnitude is seen to decrease with increasing well width. From Table 4.2 this is seen to drop from 1.55 at $L_z = 50$Å to 0.163 at $L_z = 200$Å with $x = 0.2$ A similar trend is also seen for the LH1 subband with $x = 0.3$.

As will be shown later, the performance of highly-pumped GaAs-AlGaAs quantum well lasers depends strongly on the number of bound subbands, particularly within the conduction band. For well widths larger than around 100Å, the possibility of $n = 2$ conduction subband lasing can be achieved at high injection currents and with increasing well width this will occur at lower values of injection current. To prevent this taking place requires narrower well widths, effectively giving only one bound conduction subband and with higher injection currents not adversely affecting the performance.

Effect of electric field on subband structure

The effects of an externally applied electric field on the subband dispersion is straightforward to incorporate into the theoretical calculations. In both the conduction and valence band Hamiltonians the potentials are now re-written as

$$V(z) = V_e(z) + |e|Fz \tag{4.17a}$$

$$V(z) = V_h(z) - |e|Fz\,, \tag{4.17b}$$

for the conduction and valence bands respectively. F is the magnitude of the applied field , which is here taken as along the z-direction and |e| is the magnitude of the electron charge. $V_e(z)$ and $V_h(z)$ are

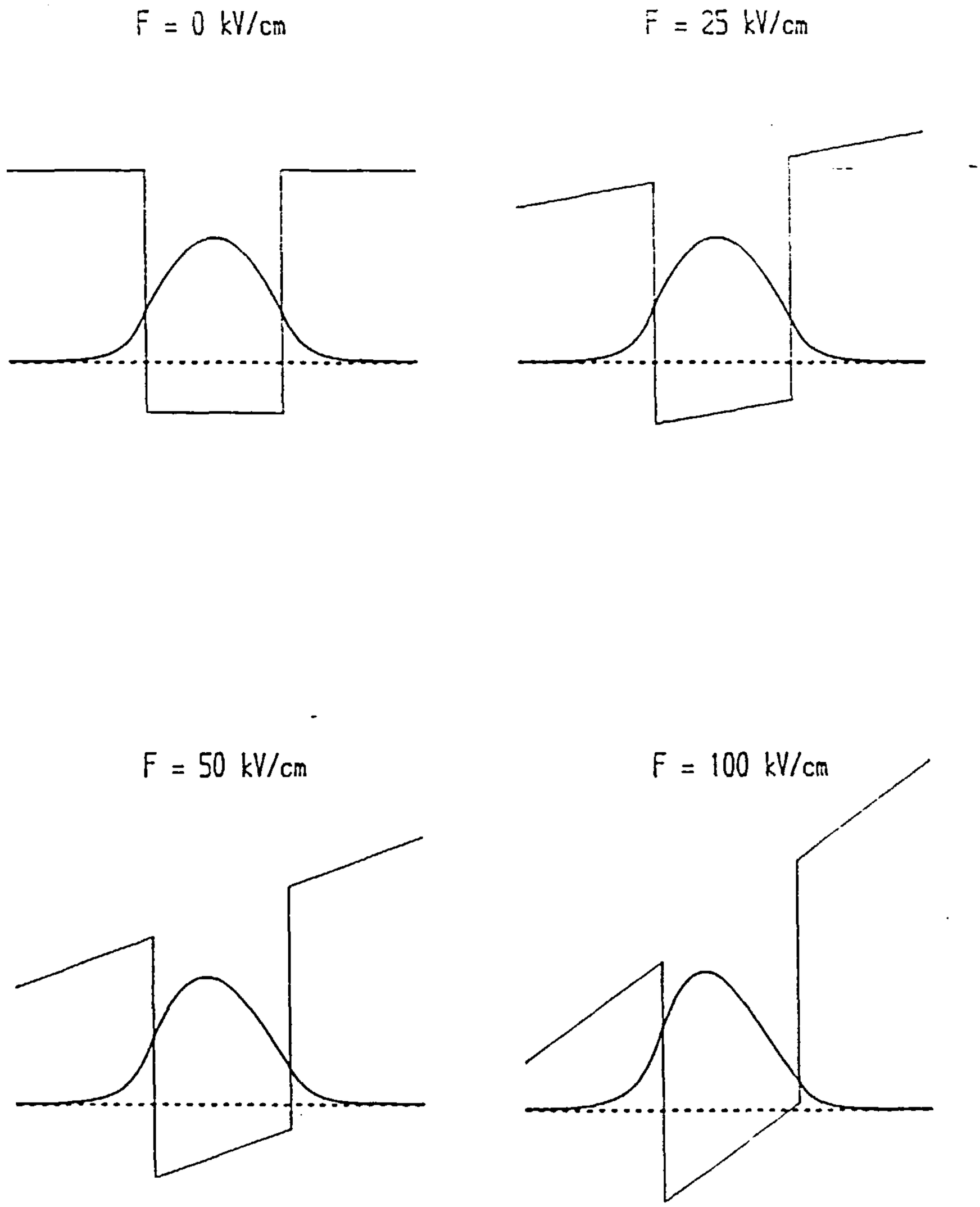

Figure 4.6 *Schematic illustration of the conduction band confinement potential for four values of electric field applied along the growth axis. Also shown (not to scale) is the n = 1 conduction subband envelope function at* $k_{||} = 0$ *for a 100Å GaAs-*$Al_{0.2}Ga_{0.8}As$ *single quantum well.*

the conduction and valence band confinement potentials respectively. Note that equation (4.17b) is here added to each diagonal term in the Luttinger-Kohn Hamiltonian.

Before making any calculations it is useful to consider the meaning of a bound eigenstate, as obtained via a finite-difference solution of the Hamiltonians. When applying boundary conditions, we normally take $\psi_n(z) = 0$ at a suitably large distance from the well centre, since this is correct for a

truly bound state. However, since the overall potential is altered by the application of the electric field, then it is reasonable to expect that for a sufficiently large field value, some eigenstates may be classed as either quasi-bound or completely unbound.

The above boundary condition alone would not be helpful in this situation. Taking the case of no applied field and a single quantum well, it is sufficient to set $\psi_n(z) = 0$ at a distance of $z = \pm 2.5L_z$, where L_z is the well width and we are considering only the $k_{||} = 0$ eigenstates. Since a potential well always has at least one bound state,[21] then this eigenstate can be taken as bound. Suppose a reasonably large electric field has been applied along the growth axis. For a bound (or indeed quasi-bound) state, then for a sufficiently remote boundary, the actual location of the boundary is not important when calculating the energy. In the present case, evaluation of the eigenenergy involves spatial integration, which obviously extends to both boundaries (at $\pm 2.5L_z$). If, upon application of all boundary conditions and iterating the relaxation method n+1 times we obtain $(E_{n+1}-E_n) < \delta$, with δ sufficiently small, then it is assumed that the bound state eigenfunction has been evaluated. Consider now removing the boundaries to several percent further, say at $2.7L_z$. If upon a single extra relaxation and recalculation of the energy, $(E_{n+2}-E_{n+1})$ is still $< \delta$, then this is taken as definitely a bound or quasi-bound state.

This method should prove reliable in determining the field values at which quantum well states can no longer be considered to be bound states. Further, if this test were not made, then all envelope functions would initially have $\psi_n(z) = 0$ at $z = \pm 2.5L_z$ and this condition would remain indefinitely in all calculations, even beyond the electric field value at which eigenfunctions were no longer truly bound, these states then being completely miscalculated by the finite-difference scheme.

If a variational approach were used instead,[22] then a trial wavefunction must be specified initially as a bound state. (The specific trial wave function used in Ref. 22 is similar to the Fang-Howard wave function[23] which successfully describes the bound-electron levels in metal-oxide-semiconductor (MOS) structures). This then automatically dictates that all states are bound, even at arbitrarily high electric fields, which is completely erroneous. Hence any region in which states become quasi-bound could not be determined by using this variational approach.

Figure 4.6 illustrates the effect of an electric field along the growth direction on the total conduction band confinement potential for four field values. The envelope function displayed is that for the CB1 $k_{||} = 0$ eigenfunction and $L_z = 100$Å, $x = 0.2$ in the barrier material. The minimum position in each potential well for the conduction and valence band states now occurs at a different location along z. The overlap integral between states of similar parity will originally decrease with applied field and those of different parity may start to increase with increasing field. Inevitably this will affect such properties as the optical absorption coefficient between each pair of confined subbands, which depends on the overlap integral of the envelope functions.

For states with similar parity, the squared overlap integral is given in Figure 4.7, as a function of the applied electric field. This is for a well width of 100Å and with $x = 0.2$ in the barrier

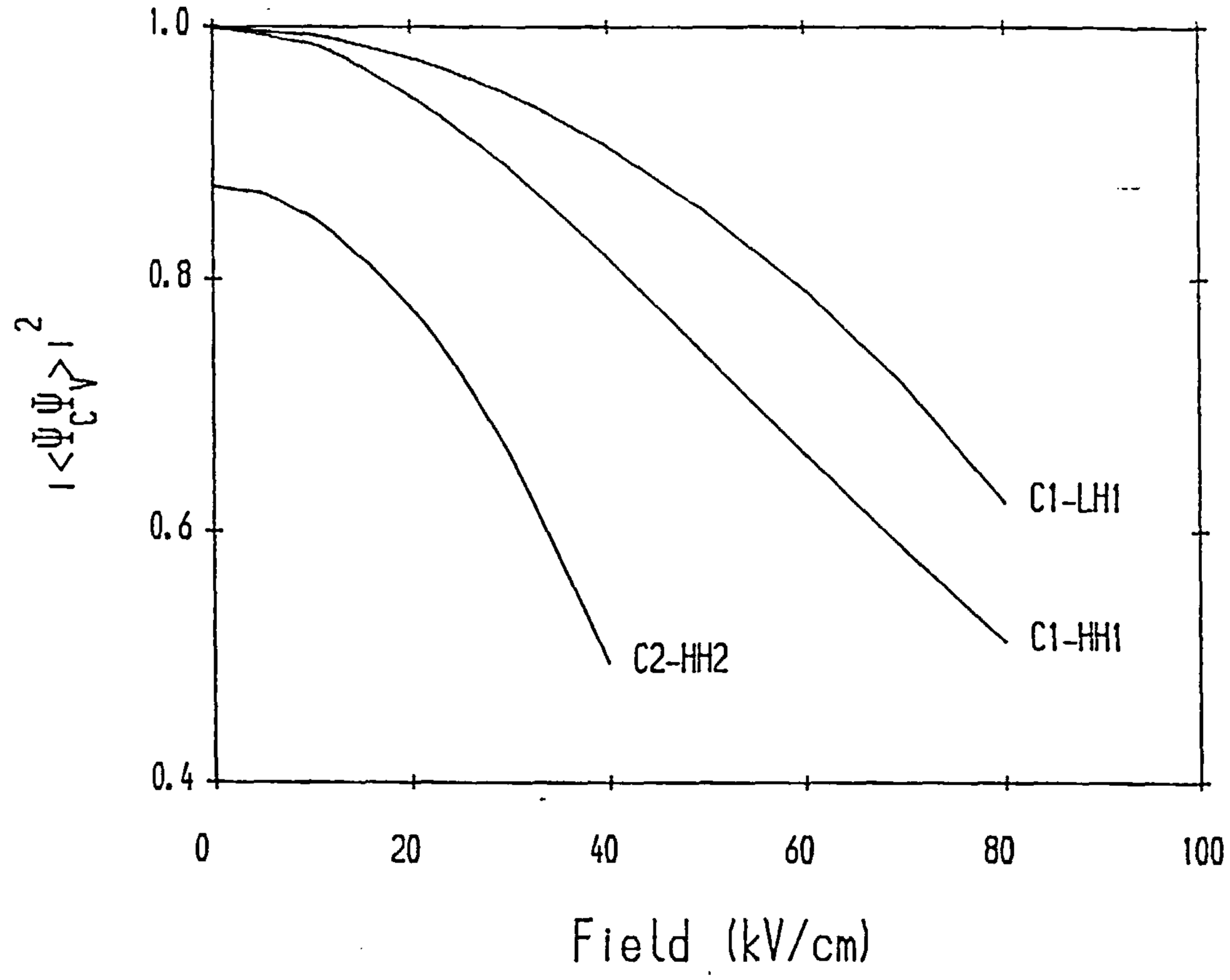

Figure 4.7 *Squared overlap integrals for the $k_{||} = 0$ envelope functions of states CB1-HH1, CB1-LH1 and CB2-HH2 in 100Å GaAs-$Al_{0.2}Ga_{0.8}As$ single quantum well as a function of the applied electric field F(z).*

material. Note that at this value of electric field (i.e. 25kV/cm) the HH1, LH1 and CB1 eigenstates are still bound. The HH2-CB2 results are only given for fields up to 40kV/cm, at which the CB2 states are no longer bound. It should be pointed out that the results in Figure 4.7 refer to the eigenfunctions at $k_{||} = 0$ only.

It has recently been suggested[24] that at moderate values of electric field, all hole states have 'leaked' out of the quantum well. It will be seen from the results given here that this is quite incorrect and owes much of the error to the method of solution (a Monte Carlo approach), which essentially 'locks on' to a resonance in the quasi-triangular potential well at the lowest point in the valence band confinement potential. This gives totally extraneous solutions, which are essentially resonance interactions between even and odd parity solutions. This can manifest itself particularly when the boundary at one side is at a potential energy equal to that in the bottom of the triangular well mentioned above especially if no allowance is made to 'move' the boundaries during the calculation as outlined in detail previously.

The effect of an external field on the valence subband dispersion is shown in Figure 4.8, where

the direction of $k_{||}$ is along <100>. For F = 0kV/cm all subbands are spin-degenerate which means that within each subband both spin components have the same energy at each wavevector value. However for non-zero electric fields the subbands split and the only degeneracy is at $k_{||} = 0$.

Note that the subband confinement energies $E_n(k_{||} = 0)$ are also different. This shift in energy has been called the quantum confined Stark effect[25] (QCSE), which has been proposed as a possible candidate for fibre optic modulator devices[26] and also switching devices.[27] The QCSE devices rely on the modulation of optical absorption due to an external modulating electric field, given that the optical absorption is directly proportional to the squared overlap integral of electron and hole subband envelope functions. In most cases of interest these are the ground state wave functions, namely CB1 and HH1.

In fact almost all modulated quantum well devices rely on some form of modulation of the quantum well eigenstates for their principal mode of operation. The effect of the electric field on the squared overlap integral of the electron and hole envelope functions has already been shown in Figure 4.7. From this Figure the term $<\psi_{CB1}|\psi_{HH1}>^2$ is seen to fall to 50% of the zero-field value at a field value of less than 80 kV/cm, with most of the change being linear in the applied field. The absorption (proportional to $<\psi_{CB1}|\psi_{HH1}>^2$) can then be modulated linearly with the applied field. However, in practice it would be necessary to consider the effect of all the other subbands. These are of less importance for optical frequencies below the fundamental bandgap but will still contribute. Their effect will of course be reduced if narrower wells are used, this serving to both reduce the number of bound eigenstates and to increase the separation in energy between them. Also, for a given value of electric electric field, $<\psi_{CB1}|\psi_{HH1}>^2$ decreases with decreasing well width. This must of course be offset against the reduced optical confinement factor due to the narrower quantum well structures.

The calculated shift in confinement energies, with respect to the centre of the well, is shown in Figure 4.9 for the CB1 and HH1 subbands. In each case energy is measured positively into each subband so that the confinement energy of these subbands actually decreases with increasing electric field. These results apply to both of the spin components in each subband since all subbands are doubly degenerate at $k_{||} = 0$.

The higher subbands, which are not shown in Figure 4.9, display an increase in confinement energy $E_n(k_{||} = 0)$ with increasing electric field. This is the opposite situation to that observed in the case of the ground states CB1 and HH1.

The effects of the applied electric field will also be taken into account later, when the optical properties of GaAs-AlGaAs quantum wells will be considered. The reduction in the overlap integral between electron and hole states reduces the contribution to the real part of the index of refraction by these states. Similarly, the absorption coefficient is reduced.

It has been mentioned previously that in some cases the overlap integral may increase. This is particularly true when the zero-field overlap integral is zero, due to the different parity of the states

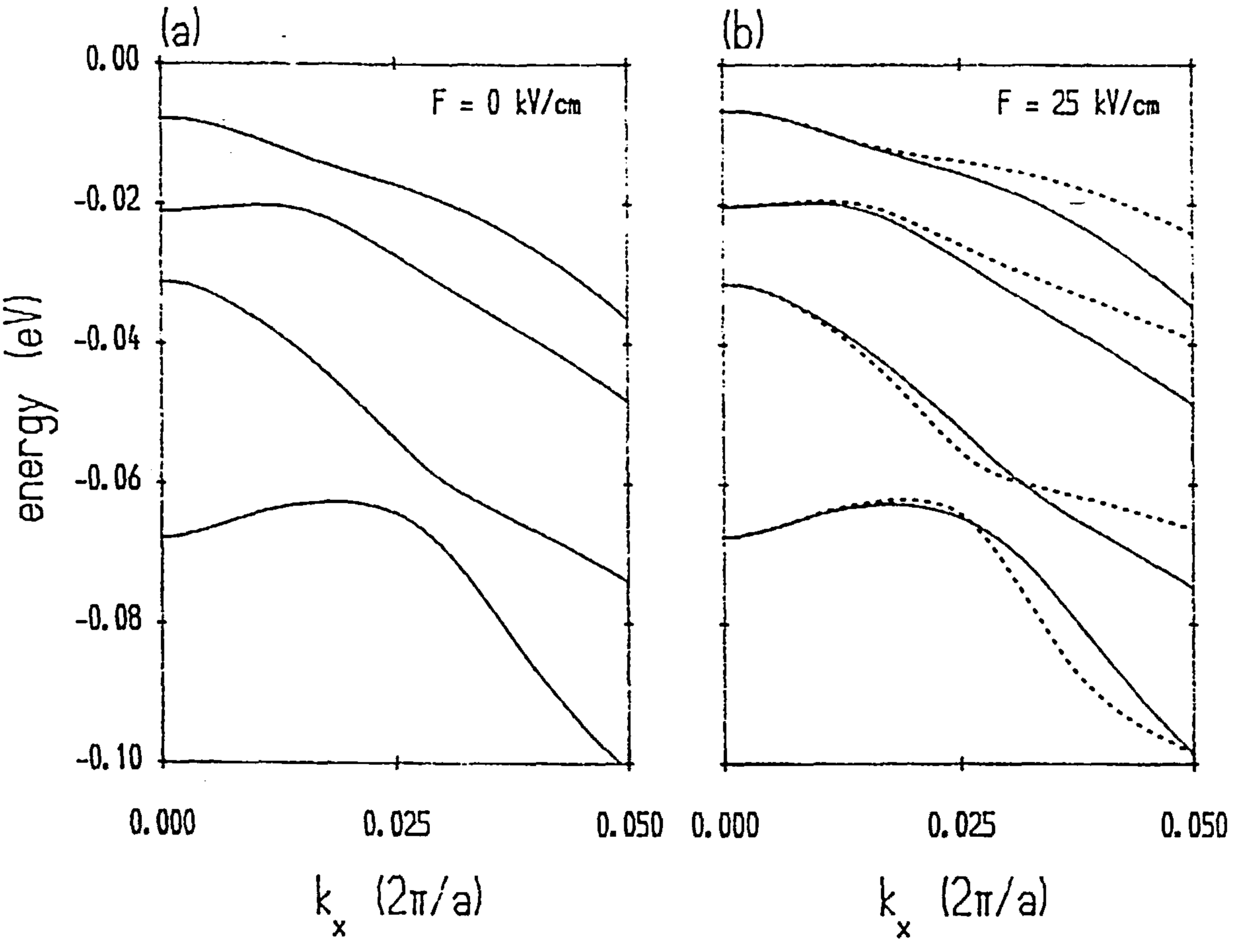

Figure 4.8 *Valence subband dispersion along the <100> direction for a GaAs-$Al_{0.2}Ga_{0.8}As$ single quantum well for (a) F = 0 kV/cm and (b) F = 25 kV/cm.*

involved. Although the most important contributions at photon energies below the bandgap, namely $\langle\psi_{CB1}|\psi_{HH1}\rangle^2$ and $\langle\psi_{CB1}|\psi_{LH1}\rangle^2$ will decrease with increasing electric field, other contributions, i.e. $\langle\psi_{CB2}|\psi_{HH1}\rangle^2$ and $\langle\psi_{CB2}|\psi_{LH1}\rangle^2$ will initially increase with an increase in the electric field. Proper calculation of the optical properties must then include all confined subbands in both the conduction and valence bands. It would not be possible to obtain correct results by including only a few selected subbands in the calculations.

Up until now we have concentrated on the subband structure in single quantum wells. However, also of great importance are the electronic and optical properties of double quantum wells. These may have different material in each of the three barrier regions and may also have different well thicknesses in each of the two well regions. The electronic structure in GaAs-AlGaAs double quantum wells will be examined in the next section.

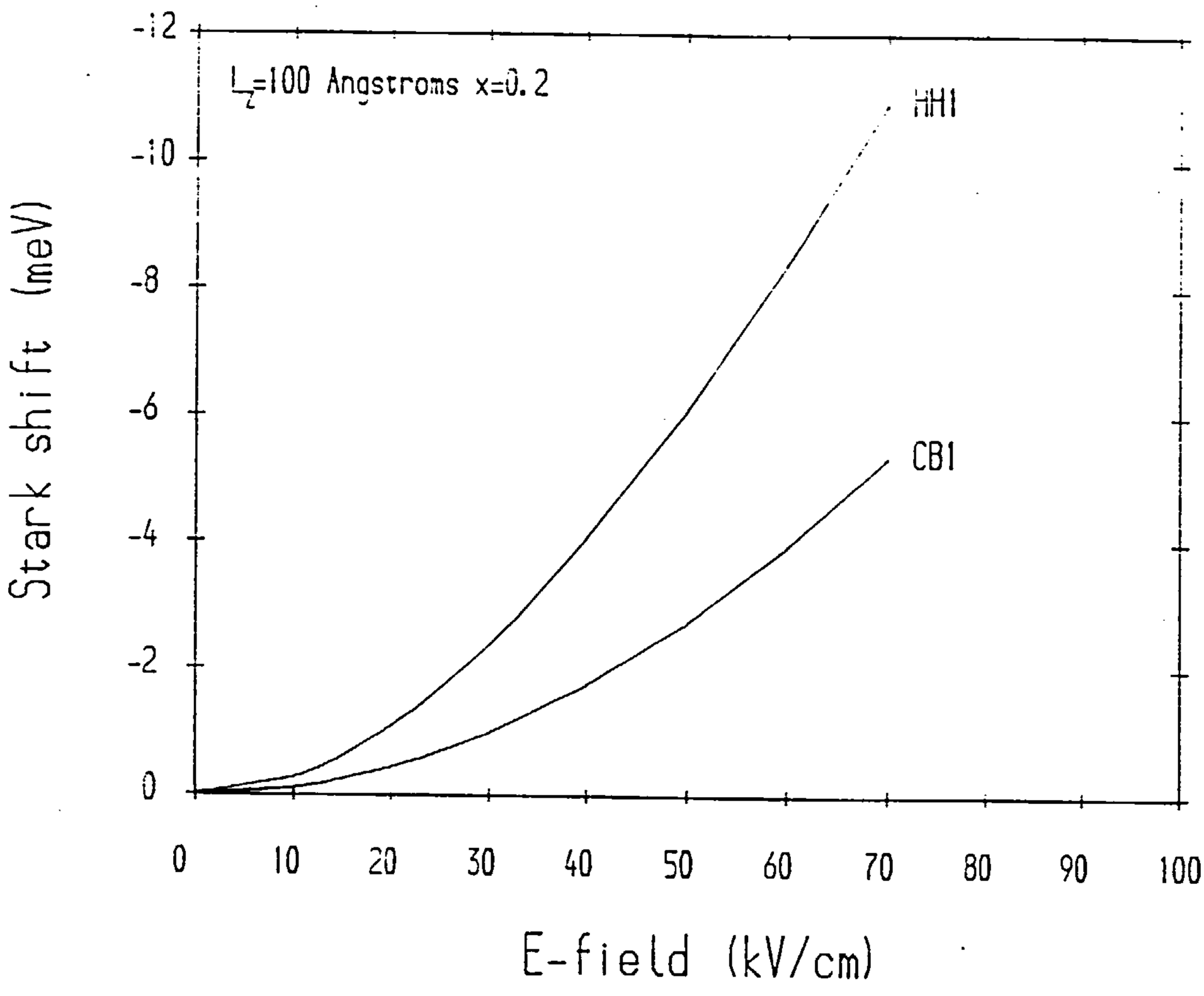

Figure 4.9 *Quantum confined stark effect (QCSE) shift of the CB1 and HH1 subband energies in a 100Å GaAs-$Al_{0.2}Ga_{0.8}As$ single quantum well. The shift is with respect to energy being measured positively into each subband.*

Double quantum wells

In the case of double quantum wells and with thin central barriers, then it may be possible for the bound single well eigenstates to couple. This would produce symmetric and anti-symmetric wave functions, in an analogous behaviour to that seen in atomic bonding.

The well widths used in the calculations so far have not been obtained by consideration of the GaAs layer thickness. Given that one single GaAs layer has a width of 5.653Å and ignoring the small difference in layer thickness in $Al_xGa_{1-x}As$ for $x \leq 0.4$, then it was chosen to consider a double quantum well structure of well thicknesses 50.877Å (9 layers) and with a central barrier thickness of 14.133Å (2.5 layers).

This is the structure which will be considered at first. Later, the central barrier will be increased to 25.439Å (4.5 layers) to examine the effect of central barrier thickness on the subband

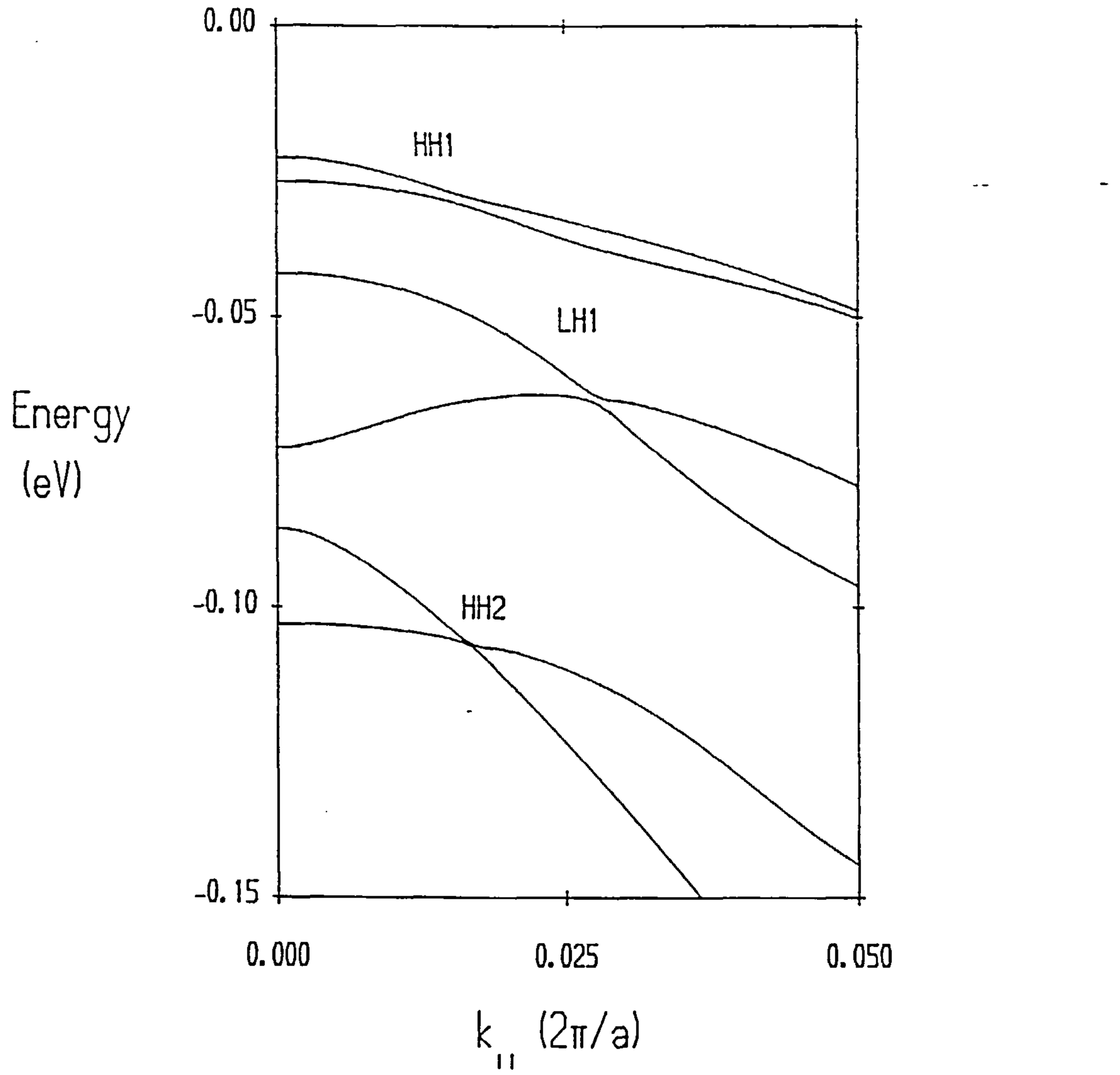

Figure 4.10 *Valence subband dispersion along <100> direction for GaAs-$Al_{0.3}Ga_{0.7}As$ double quantum well. The well widths are 50.877Å and the central barrier width is 14.133Å.*

dispersion. Although coupling will be observed in both the conduction and valence subbands, only the results for the valence subband dispersion will be displayed. The subband dispersion is more complex in the valence band, and is more important when considering the optical properties.

The calculated valence subband dispersion, along the in-plane direction <100> is illustrated in Figure 4.10. The aluminium content in the barrier is x = 0.3, which has been chosen to reduce the number of confined subbands and hence the size of the calculations. This structure is obtained using the Luttinger-Kohn Hamiltonian, described in detail previously. In this case, the continuity conditions are applied at each interface along the growth axis (four interfaces in this case) and as usual the wave functions are set to zero at a distance of several well widths into the outermost barrier regions. The aluminium fraction x = 0.3 is the same in all barrier regions in this example.

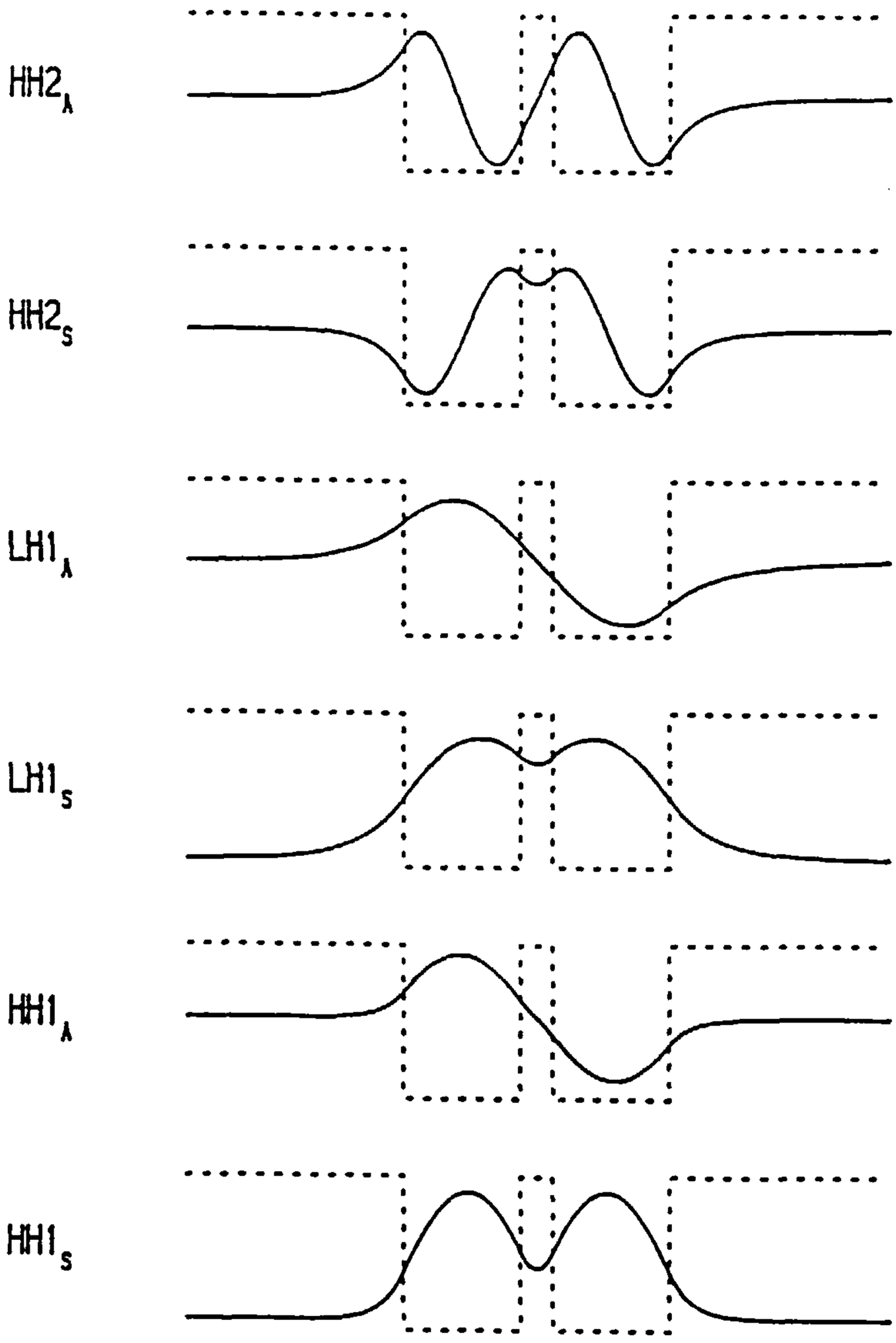

Figure 4.11 *Subband envelope functions at $k_{||} = 0$ for GaAs-AlGaAs double quantum well structure. The well widths are 50.877Å and the central barrier width is 14.133Å.*

It is clear from Figure 4.10 that the subbands in each quantum well have coupled, due to the small width of the central barrier region. Within each pair of coupled subbands, it is possible to describe each subband wave function as either symmetric or anti-symmetric. This can be seen more clearly in Figure 4.11, where the calculated envelope functions (not to scale) are illustrated. Within each pair, the energies are no longer degenerate and indeed are different for all values of $k_{||}$ in Figure 4.10. There is also a clear anti-crossing behaviour, although the symmetric and anti-symmetric partners approach each other to within less than a few meV.

Note also from Figure 4.10 that the LH1 antisymmetric wave function reaches a maximum

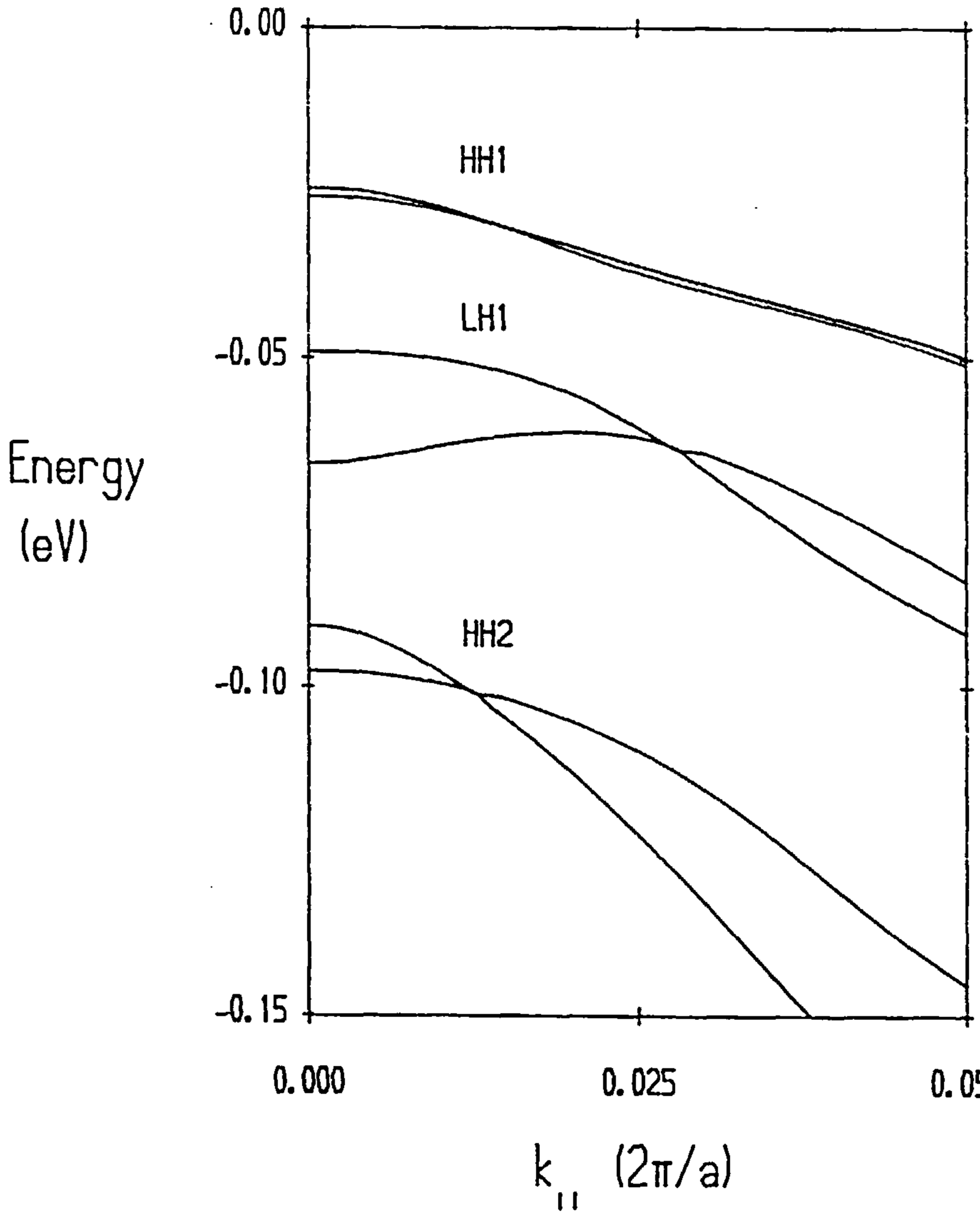

Figure 4.12 *Valence subband dispersion along <100> direction for GaAs-$Al_{0.3}Ga_{0.7}As$ double quantum well. The well widths are 50.877Å and the central barrier width is 25.439Å.*

value in energy at $k_{||} \approx (\pi/L_{tot})$ where L_{tot} is the sum of the well region and central barrier region widths. This is similar to the case of the single quantum well LH1 subband outlined earlier. In this case (π/L_{tot}) appears to be a characteristic inverse length of the quantum well structure.

In Figure 4.12 the subband dispersion is shown for the second double quantum well structure, with an increased central barrier thickness. The central barrier width has been increased from 14.133Å to 25.439Å. In this case the symmetric and anti-symmetric energy levels have moved closer together signifying a reduction in the amount of wave function coupling through the central barrier region. This effect would continue with increasing width of the central barrier region, until at sufficiently wide barrier thicknesses both wells would be completely uncoupled. For most of the quantum wells considered in this thesis, the well widths are around 100Å. For multiple quantum

well (MQW) structures with the well regions separated from each other by similarly thick barrier regions, then the structure can be considered as separate quantum wells with negligible inter-well coupling. This then simplifies calculation of the in-plane dispersion and the optical properties in such structures.

References

1 J.M. LUTTINGER and W. KOHN, Physical Review **97**, 896 (1955)

2 M. BRAUN and U. RÖSSLER, Journal of Physics **C18**, 3365 (1985)

3 B. LAMBERT, J. CAULET, A. REGRENY, M. BAUDET, B. DEVEAUD and A. CHARRETTE, Semiconductor Science and Technology **2**, 491 (1987)

4 W.I. WANG, E.E. MENDEZ and F. STERN, Applied Physics Letters **45**, 639 (1984)

5 H. KROEMER, W.Y. CHEN, J.S. HARRIS and D.D. EDWALL, Applied Physics Letters **36**, 295 (1980)

6 R.C. MILLER, A.C. GOSSARD, D.A. KLEINMAN and O. MUNTEANU, Physical Review **B29**, 3740 (1984)

7 R. DINGLE, A.C. GOSSARD and W. WEIGMANN, Physical Review Letters **34**, 1327 (1975)

8 U. EKENBERG, Physical Review **B40**, 7714 (1989)

9 J. WANG and J.P. LEBURTON, Superlattices and Microstructures **8**, 191 (1990)

10 R.C. MILLER, D.A. KLEINMANN, W.T. TSANG and A.C. GOSSARD, Physical Review **B24**, 1134 (1981)

11 G. BASTARD, E.E. MENDEZ, L.L. CHANG and L. ESAKI, Physical Review **B26**, 1974 (1982)

12 R.L. GREENE, K.K. BAJAJ and D.E. PHELPS, Physical Review **B29**, 1807 (1984)

13 M. ALTARELLI, U. EKENBERG and A. FASOLINO, Physical Review **B30**, 3569 (1984)

14 A. TWARDOWSKI and C. HERMAN, Physical Review **B35**, 8144 (1987)

15 S.S. NEDOREZOV, Soviet Physics Solid State **12**, 1814 (1971)

16 D.A. BROIDO and L.J. SHAM, Physical Review **B31**, 888 (1985)

17 E.P. O'REILLY, Semiconductor Science and Technology **4**, 121 (1989)

18 D. AHN, S.L. CHUANG and Y.C. CHANG, Journal of Applied Physics **64**, 4056 (1988)

19 D. AHN and S.L. CHUANG, Journal of Applied Physics **64**, 440 (1988)

20 S.L. CHUANG, Physical Review **B40**, 10379 (1989)

21 See for example: L.I. SCHIFF, *Quantum Mechanics* (M^{c}Graw-Hill, New York 1968)

22 G. BASTARD, E.E. MENDEZ, L.L. CHANG and L. ESAKI, Physical Review **B28**, 3241 (1983)

23 F.F. FANG and W.E. HOWARD, Physical Review Letters **16**, 797 (1966)

24 J. SINGH, Applied Physics Letters **48**, 434 (1986)

25 D.A.B. MILLER, D.S. CHEMLA, T.C. DAMEN, A.C. GOSSARD, W. WEIGMANN, T.H. WOOD and C.A. BURRUS, Physical Review **B32**, 1043 (1985)

26 S. TARUCHA and H. OKAMOTO, Applied Physics Letters **48**, 1 (1986)

27 D.A.B. MILLER, D.S. CHEMLA, T.C. DAMEN, T.H. WOOD, C.A. BURRUS, A.C. GOSSARD and W. WEIGMANN, IEEE Journal of Quantum Electronics **QE-21**, 1462 (1985)

MISSING

PAGE/PAGES

HAS NO

CONTENT

5 Absorption and Gain in Quantum Well Structures

Introduction

The optical properties of GaAs-$Al_xGa_{1-x}As$ quantum wells have attracted considerable interest during the last decade. Calculations of the index of refraction and of the absorption coefficient have concentrated on the contribution due to the electron and hole bound subbands alone and the exciton states alone.[1-11]

It is known,[12] however, that a proper calculation of the index of refraction in quantum wells must include the effect of continuum states and also the spin-orbit split-off valence band. In the case of optical absorption, then for frequencies below the fundamental bandgap, the neglect of these states makes no significant difference to the final results. It is only in the particular case of the index of refraction, where if an accuracy of $\Delta n/n$ of the order of a few percent is required that the above contributions must be included.[12]

Figure 5.1 *Schematic illustration of the valence and conduction band edges at the Γ point in GaAs. The bands are labelled according to the representations at $k_{||} = 0$. Also shown is the common notation for the energy gaps at Γ. The values of these energy gaps at room temperature are given by:*

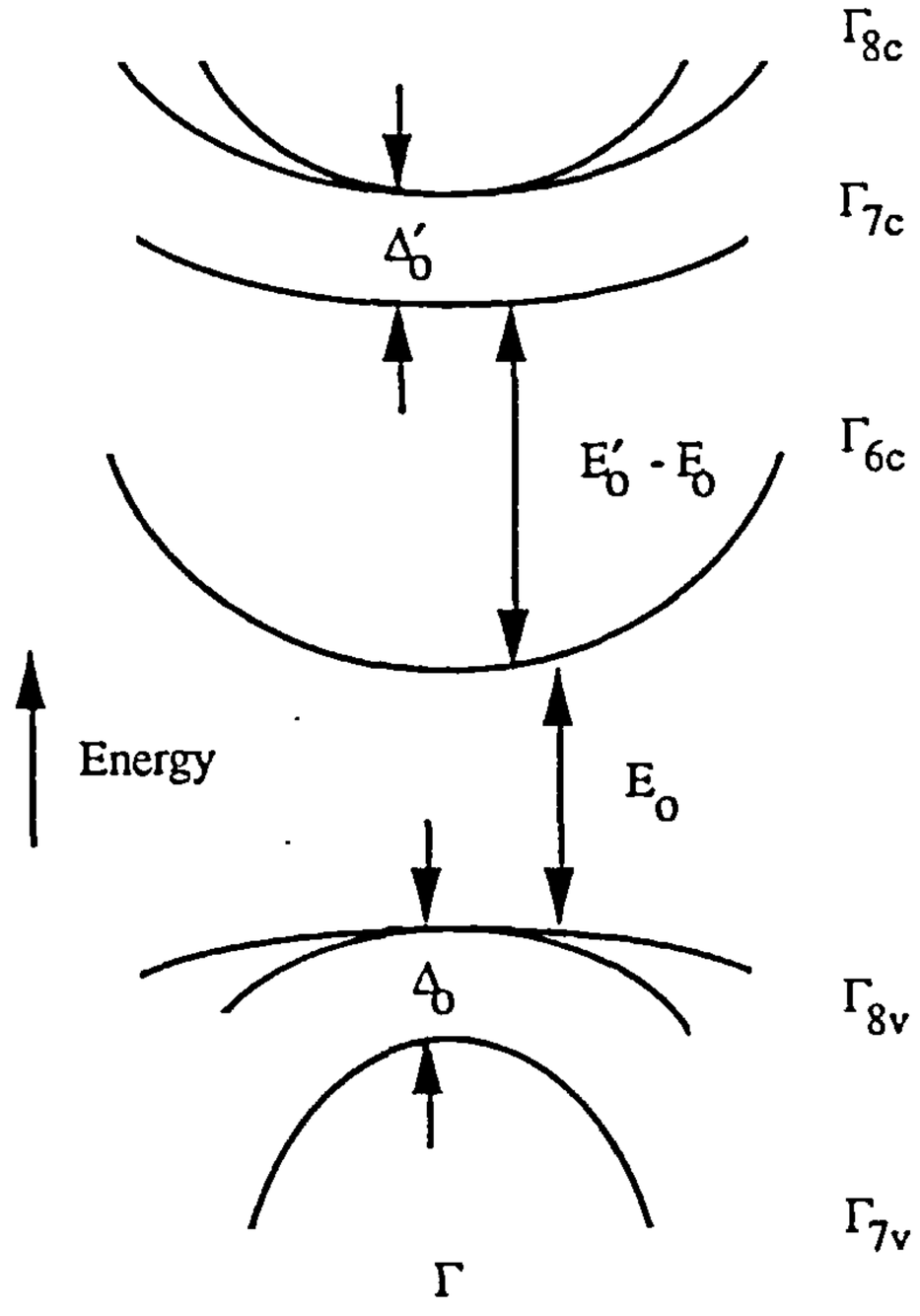

$$E_o = 1.425 \text{ eV}$$
$$E'_o = 4.44 \text{ eV}$$
$$\Delta_o = 0.34 \text{ eV}$$
$$\Delta'_o = 0.19 \text{ eV}$$

The value of Δ'_o is often given as negative, with E'_o suitably re-defined.

The optical properties include both absorption and refraction. In this Chapter, we concentrate on the absorption spectrum and deal with the index of refraction in the following Chapter.

As well as the band-to-band contribution to the absorption it is necessary to include the effects of excitons. Although difficult to resolve in bulk material, except at very low temperature, the excitonic contribution to the absorption spectrum is clearly resolved in quantum well structures, even at room temperature.[13]

Transitions and matrix elements

It is useful to recall the electronic bands considered throughout the thesis, which are illustrated in Figure 5.1. The particular bands of interest here are the Γ_{8v} and Γ_{6c} bands which in bulk GaAs are separated at the zone-centre by the fundamental bandgap E_o. From the basis given in Table 3.1, the optical matrix elements between all the bulk Γ_{8v} and Γ_{6c} bands are as given in Figure 5.2. These are proportional to the Kane parameter P, which appears in equation (3.48) in the submatrix H_{cv}. Note that this is for a given direction of angular momentum quantisation (with respect to the electron wavevector). The squared average over all directions in bulk material therefore gives the squared

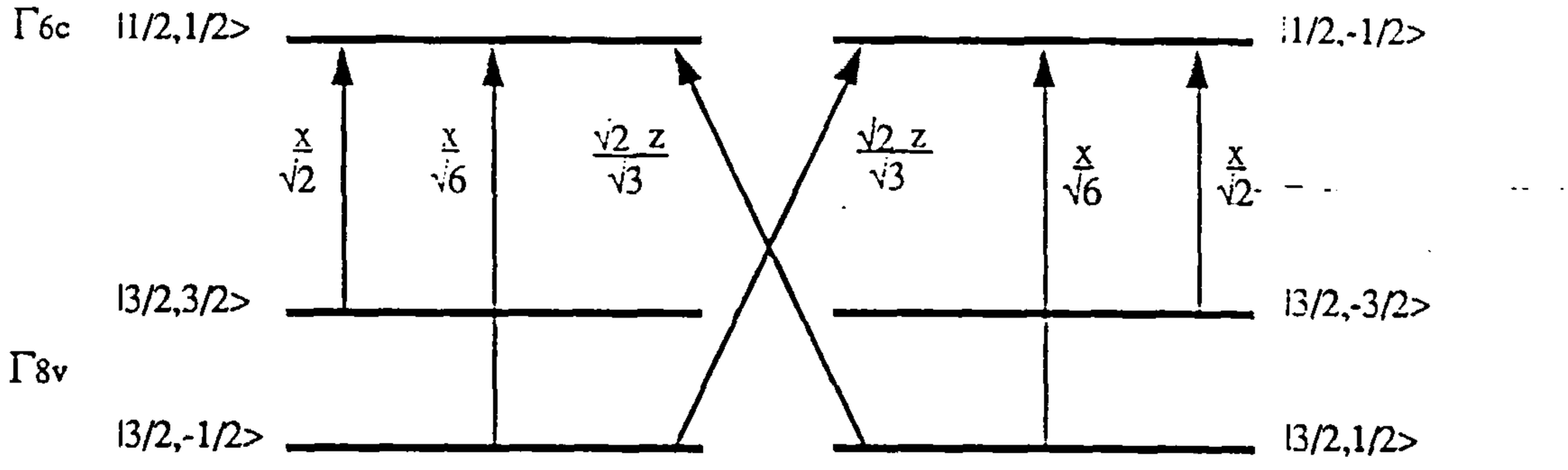

Figure 5.2 *Polarisation dependence and coupling strength for dipole allowed transition matrix elements between the Γ_8 ($J = 3/2$) valence band and the Γ_6 ($J = 1/2$) conduction band.*

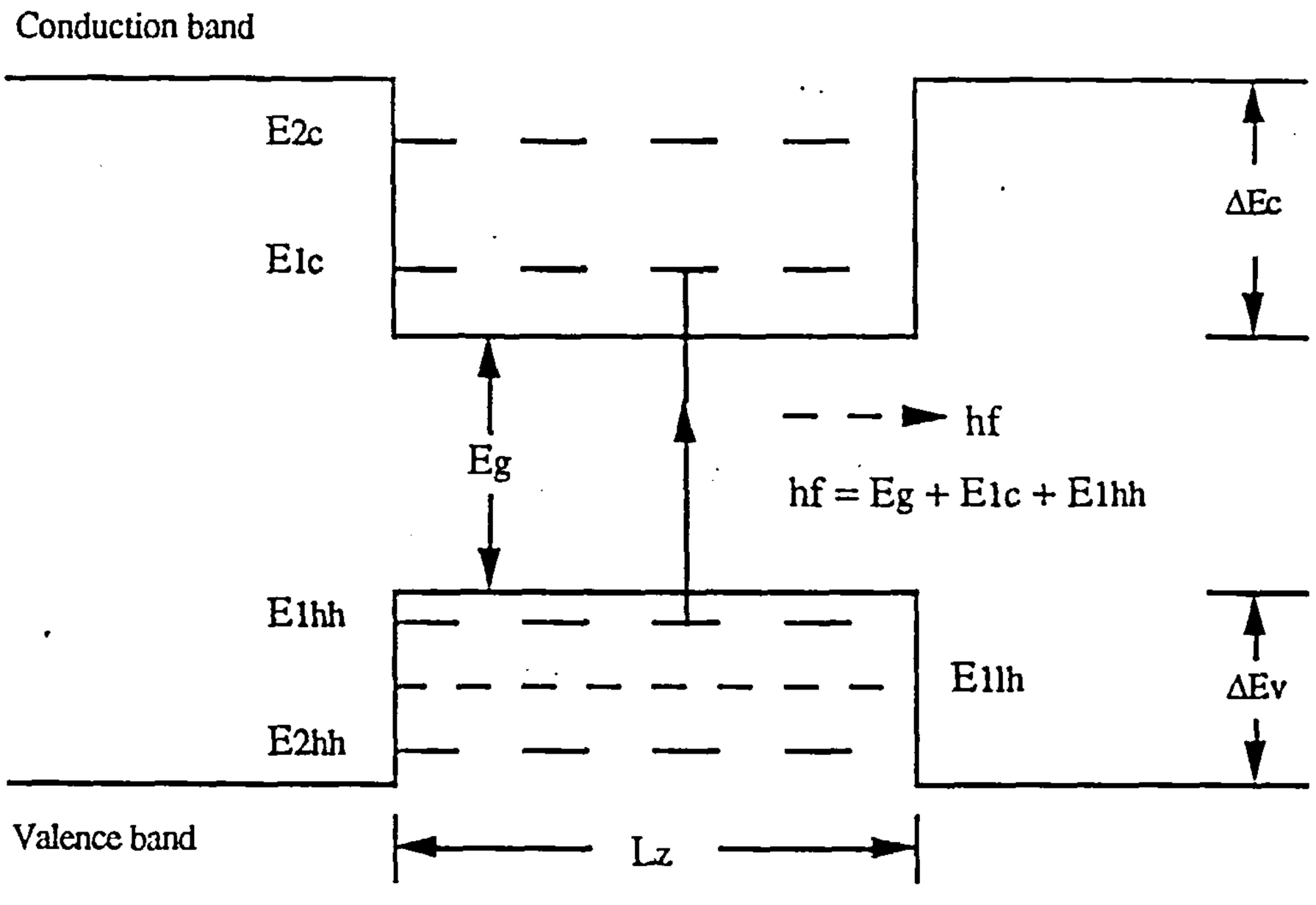

Figure 5.3 *Schematic illustration of the valence and conduction band confinement potentials and the quantised subband energy levels, for a well of width L_z. The transition energy hf for a direct band-to-band transition (or recombination process) between the HH1 and CB1 subband is indicated.*

momentum matrix elements (in eV)

$$P_{\text{bulk}}^2 = \frac{1}{3} \cdot \frac{2}{m_o} < S|p_x|X >^2 = 7.86 \text{ eV} . \tag{5.1}$$

Note that the averaging introduces the $\frac{1}{3}$ factor in equation (5.1). In using the density matrix formalism, outlined in Appendix A, the dipole matrix element is used. This is simply given by

$$< S|ex|X >^2 = \frac{e^2\hbar^2}{m_o^2 E_t^2} < S|p_x|X >^2 . \tag{5.2}$$

Note that equation (5.1) uses the value of $<S|p_x|X>$ obtained from a 14-band **k·p** scheme. The more usual value, obtained from a truncated 3-level **k·p** scheme[14] is rather larger and less accurate. Note also that frequently the bulk value of the squared momentum matrix element is wrongly quoted. This is due to an incorrect equation first appearing in Ref. 15. The principal transitions are shown in Figure 5.3.

For photon energies below and near the band gap E_o the quantised subband states are the closest in energy and hence contribute most to the optical absorption. The use of the density matrix formalism, which includes the intraband scattering rates naturally, is the most simple model to describe the so-called band-tailing effects in semiconductors. This simply accounts for the below-bandgap absorption seen in all semiconductors at non-resonant optical frequencies.

The more remote states, most importantly the quasi-continuum states in the vicinity of the top of each potential well and the true continuum states, are not as important as the quantised subband states in contributing to the absorption coefficient at energies below the bandgap E_o. However, they should be taken into account fully in a proper theoretical model. However, these states are more important in calculating the index of refraction in order to obtain accurate results.

Band-to-band absorption

By assuming that the quantisation axis is along the z-direction, the optical matrix elements can be obtained directly from the basis functions of Table 3.1. Note that so far we have neglected to include the overlap integral of the bound state envelope functions. Also, we have ignored the effect of non-zero in-plane wavevectors. For small values of $k_{||}$ this can be safely ignored but for larger values of $k_{||}$ the direction of **k** given by

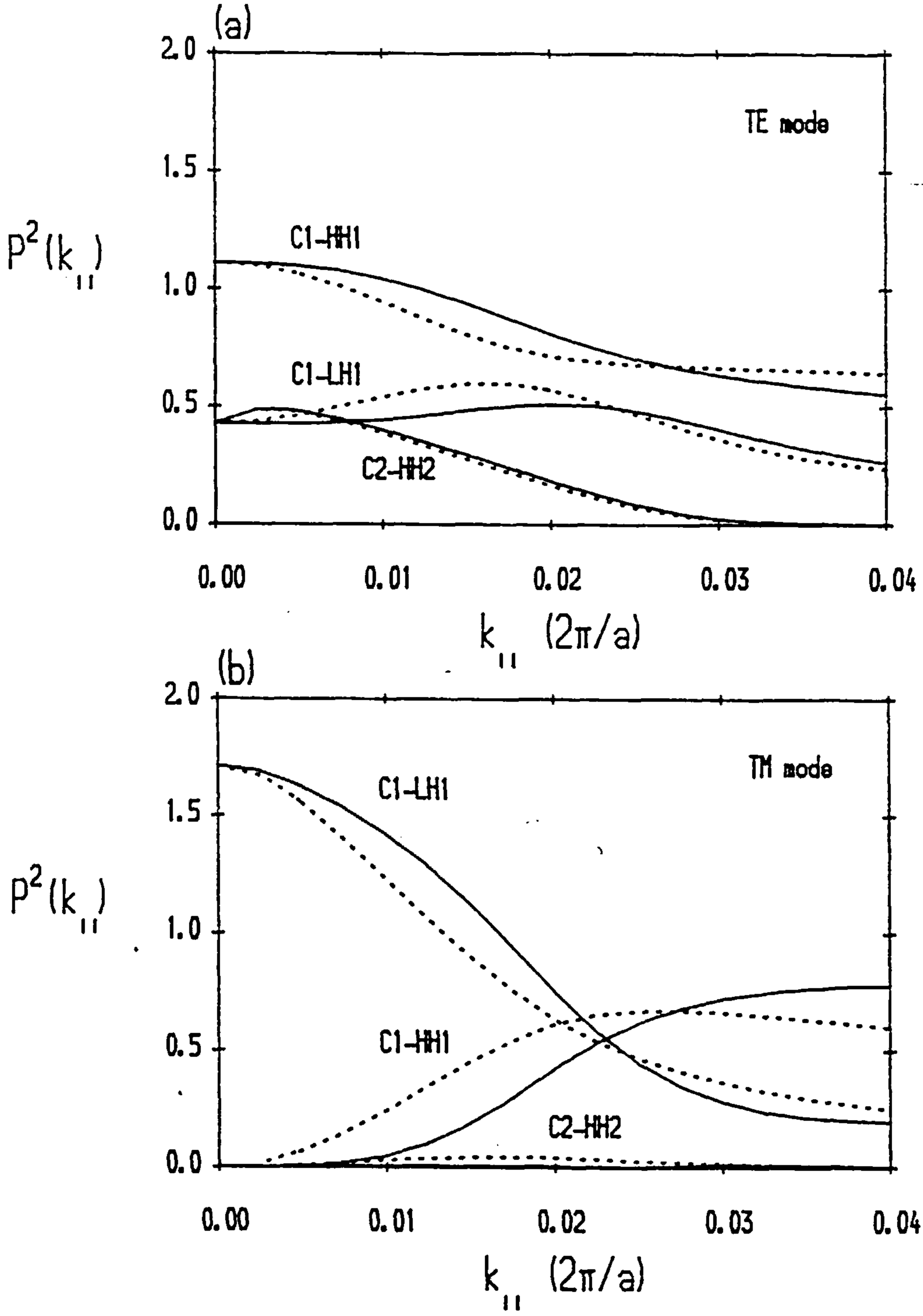

Figure 5.4 *Squared momentum matrix elements between the valence and conduction subbands in a 100Å GaAs-$Al_{0.2}Ga_{0.8}As$ single quantum well with an applied electric field of F = 50 kV/cm along the growth axis. The matrix elements are in units of the bulk averaged squared matrix element. The transitions included are HH1-CB1, LH1-CB1 and HH2-CB2. The solid curves include only the in-plane mixing of the basis given in Table 3.1, whereas the dotted curves also include the anisotropy factors which are given by equation (5.4).*

$$\theta = \tan^{-1}\frac{k_{||}}{k_z}, \tag{5.3}$$

must be considered, where k_z is the wavenumber of the bound subband envelope functions in the z-direction (growth direction). In the case of optical absorption this is the hole subband envelope function. This leads to the following additional factors for the TE and TM mode matrix elements, where TE and TM denote the plane of polarisation either in the well plane, (x-y) plane, or perpendicular to the interfaces along z.

$$P^2_{\pm 3/2}(TE) \rightarrow \frac{1}{2}(1+\cos^2\theta)P^2 \tag{5.4a}$$

$$P^2_{\pm 1/2}(TE) \rightarrow \frac{1}{6}(1+\cos^2\theta)P^2 + \frac{2}{3}(\sin^2\theta)P^2 \tag{5.4b}$$

$$P^2_{\pm 3/2}(TM) \rightarrow (\sin^2\theta)P^2 \tag{5.4c}$$

$$P^2_{\pm 1/2}(TM) \rightarrow \frac{1}{3}(\sin^2\theta)P^2 + \frac{4}{3}(\cos^2\theta)P^2, \tag{5.4d}$$

where the P^2 on the right hand side of equation (5.4) are as obtained from the basis in Table 3.1 for the envelope function components J=±1/2 and J=±3/2. This agrees with the form given in Ref. 16 but not with the other more commonly used and incorrect form.[17]

Figure 5.4 shows the calculated optical matrix elements, in units of the bulk averaged value for several transitions in a 100Å GaAs-$Al_{0.2}Ga_{0.8}As$ single quantum well. These results are for an applied perpendicular electric field of 50 kV/cm^2. The results give both the matrix elements obtained directly from Table 3.1 (solid curves) and those including the above anisotropy factors (dotted curves) in equation (5.4). From this figure it is clear that the inclusion of the anisotropy factors has a noticeable effect on the matrix element for each transition considered. The factors given on equation (5.4) will therefore be used throughout this thesis.

The band-to-band contribution to the linear optical absorption is shown in Figure 5.5 for the TE mode polarisation and in Figure 5.6 for the TM mode polarisation. In each case, several carrier densities have been assumed. These vary from $0.5\text{x}10^{18}\text{cm}^{-3}$ (top curve) to $3.0\text{x}10^{18}\text{cm}^{-3}$ (bottom curve) in steps of $5.0\text{x}10^{17}\text{cm}^{-3}$. A constant intraband scattering time of 100 fsec has been assumed in these calculations. The reduction in absorption with increasing carrier density is a consequence of the static Burstein-Moss shift,[18,19] due to the phase-space filling by the free carriers. In this case the quasi-Fermi levels in both the conduction and valence band are obtained numerically from the calculated subband dispersion. Note that for energies below the equivalent bulk GaAs bandgap at E_o the absorption falls considerably to less than 100cm^{-1} in both the TE and TM cases. At higher energies the absorption continues to steadily increase.

It is necessary at higher energies to consider transitions including quasi-continuum states and

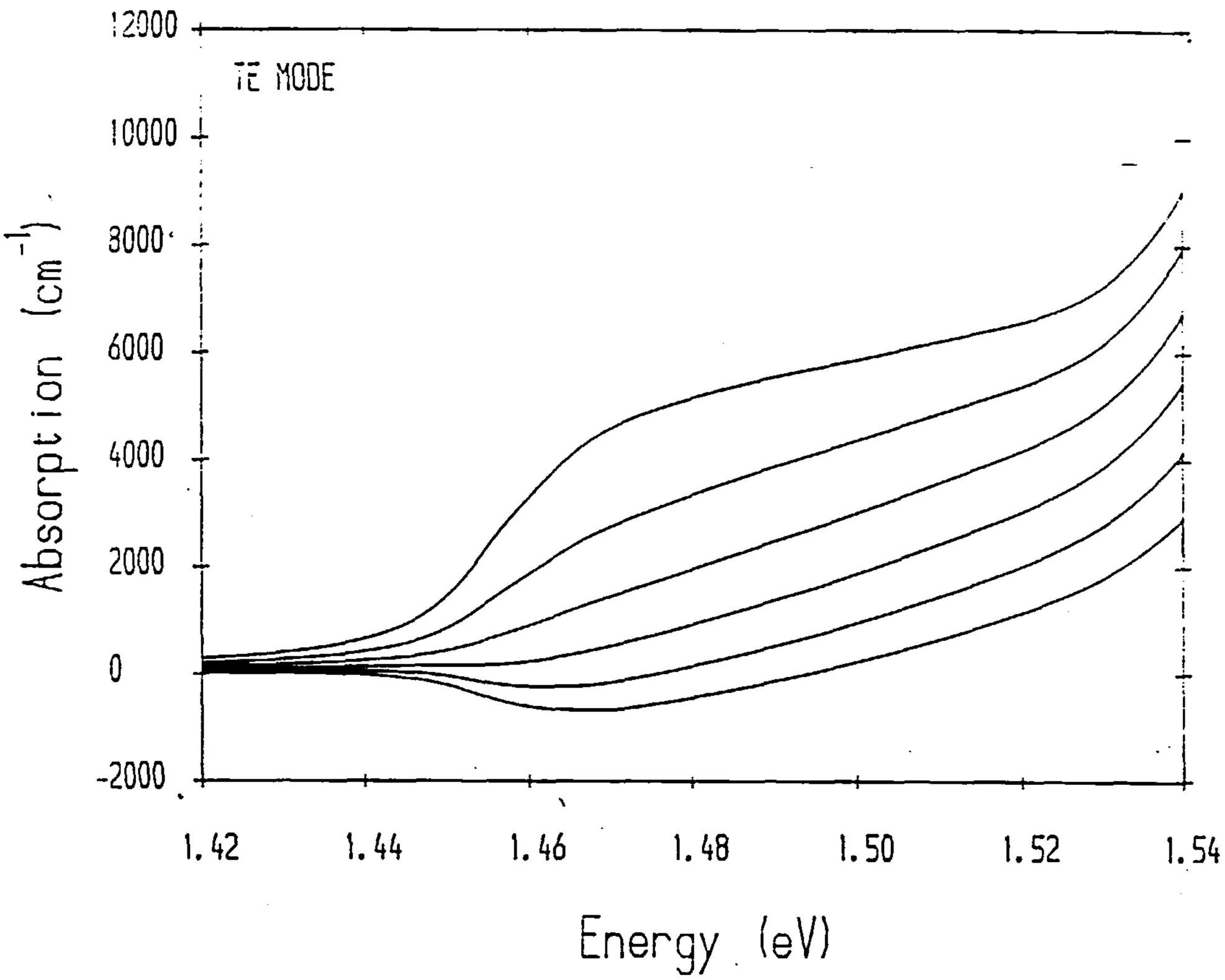

Figure 5.5 *TE mode linear band-to-band absorption spectra in a 100Å GaAs-$Al_{0.2}Ga_{0.8}As$ single quantum well with carrier densities from $n = 5x10^{17}cm^{-3}$ (top curve) to $n = 3x10^{18}cm^{-3}$ (bottom curve) in steps of $5x10^{17}cm^{-3}$.*

transitions including true continuum states. The quasi-continuum states have been discussed in the previous Chapter. For transitions involving bound valence subbands and continuum conduction band states we ignore any polarisation dependence, including only the consideration of momentum conservation. The higher conduction band states are obtained directly from the theory given in Chapter 3, using a virtual crystal approximation and the full 14-band k.p scheme but ignoring the off-diagonal terms of Luttinger and Kohn within each Γ_5 multiplet. This is expected to give reasonably accurate results and obviously includes the effects of the nonparabolic conduction band dispersion. The method is both simple to apply and computationally efficient.

As will be seen later, neglect of higher states by the introduction of an arbitrary cut-off at the top of each potential well in the conduction and valence bands, tends to decrease the calculated threshold carrier density in the case of quantum well lasers.

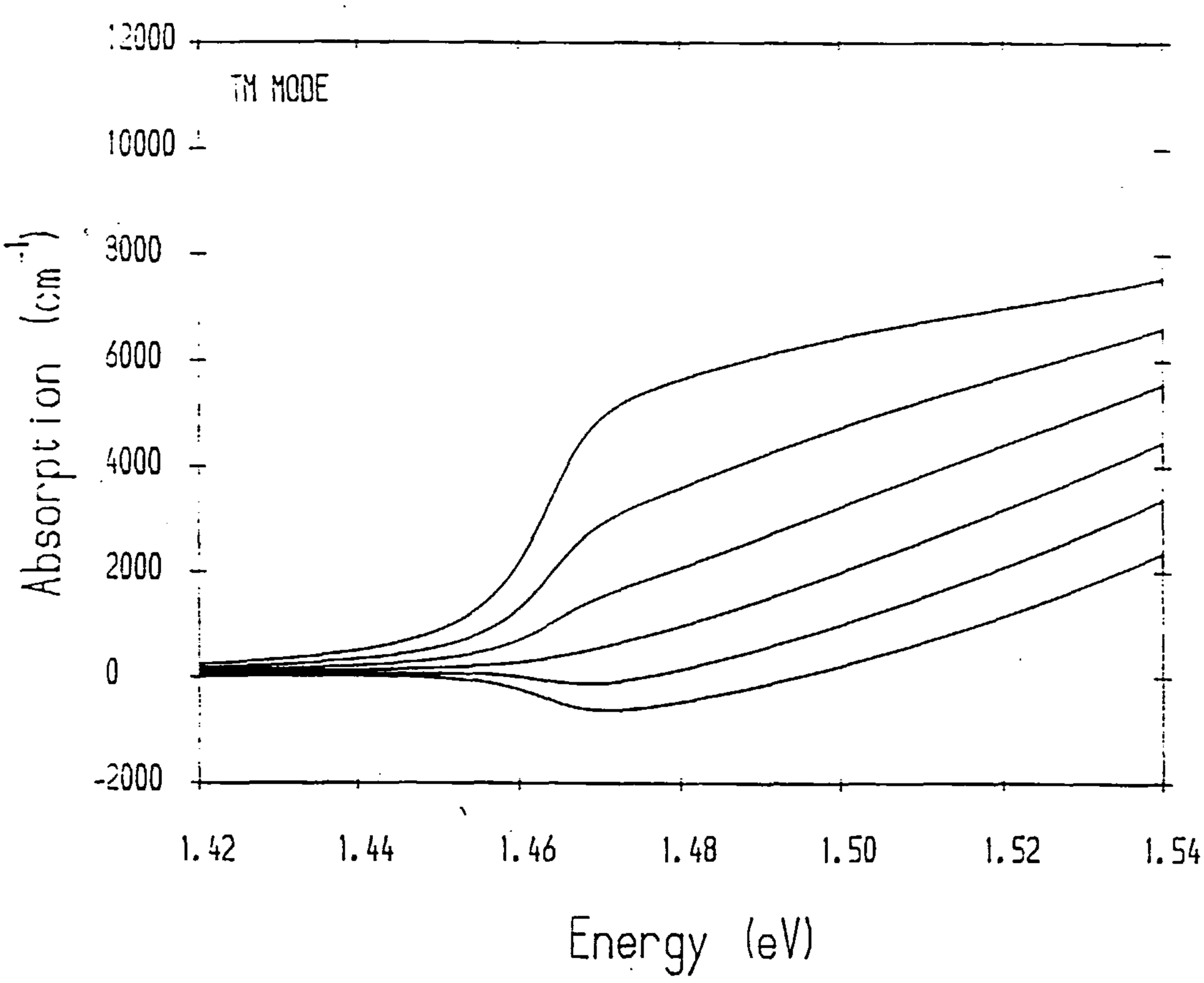

Figure 5.6 *TM mode linear band-to-band absorption spectra in a 100Å GaAs-$Al_{0.2}Ga_{0.8}As$ single quantum well with carrier densities from $n = 5x10^{17}cm^{-3}$ (top curve) to $n = 3x10^{18}cm^{-3}$ (bottom curve) in steps of $5x10^{17}cm^{-3}$.*

Absorption saturation

The effect of direct saturation under continuous optical excitation can be simply introduced into the density matrix formalism. However, it is interesting to consider first the more common approach to saturation. Note that saturation of absorption via phase space-filling also leads to a nonlinear refraction effect, which will be considered in the next chapter.

The most common model for saturation of absorption considers the number of electrons excited into the conduction band by the optical field at energy $\hbar\omega$. It is simply assumed that the optical radiation has created a conduction band population given by

$$N = \frac{\alpha(\omega) I T_1}{\hbar\omega}, \tag{5.5}$$

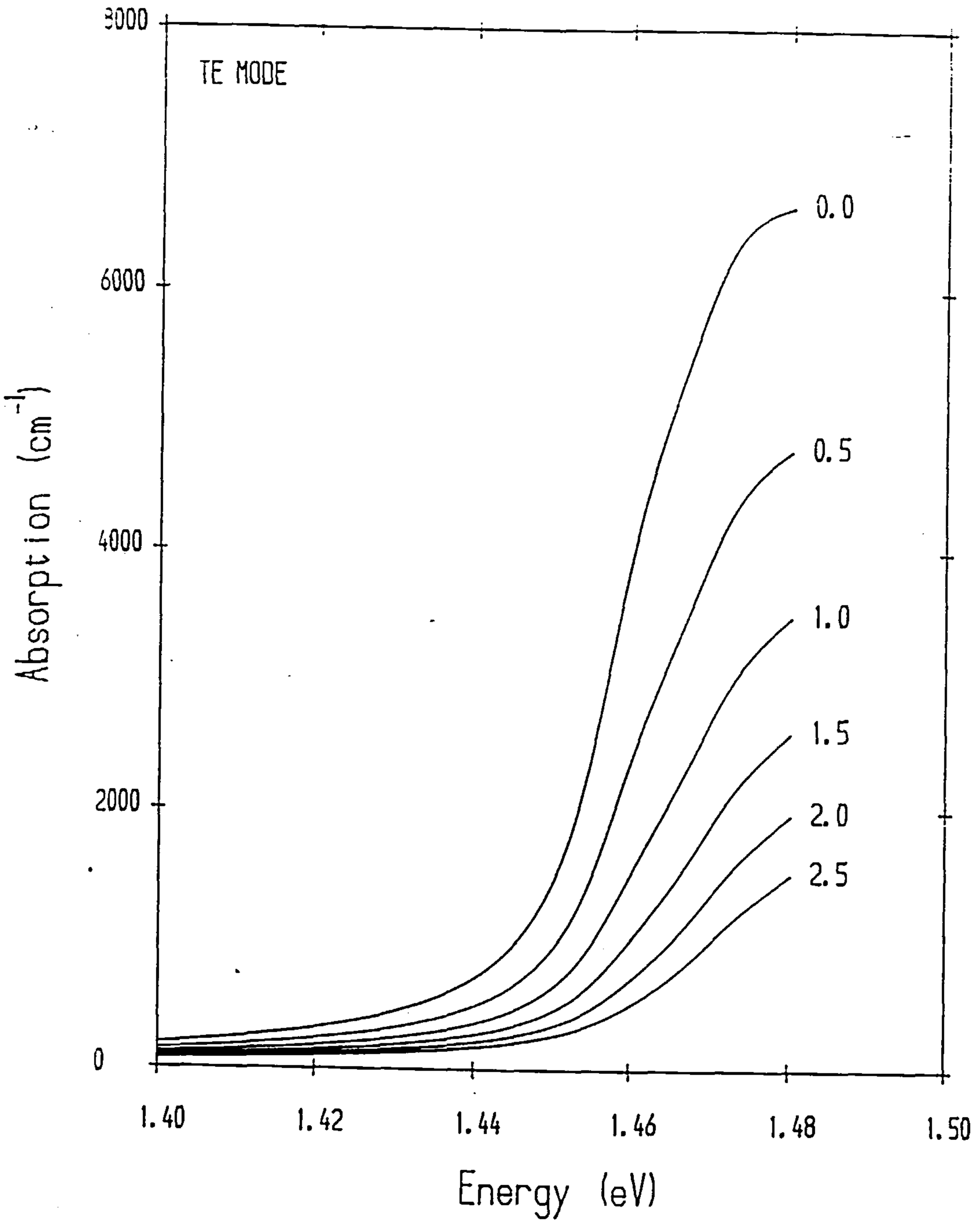

Figure 5.7 *TE mode band-to-band absorption in a 100Å GaAs-$Al_{0.2}Ga_{0.8}As$ single quantum well for six values of optical intensity. The quantum well is assumed to be under continuous wave optical excitation (except for $I = 0$). The results are obtained using the density matrix theory which is given by equation (5.10) and with a recombination lifetime given by $T_1 = 3$ nsec. The intensities indicated are in units of MW/cm^2.*

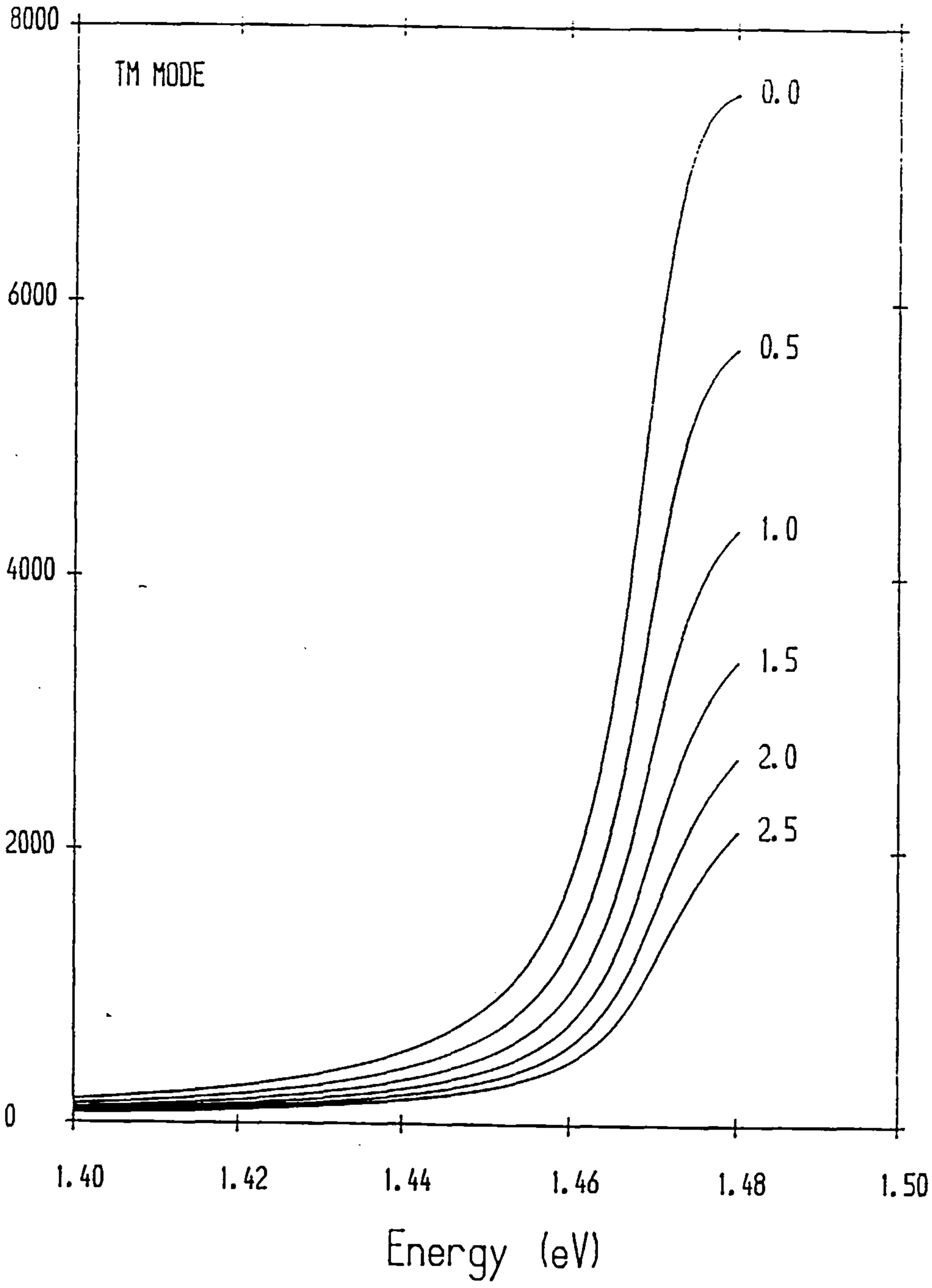

Figure 5.8 *TM mode band-to-band absorption in a 100Å GaAs-$Al_{0.2}Ga_{0.8}As$ single quantum well for six values of optical intensity. The quantum well is assumed to be under continuous wave optical excitation (except for I = 0). The results are obtained using the density matrix theory which is given by equation (5.10) and with a recombination lifetime given by T_1 = 3 nsec. The intensities indicated are in units of MW/cm^2.*

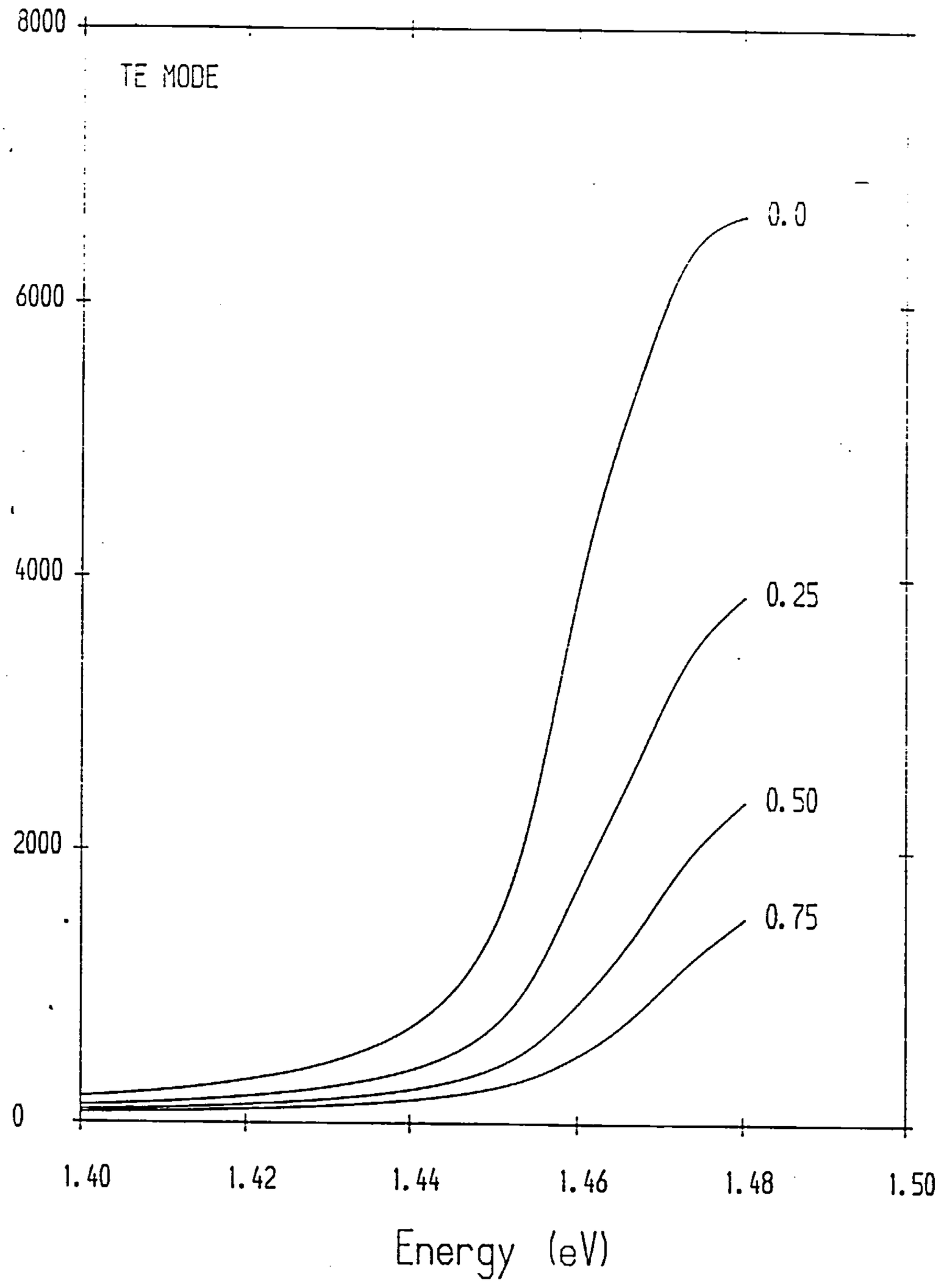

Figure 5.9 *TE mode band-to-band absorption in a 100Å GaAs-$Al_{0.2}Ga_{0.8}As$ single quantum well for four values of optical intensity. The quantum well is assumed to be under continuous wave optical excitation (except for I = 0). The results are obtained using the density matrix theory which is given by equation (5.10) and with a recombination lifetime given by T_1 = 10 nsec. The intensities indicated are in units of MW/cm^2.*

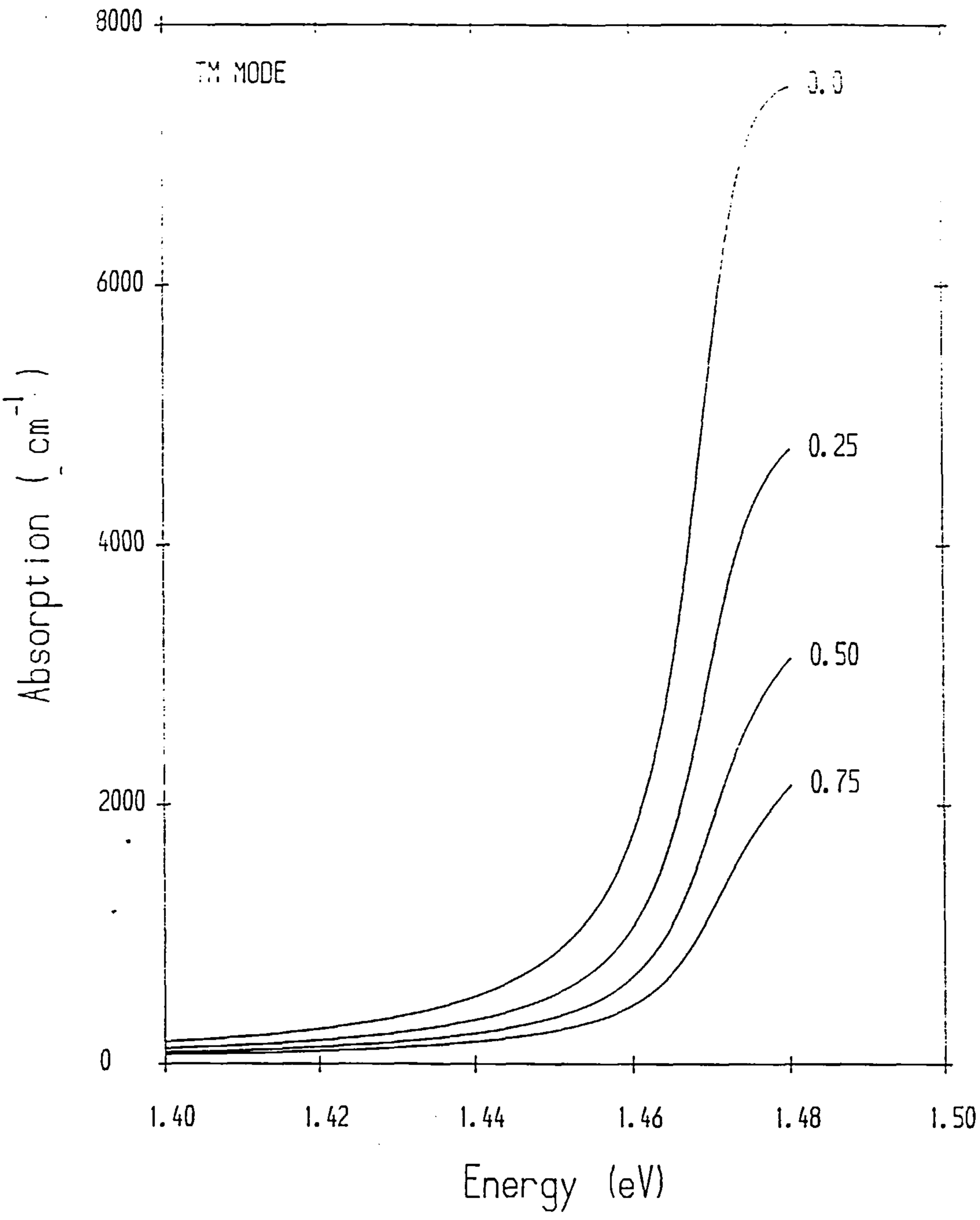

Figure 5.10 *TM mode band-to-band absorption in a 100Å GaAs-$Al_{0.2}Ga_{0.8}As$ single quantum well for four values of optical intensity. The quantum well is assumed to be under continuous wave optical excitation (except for I = 0). The results are obtained using the density matrix theory which is given by equation (5.10) and with a recombination lifetime given by T_1 = 10 nsec. The intensities indicated are in units of MW/cm^2.*

where I is the intensity of the radiation, $\alpha(\omega)$ is the linear absorption coefficient at energy $\hbar\omega$ (usually taken as an empirical factor) and T_1 is the relaxation time which describes the decay of the conduction band population to the zero-field value (thermal distribution). Typically T_1 is taken to be independent of $k_{||}$.

The constant population now created in the conduction band is therefore seen as a blocking mechanism to further transitions. Note that the origin of the absorption is not considered explicitly. It is simply assumed that some interband absorption does occur without asking which processes are involved. In the region of interest, it is known that some small absorption will occur and this is assumed to be the cause of the interband transitions. Since the excited electrons rapidly thermalise to the bottom of the conduction band, a steady-state population can be easily obtained. This is seen as causing a shift in the effective bandgap, known as the dynamic Burstein-Moss shift,[18,19] which is intensity-dependent and leads to an associated intensity-dependent contribution to the index of refraction.

To consider the active material process involved in saturation it is necessary to either use a properly coupled perturbation and rate-equation method[20] or to employ density matrix theory. From Appendix A, the two-level elements of the density matrix evolve (at frequencies ω_1,ω_2) as

$$\frac{d\rho}{dt} = \frac{1}{i\hbar}[H_o + H', \rho] + \left(\frac{\partial\rho}{\partial t}\right)_{\text{relax}} , \tag{5.6}$$

where

$$H' = \left\{\frac{-e}{m_o}\mathbf{p}\cdot\mathbf{A}(\omega_1)e^{-i\omega_1 t} + \frac{-e}{m_o}\mathbf{p}\cdot\mathbf{A}(\omega_2)e^{-i\omega_2 t} + \text{c.c.}\right\} . \tag{5.7}$$

$\mathbf{A}(\omega_1)$, $\mathbf{A}(\omega_2)$ are the magnitudes of the vector potential of the radiation fields at ω_1, ω_2 respectively and $\mathbf{p}$ is the momentum vector of the electron in the crystal. The elements of ρ satisfy, at a resonant frequency ω_{ab}

$$\frac{d}{dt}\rho_{ab} = -\frac{1}{i\hbar}H_{ab}d_{ab} - i\omega_{ab}\rho_{ab} - \Gamma_{ab}\rho_{ab} \tag{5.8a}$$

$$\frac{d}{dt}d_{ab} = \frac{2}{i\hbar}H_{ab}\rho_{ba} - \frac{2}{i\hbar}H_{ba}\rho_{ab} - \frac{d_{ab}-1}{T_{ab}} , \tag{5.8b}$$

where $d_{ab} = \rho_{aa}-\rho_{bb}$ is the excess ground state population in the one-electron model. $\Gamma_{ab} = \Gamma_{ba} = \Gamma$ is the dephasing rate of the polarisation and $T_{ab} = T_1$ is the recombination time discussed previously. From Ref. 22 an exact solution of this problem gives the susceptibility in the form

$$\chi(\omega,\mathbf{E}) = \frac{|\hat{\varepsilon}\cdot\mathbf{M}_{ab}|^2}{E_{ab}-\hbar\omega-i\left(\frac{\hbar}{T_2}\right)}\cdot\frac{(E_{ab}-\hbar\omega)^2+\left(\frac{\hbar}{T_2}\right)^2}{(E_{ab}-\hbar\omega)^2+(\hbar/T_2)^2+4\left(\frac{T_1}{T_2}\right)|\mathbf{E}\cdot\mathbf{M}_{ab}|^2}, \qquad (5.9)$$

where **E** is the radiation field field strength, $\hat{\varepsilon}$ is the photon polarisation vector and $\mathbf{M}_{ab}$ is the dipole matrix element. Comparison with the results in Appendix A gives the form of equation (5.9) to be used in this case

$$\chi(\omega,\mathbf{E}) = \frac{1}{\varepsilon_o V}\sum_{k_{||}}\sum_{c,v}\frac{|\mathbf{E}\cdot\mathbf{M}_{cv}(k_{||})|^2\left(f_v(k_{||})-f_c(k_{||})\right)}{E_c(k_{||})-E_v(k_{||})-\hbar\omega-i\left(\frac{\hbar}{\tau_{in}}\right)}$$
$$\times\left\{1+\frac{4\left(\frac{T_1}{\tau_{in}}\right)|\mathbf{E}\cdot\mathbf{M}_{cv}(k_{||})|^2}{\left(E_c(k_{||})-E_v(k_{||})-\hbar\omega\right)^2+\left(\frac{\hbar}{\tau_{in}}\right)^2}\right\}^{-1}. \qquad (5.10)$$

We have previously taken τ_{in} = 100 fsec so that T_1 is now the only unknown quantity in equation (5.10). Several experimental estimates of this are available and it is clear that the magnitude of the saturation strongly depends on the value chosen.

Figures 5.7 to 5.10 give the TE and TM mode calculations of the absorption obtained directly from equation (5.10) for two values of T_1 and for four values of intensity. The results are for a 100Å GaAs-$Al_{0.2}Ga_{0.8}As$ single quantum well. The two different values of T_1 used are T_1 = 3 nsec and T_1 = 10 nsec.

If there were only a single energy gap (i.e. if an ensemble of identical atoms was being considered) and a single constant value of the matrix element **M**, then it would be trivial to calculate a saturation intensity from equation (5.10). This is the value at which the absorption has fallen to 50% of the zero-field value. However since the calculation must be summed over $k_{||}$-space then this simple calculation is no longer valid. In the results shown in Figures 5.7 to 5.10 the $k_{||}$-dependence of T_1 and τ_{in} has been neglected.

Effect of doping

A reduction in absorption also results from either p-type or n-type doping. In this case we consider modulation doping, where only the barrier regions are doped and the free electrons or holes are thus

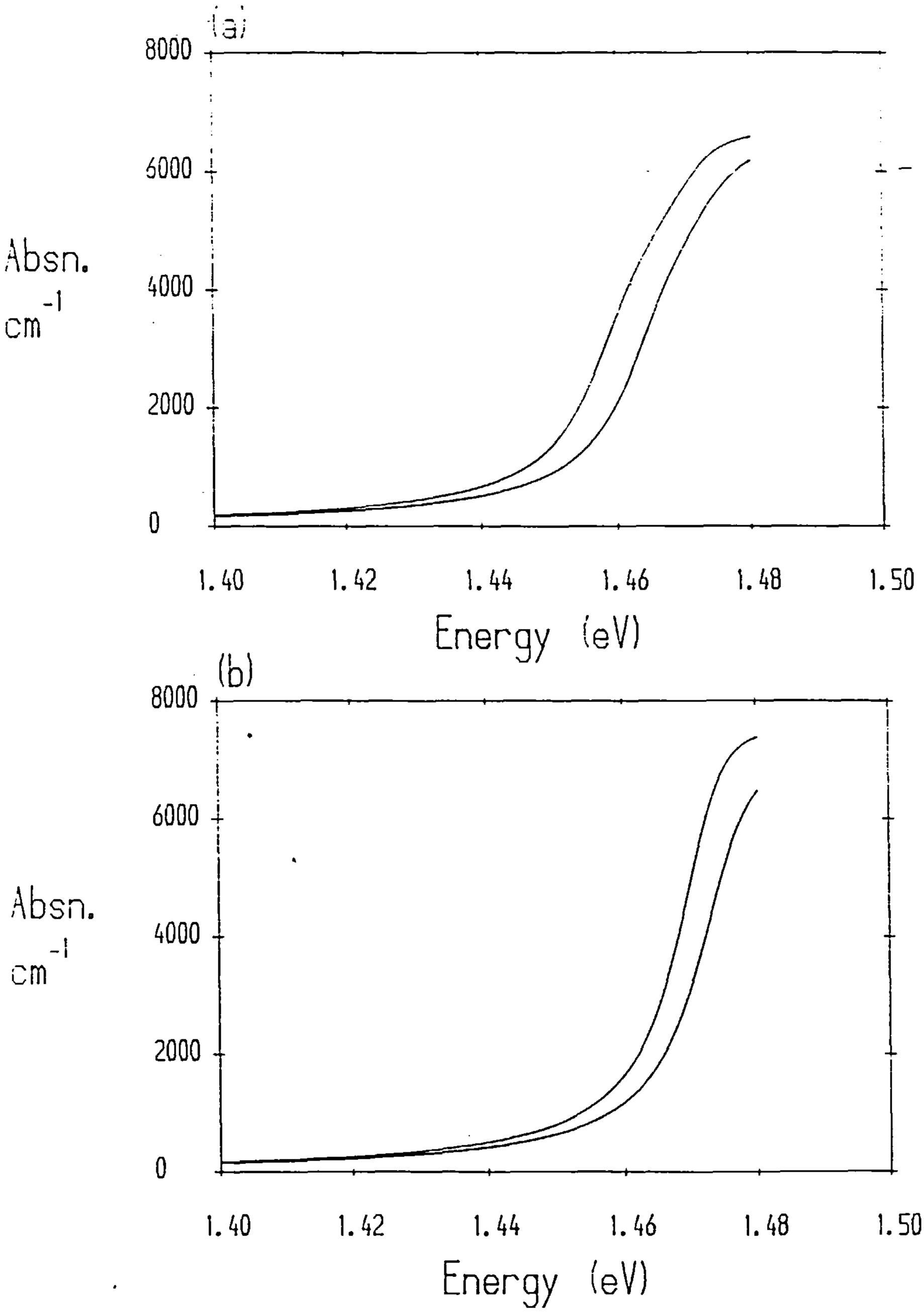

Figure 5.11 *Band-to-band contribution to the linear absorption coefficient for a p-type modulation doped single quantum well for (a) TE-mode and (b) TM-mode polarisation. The well width is 100Å and the barrier aluminium concentration is x=0.2. The top curve in each figure has a doping density of* $n=10^{10}cm^{-2}$ *and the lower curve has* $n=10^{11}cm^{-2}$.

confined within the quantum well regions. Since a similar method of analysis applies to either p-type and n-type modulation doping, the following discussion will treat only the specific case of p-type modulation doping. It will also be assumed that only band-to-band contributions to the linear absorption coefficient need be considered.

The presence of free holes in the quantum well regions means that the potential appearing in the Hamiltonians is no longer simply due to the difference in the well and barrier materials as assumed previously. In this case a self-consistent solution must be sought for the electron wave functions which includes the potential due to the hole population in the valence band. The total potentials can then be written as

$$\begin{aligned} V_e(z) &= V_w^e(z) + |e|Fz - |e|\phi(z) \\ V_h(z) &= V_w^h(z) - |e|Fz + |e|\phi(z) , \end{aligned} \tag{5.11}$$

where $V_w(z)$ is the material confinement potential, F allows for inclusion of an applied external electric field and ϕ represents the screening potential due to the free holes in the quantum well region. The potential $\phi(z)$ is the solution of Poisson's equation

$$\frac{d^2\phi(z)}{dz^2} = \frac{-|e|}{\varepsilon}\left[p(z) - n(z) + N_D(z) - N_A(z)\right] , \tag{5.12}$$

where ε is the background dielectric constant, p(z) and n(z) are the charge densities of holes and electrons respectively and N_A and N_D are the densities of ionised acceptors and donors respectively. The charge density p(z) is given by

$$p(z) = \frac{1}{A}\sum_{n}\sum_{k_{||}} |\varphi_{n,k_{||}}(r)|^2\left[1 - f_n(k_{||})\right] , \tag{5.13}$$

where A is the area of the quantum well region and $f_n(k_{||})$ is the Fermi function for the n^{th} valence subband. The $\psi_{k_{||}}^n(r)$ are the envelope-function solutions of each Hamiltonian.

In this case the Hamiltonians for the conduction and valence subbands are solved, then Poisson's equation is solved to re-estimate the potentials. These potentials are then substituted back into the Hamiltonians. This process is iterated self-consistently until the eigenvalues $E_m(k_{||})$ for each subband converge, or change by less than an amount, δ say, between iteration n and iteration (n+1). We take p(z) and n(z) typical of a thermal distribution at room temperature such that

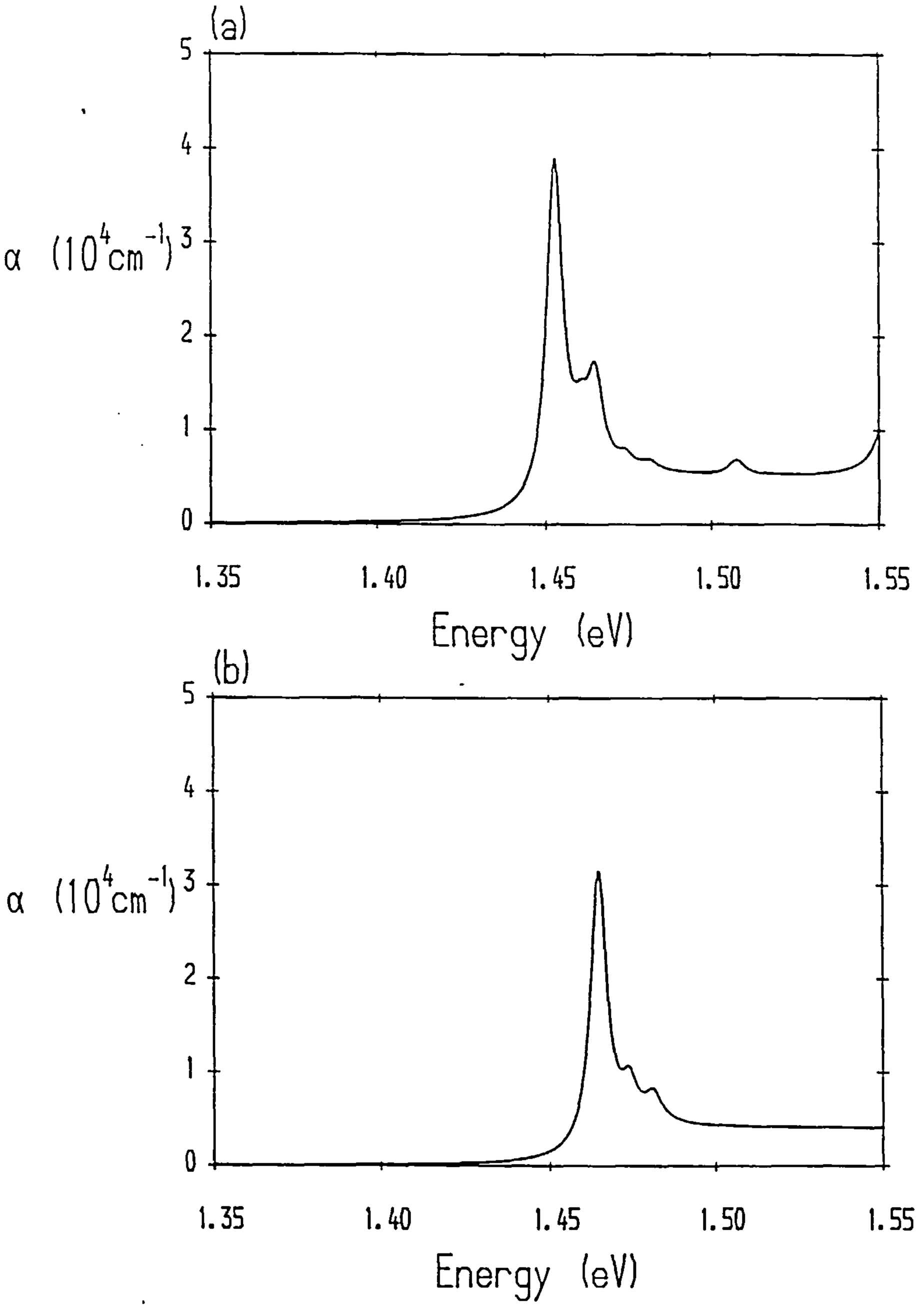

Figure 5.12 *Linear absorption spectra for 100Å GaAs-$Al_{0.25}Ga_{0.75}As$ quantum well for (a) TE polarisation and (b) TM polarisation. A total of fifteen exciton states have been included in the calculations in addition to the band-to-band contribution. Not all of these exciton states can be resolved in the spectra.*

$$\frac{1}{L_z}\int p(z) = \frac{1}{L_z}\int n(z) = N_{RT}\ , \tag{5.14}$$

and $N_D = 0$, N_A = the p-type doping density. The acceptors N_A are assumed to be uniformly distributed within the barrier material.

The calculated linear absorption spectra for a 100Å single quantum well with x = 0.2 are shown in Figure 5.11 for both the TE and TM polarisations and for several doping levels. The maximum doping level was chosen such that the potential due to the p-type doping was less than that due to the material confinement.

For doping levels of these magnitudes it is possible to introduce some approximations into the above theory. Assuming that all hole states are filled up to the hole Fermi level k_F, an approximation would be to consider only those transitions involving in-plane wavevectors outside the Fermi wavevector. Electrons can recombine to these states from the conduction band following direct transitions, this process being automatically included in the density matrix formalism used here. The above approximation is a static band-filling model.

A better approximation is to obtain the quasi-Fermi level for the valence bands alone and introduce a factor $[1 - f_h(k_{||})]$ when calculating the susceptibility. This has been the basis for previous studies[25,26] of absorption in doped quantum wells. The results given so far have included the band-to-band contribution to the absorption. The remainder of this chapter will include the effects of excitonic states on the optical absorption.

Exciton absorption

The inclusion of excitons follows from the theory given in Appendix B. The envelope function for an exciton using the two-band model is taken to be of Gaussian form $\phi_{eh}(k)=(2\pi\lambda)^{1/2}\exp(-k^2\lambda/4)$ with λ to be determined variationally. The total exciton wave function is then simply given by

$$\Psi(r) = \sum_{c,v}\sum_{k_{||}} \psi_c(k_{||},z)u_c\left[\sum_j \psi_v^j(k_{||},z)u_v^j\right]\phi_{eh}(k_{||})e^{ik_{||}\rho}\ , \tag{5.15}$$

where the u_c, u_v are the zone-centre Bloch functions and ψ_v, ψ_v are the single-particle envelope functions for the conduction subband and valence subband. As usual we order the states at Γ using the (J, mJ) "cubic harmonics" of the zincblende lattice.

If the exciton lineshape is assumed to be Lorentzian then the calculated absorption for a 100Å GaAs-$Al_{0.25}Ga_{0.75}As$ single quantum well is as shown in Figure 5.12. This assumes an excitonic

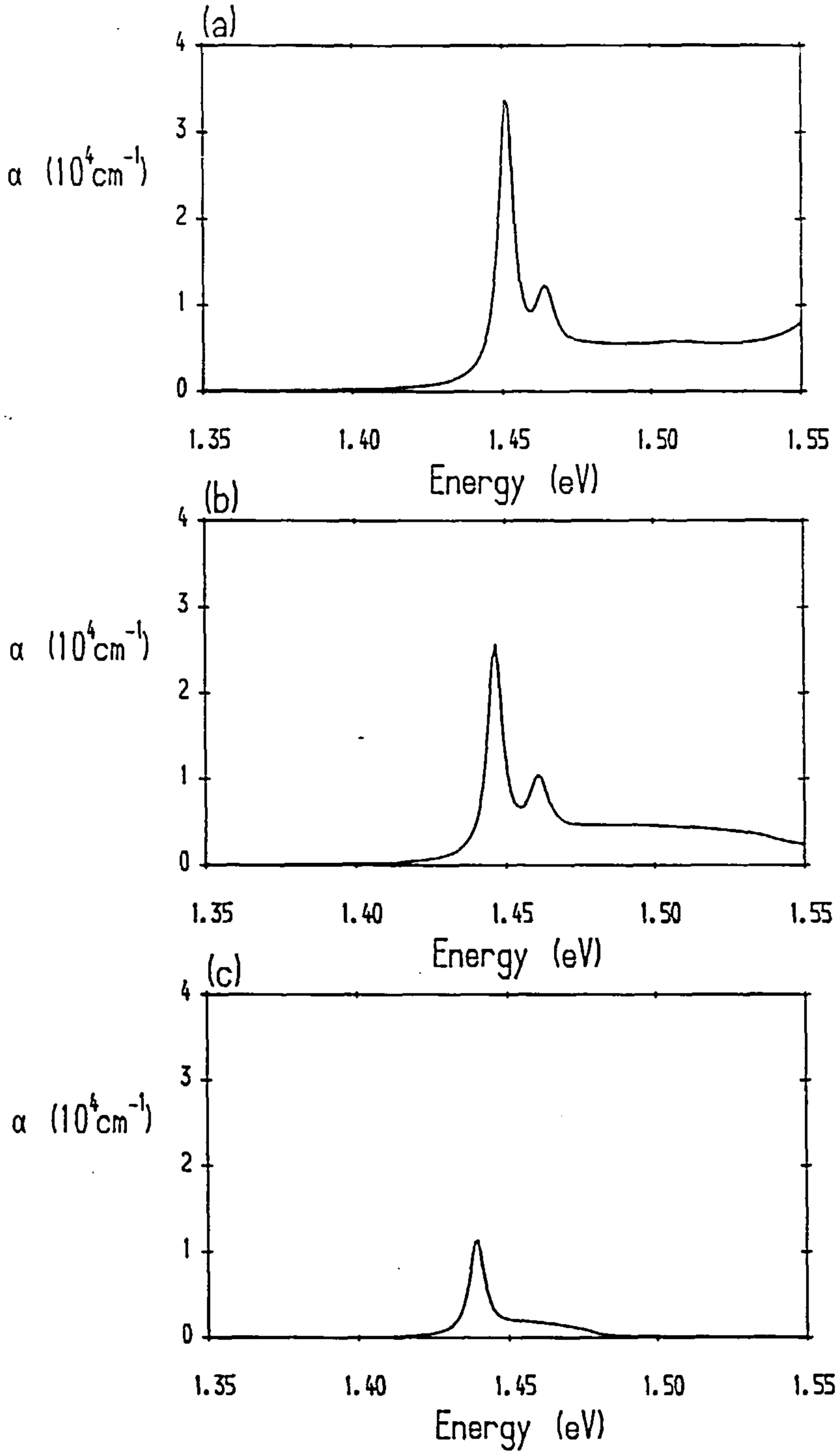

Figure 5.13 *TE mode linear absorption spectra for 100Å GaAs-$Al_{0.25}Ga_{0.75}As$ quantum well for three values of perpendicular electric field. The field values are (a) 25 kV/cm (b) 50 kV/cm and (c) 75 kV/cm. The HH1-CB1 (1s) exciton can still be clearly resolved at the highest field value of 75 kV/cm.*

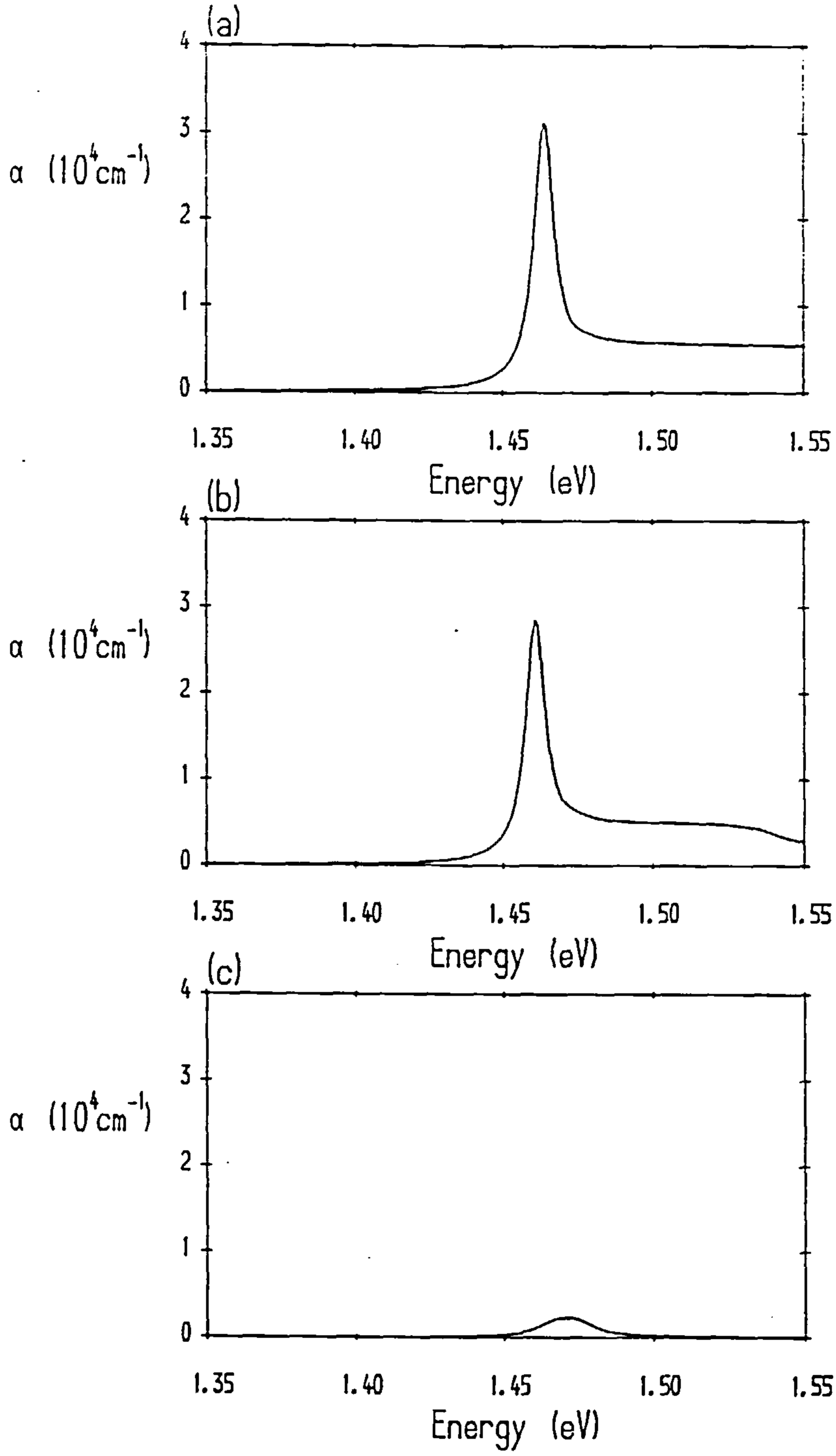

Figure 5.14 *TM mode linear absorption spectra for 100Å GaAs-$Al_{0.25}Ga_{0.75}As$ quantum well for three values of perpendicular electric field. The field values are (a) 25 kV/cm (b) 50 kV/cm and (c) 75 kV/cm. The LH1-CB1 (1s) exciton is essentially quenched at the field value of 75 kV/cm. This is in contrast to the HH1-CB1 (1s) exciton in Figure 5.13.*

linewidth[13] of 3meV for each bound exciton state. It has been assumed that only the HH1-CB1 exciton can be obtained using the two-band model. To obtain the other excitons we use the coupled-exciton model, detailed also in Appendix B.

The lowest excitons are clearly resolved in both TE and TM absorption. Since the exciton calculations are performed in $k_{||}$-space, then since all the single-particle states may be coupled by the Coulomb interaction, the HH2-CB1 (2p) exciton is clearly resolved. This is particularly interesting since at $k_{||} = 0$ the single-particle electron and hole envelope functions for these two subbands have zero overlap. If we compare the absorption coefficient for this exciton with experimental results, it is seen that the results given in Figure 5.12 agree with the experimental absorption results.[27] This disagrees with the frequently-used[27] choice of exciton linewidth $\Gamma = \Gamma_o(n_e n_h)$ meV, where Γ_o represents the CB1-HH1 exciton linewidth, and where n_e and n_h represent the subband level indices of the electron hole subbands.

The effect of a perpendicular electric field on the absorption is shown in Figures 5.13 and 5.14. For exciton states principally arising from single-particle states with similar zone-centre parity, the absorption is seen to initially decrease with the application of the electric field. The field reduces the overlap between these subbands, and hence reduces the exciton binding energy and matrix element. For exciton states built from subbands of different parity, the initially low electric field values can actually increase the overlap integral, resulting in an increased matrix element. This is clearly seen from the results given in Figures 5.13 and 5.14.

The oscillator strengths for the HH1-CB1 (1s) and LH1-CB1 (1s) excitons are given in Figure 5.15 for TE polarisation. It is found that in this quantum well structure, the HH1-CB1 (1s) exciton absorption remains unquenched even at fields greater than F = 80 kV/cm.

In the case of an optical switching device based on the quantum-confined Stark effect (QCSE), the change in absorption with applied electric field gives the modulation depth for the device. This can be represented by δ_{mod} given as

$$\delta_{mod}(\omega,F) = \frac{|\alpha(\omega,F) - \alpha(\omega,F=0)|}{\alpha(\omega,F=0)}, \tag{5.16}$$

for a particular optical frequency ω. To increase this modulation depth requires increased quenching of the optical absorption for a given electric field value. If this can be achieved then operation of optical modulation devices can be obtained at lower voltages.

To examine the structure dependence we take the case of (a) a single quantum well, (b) a double symmetric quantum well and (c) an asymmetric double quantum well structure. The parameters used in each case are GaAs wells with $Al_{0.25}Ga_{0.75}As$ barriers with widths in each structure given by

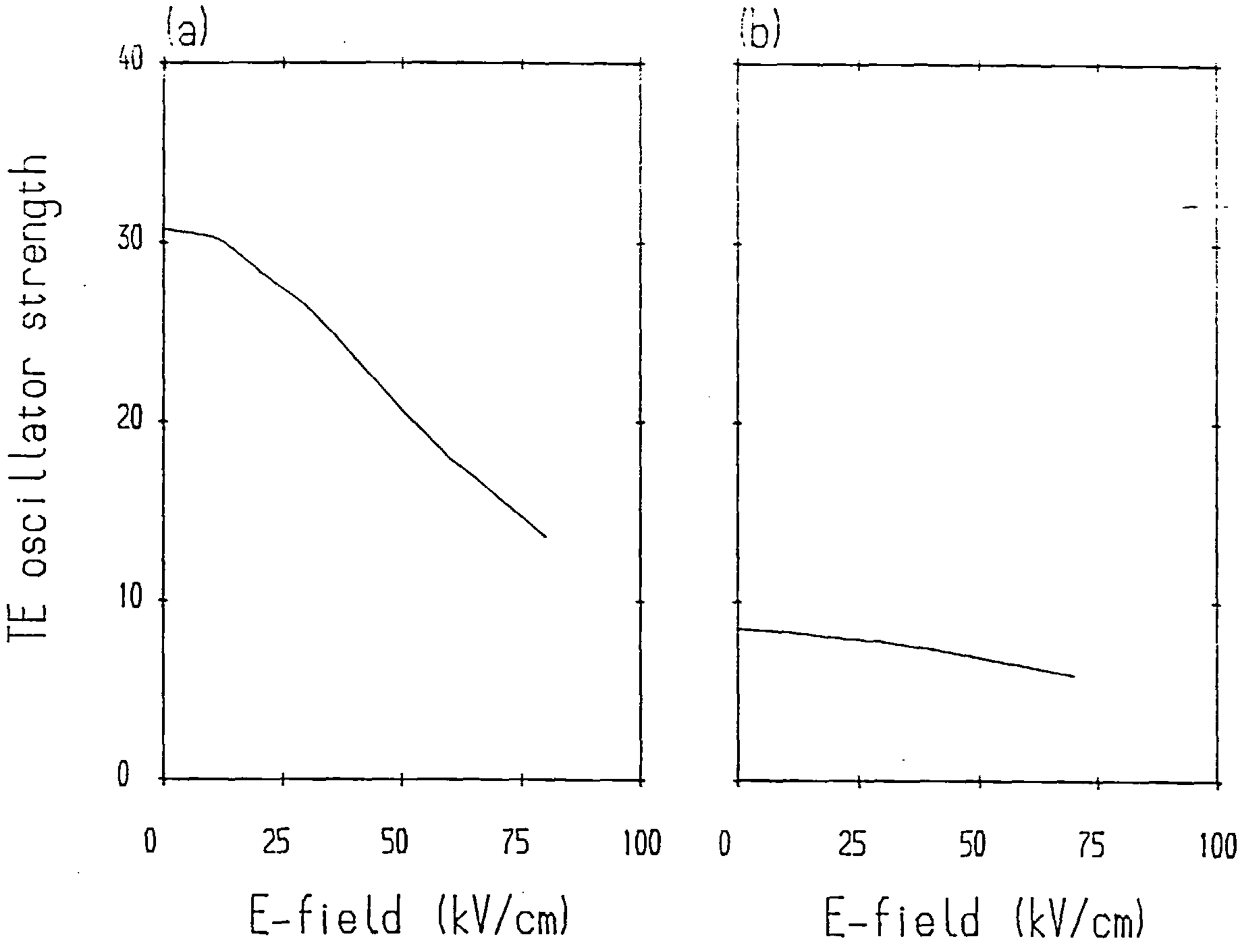

Figure 5.15 *TE polarisation oscillator strengths of the HH1-CB1 (1s) and LH1-CB1 (1s) excitons in a 100Å GaAs-$Al_{0.25}Ga_{0.75}As$ single quantum well as a function of the external electric field.*

(a) $L_z = 98.93$Å

(b) $L_{z1} = L_{z2} = 42.4$Å $L_b(\text{centre}) = 14.13$Å

(c) $L_{z1} = 56.53$Å $L_b(\text{centre}) = 14.13$Å $L_{z2} = 28.27$Å

This gives a total effective well width of around 99Å in each case, assuming similar lattice constants in both GaAs and $Al_{0.25}Ga_{0.75}As$.

The TE and TM absorption coefficients for each of the above structures with the exciton linewidths given by $\Gamma = 3\ (n_e n_h)$ meV is shown in Figure 5.16. Note that in a recent calculation of the double quantum well excitons,[1] the density matrix expression for the exciton absorption is entirely incorrect. The number of states included in the calculation is subsumed within the calculation of the exciton matrix element (see Appendix B) and not as in equation (13) of Ref. 1.

For structures (a) and (b) which are both symmetric under reflection in the plane $z = 0$, the direction of the external electric field does not matter. However, for the asymmetric quantum well

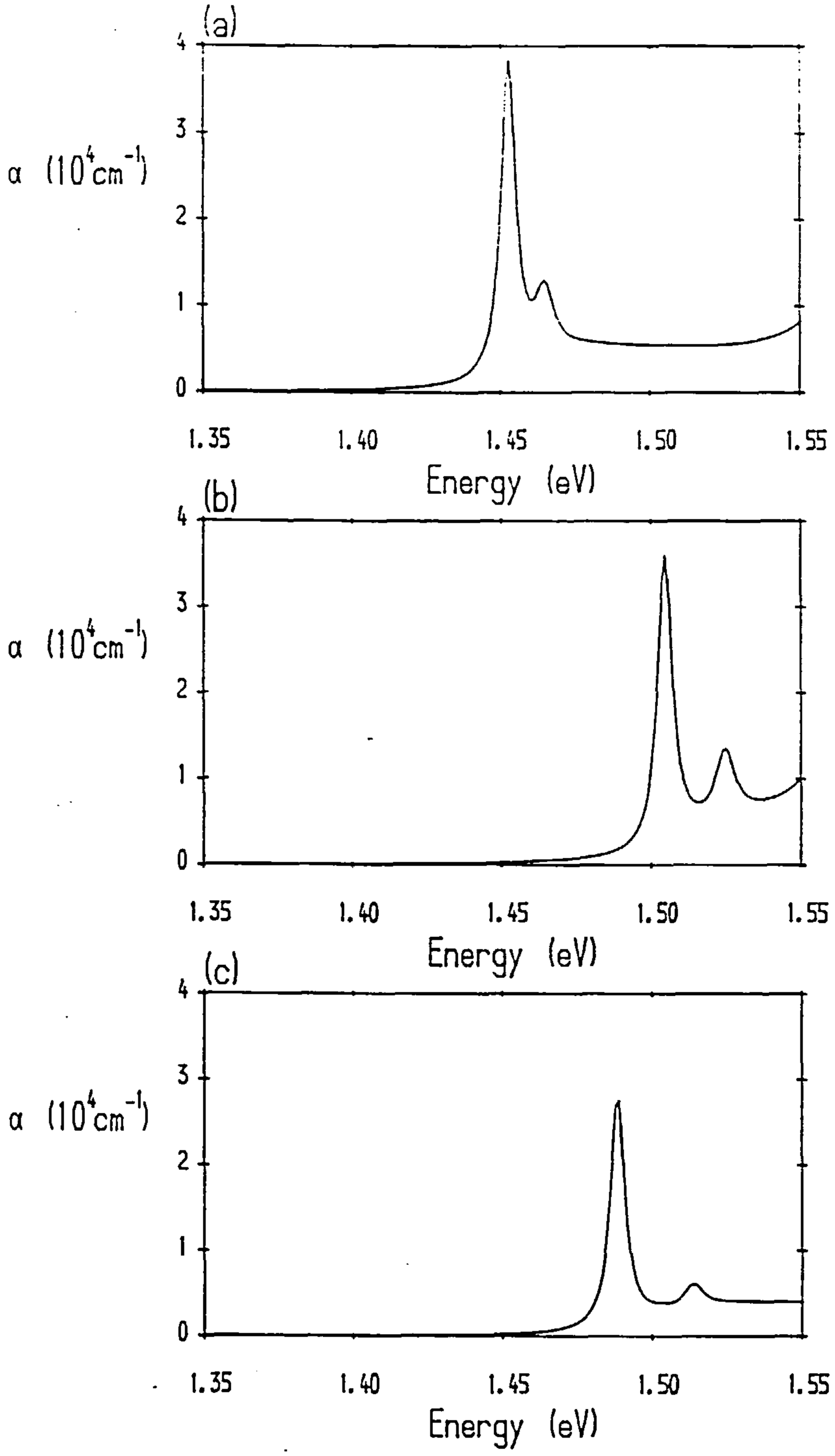

Figure 5.16 *TE mode linear absorption spectra for the three quantum well structures discussed in the text. These are (a) single quantum well (b) symmetric double quantum well and (c) asymmetric double quantum well. Only the results for the ground state (1s) excitons have been included, although the coupled-exciton model was employed.*

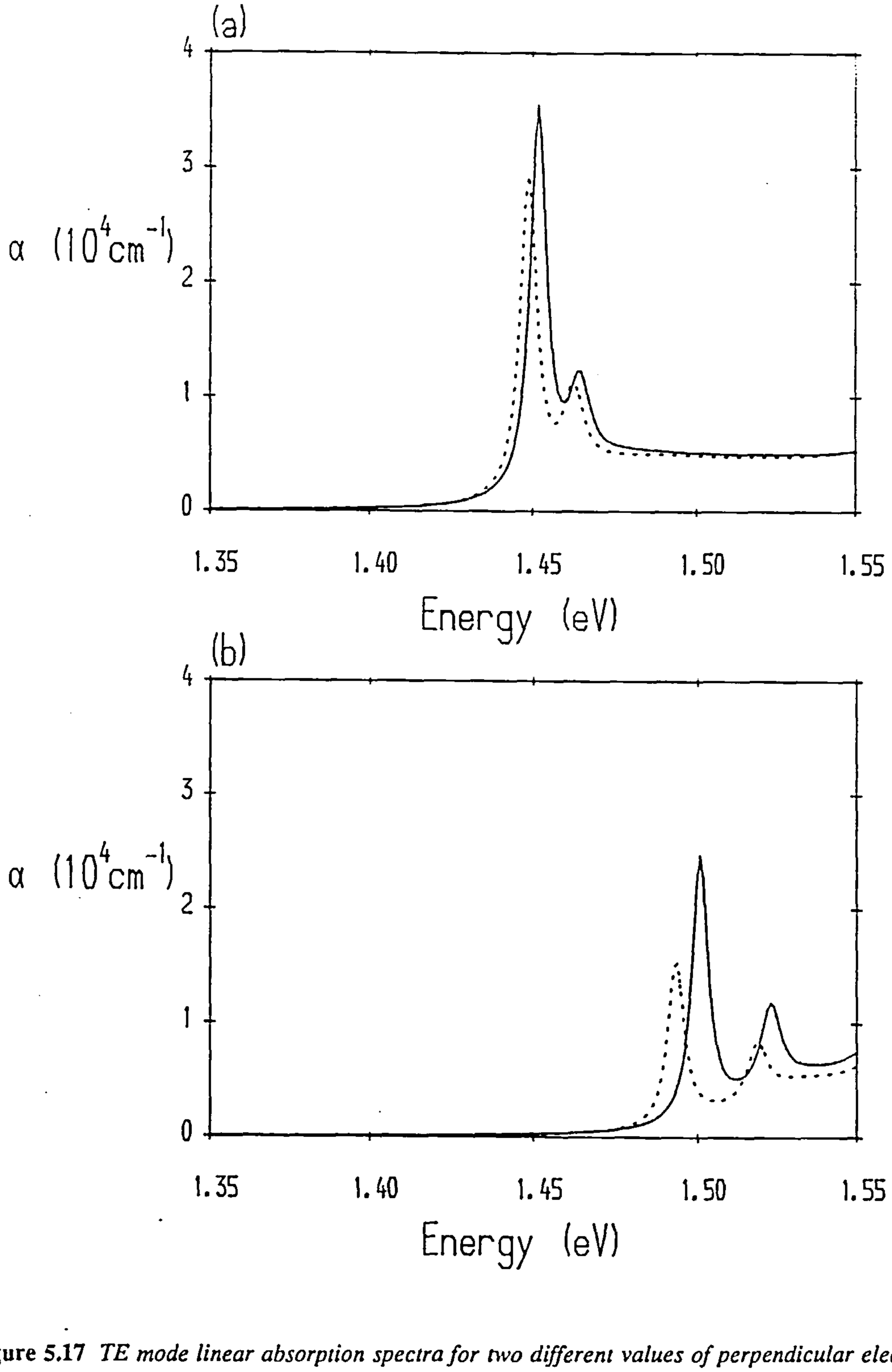

Figure 5.17 *TE mode linear absorption spectra for two different values of perpendicular electric field for (a) the single quantum well structure and (b) the symmetric double quantum well structure. The electric field values are 20 kV/cm (solid curves) and 40 kV/cm (dotted curves). The total effective well width of both structures is approximately 100Å.*

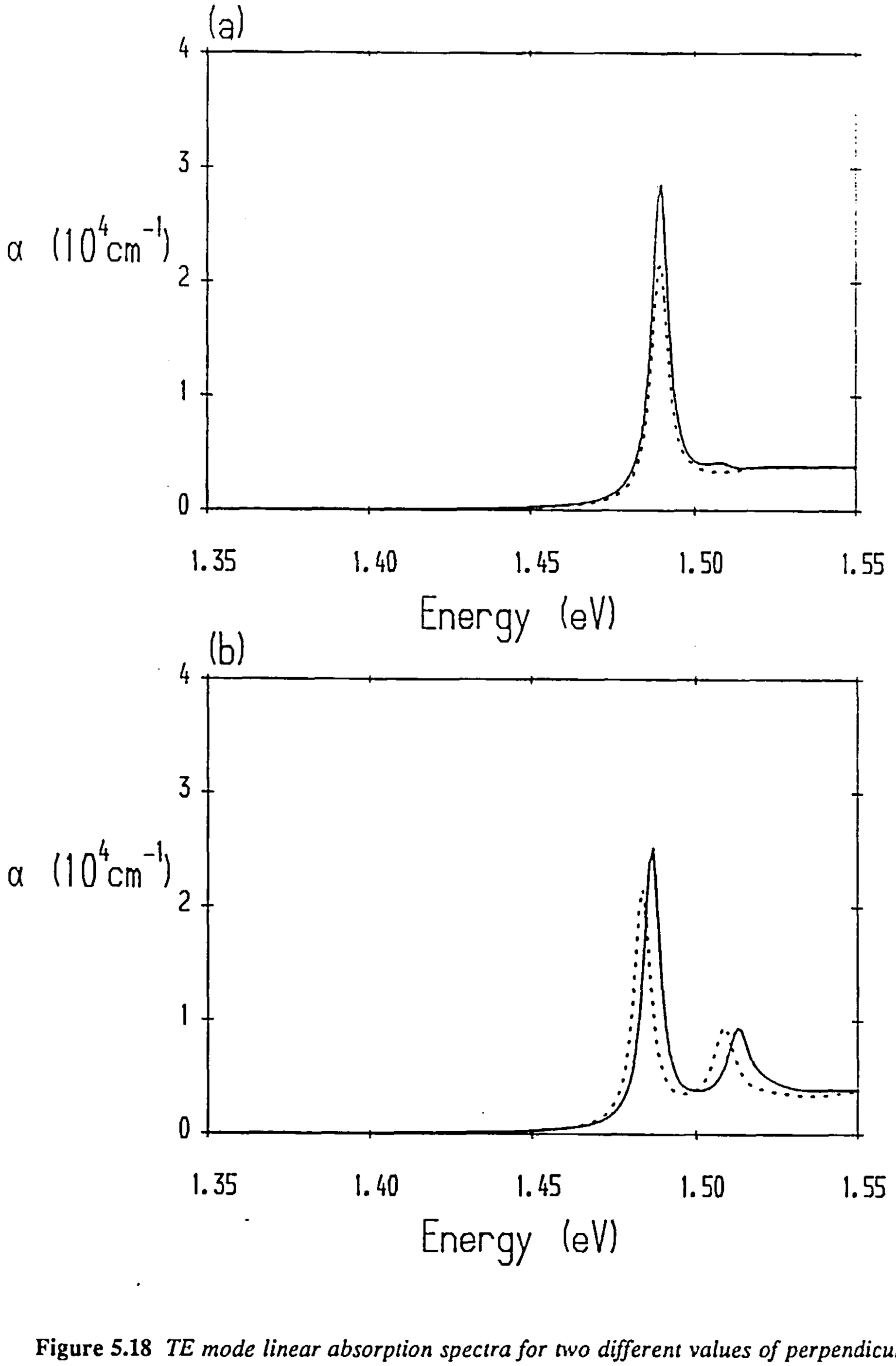

Figure 5.18 *TE mode linear absorption spectra for two different values of perpendicular electric field for the asymmetric double quantum well structure. The electric field values are 20 kV/cm (solid curves) and 40 kV/cm (dotted curves). The total effective well width is approximately 100Å. The top graph has the positive field orientation and the bottom graph the negative field orientation. By positive we mean that the wider well region is at a higher electric potential.*

structure (c) the electric field direction is important.

Figure 5.17 shows the TE mode absorption for structures (a) and (b) for several field values. Figure 5.18 shows the TE mode absorption for the double well structure (c) for the two different perpendicular field directions. The top graph in Figure 5.18 is for the wider well region at a higher potential. The lower graph in Figure 5.18 is for the opposite field direction. Again, this is shown for TE mode polarisation only.

The HH1s-CB1s ground state exciton transition energy for all four structure-field combinations is shown in Figure 5.19. Note from Figure 5.18 that initially, for small field values, there is a clear difference in the results for the different field directions. In the first case, there is an initial increase in the transition energy. This is also true for the HH1s-CB1s (1s) exciton oscillator strength. The explanation for this unintuitive behaviour is quite simple. The system parameters are such that in the asymmetric structure, with F = 0 kV/cm, the HH1s envelope function and CB1s envelope function have maximum values at different z-coordinates. The application of a finite electric field can produce an increased overlap between these envelope functions for small field values. This can increase the oscillator strength. However, the overlap integral between both envelope functions and the central barrier region actually increases slightly. This increase is extremely small but is sufficient to counteract the Stark shift of the single-particle states. This then serves to produce a slight increase in the overall energy of the single-particle states given by $E(k) = E_c(k) - E_v(k)$. Further increase in the electric field will reduce the envelope function overlap and the effect of the single-particle quantum-confined Stark shifts to lower energies becomes the more dominant effect.

Exciton saturation

To consider the effect of free carriers (electrons or holes) on the exciton absorption it is necessary to use many-body theory. In Appendix B, the equation for the exciton states is given in the form

$$\left[E_c(k) - E_v(k)\right]\phi_{eh}(k) - \sum_{k'} V(k-k')\phi_{eh}(k') = E\phi_{eh}(k)\ , \qquad (5.17)$$

where E_c and E_v represent the single-particle electron and hole energies and $V(k_{||}\text{-}k_{||}')$ is the Coulomb potential screened by the static dielectric constant.

Strictly, the use of the static dielectric constant gives only a lower limit to the calculation of the exciton binding energy. As shown by Haken,[28] the exciton Coulomb interaction (in real space) has the form

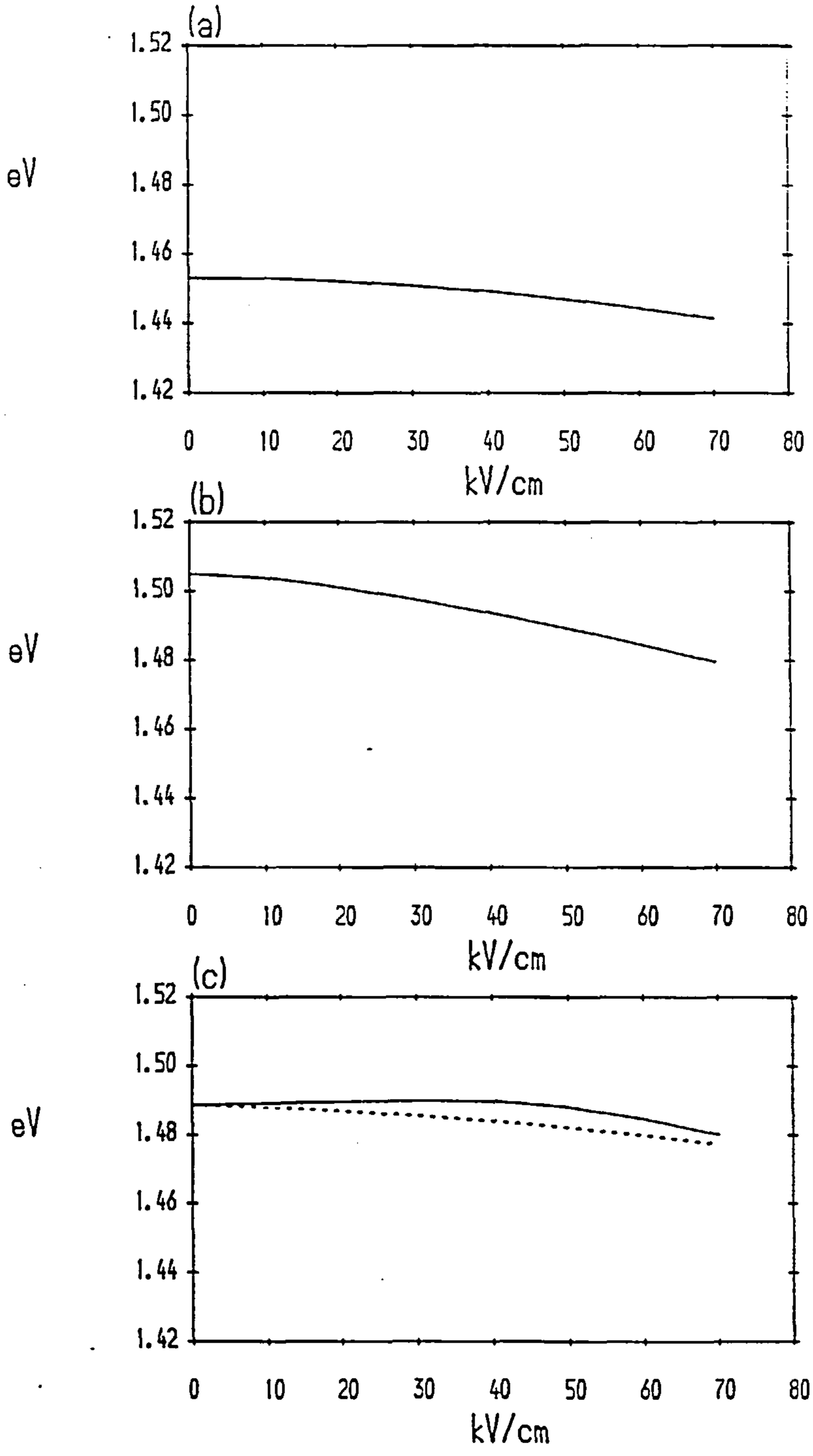

Figure 5.19 *Transition energy of the lowest ground state (1s) exciton in each of the three different quantum well structures as a function of external perpendicular electric field. Graph (a) is the single quantum well, (b) is the symmetric double quantum well and (c) is the asymmetric double quantum well. In graph (c) the positive field direction results are given by the solid curve. In (a) the exciton is HH1-CB1. In (b) and (c) the exciton is HH1s-CB1s.*

$$V(r) = \frac{-e^2}{\varepsilon_\infty r} + \frac{e^2}{r}\left[\frac{1}{\varepsilon_\infty} - \frac{1}{\varepsilon_o}\right]\left[1 - \frac{1}{2}(e^{-q_e r} + e^{-q_h r})\right], \tag{5.18}$$

where

$$q_e = \left(\frac{2m_e\omega_{LO}}{\hbar}\right)^{1/2}$$
$$q_h = \left(\frac{2m_h\omega_{LO}}{\hbar}\right)^{1/2}. \tag{5.19}$$

In bulk GaAs, $\hbar\omega_{LO}$ is about 35meV and therefore $q_e = (40\text{Å})^{-1}$, $q_h = (15\text{Å})^{-1}$. For an electron-hole Bohr radius greater than 40Å the static dielectric constant is therefore more important. For a radius less than 15Å the optical dielectric constant is of more importance. In between these values an interpolated expression like equation (5.18) should be used. For typical Bohr radii in quantum wells, however, the static dielectric constant gives a reasonable approximation to equation (5.18). The small decrease in $V(k_{||}-k_{||}')$ resulting from the use of ε_o therefore leads to the calculated binding energy being a lower limit to the true value. The error is small however, and will be neglected. The expressions for exciton absorption given in Appendix B were essentially of the form

$$\alpha(\hbar\omega) \propto \sum_{ch}\sum_{k,k'} \phi^*_{ch}(k)\,\phi_{ch}(k') . \tag{5.20}$$

Since the largest contribution is at $k_{||} = 0$, the sum over exciton states is often approximated by

$$\sum_{k,k'} \phi^*_{ch}(k)\,\phi_{ch}(k') \rightarrow |\phi_{ch}(r=0)|^2 . \tag{5.21}$$

With the introduction of N charges, the effects are phase-space filling and screening. The Coulomb potential is now

$$V_s(q) = \frac{V(q)}{\varepsilon(q,\omega)}, \tag{5.22}$$

where $q = (k_{||}-k_{||}')$ and $\varepsilon(q,\omega)$ is the new dielectric constant which takes account of the introduction of the charges.

Several modifications to the electronic structure now arise due to the presence of the free carriers. The single-particle energies are renormalised. A useful classical concept is that of the self-

energy, which expresses how the energy of a particle due to its own potential can be altered in the presence of other particles.[29] A correct quantum mechanical description of this effect accounts for the modified Coulomb interaction. The principal effects are seen in the exchange interaction and direct screening. The origin of the exchange interaction lies in the fact that the distribution of electron charge is controlled by the principle of anti-symmetry. This produces the requirement that a many-body wavefunction be anti-symmetric with respect to the exchange of two electrons. This is also seen in the Pauli exchange principle, which states that no two electrons can have the same set of quantum numbers. This is trivially seen where two electrons in the same orbital or energy band at the same energy must then have opposite spin quantum numbers. In a free electron gas, the exchange term in the Hamiltonian is given by

$$V_{ex} = \int\int \phi_i(r_1)\,\phi_j(r_1)\,\frac{e^2}{|r_1 - r_2|}\,\phi_i(r_2)\,\phi_j(r_2)\,dr_1\,dr_2 \,, \tag{5.23}$$

where $\phi_i(r_1)$ is the wavefunction for orbital site i, and electron with position r_1. The term $\phi_i(r_1)\phi_j(r_1)$ is known as the exchange charge. Equation (5.22) then obtains the electrostatic self-energy of the exchange charge.

The theories which attempt to calculate both the electron-hole interaction including exchange and correlation and the band-filling effect are extremely complicated. Typically a many-body Green's function technique is used in a *k*-space representation.[30-33] However, numerical results performed for quasi-two-dimensional GaAs have shown that the exchange-correlation potential can be fairly accurately given by

$$\mu_{xc} = -3.1R_y^{2D}(Na_{2D}^2)^{1/3} \,, \tag{5.24}$$

where R^{2D} and a_{2D} are the two-dimensional exciton Rydberg and Bohr radius respectively. The bandgap reduction is obtained as[34]

$$\Delta E = \frac{\partial}{\partial N}(N\mu_{xc}) \,, \tag{5.25}$$

where N is the density of free carriers. In GaAs-AlGaAs quantum wells, using GaAs parameters, this leads to the simple expression for the carrier-dependent bandgap renormalisation given by

$$\Delta E_g\,(\text{eV}) = -1.4\text{x}10^{-6}(L_z N)^{1/3} \,, \tag{5.26}$$

where N is the free carrier density (cm^{-3}) and L_z is the well width (cm).

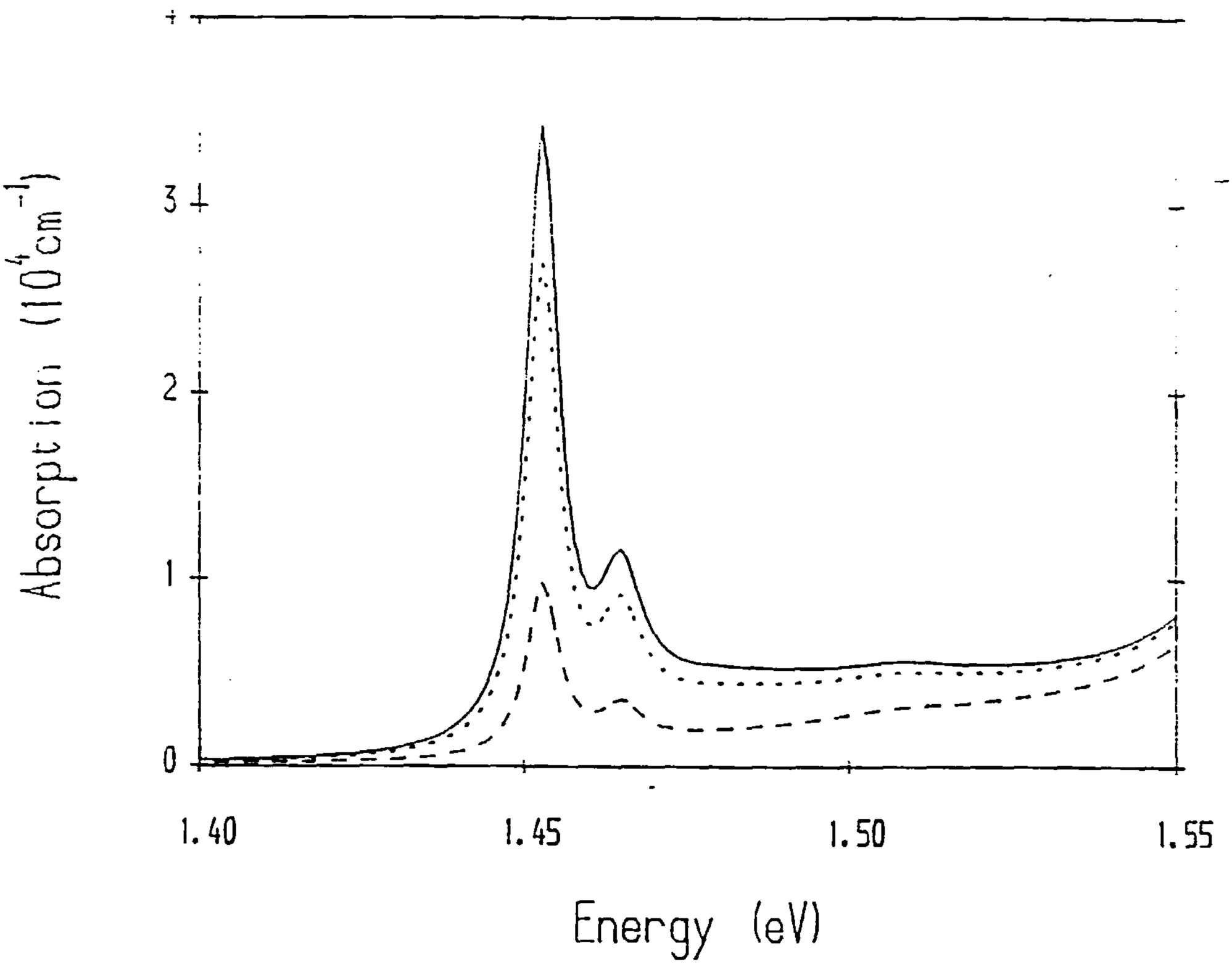

Figure 5.20 *Absorption coefficient for 100Å quantum well in the presence of a free carrier plasma. The 2D carrier densities are $10^{10}cm^{-2}$, $3x10^{11}cm^{-2}$ and $10^{11}cm^{-2}$.*

Although in principle the band curvature resulting from the renormalised energies is now altered, a good approximation is to consider rigid bandgap shifts[33] and ignore any change in the intersubband energies within the conduction band or valence band. The effects of phase-space filling are naturally described by the quantity $F(k_{||}) = [1 - f_e(k_{||}) - f_h(k_{||})]$. Therefore, in obtaining the exciton states, we now consider the Hamiltonian[33,34]

$$\left[E_e(k) - E_v(k)\right]\phi_{eh}(k) - \sum_{k'} \mathrm{sgn}\left[F(k)\right]|F(k)|^{1/2} V_s(k-k')\,|F(k')|^{1/2}\phi_{eh}(k) \,. \qquad (5.27)$$

The absorption coefficient is also re-defined as[36]

$$\alpha(\hbar\omega, N) \;\propto\; \sum_{e,h}\sum_{k,k'} |F(k')|^{1/2}\phi^{*}_{eh}(k')\,|F(k)|^{1/2}\,\phi_{eh}(k) \,. \qquad (5.28)$$

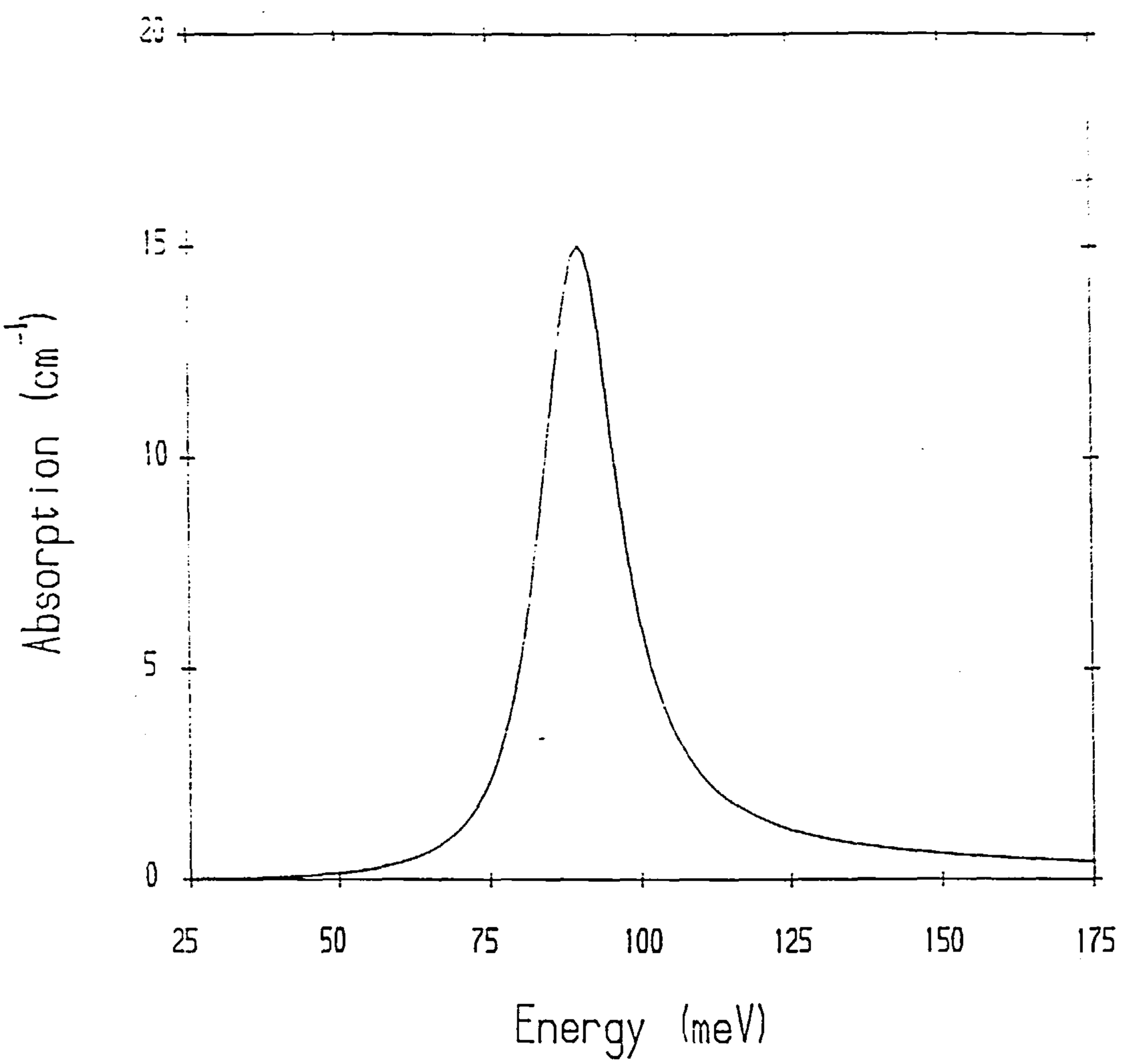

Figure 5.21 *CB1 to CB2 intersubband absorption in a 100Å GaAs-$Al_{0.3}Ga_{0.7}As$ modulation-doped single quantum well. The free carrier density in the well region is taken to be $4x10^{17}cm^{-3}$.*

Obtaining the exciton energies and wave functions is therefore as straightforward as in the case of N = 0, which is the situation considered in Appendix B. The calculation of the single-particle states follows that outlined in the previous discussion on modulation-doping.

We now consider the situation of the optical absorption, including excitons, in modulation-doped quantum wells. With the results given above, the calculated absorption spectra for a 100Å GaAs-$Al_{0.25}Ga_{0.75}As$ single well are shown in Figure 5.20. One significant difference between the exciton and band-to-band contributions is that the exciton contribution decreases much more rapidly with doping density than does the band-to-band contribution.

The reduction in the exciton oscillator strengths is affected by two distinct processes. The first is due to the exclusion principle, which introduces the $F(k_{||})$ factors given above. Also, the exciton wave function is found to become less localised in terms of the electron-hole orbital. The

real-space correlation enhancement, given by the right hand side of equation (5.20) is therefore decreased. The results given in Figure 5.20 follow by numerical calculations only. Exact analytical expressions are not possible, without introducing wholescale approximations, reducing the validity of the final results.

Intersubband transitions

So far we have neglected intersubband transitions. These are normally defined as transitions between the valence subbands and transitions between the conduction subbands. These must not be confused with the transitions from valence to conduction subbands. The reason for not including these transitions in the preceding analysis is due simply to the fact that the oscillator strength for these transitions is much smaller than those transitions which we have considered. For completeness, however, we briefly discuss these transitions.

We concentrate on the simple method of calculating the intersubband absorption. The transition from the n = 1 to n = 2 conduction subbands is of possible use in quantum well infra-red detectors. For this purpose the quantum well structure should be such that the n = 1 subband has free carriers at room temperature. The optical dipole matrix element M_{ba} for a transition from subband state |a> to subband state |b> is simply given by

$$\begin{aligned} M_{ba} &= < b \mid |e|z \mid a> \\ &= \int \phi_b(z) \mid e \mid z \, \phi_a(z) \, \delta_{k_b k_a} dz \, . \end{aligned} \tag{5.29}$$

The delta function is usually replaced by a Lorentzian linewidth function, resulting in the familiar density-matrix expression for the absorption coefficient.

The matrix element only exists for polarisation along the growth axis, or more exactly for a component of the polarisation along the growth axis. This dependence on polarisation simply arises due to the symmetry of the envelope functions. In general for an arbitrary polarisation this will result in an additional factor of cos(θ) appearing in equation (5.29), where θ is the angle between the photon polarisation vector and the z-axis.

For the valence intersubband transitions the matrix element depends on the spatial Bloch basis functions. For transitions between the LH1 and LH2 valence subbands, for example, this results in an additional factor of (2/3) appearing in equation (5.29) for the case of TM polarisation. In most practical cases however, the difference in the Fermi functions will be smaller for these valence subbands than between those for the conduction subbands. The transitions between the conduction

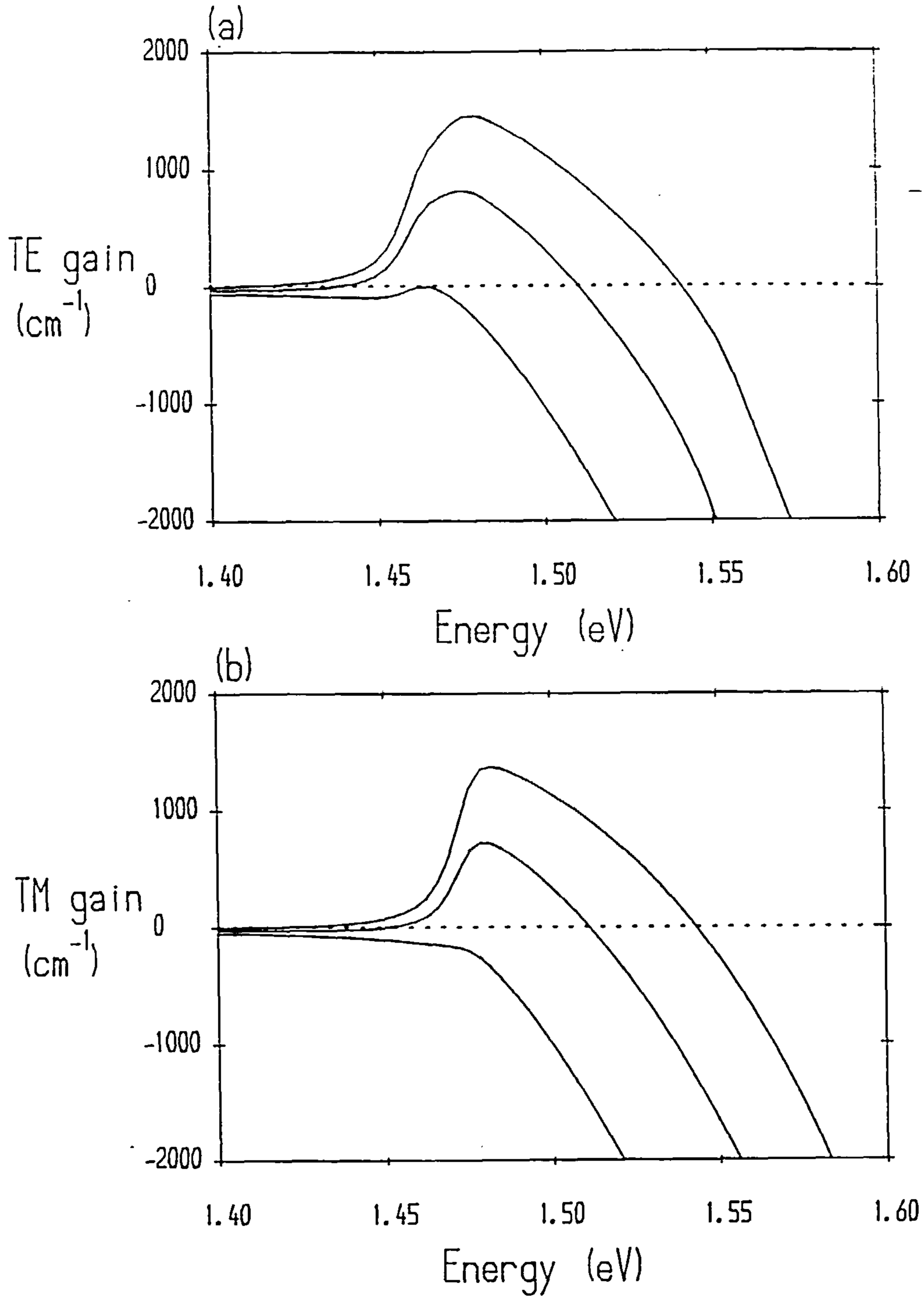

Figure 5.22 *Linear gain spectra for (a) TE-mode and (b) TM-mode polarisation in 100Å single quantum well with x = 0.25 in the barrier regions. The injected carrier densities are $2x10^{18}cm^{-3}$, $3x10^{18}cm^{-3}$ and $4x10^{18}cm^{-3}$. The gain spectra represent the material (or local) gain and not the mode gain resulting from the overlap of the optical field with the narrow active well region.*

subbands will therefore be larger than those between the LH valence subbands in a typical quantum well device.

As an example we show the calculated CB1-CB2 intersubband absorption for a modulation-doped GaAs-$Al_{0.3}Ga_{0.7}As$ single quantum well in Figure 5.21. The well width for this structure is taken to be 100Å, and the electron density in the well region is taken to be $4x10^{17}cm^{-3}$. The peak absorption is seen to occur at around 90meV. The effect of this absorption at near-bandgap frequencies will therefore be negligible. Further, the contribution to the bandgap-resonant index of refraction will be equally negligible.

Linear gain spectra

We conclude this Chapter by briefly considering the linear gain in quantum well lasers. This may be calculated directly from the density-matrix expressions for absorption given previously. In Figure 5.22 we show the calculated gain spectra for a 100Å quantum well, with x = 0.25 in the barrier regions. The injected carrier densities are $2x10^{18}cm^{-3}$, $3x10^{18}cm^{-3}$ and $4x10^{18}cm^{-3}$. Note that at currents near threshold the TE-mode gain dominates. However, at larger injection currents the TM-mode gain increases as the valence band quasi-Fermi level moves well into the HH1 subband. External control is therefore required to stop TE-TM mode hopping. The intraband scattering time used is taken to be constant, with a value of 100fsec, independent of wavevector.

At the time of writing the extensive literature on quantum well lasers includes no theoretical calculation using a **k**-dependent intraband scattering time. This then represents a useful and possibly fruitful area for further theoretical work. However, the role of scattering mechanisms in semiconductor quantum wells is still a relatively new field, with no overall concensus on the relative magnitudes of all possible scattering mechanisms.

We have included this short section for completeness only. The calculation of the index of refraction in quantum well lasers is only an application of the model which we will obtain in the next Chapter. It contributes nothing to that model.

References

1 D. AHN, IEEE Journal of Quantum Electronics QE-25, 2260 (1989)

2 C.R. PROETTO, Physical Review B41, 6036 (1990)

3 G.E.W. BAUER and T. ANDO, Physical Review B38, 6015 (1988)

4 M.M. DIGNAM and J.E. SIPE, Physical Review **B41**, 2865 (1990)

5 S. SCHMITT-RINK, D.S. CHEMLA and D.A.B. MILLER, Physical Review B32, 6601 (1985)

6 T. TAKAGAHARA, M. KUMAGAI and E. HANAMURA, IEEE Journal of Quantum Electronics **QE-23**, 983 (1987)

7 S. RUDIN and T.C. REINECKE, Physical Review **B39**, 8488 (1989)

8 N. DEBBAR, S. HONG, J. SINGH and P.B. BHATTACHARYA, Journal of Applied Physics **65**, 383 (1989)

9 T. HIROSHIMA, Applied Physics Letters **50**, 968 (1987)

10 H. NAGAI, Y. KAN, M. YAMANISHI and I. SUEMUNE, Japanese Journal of Applied Physics **25**, L640 (1986)

11 G.D. SANDERS and Y.C. CHANG, Physical Review **B31**, 6892 (1985)

12 A.T. MENEY, Superlattices and Microstructures (in press)

13 D.S. CHEMLA, D.A.B. MILLER, P.W. SMITH, A.C. GOSSARD and W. WEIGMANN, IEEE Journal of Quantum Electronics **QE-20**, 265 (1984)

14 E.O. KANE, Journal of Physics and Chemistry of Solids **1**, 82 (1956)

15 H.C. CASEY and M.B. PANISH, *Heterostructure Lasers* : Part A (Academic Press, New York 1978)

16 M. YAMANISHI and I. SUEMUNE, Japanese Journal of Applied Physics **23**, L35 (1984)

17 M. ASADA, A. KAMEYAMA and Y. SUEMATSU, IEEE Journal of Quantum Electronics **QE-20**, 745 (1984)

18 E. BURSTEIN, Physical Review **93**, 632 (1954)

19 T.S. MOSS, Proceedings of the Physical Society of London **B67**, 755 (1954)

20 B.S. WHERRETT and N.A. HIGGINS, Proceedings of the Royal Society of London **A379**, 67 (1982)

21 B.S. WHERRETT, Proceedings of the Royal Society of London **A390**, 373 (1983)

22 A. YARIV, *Quantum Electronics* (Wiley, New York 1975)

23 H.M. GIBBS, S.C. McCALL, T.N. VENKATESAN, A. PASSNER, A.C. GOSSARD and W. WEIGMANN in: *Optical Bistability*, edited by C.M. BOWDEN, M. CIFTAN and H.R. ROBL (Plenum Press, New York 1980)

24 D.A.B. MILLER, D.S. CHEMLA, D.J. EILENBERGER, P.W. SMITH, A.C. GOSSARD and W.WEIGMANN, Applied Physics Letters **42**, 925 (1983)

25 G.D. SANDERS and Y.C. CHANG, Physical Review **B31**, 6892 (1985)

26 G.D. SANDERS and Y.C. CHANG, Physical Review **B35**, 1300 (1987)

27 W.T. MASSELINK, P.J. PEARAH, J. KLEM, C.K. PENG, H. MORKOC, G.D. SANDERS and Y.C. CHANG, Physical Review **B32**, 8027 (1985)

28 H. HAKEN, Journal of Physics and Chemistry of Solids **8**, 166 (1959)

29 See for example: G.D. MAHAN, *Many Particle Physics* (Plenum Press, New York 1981)

30 S. SCHMITT-RINK, D.B. TRAN THOAI and H. HAUG, Zeitschrift für Physik **B39**, 25 (1980)

31 C. KLINGSHIRN and H. HAUG, Physics Reports **70**, 325 (1981)

32 K. ARYA and W. HAAKE, Solid State Communications **33**, 739 (1980)

33 H. HAUG and S. SCHMITT-RINK, Progress in Quantum Electronics **9**, 3 (1984)

34 S. SCHMITT-RINK and C. ELL, Journal of Luminescence **30**, 585 (1985)

35 D.A. KLEINMANN and R.C. MILLER, Physical Review **B32**, 2266 (1985)

36 D.S. CHEMLA, I. BAR JOSEPH, J.M. KUO, T.Y. CHANG, C. KLINGSHIRN, G. LIVESCU and D.A.B. MILLER, IEEE Journal of Quantum Electronics **QE-24**, 1664 (1988)

6 Index of Refraction in Quantum Well Structures

Introduction

The close lattice-matching of binary $Al_xGa_{1-x}As$ alloy material has led to many novel structures being grown for possible use in semiconductor optoelectronic devices. The lattice-matching enables the growth of material whose electronic properties can be easily tailored. In quantum-confined devices, the energy levels can be tailored over a wide range, thus allowing a concomitant tailoring of the resonant index of refraction.

Very few calculations have appeared in the literature which obtain the frequency dependence of the index of refraction in quantum well structures. Recently, several theoretical studies[1-4] have reported calculation of the index of refraction in superlattice structures, neglecting the contribution due to excitons. Similarly, Tsu and Ioratti[5] used a simplified model of the electronic dispersion to obtain the static dielectric constant, relying heavily on bulk GaAs band structure parameters, and

again neglecting the contribution due to excitons. In this case, since absorption can be neglected, the real part of the dielectric function is straightforward to obtain and gives the required result immediately.

The dielectric function in GaAs-AlGaAs superlattices has generally been obtained by considering the quantised subband dispersion and bulk-like contributions from higher points in the Brillouin zone. These calculations have both ignored the contribution due to excitons and chosen to consider the electronic states within a small region of **k**-space in the vicinity of a few special points of high symmetry.

In bulk material,[6-8] for frequencies in the vicinity of the fundamental Γ_6-Γ_8 energy gap, the ease in obtaining the electronic dispersion allows for rather simple calculations of $n(\omega)$. The excitonic states in quantum wells at room temperature, and the more complicated energy dispersion, increases the complexity of the calculations required. It is fairly commonplace to consider the contribution due to the lowest exciton states alone. This assumes that there is a constant background dielectric constant[9,10] due to all other energy states excluded from the calculation. If there is only a single bound exciton state, then in the immediate vicinity of the exciton transition, a calculation of the change in refractive index due to external perturbation, which includes only the exciton state, is a useful although crude approximation.

The majority of the published literature on the index of refraction in GaAs and AlGaAs alloys pertains to bulk material only. This includes the linear index of refraction[6,7] the effects of screening[11,12] and the nonlinear intensity-dependent index of refraction.[11,13] Most of these results are for frequencies near (usually below) the Γ_6-Γ_8 energy gap and also use completely parabolic approximations to the energy dispersion. The use of parabolic energy bands necessitates truncation at moderate wave vectors, to avoid divergence.

Systematic experimental studies[14] of the dielectric function in $Al_xGa_{1-x}As$ alloys have been performed for energies from 1.5eV to 6.0eV with aluminium composition x varying from x=0 to x=0.8. These results also provide useful information concerning the compositional dependence of various material parameters.

When considering the effects of screening, as in the preceding Chapter, only free-carrier screening need be considered. If excitons are included in the theory, this simplifies the calculations. This can be understood as follows: due to the rapid thermal ionisation by optical phonons, which occurs within a fraction of a picosecond,[15] the effects of screening by occupied exciton states can reasonably be neglected. This was the case in the preceding Chapter, where the effects of screening on optical absorption were calculated. The results given there will therefore be equally relevant in the case of refraction in quantum wells.

Construction of dielectric function

There are two straightforward approaches to the calculation of the index of refraction in quantum well structures. In the first method, the contribution of states with transition energies in close resonance with the optical frequency of interest is added to a constant background contribution, n_b. The background index n_b is therefore considered to be frequency-independent over the range of energies (frequencies) of interest. This simpler 'constant background' model can be obtained as

$$n(\omega) \equiv n_b + \Delta n(\omega) \tag{6.1}$$

The real part of the dielectric function is then given approximately by

$$\varepsilon_r(\omega) \approx [n(\omega)]^2 \approx \varepsilon_b + 2n_b \Delta n(\omega) \tag{6.2}$$

where $\varepsilon_b = n_b^2$. The contribution due to the states of interest is then given by

$$\Delta n(\omega) = \frac{1}{2n_b} \varepsilon_r(\omega) \tag{6.3}$$

where $\varepsilon_r(\omega)$ is the calculated contribution.

However, the method used here considers the bulk frequency-dependent index of refraction in the energy range of interest. We consider that the effects of quantisation are of importance for the lowest conduction band and highest valence bands. The contributions of these bulk bands are calculated and subtracted from the frequency-dependent index of refraction $n(\omega)$. The new dispersion of the quantum well structure is then calculated. The contribution to the index of refraction from the new energy dispersion is then added. This gives the general form as

$$n(\omega) = n_B(\omega) - n_{bulk}(\omega) + n_{QW}(\omega) \tag{6.4}$$

where $n_B(\omega)$ is the known bulk refractive index, $n_{bulk}(\omega)$ is the contribution to $n_B(\omega)$ from the original bulk states included in the calculation over the energy range of interest and $n_{QW}(\omega)$ is the calculated contribution due to the quantum well energy dispersion. In general, at frequencies close to resonances, the imaginary part of the dielectric function cannot be ignored. The real part of the index of refraction is then given by

$$n(\omega) = \frac{1}{\sqrt{2}} \left\{ \left[\varepsilon_r^2(\omega) + \varepsilon_i^2(\omega) \right]^{1/2} + \varepsilon_r(\omega) \right\}^{1/2} . \tag{6.5}$$

If the imaginary part of the dielectric function is known over a significant range of energies, then the real part may be approximately obtained from the Kramers-Kronig relation by using

$$\varepsilon_r(\omega) - \varepsilon_\infty = \frac{2}{\pi} P \int_{\omega_{min}}^{\omega_{max}} \frac{\omega' \varepsilon_i(\omega)}{(\omega')^2 - \omega^2} d\omega' \qquad (6.6)$$

In equation (6.6) *P* denotes the principal part of the integral. This relation is actually only exact for integration over all frequencies from ω=0 to ω=∞. Limiting the range of integration thus gives an approximation only. However, if the imaginary part of the dielectric function is known over a significant range of energies, the use of equation (6.6) is expected to give good results. Similarly, for a change in absorption, the resulting change in refraction may be obtained from the Kramers-Kronig relation. If the absorption α(ω) changes only within a limited range of energies, to a good approximation, then the change in refractive index can be usefully obtained as

$$\Delta n(\omega) = \frac{c}{\pi} P \int_{min}^{max} \frac{\Delta\alpha(\omega)}{(\omega')^2 - \omega^2} d\omega' . \qquad (6.7)$$

The use of the Kramers-Kronig relation in this form, using n_b instead of obtaining $\Delta\varepsilon_r(\omega)$, reduces the accuracy of the calculation. The presence of ε_∞ in equation (6.6) signifies the fact that there is an upper limit where ε_i is essentially zero and the physics of the problem suggests that the integration has gone far enough. If the integration could actually be performed to ω=∞, then ε_∞ must be replaced by 1.

Optical frequency contributions

At frequencies close to the fundamental band gap, there are several important contributions to the index of refraction. The most important are those arising from the quantised subbands. This obviously includes the exciton states, which have a significantly large contribution at near-band gap frequencies. The contribution from other states will in general decrease with increasing magnitude of the detuning $\Delta=(E_i-\hbar\omega)$. E_i is the energy under consideration and $\hbar\omega$ is the photon energy. Ignoring the presence of these states has too often become the norm in the literature. It is not correct to say that their contribution is negligible.[16]

In order to improve the calculations in terms of accuracy, it is better to explicitly include the k-dependent mixing of the states included. This is most conveniently done using an 8x8 **k·p** Hamiltonian for the Γ-valley dispersion. In this manner all of the Γ-states of interest are

automatically coupled, even at the zone centre. The method allows a fully self-consistent set of parameters to be obtained. An earlier 8x8 **k·p** theory by Eppenga *et al* [17] was much simpler, although their method of dealing with the decoupling of the conduction band dispersion leads to numerical instabilities and is less accurate.

In addition to the usual **k·p** parameters we also include the 2nd-order Kane parameter which contributes to the conduction band dispersion, and which is usually omitted. The 8x8 **k·p** matrix removes the explicit Γ_{6c}-Γ_{5c} coupling used in the previous Hamiltonians. The basis set used in the Hamiltonian is given in Table 6.1. The Hamiltonian (in atomic units) is therefore represented by the matrix

$$\mathrm{H} = \begin{vmatrix} E_{\mathrm{el}} & -\sqrt{3}A_+ & \sqrt{2}B & -B & 0 & 0 & -A_- & -\sqrt{2}A_- \\ -\sqrt{3}A_+^* & E_{\mathrm{hh}} & \sqrt{2}L & -L & 0 & 0 & -S & -\sqrt{2}S \\ \sqrt{2}B^* & \sqrt{2}L^* & E_{\mathrm{lh}} & Q & A_+^* & S & 0 & \sqrt{3}L \\ -B^* & -L^* & Q & E_{\mathrm{so}} & \sqrt{2}A_+^* & \sqrt{2}S & -\sqrt{3}L & 0 \\ 0 & 0 & A_+ & \sqrt{2}A_+ & E_{\mathrm{el}} & -\sqrt{3}A_- & \sqrt{2}B & -B \\ 0 & 0 & S^* & \sqrt{2}S^* & -\sqrt{3}A_-^* & E_{\mathrm{hh}} & \sqrt{2}L^* & -L^* \\ -A_-^* & -S^* & 0 & -\sqrt{3}L^* & \sqrt{2}B^* & \sqrt{2}L & E_{\mathrm{lh}} & Q \\ -\sqrt{2}A_-^* & -\sqrt{2}S^* & \sqrt{3}L^* & 0 & -B^* & -L & Q & E_{\mathrm{so}} \end{vmatrix}, \qquad (6.8)$$

where

$$\begin{aligned} E_{\mathrm{el}} &= E_g + E_\Delta^c + \left(F+\tfrac{1}{2}\right)k^2 + \left(F+\tfrac{1}{2}\right)k_z^2 , \\ E_{\mathrm{hh}} &= E_+ , \quad E_{\mathrm{lh}} = E_- , \\ E_\pm &= -E_\Delta^v - \tfrac{1}{2}(\gamma_1 \pm \gamma_2)k^2 - \tfrac{1}{2}(\gamma_1 \mp 2\gamma_2)k_z^2 , \\ E_{\mathrm{so}} &= -\Delta_o - E_\Delta^{so} - \tfrac{1}{2}\gamma_1 k^2 - \tfrac{1}{2}\gamma_1 k_z^2 , \\ A_\pm &= \tfrac{1}{\sqrt{6}}Pk_z \pm \sqrt{\tfrac{2}{3}}\{G, k_z\}k_\mp , \\ B &= \tfrac{1}{\sqrt{3}}\{P, k_z\} - \tfrac{2\mathrm{i}}{\sqrt{3}}Gk_x k_y , \\ L &= \sqrt{\tfrac{3}{2}}(\gamma_3, k_z)k_- , \\ S &= \tfrac{\sqrt{3}}{2}(\bar{\gamma}k_-^2 - \mu k_+^2) , \\ \bar{\gamma} &= \tfrac{1}{2}(\gamma_2+\gamma_3), \quad \mu = \tfrac{1}{2}(\gamma_3-\gamma_2) , \\ Q &= \sqrt{2}\gamma_2 k_z^2 - \tfrac{1}{\sqrt{2}}\gamma_2 k^2 , \\ k^2 &= k_x^2 + k_y^2, \; k_\pm = k_x \pm ik_y = k\exp(\mathrm{i}\theta) , \\ \{\alpha, \beta\} &\equiv \tfrac{1}{2}(\alpha\beta + \beta\alpha) . \end{aligned} \qquad (6.9)$$

The γ_i are simply the Luttinger parameters, minus the explicit coupling of the states now included in the Hamiltonian matrix. This was detailed in Chapter 4. The term G is an inversion asymmetry

term which will be omitted since it is small. E_g is the smallest band gap (well material) and the terms E_Δ^i are the relevant band edge offsets. P (F) is the first-order (second-order) Kane parameter, where $P = \langle S|p_x|X\rangle$, in atomic units. The Hamiltonian in this form can be block-diagonalised rather simply. This gives the upper block as

$$H_{upper} = \begin{vmatrix} E_{el} & A_1 & A_2 & A_3 \\ A_1^* & E_{hh} & B_1 & B_2 \\ A_2^* & B_1^* & E_{lh} & C_1 \\ A_3^* & B_2^* & C_1^* & E_{so} \end{vmatrix}, \tag{6.10}$$

where

$$\begin{aligned} A_1 &= -\tfrac{1}{\sqrt{2}}Pk\,, \\ A_2 &= \sqrt{\tfrac{2}{3}}\{P, k_z\} + \tfrac{i}{\sqrt{6}}Pk\,, \\ A_3 &= -\tfrac{1}{\sqrt{3}}\{P, k_z\} + \tfrac{i}{\sqrt{3}}Pk\,, \\ B_1 &= \sqrt{3}k\{\gamma_3, k_z\} + \tfrac{\sqrt{3}i}{2}k^2\left[\gamma_3 - 2\mu\cos^2(2\theta)\right], \\ B_2 &= -\sqrt{\tfrac{3}{2}}k\{\gamma_3, k_z\} + i\sqrt{\tfrac{3}{2}}k^2\left[\gamma_3 - 2\mu\cos^2(2\theta)\right], \\ C_1 &= \sqrt{2}\gamma_2 k_z^2 - \tfrac{1}{\sqrt{2}}\gamma_2 k^2 - \tfrac{3i}{\sqrt{2}}k\{\gamma_3, k_z\}\,. \end{aligned} \tag{6.11}$$

The lower Hamiltonian block is simply given by $H_{lower} = H_{upper}^{\dagger}$.

In solving the above equations, continuity of probability current at each quantum well interface is obtained by continuity of both the envelope functions and the vector

$$\begin{vmatrix} \left(F+\frac{1}{2}\right)\frac{\partial}{\partial z} & 0 & \frac{i}{\sqrt{6}}P & -\frac{i}{\sqrt{12}}P \\ 0 & -\frac{1}{2}(\gamma_1 - 2\gamma_2)\frac{\partial}{\partial z} & \frac{\sqrt{3}i}{2}\gamma_3 k & -i\sqrt{\frac{3}{8}}\gamma_3 k \\ -\frac{i}{\sqrt{6}}P & \frac{-\sqrt{3}i}{2}\gamma_3 k & -\frac{1}{2}(\gamma_1 + 2\gamma_2)\frac{\partial}{\partial z} & \sqrt{2}\gamma_2\frac{\partial}{\partial z} + \sqrt{3}ik \\ \frac{i}{\sqrt{12}}P & i\sqrt{\frac{3}{8}}\gamma_3 k & \sqrt{2}\gamma_2\frac{\partial}{\partial z} - \sqrt{3}ik & -\frac{1}{2}\gamma_1\frac{\partial}{\partial z} \end{vmatrix} \begin{vmatrix} f_1 \\ f_2 \\ f_3 \\ f_4 \end{vmatrix}. \tag{6.12}$$

where the f_i are the individual components of each wave function.

Obtaining the continuum states with this method is computationally burdensome. To simplify this part of the calculation, it is assumed that the quantum well is surrounded by an infinite well. The distance is chosen so that the bound eigenstate confinement energies are not noticeably perturbed by the introduction of the infinite well. The criterion chosen was that the change in the confinement energies be less than 0.1% after introduction of the surrounding well. This simplifies the calculations considerably and allows the continuum states above the quasi-bound states to now be

Table 6.1 *Basis functions used to construct the 8x8* **k·p** *Hamiltonian which is given by equation (6.8).*

$\|u_i\rangle = (J, m_J)$	Basis function
$\|u_1\rangle = (\frac{1}{2}, \frac{1}{2})$	$\|S\rangle\uparrow$
$\|u_2\rangle = (\frac{3}{2}, \frac{3}{2})$	$\frac{i}{\sqrt{2}}\|X+iY\rangle\uparrow$
$\|u_3\rangle = (\frac{3}{2}, \frac{1}{2})$	$\frac{i}{\sqrt{6}}\{\|X+iY\rangle\downarrow - 2\|Z\rangle\uparrow\}$
$\|u_4\rangle = (\frac{1}{2}, \frac{1}{2})$	$\frac{i}{\sqrt{3}}\{\|X+iY\rangle\downarrow + \|Z\rangle\uparrow\}$
$\|u_5\rangle = (\frac{1}{2}, -\frac{1}{2})$	$-\|S\rangle\downarrow$
$\|u_6\rangle = (\frac{3}{2}, -\frac{3}{2})$	$-\frac{i}{\sqrt{2}}\|X-iY\rangle\downarrow$
$\|u_7\rangle = (\frac{3}{2}, -\frac{1}{2})$	$-\frac{i}{\sqrt{6}}\{\|X+iY\rangle\uparrow + 2\|Z\rangle\downarrow\}$
$\|u_8\rangle = (\frac{1}{2}, -\frac{1}{2})$	$\frac{i}{\sqrt{3}}\{\|X+iY\rangle\uparrow - \|Z\rangle\downarrow\}$

obtained relatively easily. They are therefore now given by closely-spaced discrete states, which merge in energy spacing at higher energies. The surrounding infinite well is placed at z = ±2500Å which we find easily satisfies the above criterion.

The states at the special points X and L, important due to the large joint density-of-states at these points, can be obtained simply using effective mass theory. Due to the different Brillouin zone locations of these points, the effects of polarisation are seen to be negligible, when averaged over all equivalent points. Note that the number of equivalent conduction band minima at X which need to be included is three. There are obviously six equivalent points in elemental semiconductors, but in zinc-blende structures there are only three within the first Brillouin zone. This is explained in detail in Ref. 18. For the quantum wells considered here, the difference in energy at the X-point in the well and barrier material is sufficiently small to prompt the assumption that the contribution is relatively unchanged from that of the equivalent bulk alloy. We therefore include only the L-point contribution. As noted above this shows no electro-optic anisotropy. The squared momentum matrix element (in eV), considering only the L_1, L_4 and L_6 bands, can be simply obtained from standard **k·p** theory.[19] This gives

$$\frac{1}{m_L^t} = 1 + P_L^2\left(\frac{1}{E_1} + \frac{1}{E_1 + \Delta_1}\right), \tag{6.13}$$

where m_L^t is the transverse L-point conduction band effective mass.[18]

We apply the simple **k·p** theory of Ref. 19 directly. Since we make no changes to the theory (apart from quantisation) the details are not repeated here in full. Briefly, however, since the valence bases are simply taken as p-orbitals, the growth axis component is immediately obtained at each point. The small matrices are easily solved (the [111] valence dispersion is uncoupled) for the quantised levels. Above this we assume barrier-like material parameters and simply diagonalise the Hamiltonian, taking all components of **k** to be good quantum numbers. The optical matrix elements and joint density-of-states for these bulk-like eigenstates are straightforward to obtain. The band offsets at the L-points can be extrapolated from knowledge of the band offsets at Γ. These are relatively small and so there are in practice only a few quantised states. Accordingly, this part of the calculation is much simpler than obtaining the eigenfunctions at Γ, where both the size of the Hamiltonian used is larger and the effects of quantisation are more pronounced.

A simpler method of including the spin-orbit split-off valence bands at Γ is to use the 6x6 Luttinger-Kohn Hamiltonian[20] for the hole states, and with the conduction band states obtained as before. The hole Hamiltonian is then represented by the matrix

$$\mathrm{H} = -\begin{vmatrix} P+Q & L & M & 0 & \frac{\mathrm{i}}{\sqrt{2}}L & -i\sqrt{2}M \\ L^* & P-Q & 0 & M & F & i\sqrt{\frac{3}{2}}L \\ M^* & 0 & P-Q & -L & -i\sqrt{\frac{3}{2}}L^* & F \\ 0 & M^* & -L^* & P+Q & -i\sqrt{2}M & -\frac{\mathrm{i}}{\sqrt{2}}L \\ -\frac{\mathrm{i}}{\sqrt{2}}L^* & F^* & i\sqrt{\frac{3}{2}}L & i\sqrt{2}M^* & G & 0 \\ i\sqrt{2}M^* & -i\sqrt{\frac{3}{2}}L^* & F^* & \frac{\mathrm{i}}{\sqrt{2}}L^* & 0 & G \end{vmatrix}, \qquad (6.14)$$

where

$$\begin{aligned} P+Q &= \tfrac{1}{2}(\gamma_1+\gamma_2)\left(k_x^2+k_y^2\right)+\tfrac{1}{2}(\gamma_1-2\gamma_2)k_z^2 \\ P-Q &= \tfrac{1}{2}(\gamma_1+\gamma_2)\left(k_x^2-k_y^2\right)+\tfrac{1}{2}(\gamma_1+2\gamma_2)k_z^2 \\ L &= -\sqrt{3}\gamma_3\left(k_y+ik_x\right)k_z \\ M &= \tfrac{\sqrt{3}}{2}\gamma_2\left(k_x^2-k_y^2\right)-\sqrt{3}i\gamma_3 k_x k_y \\ F &= \tfrac{-\mathrm{i}}{\sqrt{2}}\gamma_2\left(k_x^2+k_y^2\right)+\sqrt{2}i\gamma_2 k_z^2 \\ G &= \tfrac{1}{2}\gamma_1\left(k_x^2+k_y^2\right)+\tfrac{1}{2}\gamma_1 k_z^2+\Delta_o\,. \end{aligned} \qquad (6.15)$$

This matrix can be easily block-diagonalised as before, when suitably reordered. This gives an upper block for the |3/2,3/2>, |3/2,1/2> and |1/2,1/2> basis functions and a lower block for the |3/2,-3/2>, |3/2,-1/2> and |1/2,-1/2> basis functions. The upper block is then given by

$$H_{upper} = -\begin{vmatrix} P+Q & M-iL & A \\ M+iL & P-Q & B \\ A^* & B^* & G \end{vmatrix}, \tag{6.16}$$

where

$$\begin{aligned} A &= \tfrac{\sqrt{3}}{2}(\gamma_2+\gamma_3)\left(k_x^2+k_y^2\right)+i\sqrt{\tfrac{3}{2}}\gamma_3\left(k_x^2+k_y^2\right)^{1/2}k_z \\ B &= \sqrt{2}\gamma_2 k_z^2-\tfrac{1}{\sqrt{2}}\gamma_2\left(k_x^2+k_y^2\right)-i\tfrac{3}{\sqrt{2}}\gamma_3\left(k_x^2+k_y^2\right)^{1/2}k_z\,, \end{aligned} \tag{6.17}$$

and where the lower Hamiltonian block is given by $H_{lower} = H_{upper}^{\dagger}$.

Although not used here, this 6x6 Hamiltonian and its block-diagonalised form are only given here for completeness and to assist those requiring to copy this work.

Resonant excitonic contribution

Although the refractive index will be obtained using the contributions from all the states discussed above, it is instructive to consider the contribution due to the exciton states alone. At frequencies resonant with the fundamental band gap the contribution of these states is extremely important.

We first consider a 100Å GaAs-$Al_{0.25}Ga_{0.75}As$ single quantum well. The excitons which are coupled to the (1s) excitons are given in Table 6.2. These are then used in the coupled exciton model explained in Appendix B. It must be made clear that the simpler two-band model, ignoring the angular momentum character of each exciton and used illustratively in the preceding Chapter, does not give as accurate results. For the excited states of each exciton it is expected that the simpler model would fail completely. For the ground states the simpler model leads to a non-zero TM-polarisation oscillator strength for all HH excitons. The proper model, however, shows quite clearly that this oscillator strength is zero. This is also in contrast to the case for band-to-band absorption. In that particular case all of the spinor components of the valence subbands contribute.

The contribution to the index of refraction of each exciton is obtained from the imaginary part of the dielectric function, using the Kramers-Kronig relation. This is expected to give accurate results since the contribution to the dielectric function of each exciton has only a very limited spectral range.

We first consider the individual contributions from each bound exciton state. In Tables 6.3 and 6.4 we give the calculated exciton binding energies and oscillator strengths for a 100Å GaAs-$Al_{0.25}Ga_{0.75}As$ single quantum well, obtained using the coupled exciton theory, and for the ground

state and excited state excitons respectively. From these results the following observations can be made:

(a) for both the (1s) and (2s) excitons only the LH excitons have TM oscillator strength

(b) the normally parity-forbidden (2p) excitons have TM oscillator strength in the case of the HH excitons only

(c) in the case of the (3d) excitons only the HH excitons have TM oscillator strength

(d) all normally parity-allowed excitons are either (1s), (2s) or (3d)

(e) all normally parity-forbidden excitons are (2p)

(f) the ground state (1s) excitons show both the largest oscillator strengths and largest binding energies of all the excitons considered here

(g) for excitons which have both TE and TM oscillator strength, the TM oscillator strength is four times that of the TE oscillator strength

Table 6.2 *The ground state (1s) excitons included in the calculations and the excitons to which they are coupled via the Coulomb interaction. Only excitons with nonvanishing oscillator strength have been included in the basis for the variational calculations.*

(1s) exciton	Coupled excitons
HH1-CB1	LH1-CB1 (3d), HH3-CB1 (1s)
LH1-CB1	HH1-CB1 (3d), HH2-CB1 (2p), HH3-CB1 (3d)
HH2-CB2	LH1-CB2 (2p)
HH3-CB1	HH1-CB1 (1s), LH1-CB1 (3d)

Table 6.3 *Binding energies and TE, TM oscillator strengths of ground state (1s) excitons in a 100Å GaAs-$Al_{0.25}Ga_{0.75}As$ single quantum well. The results were obtained using the coupled exciton model.*

Exciton	E_b (meV)	f_{TE} (10^{-5}Å^{-2})	f_{TM} (10^{-5}Å^{-2})
HH1-CB1 (1s)	9.44	33.96	0.0
LH1-CB1 (1s)	11.39	9.56	38.20
HH2-CB2 (1s)	6.74	16.86	0.0
HH3-CB1 (1s)	1.12	1.53	0.0

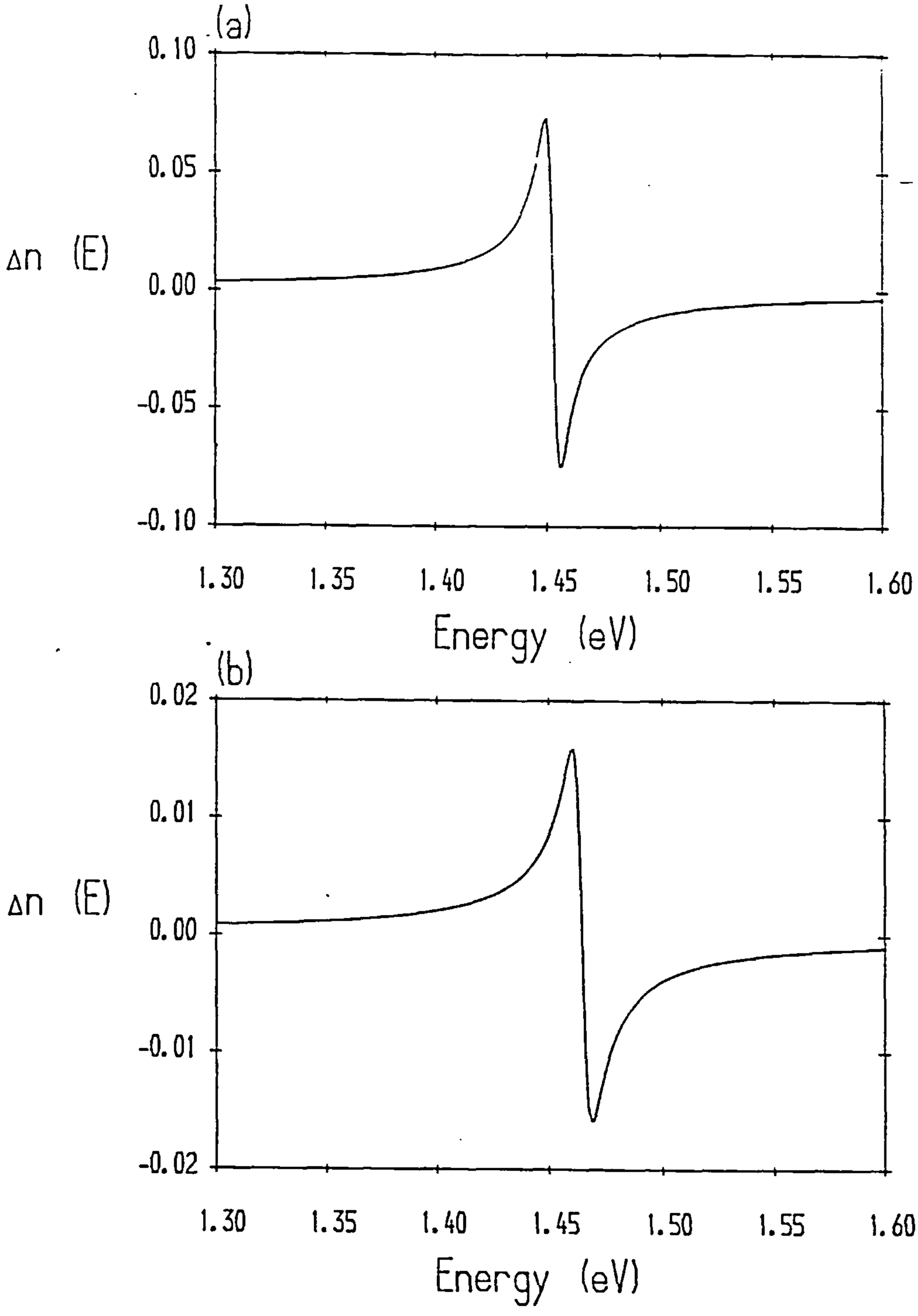

Figure 6.1 *Contributions to the TE-mode index of refraction from (a) the HH1-CB1 ground state (1s) exciton and (b) the LH1-CB1 ground state (1s) exciton. The width of the quantum well region is 100Å and the barrier aluminium concentration is x = 0.25. The exciton linewidths are assumed to have the value of 3meV, for each exciton.*

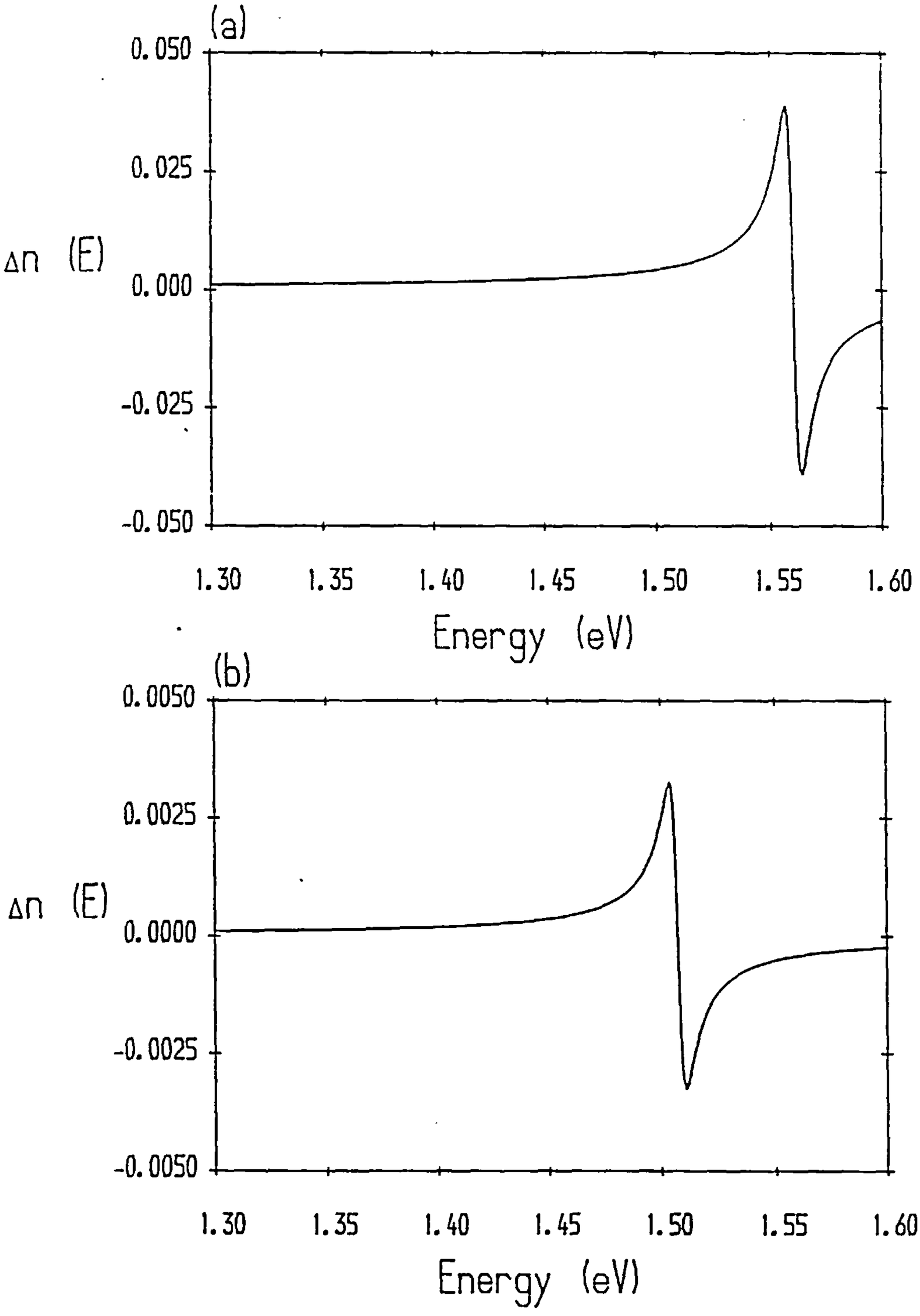

Figure 6.2 *Contributions to the TE-mode index of refraction from (a) the HH2-CB2 ground state (1s) exciton and (b) the HH3-CB1 ground state (1s) exciton. The width of the quantum well region is 100Å and the barrier aluminium concentration is x = 0.25. The exciton linewidths are assumed to have the value of 3meV, for each exciton.*

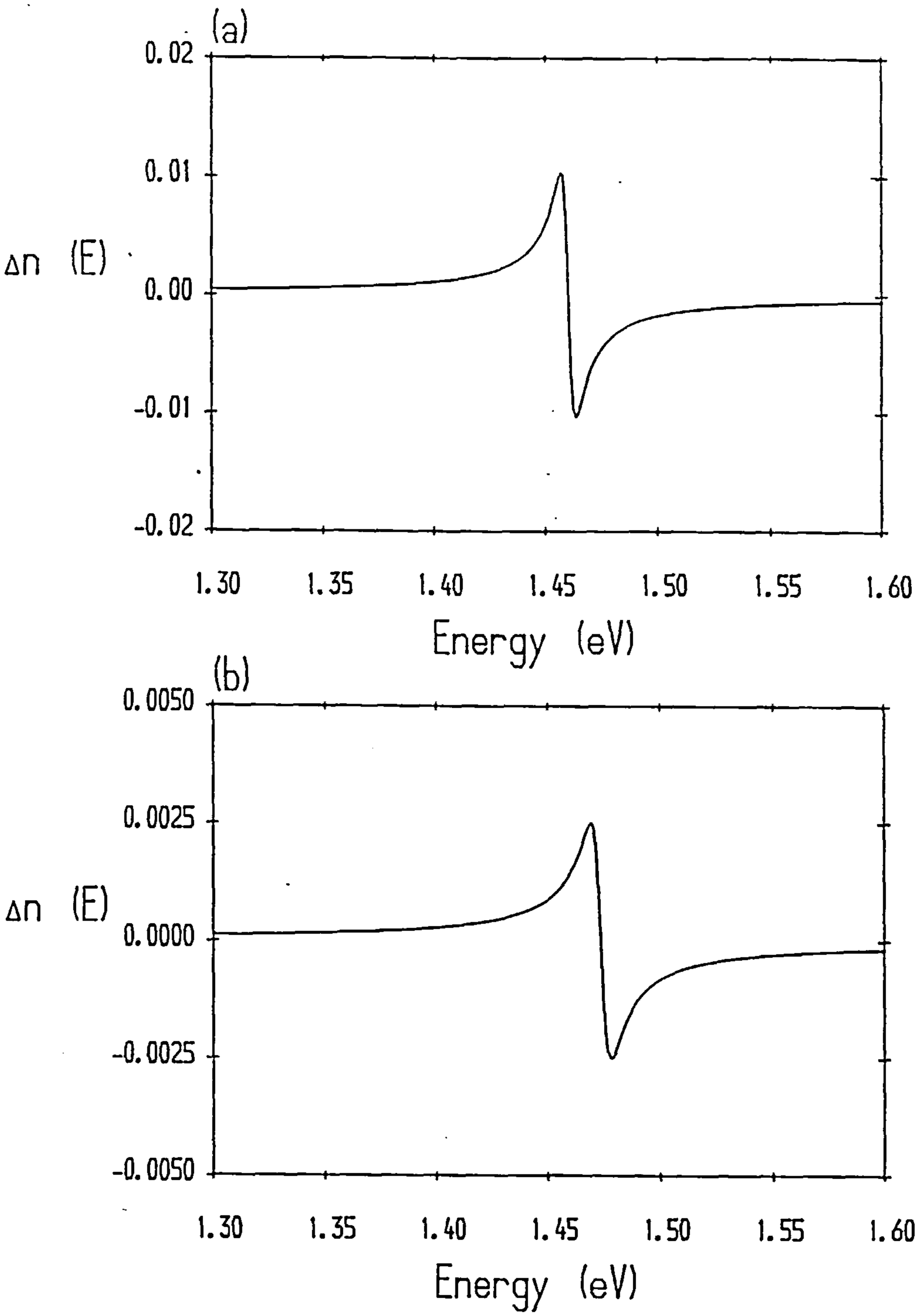

Figure 6.3 *Contributions to the TE-mode index of refraction from (a) the HH1-CB1 (2s) excited state exciton and (b) the LH1-CB1 (2s) excited state exciton. The width of the quantum well region is 100Å and the barrier aluminium concentration is x = 0.25. The exciton linewidths are assumed to have the value of 3meV, for each exciton.*

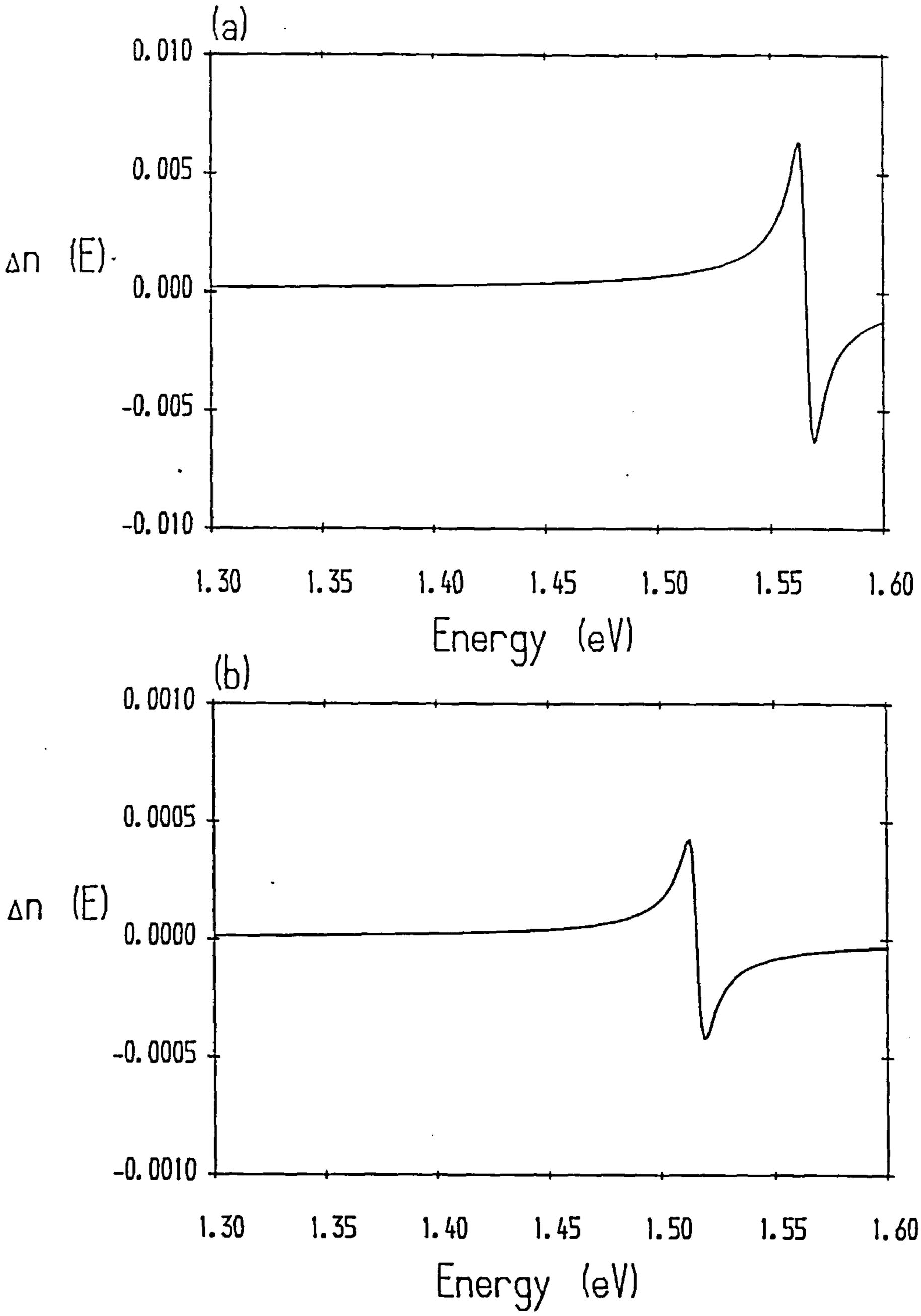

Figure 6.4 *Contributions to the TE-mode index of refraction from (a) the HH2-CB2 (2s) excited state exciton and (b) the HH3-CB1 (2s) excited state exciton. The width of the quantum well region is 100Å and the barrier aluminium concentration is x = 0.25. The exciton linewidths are assumed to have the value of 3meV, for each exciton.*

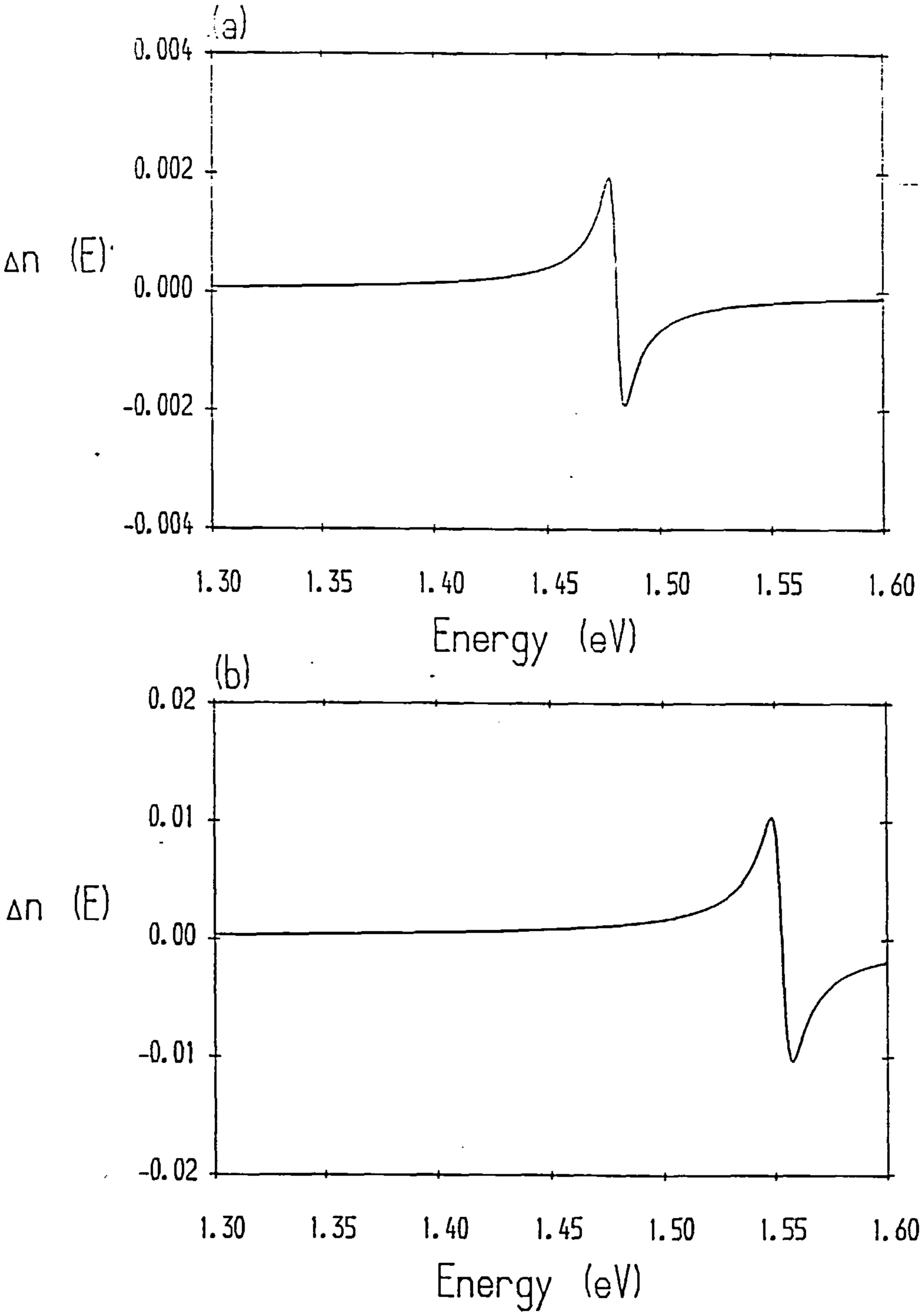

Figure 6.5 *Contributions to the TE-mode index of refraction from (a) the HH2-CB1 (2p) excited state exciton and (b) the LH1-CB2 (2p) excited state exciton. The width of the quantum well region is 100Å and the barrier aluminium concentration is x = 0.25. The exciton linewidths are assumed to have the value of 3meV, for each exciton.*

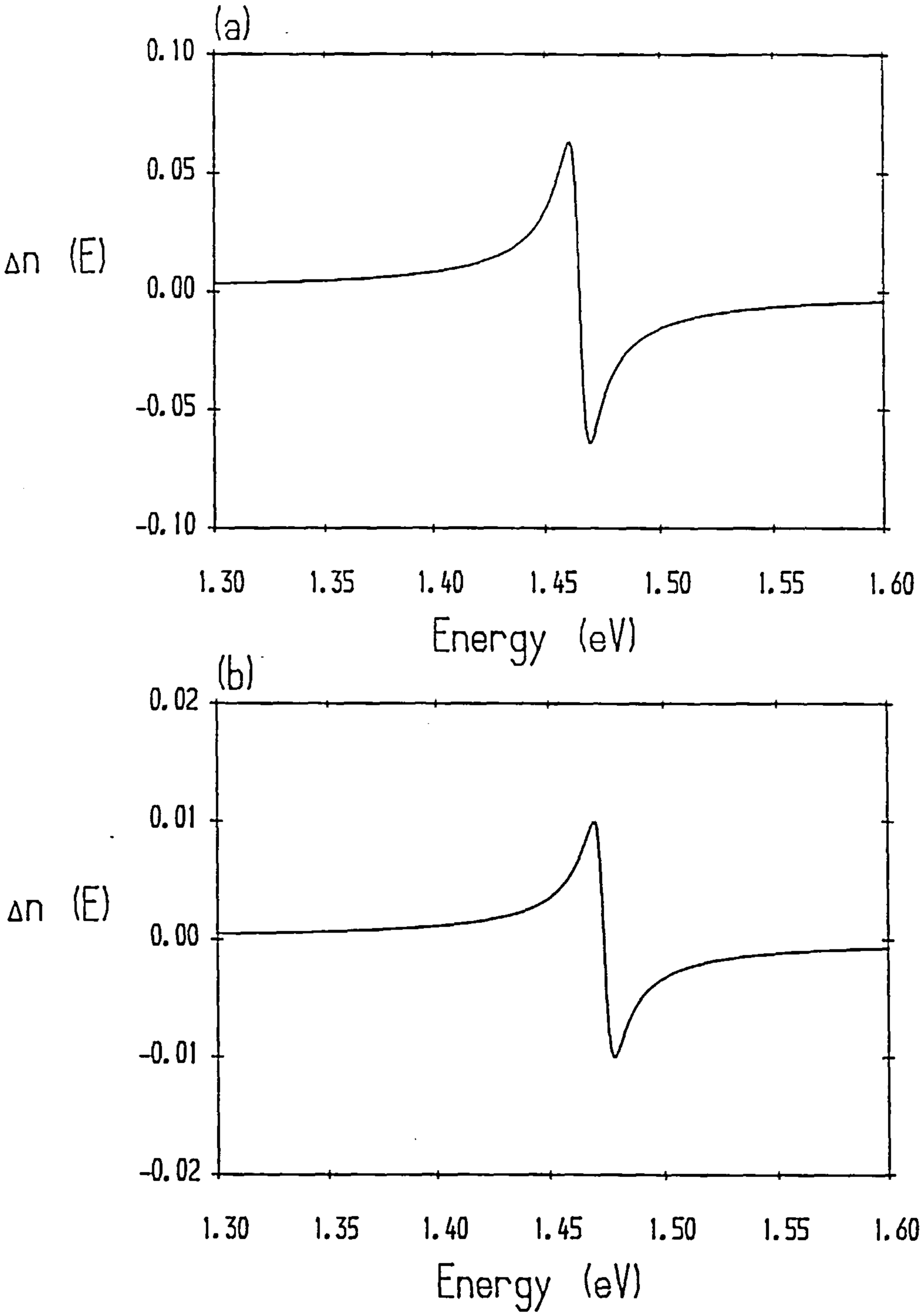

Figure 6.6 *Contributions to the TM-mode index of refraction from (a) the LH1-CB1 ground state (1s) exciton and (b) the LH1-CB1 (2s) excited state exciton. The width of the quantum well region is 100Å and the barrier aluminium concentration is x = 0.25. The exciton linewidths are assumed to have the value of 3meV, for each exciton.*

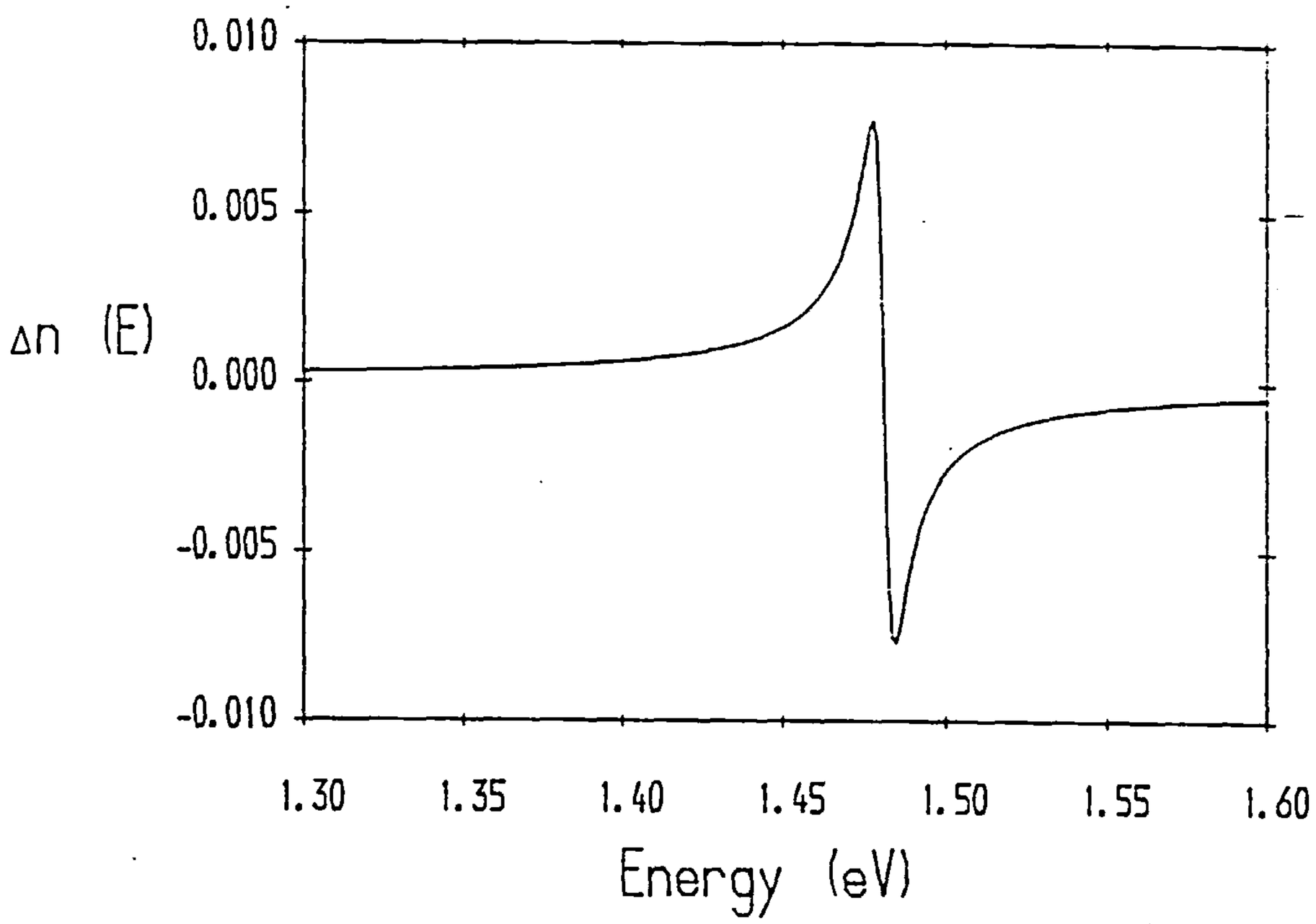

Figure 6.7 *Contribution to the TM-mode index of refraction from the HH2-CB1 (2p) excited state exciton, for a 100Å GaAs-Al0.25Ga0.75As single quantum well. The exciton linewidth is assumed to have the value of 3meV.*

Table 6.4 *Binding energies and TE, TM oscillator strengths of (2s), (2p) and (3d) excited state excitons in a 100Å GaAs-$Al_{0.25}Ga_{0.75}As$ single quantum well.*

Exciton	E_b (meV)	f_{TE} (10^{-5}Å^{-2})	f_{TM} (10^{-5}Å^{-2})
HH1-CB1 (2s)	1.58	4.72	0.0
LH1-CB1 (2s)	2.25	1.47	5.87
HH2-CB2 (2s)	1.06	2.71	0.0
HH3-CB1 (2s)	2.48	0.19	0.0
HH1-CB2 (2p)	3.95	0.064	0.27
LH1-CB2 (2p)	5.98	5.23	0.0
HH2-CB1 (2p)	2.76	0.83	3.32
HH1-CB1 (3d)	3.58	0.26	1.03
LH1-CB1 (3d)	4.56	0.69	0.0
HH2-CB2 (3d)	2.67	0.0020	0.0080
HH3-CB1 (3d)	4.83	0.0062	0.025

In Figures 6.1 to 6.7 we show the contribution to the index of refraction of these exciton states, excluding the (3d) excitons, in a 100Å GaAs-$Al_{0.25}Ga_{0.75}As$ single quantum well. These results are obtained directly from the Kramers-Kronig expression given by equation (6.7). A linewidth of 3meV has been assumed for all the exciton states considered.

The magnitude of the contribution in each case can be directly related to the TE and TM oscillator strengths given in Tables 6.3 and 6.4. It is seen that by far the largest contributions arise from the HH1-CB1, LH1-CB1 and HH2-CB2 (1s) excitons. The HH3-CB1 (1s) exciton contribution is small, and is exceeded by the contributions of the HH1-CB1 (2s), HH2-CB2 (2s) and LH1-CB2 (2p) excitons.

Note that these contributions, and the previous analysis of the results given in Tables 6.3 and 6.4 are for the particular case of a symmetric quantum well. Differences will arise in the case of an asymmetric quantum well. Asymmetry can be achieved by several means. These include different outer barrier compositions and different doping levels in each barrier region. The effect of an electric field, applied along the growth axis also leads to asymmetry. In this case, excitons excluded from Tables 6.3 and 6.4 can acquire finite non-zero oscillator strength. For the particular example of an applied electric field, the oscillator strengths of several excitons are given in Table 6.5, for several field strengths. These excitons have zero oscillator strength in a symmetric quantum well structure. Note however that the application of a magnetic field along the growth axis does not alter the symmetry of the Hamiltonian.

In Table 6.5 only the (1s) and (2s) excitons are considered. It is seen that the increase in electric field increases the oscillator strength. For each exciton, however, a maximum field value exists beyond which no bound exciton state can exist. The actual values of these oscillator strengths are rather small, and the contribution to the index of refraction is correspondingly small. Nevertheless it is best to include these particular excitons when external perturbations, breaking the quantum well symmetry, are considered. This keeps the model as complete and accurate as possible.

Table 6.5 *TE oscillator strengths of normally parity-forbidden excitons in a 100Å GaAs-$Al_{0.25}Ga_{0.75}As$ single quantum well in the presence of an external electric field.*

(n,m) state	Exciton	10kV/cm	20kV/cm	30kV/cm	35kV/cm
(1s)	HH2-CB1	0.37	1.27	2.64	3.48
	HH1-CB2	0.72	1.97	3.44	1.50
	LH1-CB2	0.18	0.29	0.44	0.18
(2s)	HH2-CB1	0.06	0.20	0.41	0.54
	HH1-CB2	0.11	0.30	0.53	0.40
	LH1-CB2	0.03	0.04	0.07	0.06

Note that the oscillator strengths given in Table 6.5 can oscillate in value as the field strength is increased. This depends on the overlap of the single-particle envelope functions. This is only seen in exciton states built mainly from the $n \neq 1$ single-particle states.

Before considering the effects of external perturbations, which is done in the following two sections, it is useful to consider the errors introduced by simpler models. In general the most complicated calculations are those dealing with the excitons. It is fairly commonplace to consider only the HH1-CB1 (1s) exciton. The error resulting from the neglect of other excitons, in particular the excited exciton states, should therefore be carefully quantified.

Before doing this, consider other sources of error. Typically the nonparabolicity of the conduction band dispersion is neglected. Also, the material parameters used vary considerably in the literature. The differences in binding energies and oscillator strengths resulting from different material parameters and parabolic versus nonparabolic conduction band dispersion are not particularly great. This statement applies to the HH1-CB1 (1s) and LH1-CB1 (1s) excitons only.

In Table 6.6 we give the binding energies and TE oscillator strengths obtained using three different sets of parameters. These are (a) parabolic conduction bands and the valence band parameters from Ref. 21, (b) as (a) but with nonparabolic conduction band dispersion, and (c) as (b) but with the valence band parameters used in this thesis. In general the results do not differ greatly. The use of nonparabolic conduction band dispersion increases the calculated binding energies. The results using parameters (b) and (c), differing only in the valence band parameters employed, are fairly similar.

Other simpler methods of calculation (see Appendix B) are not considered here since the results have little physical validity, and would in any case fail completely for the excited exciton states.

Consider now the neglect of exciton states in the calculation of the total index of refraction. To do this we consider four different models. Model 1 includes only the HH1-CB1 (1s) exciton, although still obtained using a coupled-exciton model. Model 2 includes four parity-allowed (1s) excitons, the additional ones being LH1-CB1, HH2-CB2 and HH3-CB1. Model 3 further includes

Table 6.6 *Binding energies and TE oscillator strength of HH1-CB1 (1s) and LH1-CB1 (1s) excitons in GaAs-$Al_{0.25}Ga_{0.75}As$ quantum well. The parameters used are (a) parabolic conduction bands and valence band parameters from Ref. 21, (b) as (a) but with nonparabolic conduction bands, (c) as (b) but using the valence band parameters from this thesis.*

Exciton		set (a)	set (b)	set (c)
HH1-CB1 (1s)	E_B (meV)	8.79	9.52	9.44
	f_{TE} (10^{-5}Å^{-2})	29.57	34.74	33.96
LH1-CB1 (1s)	E_B (meV)	11.44	11.65	11.39
	f_{TE} (10^{-5}Å^{-2})	7.27	8.60	9.72

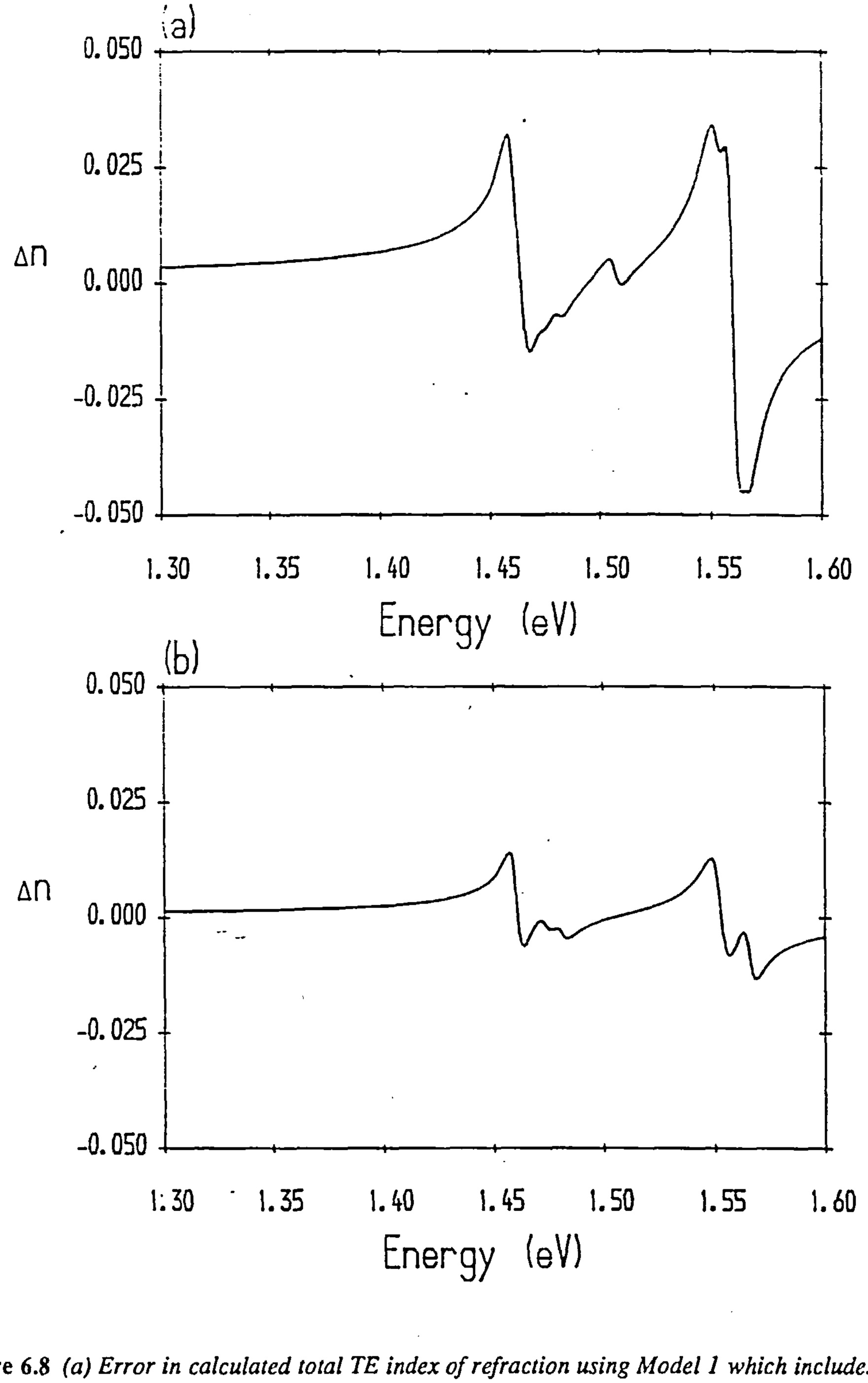

Figure 6.8 *(a) Error in calculated total TE index of refraction using Model 1 which includes only the HH1-CB1 (1s) exciton. (b) Error in calculated total TE index of refraction using Model 2 which includes only the four (1s) excitons HH1-CB1, LH1-CB1, HH2-CB2 and HH3-CB1. The results are obtained for a 100Å GaAs-$Al_{0.25}Ga_{0.75}As$ single quantum well, and the error obtained by comparison with Model 4 which includes four (1s), three (2s) and two (2p) excitons. Figure 6.8 (c) is given overleaf.*

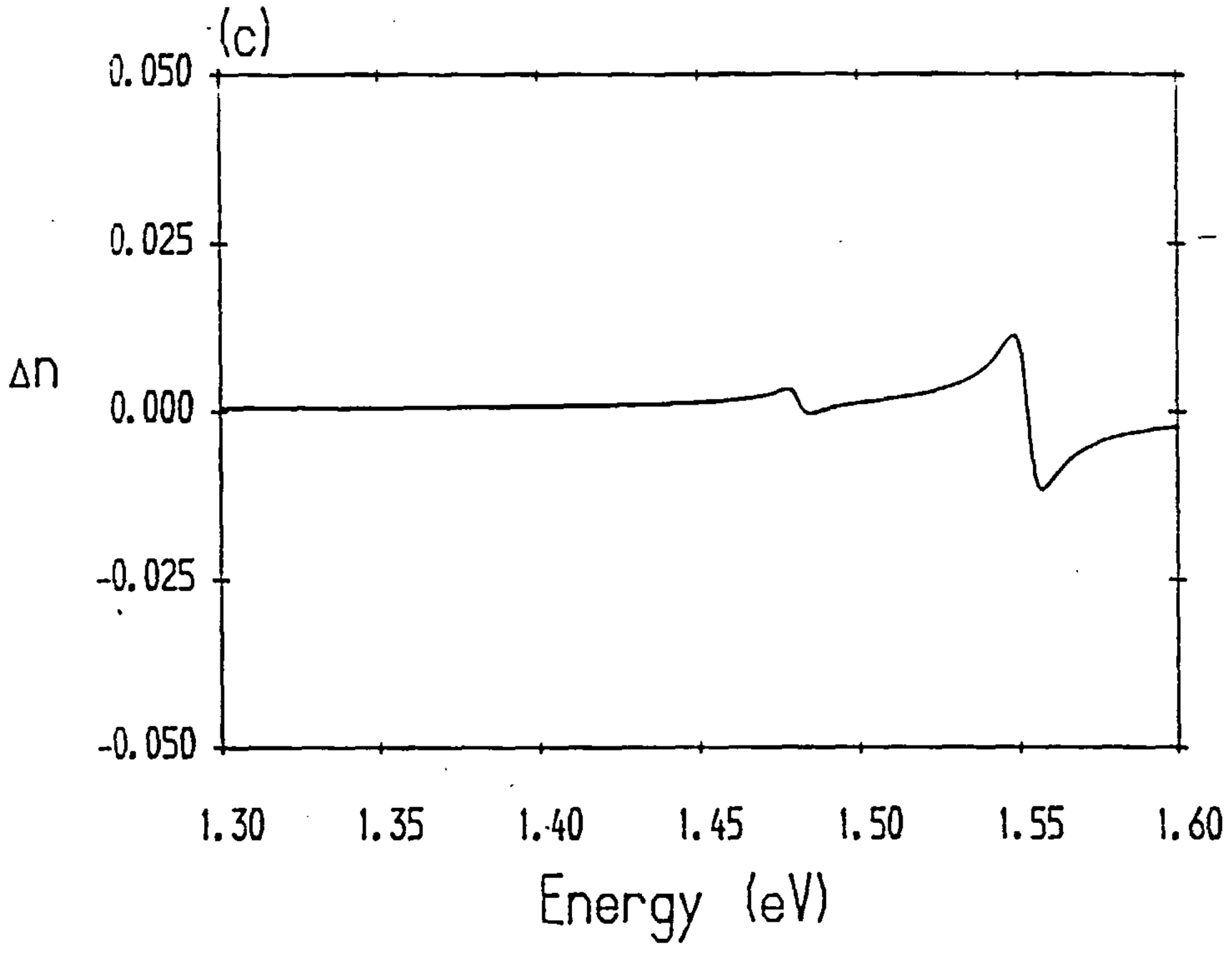

Figure 6.8 *(c) Error in calculated total TE index of refraction using Model 3 which includes the three additional (2s) excitons HH1-CB1, LH1-CB1 and HH2-CB2. The results are obtained for a 100Å GaAs-$Al_{0.25}Ga_{0.75}As$ single quantum well, and the error is obtained by comparison with the results of Model 4 which includes four (1s), three (2s) and two (2p) excitons.*

three (2s) excited state excitons, these being HH1-CB1, LH1-CB1 and HH2-CB2. Finally, Model 4 adds two (2p) excitons, HH2-CB1 and LH1-CB2. For all of these calculations the coupled-exciton model and nonparabolic conduction band dispersion are employed.

If we assume that Model 4 is essentially complete, all other excitons contributing little, then we obtain the neglected contributions to the total index of refraction resulting from each of the Models considered. These results are shown in Figure 6.8. From these results it is immediately obvious that by including more excitons the error is considerably reduced. The error obtained using Model 1, which considers only the ground state HH1-CB1 (1s) exciton is fairly large. The maximum magnitude of error is indeed comparable to the contribution of the HH1-CB1 (1s) exciton to the index of refraction alone. This can be seen from the results given in Figure 6.1.

The size of the errors shown in Figure 6.8 indicates clearly the requirements for accurate calculation of the resonant index of refraction. For frequencies considerably below the fundamental band gap it may be possible to include only a few excitons in the calculations. However, for frequencies in the vicinity of the fundamental band gap it is clear that a considerable number of exciton states must be included in the calculations. From the results given in Figure 6.8 (a) it is

evident that for frequencies above the fundamental band gap, these additional excitons introduce considerable structure into the index of refraction.

We conclude this section by obtaining the total index of refraction. This is done for a 100Å GaAs-$Al_{0.25}Ga_{0.75}As$ single quantum well. The contributions included in this calculation are the confined subband, quasi-continuum states and continuum states at Γ, and also the contribution from the L-valley. These contributions have been discussed in detail previously in this Chapter.

The excitons included are those which are parity-allowed in the absence of an external electric field. The complete list of exciton states is therefore HH1-CB1 (1s,2s,3d), LH1-CB1 (1s,2s,3d), HH2-CB2 (1s,2s,3d), HH3-CB1 (1s,2s,3d), HH1-CB2 (2p), HH2-CB1 (2p) and LH1-CB2 (2p).

The calculated index of refraction for TE polarisation is shown in Figure 6.9, and the index of refraction for TM polarisation is shown in Figure 6.10. Note that the results for TM polarisation appear to have less structure than those for TE polarisation. Of the fifteen excitons included it is found that only six have non-zero TM polarisation oscillator strength. These are the LH1-CB1 (1s,2s,3d), HH1-CB2 (2p) and HH2-CB1 (2p) excitons. However, all of the excitons included have non-zero TE polarisation oscillator strength.

For most of the frequency (energy) range considered in Figures 6.9 and 6.10 the refractive index for TE polarisation exceeds that for TM polarisation. This bi-refringence will be considered in more detail when the effects of external perturbations are included. In the particular case of an external electric field it has already been shown that several more excitons must be included in our model.

The peak value in this frequency range is nearly 3.39 in the case of TE polarisation. The peak value for the TM polarisation is slightly less at about 3.38. These values will of course strongly depend on the actual structure. Influencing factors will include the well width and the composition of the barrier material. These factors, along with the effects of a double quantum well structure (both symmetric and antisymmetric) will be considered later.

At frequencies close to the fundamental band gap, however, the above factors will mostly influence the excitonic contributions. In all cases therefore an accurate determination of the exciton wave functions is of paramount importance. The coupled-exciton model employed here is considered to be the most accurate in this respect. The excited exciton states which have been seen to contribute strongly to the resonant index of refraction can only be obtained accurately within this theoretical model. This has been seen to be more important than the precise choice of material parameters used as input to the calculations.

It can clearly be seen from all of the results given so far that the hope of accurately obtaining the index of refraction by considering only the ground state HH1-CB1 exciton and a constant additive background contribution from all other states now seems rather optimistic.

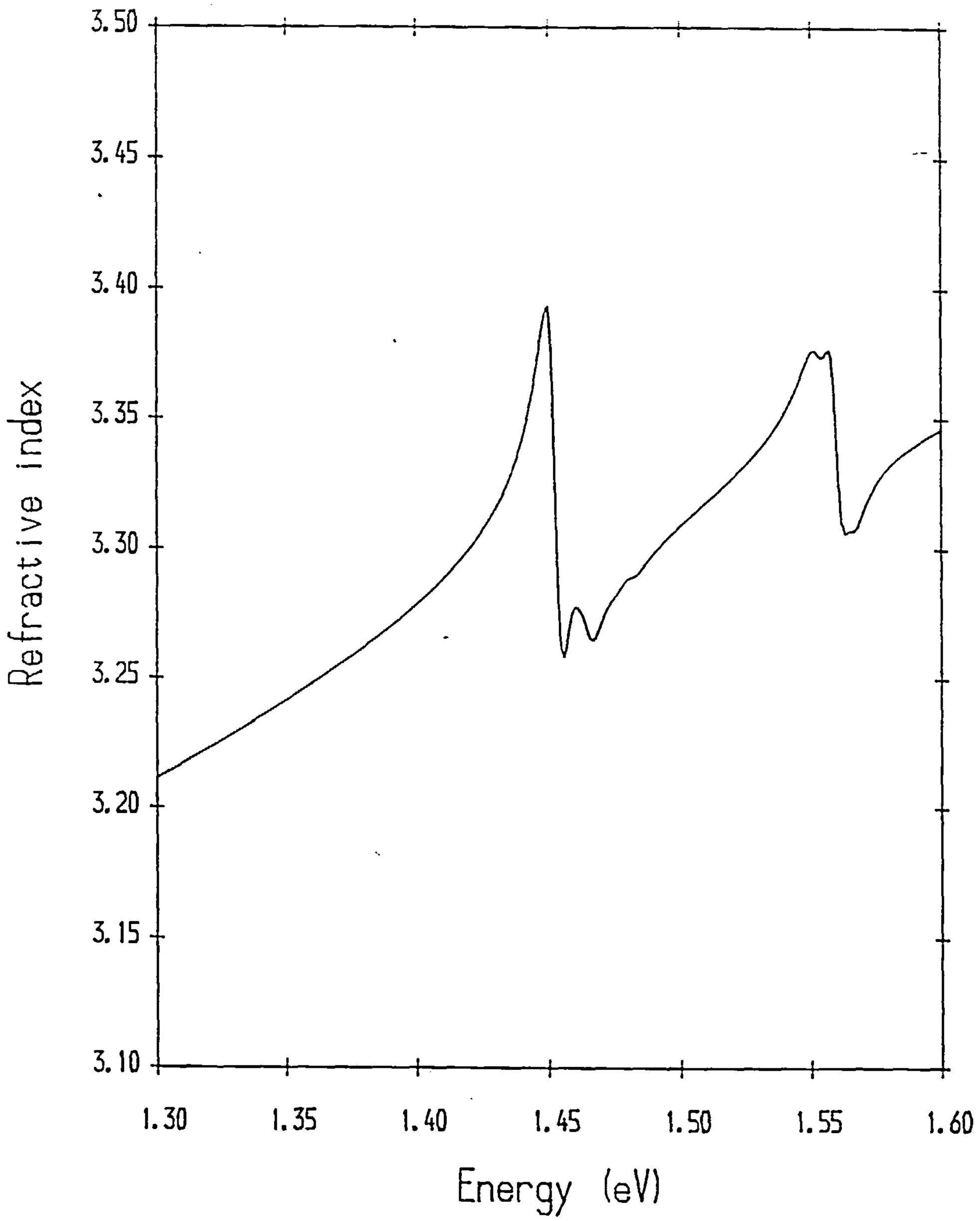

Figure 6.9 *Calculated total index of refraction for TE-mode polarisation for a 100Å GaAs-$Al_{0.25}Ga_{0.75}As$ single quantum well. A total of fifteen exciton states have been included in the calculation. The other contributions included arise from the confined subband, quasi-continuum and continuum states at Γ, and from the L-valley states.*

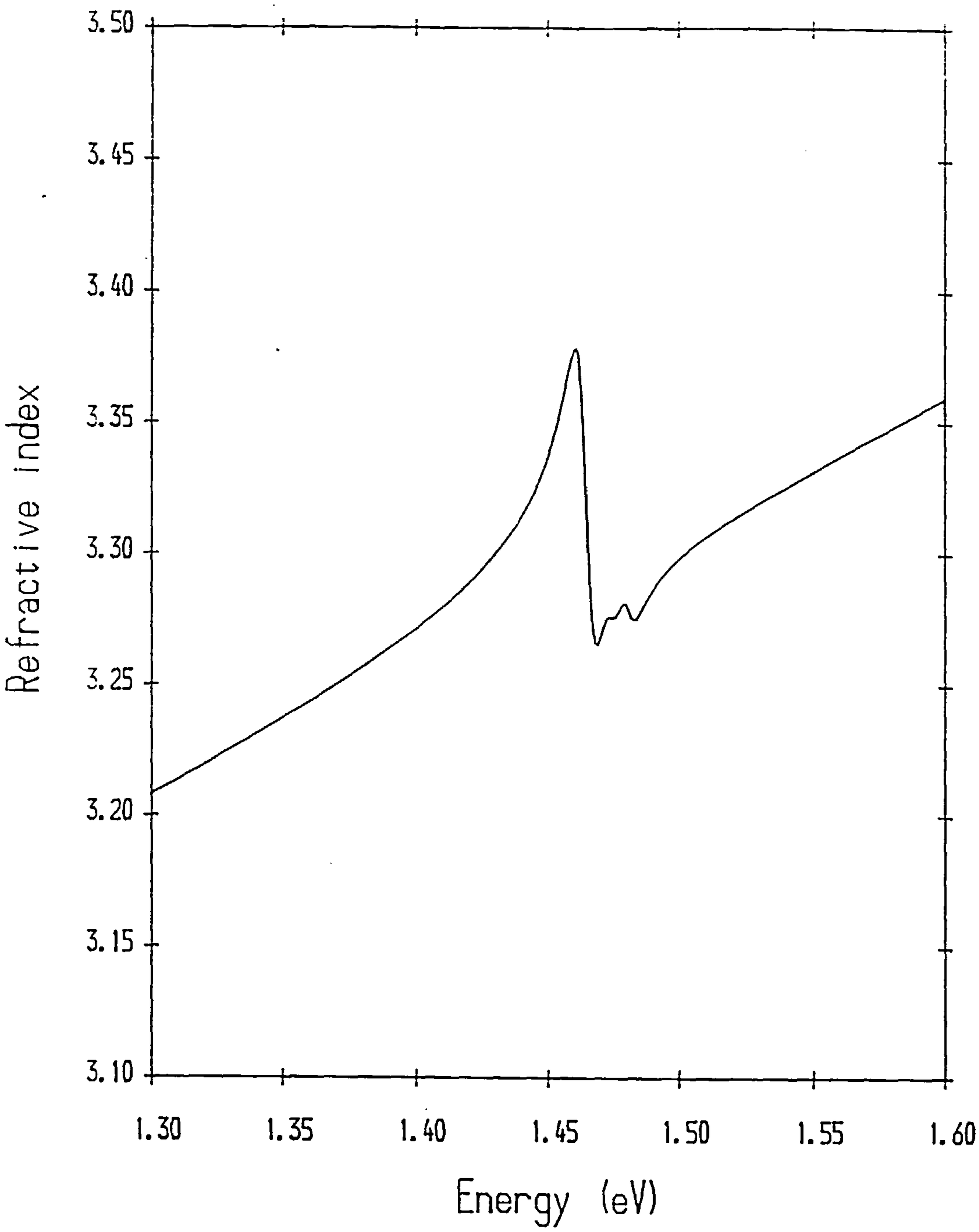

Figure 6.10 *Calculated total index of refraction for TM-mode polarisation for a 100Å GaAs-$Al_{0.25}Ga_{0.75}As$ single quantum well. A total of fifteen exciton states have been included in the calculation. The other contributions included arise from the confined subband, quasi-continuum and continuum states at Γ, and from the L-valley states.*

Electric field effects

In this section we consider the effect of an external electric field on the index of refraction. It is assumed that the electric field is applied along the growth axis, perpendicular to the quantum well interfaces. The application of an electric field in the quantum well plane only results in a general broadening of the energy levels. This is the well-known Franz-Keldysh effect. The differences in this particular case, between bulk material and quantum-confined structures, are negligible. An analysis of the Franz-Keldysh effect in bulk semiconductors can be found in Ref. 22. The theory and discussion presented there can be immediately applied to the case of quantum well structures. However, due to the small effect, it is not considered further.

In the absence of an electric field, the largest excitonic contributions to the index of refraction in a 100Å GaAs-$Al_{0.25}Ga_{0.75}As$ single quantum well arise from the HH1-CB1 (1s), LH1-CB1 (1s) and HH2-CB2 (1s) excitons. The individual contributions are shown in Figure 6.12, for electric field values of F = 0 and F = 35 kV/cm. The reduction is greatest for the HH2-CB2 (1s) exciton, with the lower subbands still well-confined at F = 35 kV/cm. This reduction indicates that an accurate calculation of the changes in the refractive index with increasing field cannot be confined to the lowest ground state excitons. An important factor in this reduction arises from the decreasing overlap integral of the electron and hole envelope functions as the electric field is increased. As seen previously, however, this is not the case for the normally parity-forbidden excitons.

It is instructive to consider the change in the index of refraction calculated by including only the HH1-CB1 (1s) exciton, and compare this with a more accurate calculation which includes several

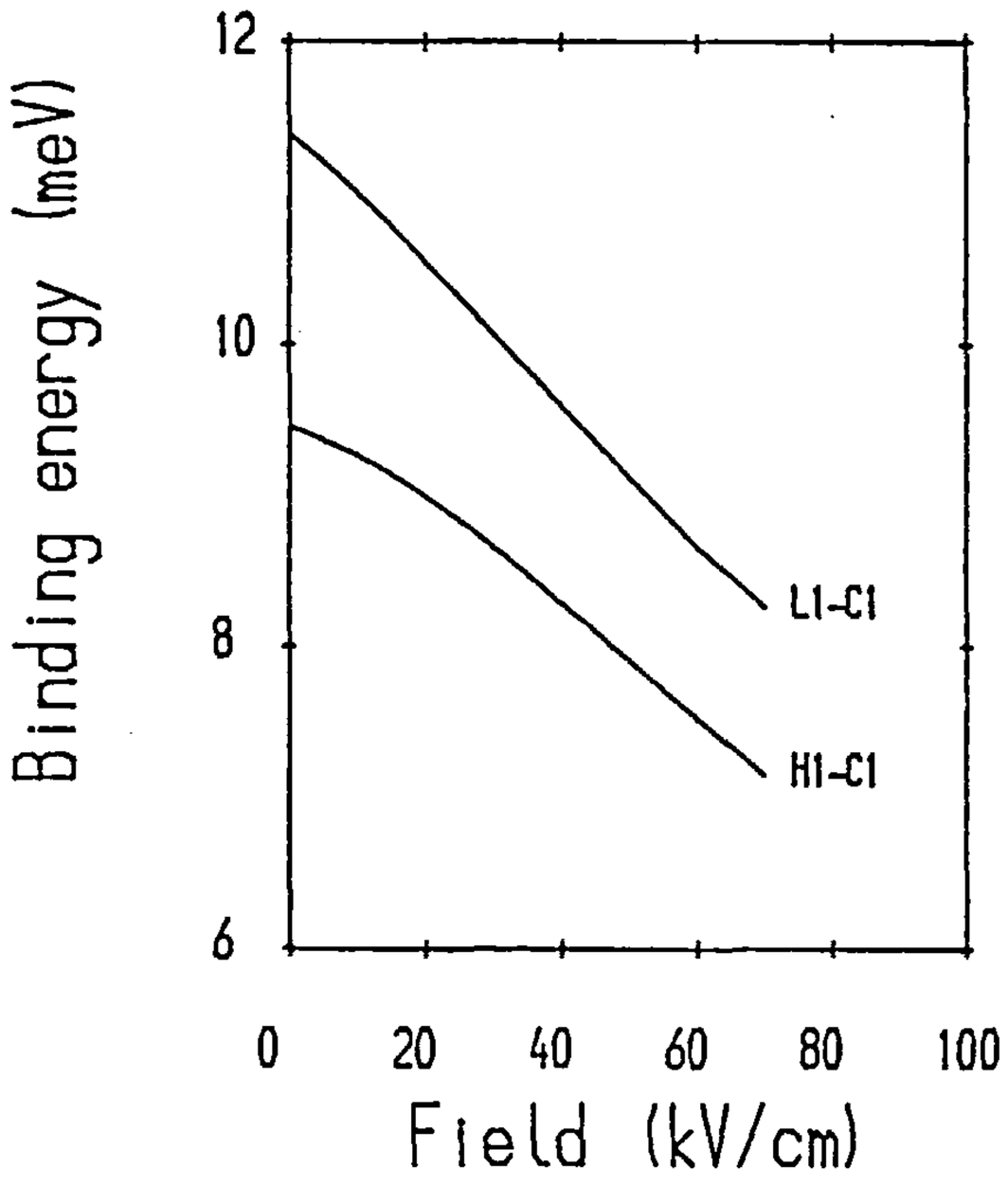

Figure 6.11 *Binding energies of the HH1-CB1 (1s) and LH1-CB1 (1s) excitons in the presence of an external electric field, applied along the quantum well growth axis. The single GaAs-$Al_{0.25}Ga_{0.75}As$ quantum well has a well width of 100Å. The trend shown in this Figure will generally apply to all of the normally parity-allowed excitons.*

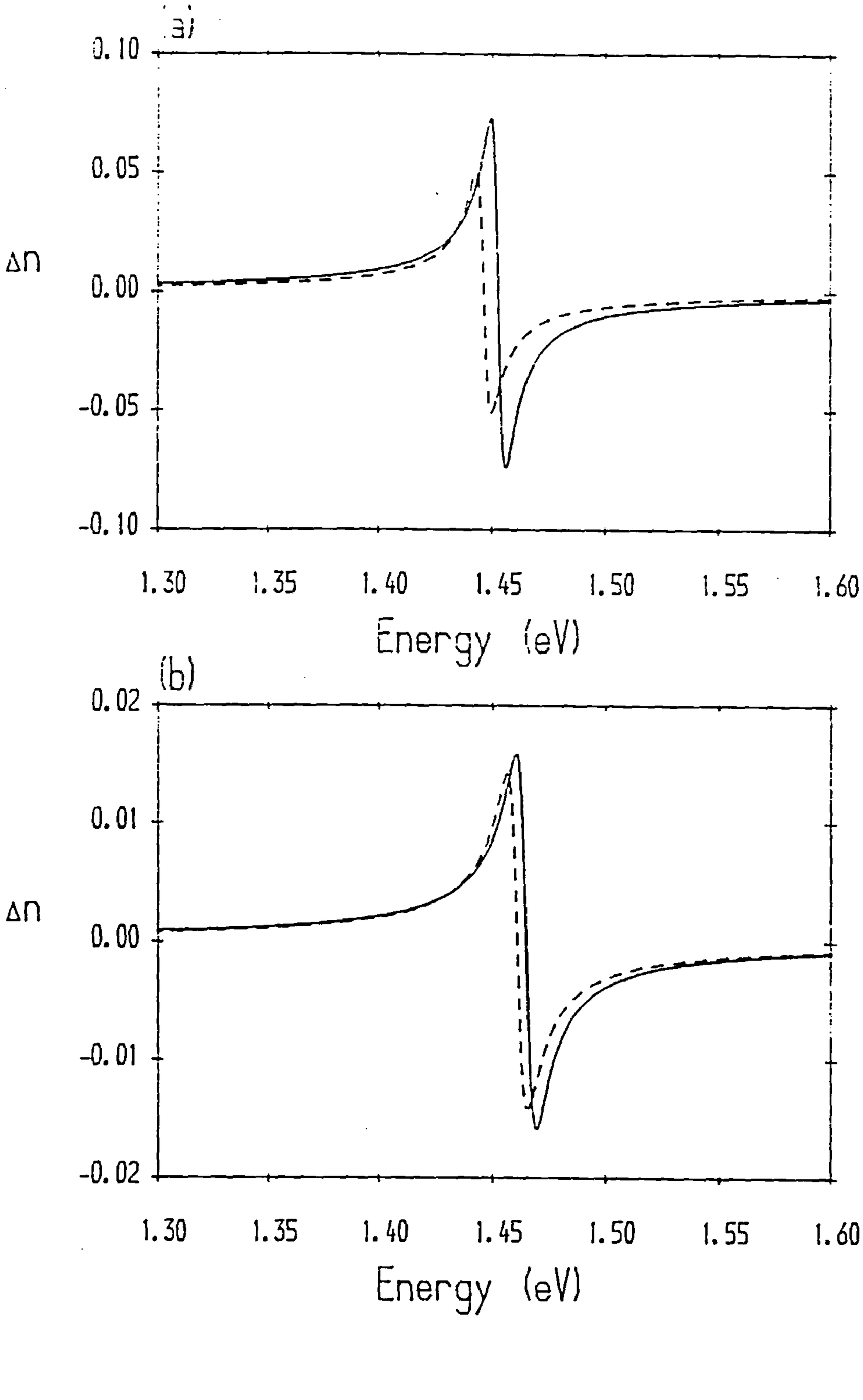

Figure 6.12 *Contribution to the index of refraction of (a) the HH1-CB1 (1s) exciton and (b) the LH1-CB1 (1s) exciton, for electric field values of F = 0 kV/cm (solid curves) and F = 35 kV/cm (dashed curves). The quantum well structure considered is a symmetric 100Å GaAs-$Al_{0.25}Ga_{0.75}As$ single quantum well.* *(continued overleaf)*

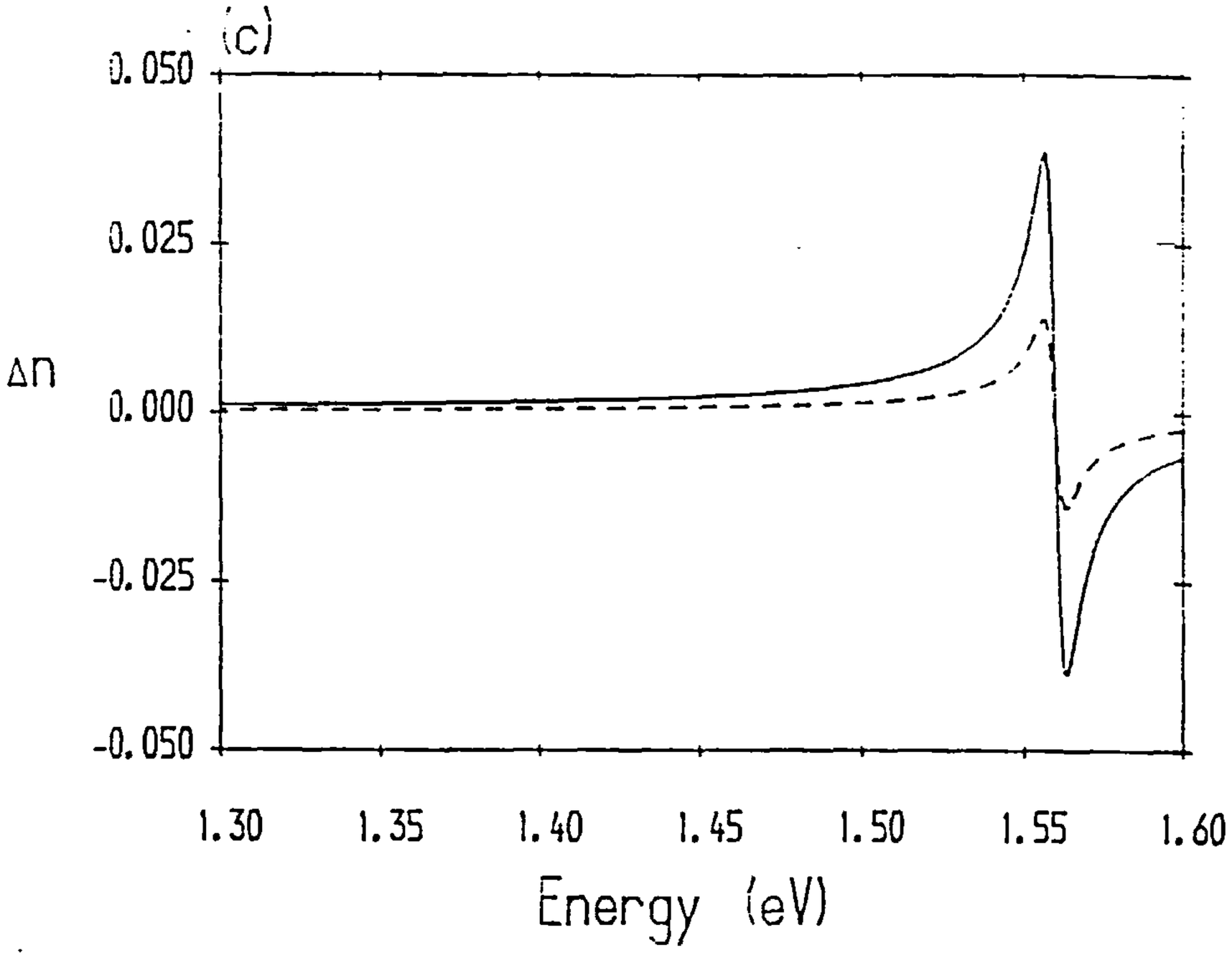

Figure 6.12 *(contd.) (c) Contribution to the index of refraction of the HH2-CB2 (1s) exciton, for electric field values of F = 0 kV/cm (solid curve) and F = 35 kV/cm (dashed curve). The quantum well structure considered is a symmetric 100Å GaAs-$Al_{0.25}Ga_{0.75}As$ single quantum well.*

excitons, including the excited states. The results of these calculations are shown in Figure 6.13. The top graph shows the results obtained by including only the HH1-CB1 (1s) exciton in the calculation. A simple two-band model is used to obtain the exciton wave function. The bottom graph shows the results obtained by including all of the exciton states which we have discussed previously, including several which are normally parity-forbidden at zero electric field.

The results shown in Figure 6.13 are given in the form $\Delta n/n$ where n is the index of refraction at F = 0 kV/cm. It is assumed that the results given in Figure 6.13(b) represent an accurate calculation of the field-induced change in the index of refraction. If the results given in Figure 6.13(a), which are obtained using only the HH1-CB1 (1s) exciton within a simple two-band model, are also taken to be a good approximation then the difference between these two graphs will of course be negligible. This difference (i.e. the difference in the calculated $\Delta n/n$ values) is shown in Figure 6.14. It is immediately obvious that for photon energies well below the fundamental band gap the approximation obtained using only the HH1-CB1 (1s) exciton is actually quite reasonable. For photon energies above the fundamental band gap, however, the approximation is very poor. The maximum differences, positive and negative, are +1.95% at $\hbar\omega$ = 1.449eV and -1.3% at $\hbar\omega$ = 1.567eV. The complicated structure of the results shown in Figure 6.14 indicate quite clearly that for photon energies above the fundamental band gap the use of a theoretical model which incorporates

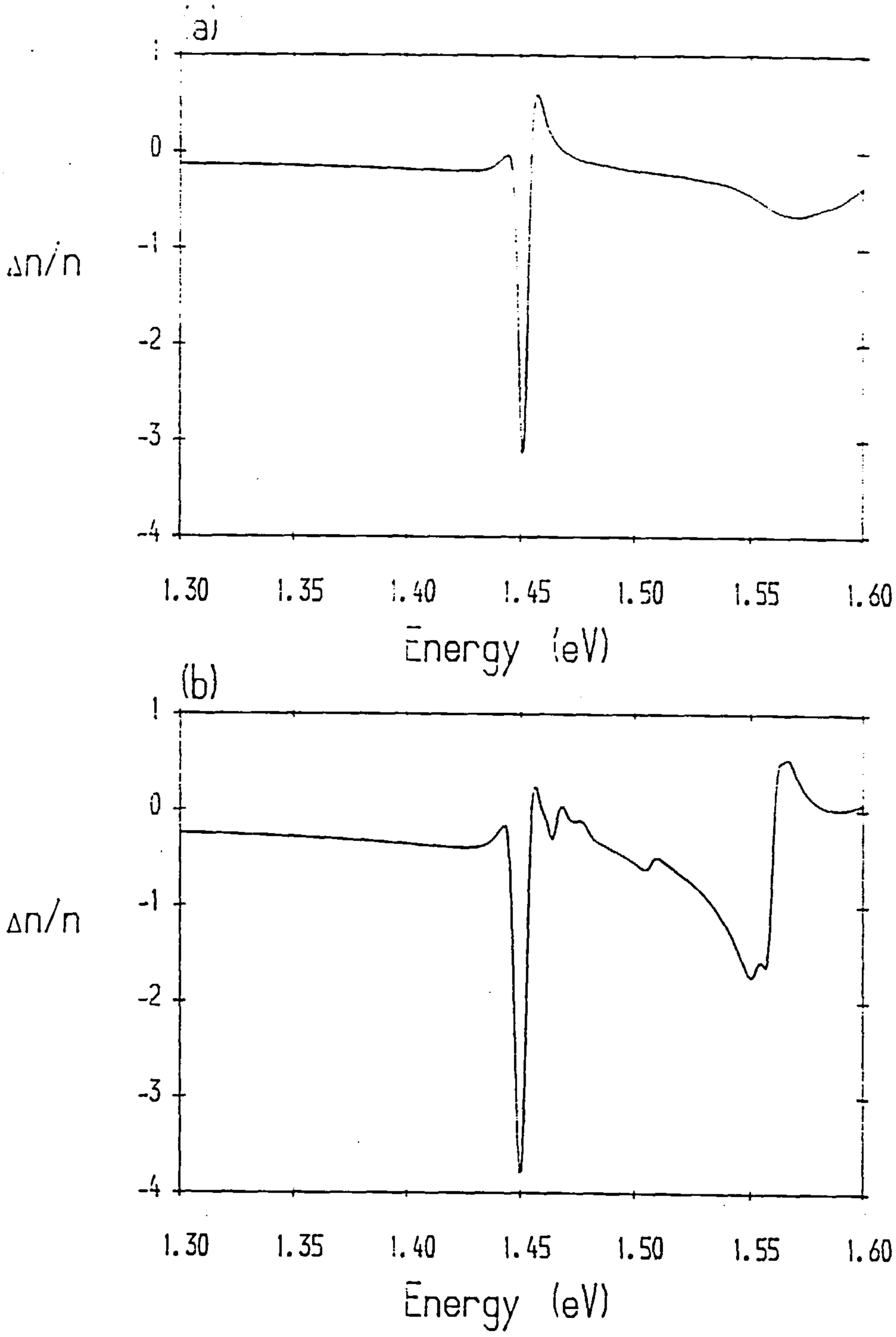

Figure 6.13 *Index of refraction changes Δn/n (in percent) obtained by the application of an external electric field F = 35 kV/cm calculated with the inclusion of the exciton states (a) HH1-CB1 (1s) within a two-band approximation and (b) all of the exciton states discussed previously. The results shown are for a symmetric 100Å GaAs-$Al_{0.25}Ga_{0.75}As$ single quantum well.*

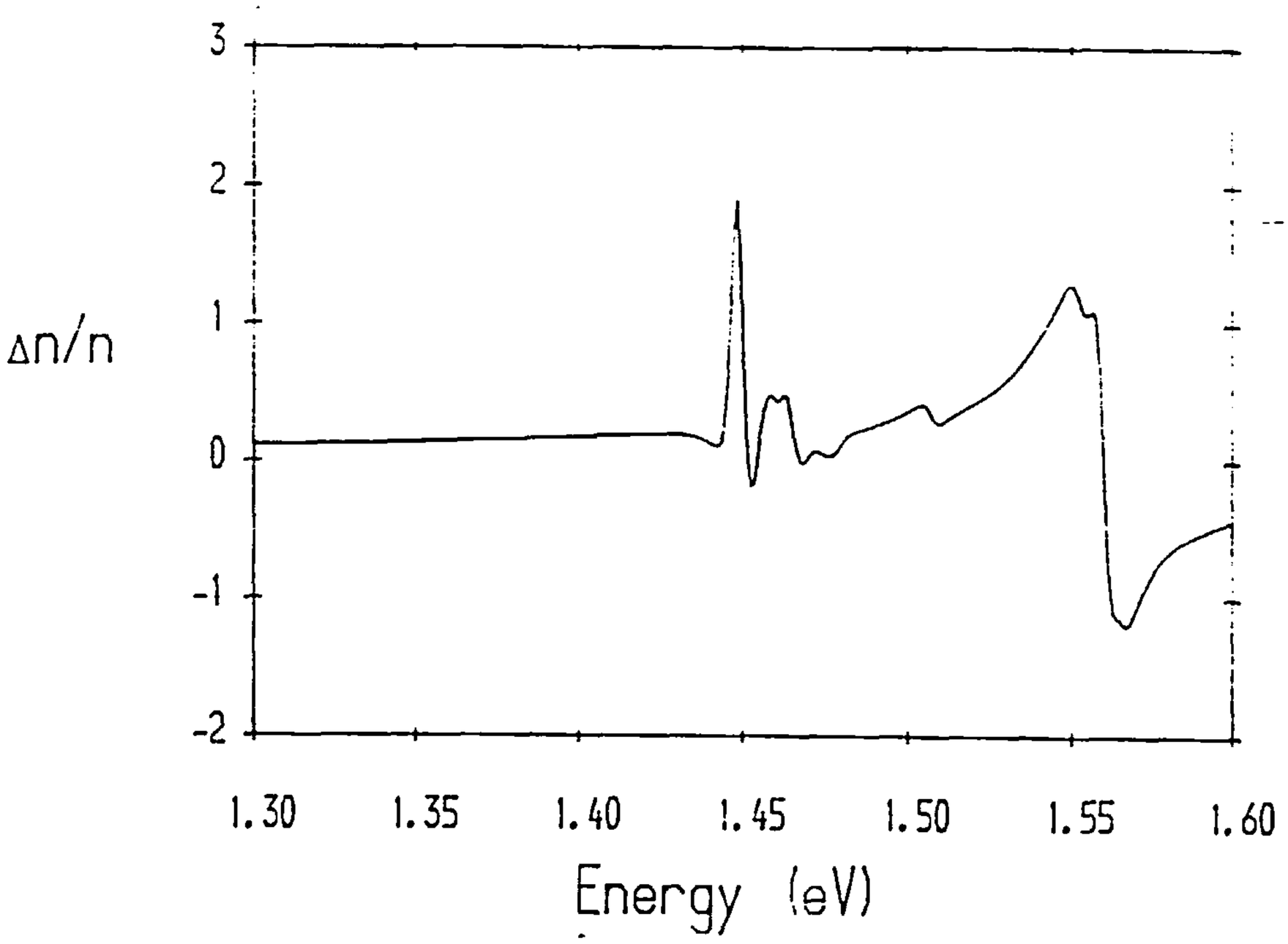

Figure 6.14 *Difference between the results of Figure 6.13(a) and those of Figure 6.13(b) to illustrate the relative acccuracy of the simpler model shown in Figure 6.13(a).*

only a single exciton state is quite unlikely to provide results of useful accuracy. Additionally, we find that when considering the effects of saturation on the index of refraction, the inclusion of only the HH1-CB1 (1s) exciton does not in this case give particularly useful results for photon energies below the band gap. The changes in refraction due to the effects of saturation will be considered in detail later in this Chapter.

The changes in refraction for a range of electric field values are shown in Figures 6.15 to 6.17. The values of electric field used to obtain the results given in these Figures are 15kV/cm, 30kV/cm and 45kV/cm respectively. Note that in all cases the overall change is larger for TE polarisation than for TM polarisation. This is due to the fact that for the (1s) and (2s) excitons, only those excitons principally derived from light-hole valence subbands have non-zero oscillator strength for TM polarisation. This differs from the results for the (2p) and (3d) excitons where only those excitons built principally from heavy-hole valence subbands have non-zero oscillator strength for TM polarisation. This applies to both the parity-allowed and parity-forbidden excitons. Also, the (2p) and (3d) excitons typically have smaller oscillator strengths than the (1s) and (2s) excitons. Specific values of exciton oscillator strengths for a 100Å GaAs-$Al_{0.25}Ga_{0.75}As$ quantum well were given in Tables 6.3 to 6.5, including several excitons which are parity-forbidden at zero electric field.

The total index of refraction for TE polarisation and for electric field values F = 0, 20 and 40kV/cm is shown in Figure 6.18. The higher exciton states are quenched at much lower field values

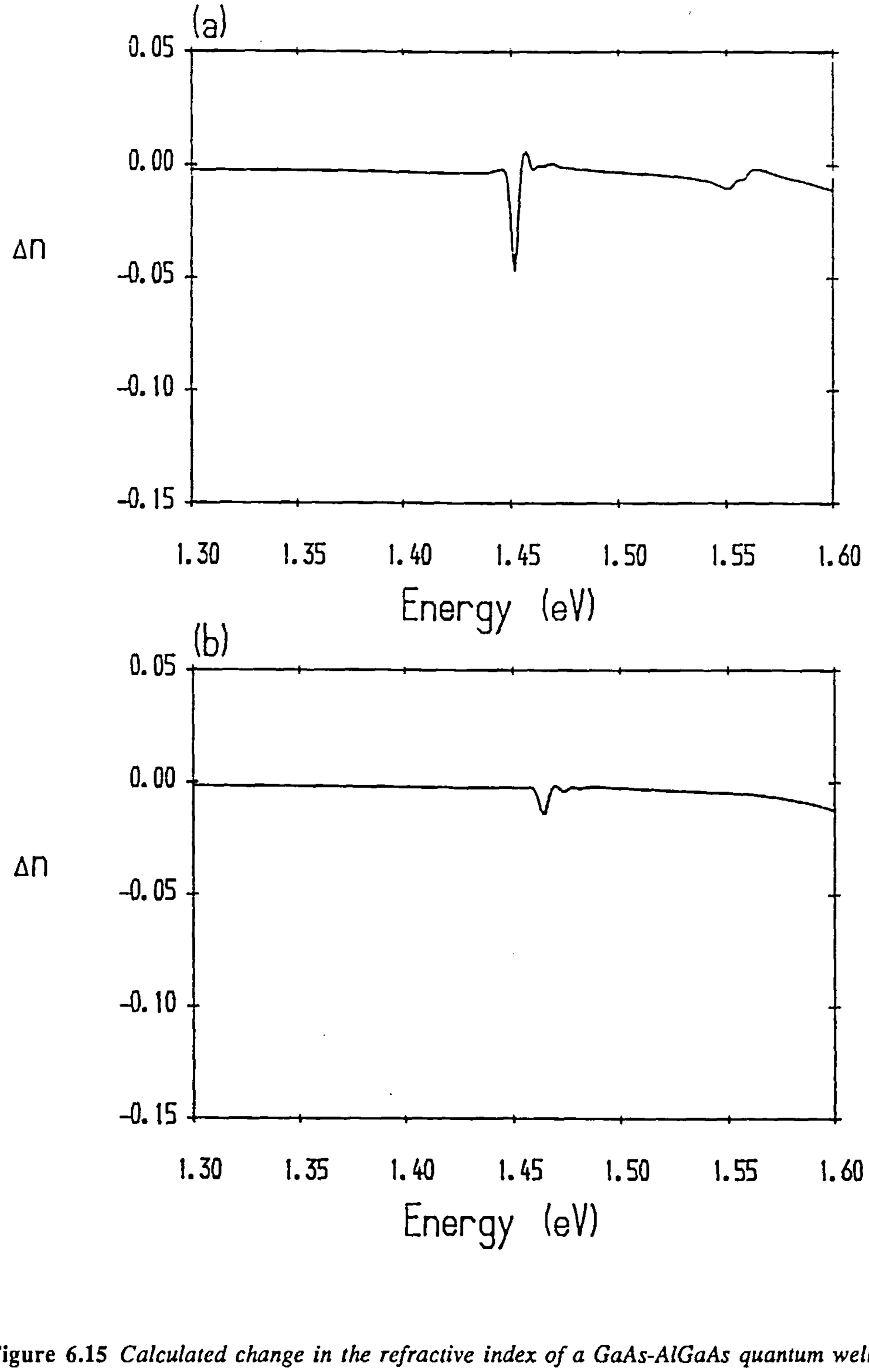

Figure 6.15 *Calculated change in the refractive index of a GaAs-AlGaAs quantum well in the presence of an external electric field for (a) TE polarisation and (b) TM polarisation. The value of the electric field is 15kV/cm, applied normal to the quantum well interfaces. The quantum well structure considered is a symmetric 100Å GaAs-$Al_{0.25}Ga_{0.75}As$ single quantum well.*

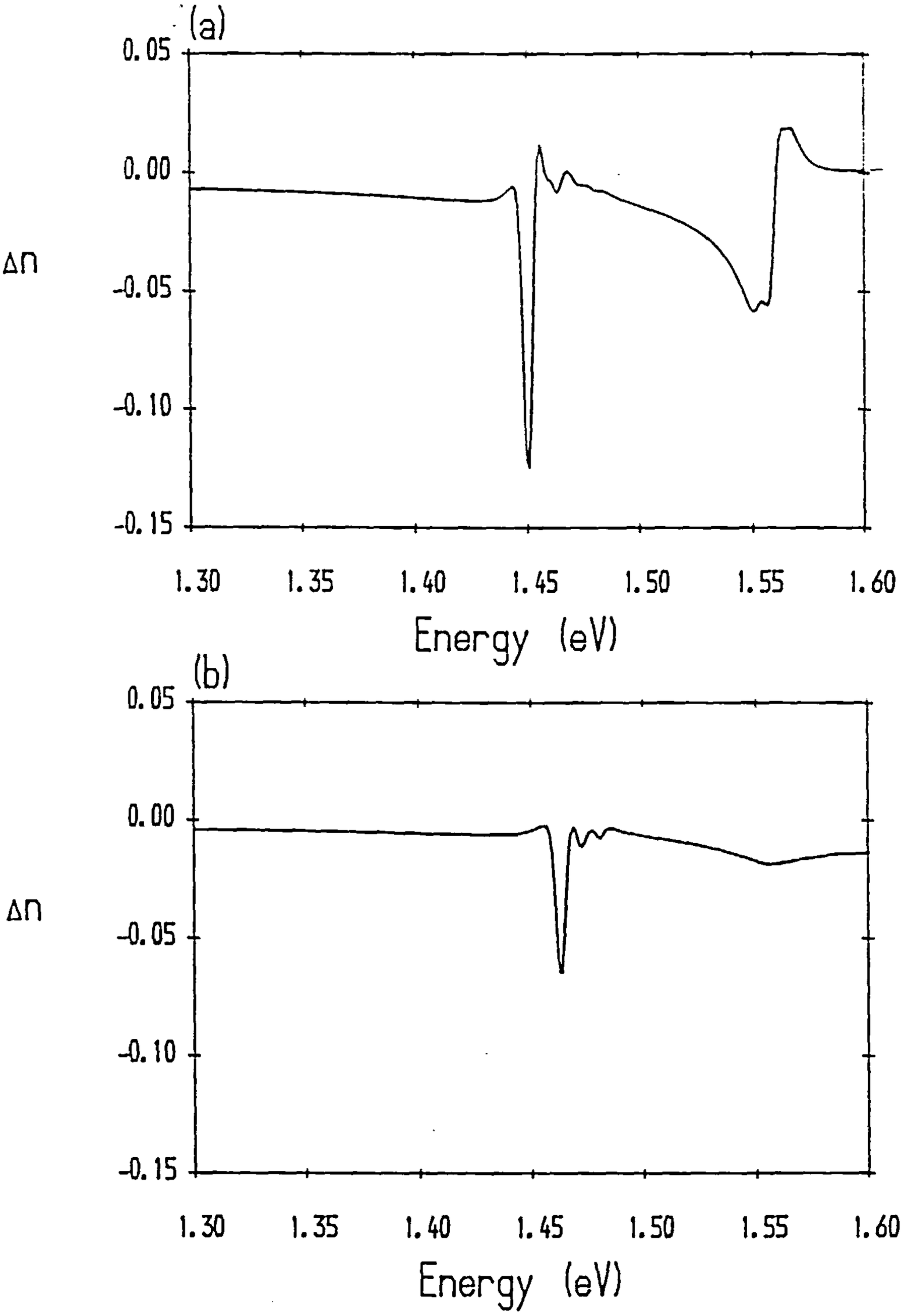

Figure 6.16 *Calculated change in the refractive index of a GaAs-AlGaAs quantum well in the presence of an external electric field for (a) TE polarisation and (b) TM polarisation. The value of the electric field is 30kV/cm, applied normal to the quantum well interfaces. The quantum well structure considered is a symmetric 100Å GaAs-$Al_{0.25}Ga_{0.75}As$ single quantum well.*

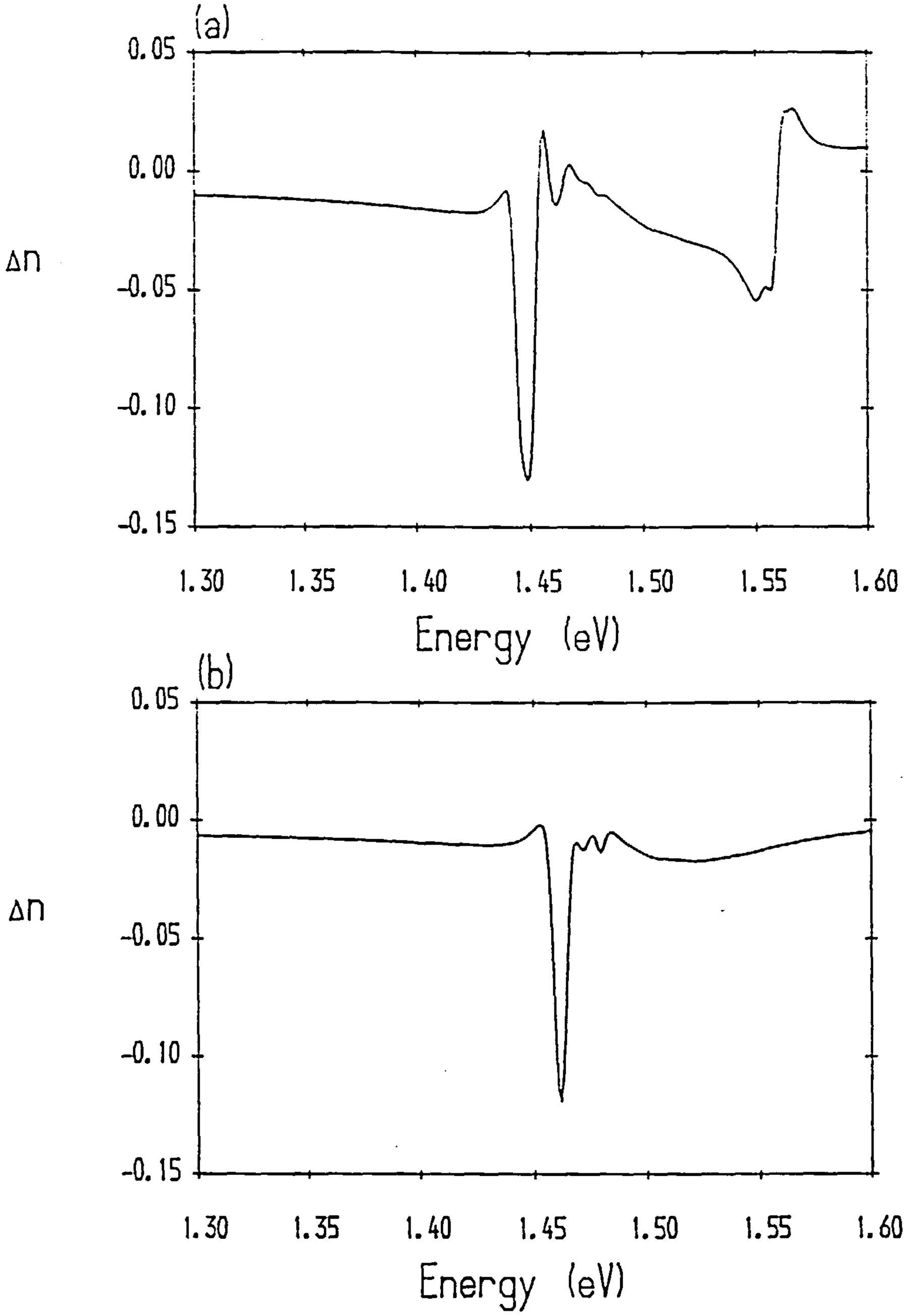

Figure 6.17 *Calculated change in the refractive index of a GaAs-AlGaAs quantum well in the presence of an external electric field for (a) TE polarisation and (b) TM polarisation. The value of the electric field is 45kV/cm, applied normal to the quantum well interfaces. The quantum well structure considered is a symmetric 100Å GaAs-$Al_{0.25}Ga_{0.75}As$ single quantum well.*

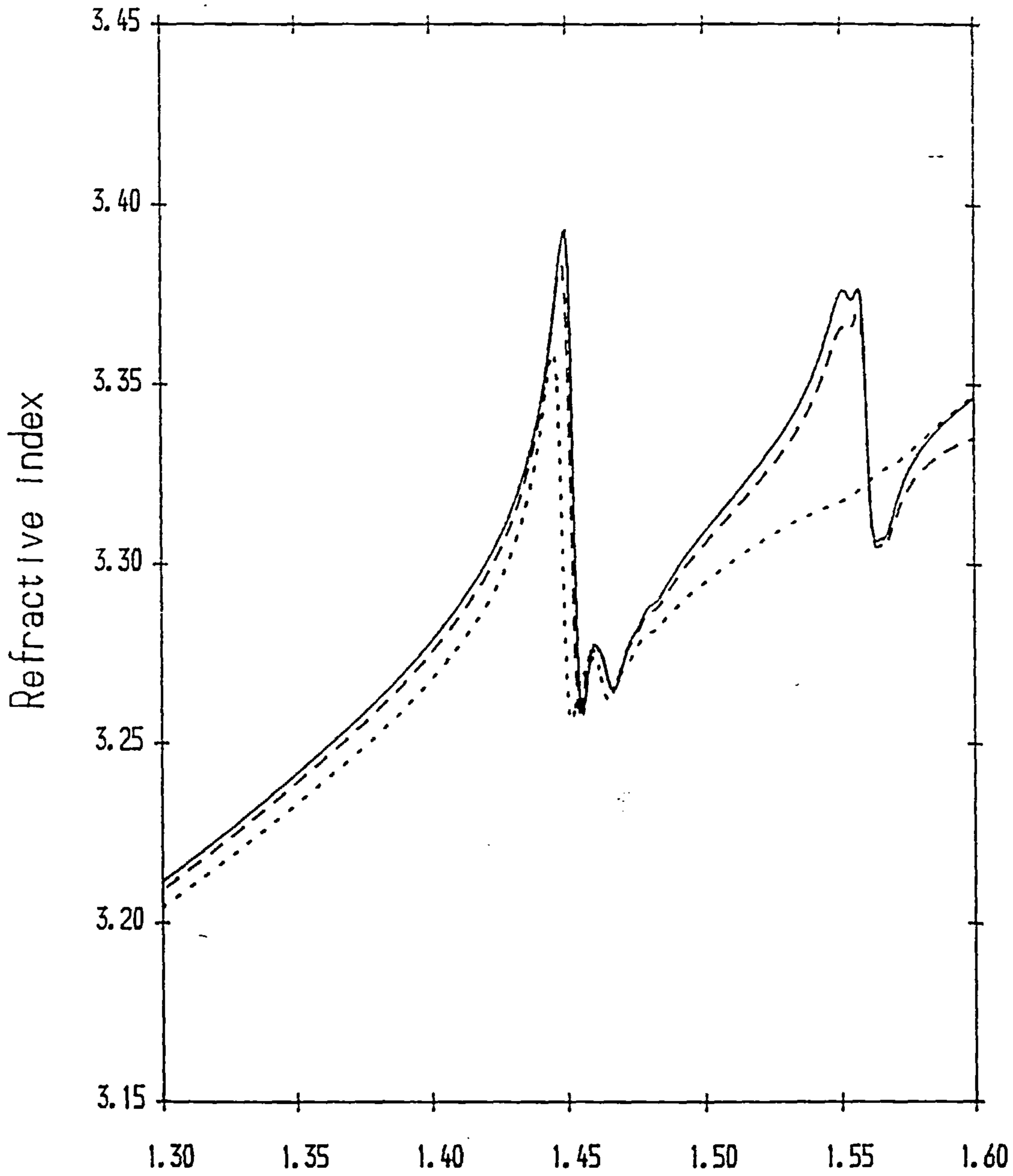

Figure 6.18 *The calculated total index of refraction of a 100Å GaAs-$Al_{0.25}Ga_{0.75}As$ single quantum well structure for TE polarisation and with an external electric field applied perpendicular to the quantum well interfaces. The values of the electric field are F=0kV/cm (solid curve), F=20kV/cm (dashed curve) and F=40kV/cm (dotted curve).*

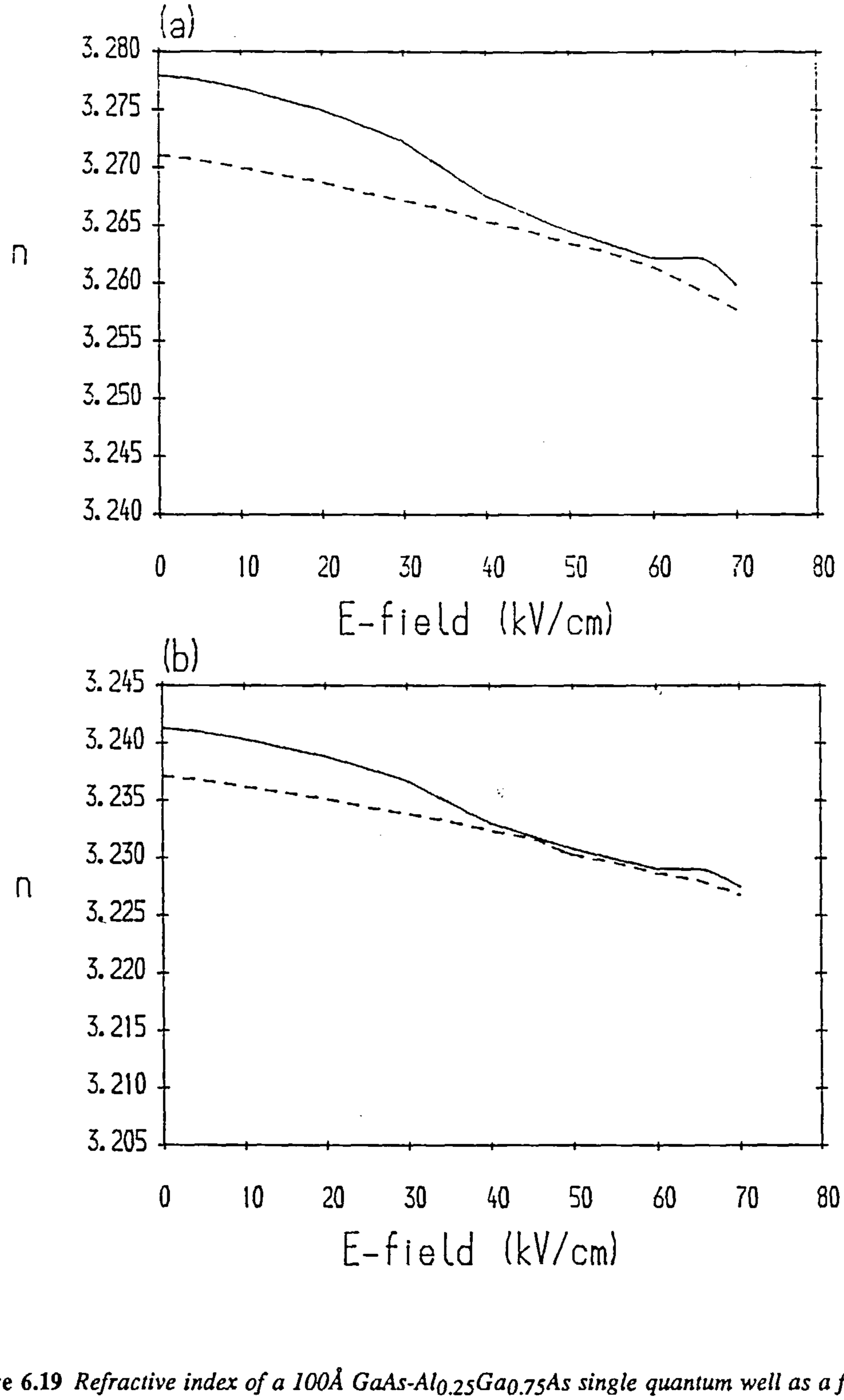

Figure 6.19 *Refractive index of a 100Å GaAs-$Al_{0.25}Ga_{0.75}As$ single quantum well as a function of electric field value for both TE polarisation (solid curves) and TM polarisation (dashed curves). The electric field is applied along the growth direction, perpendicular to the quantum well interfaces. The top graph is for photon energy 1.4eV and the bottom graph is for photon energy 1.35eV.*

values than the ground state excitons derived mainly from the lower quantum well subbands. This is seen by the significant reduction in the HH2-CB2 (1s) oscillator strength at F = 40kV/cm.

The actual variation in the index of refraction with electric field at fixed photon energy $\hbar\omega$ is extremely important for optoelectronic device applications. For the particular example of a symmetric 100Å GaAs-$Al_{0.25}Ga_{0.75}As$ quantum well, the variation in refractive index at the photon energies 1.35eV and 1.4eV is shown in Figure 6.19. Results are given for both TE and TM polarisation. The overall trend is for the refractive index to decrease as the electric field strength is increased. Note, however, that at higher field values the effect of the normally parity-forbidden excitons is clearly seen in this Figure. These particular excitons have vanishing oscillator strength at zero field. At finite electric fields these excitons can acquire finite non-zero oscillator strength due to the now non-zero overlap integral of the contributing hole subband spinor component envelope functions and the conduction subband envelope functions.

The effects of an electric field are also considered in the next section which deals solely with double quantum well structures.

Double quantum wells

In this section we consider the dependence of the index of refraction on double quantum well structure. Both symmetric and asymmetric double quantum wells are considered. In each case the thickness of the central barrier ($Al_xGa_{1-x}As$) region is assumed to be thin enough to allow significant coupling between the two quantum well (GaAs) regions. Typical bound state electronic dispersion in these structures has already been shown in Chapter 5.

To consider the effects of the central barrier thickness on the optical properties of symmetric double quantum well structures two distinct methods are possible. Firstly, the 'total' quantum well width may be kept constant while the central barrier thickness is allowed to vary. By 'total' we mean the sum of the thicknesses of the central barrier and two well regions. Secondly, the individual quantum well widths may be kept constant and the central barrier region allowed to vary in thickness. To compare these structures with single quantum well structures it must be made clear which of the above methods is being used in the comparison. The constancy of both 'total' width and individual quantum well width is illustrated in Figure 6.20. Consider first the case of symmetric double quantum well structures. In all cases the quantum well regions are taken as GaAs and the barrier regions are taken as $Al_{0.25}Ga_{0.75}As$. The first type of structure considered has constant well widths, each well region comprising 14 monolayers of GaAs. The separation between the two quantum well regions is varied from 4 monolayers to 14 monolayers of $Al_{0.25}Ga_{0.75}As$. It is still questionable whether it is strictly possible for 4 atomic monolayers to be defined as $Al_{0.25}Ga_{0.75}As$

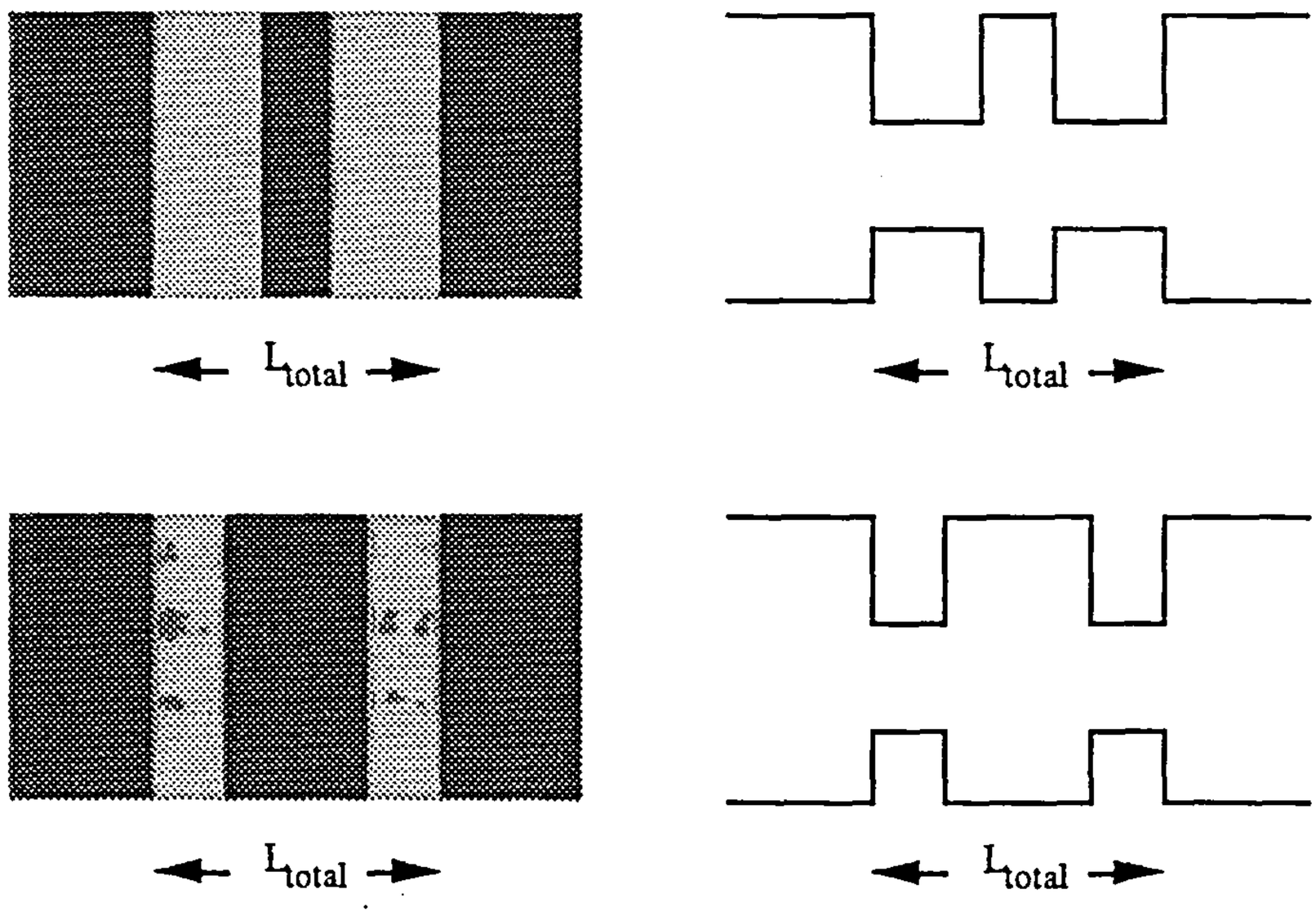

Figure 6.20 (a) *Schematic illustration of double quantum well structures with constant 'total' width (left) and the corresponding confinement potentials (right). The light areas represent the GaAs well regions and the dark areas represent the $Al_{0.25}Ga_{0.75}As$ barrier regions.*

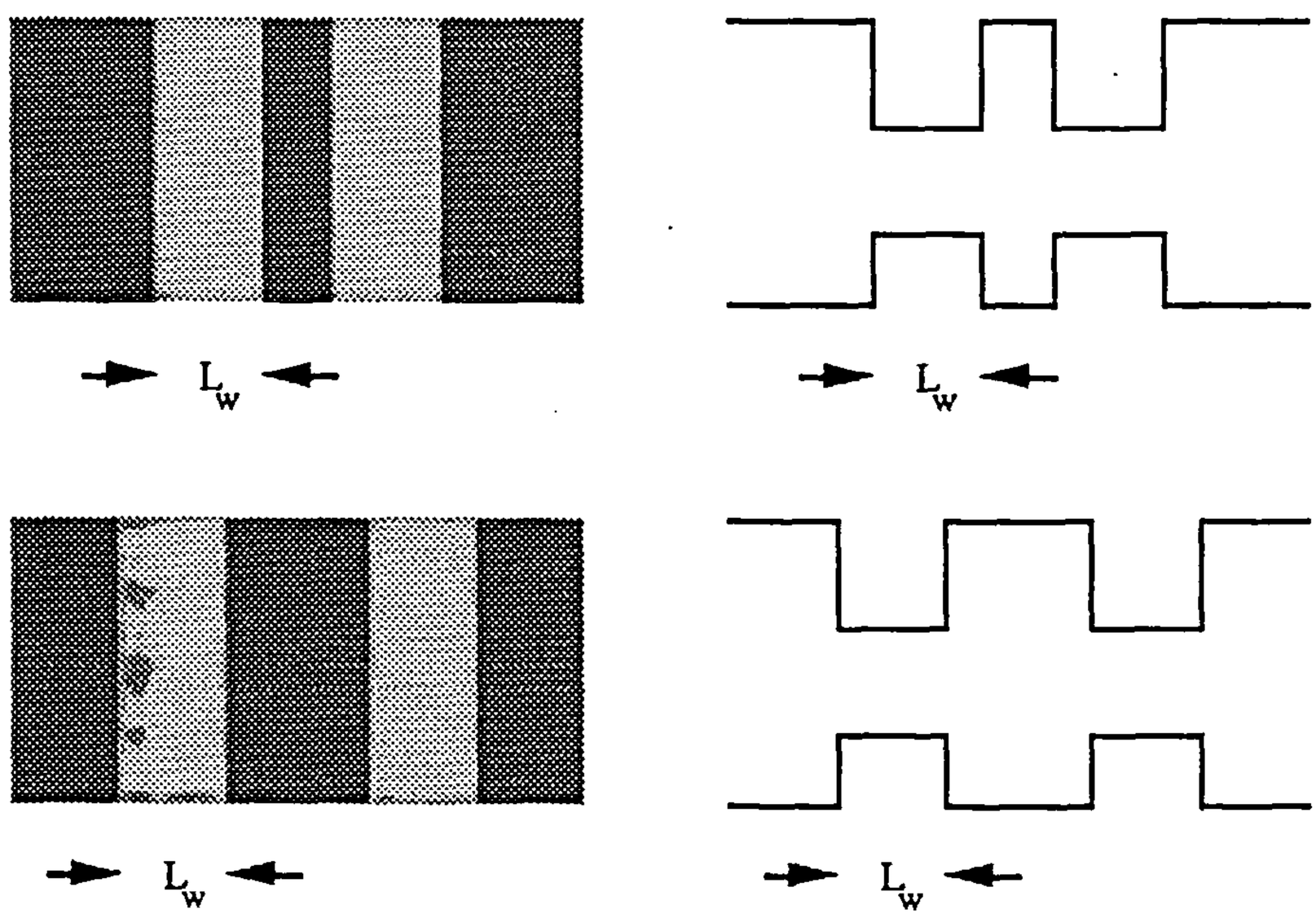

Figure 6.20 (b) *Schematic illustration of double quantum well structures with constant well width (left) and the corresponding confinement potentials (right). In this case the distance between the well regions is varied.*

with in-plane parameters derived from bulk $Al_{0.25}Ga_{0.75}As$. Since this is beyond the brief of this thesis, it is assumed henceforth that the definition is valid for the purpose at hand. The index of refraction for this structure is calculated at the fixed photon energies of 1.4eV and 1.42eV. Although the exciton states are now more properly labelled in terms of the principal contributing eleetron and hole spinor components and the envelope function symmetries (symmetric or antisymmetric), the calculations proceed exactly as before. For the range of structures considered it is found that the order of the first six hole subbands can be given as HH1s, HH1a, LH1s, LH1a, HH2s, HH2a where s(a) denotes symmetric(antisymmetric). The order is different for the asymmetric structures considered later in this section. The calculated TE and TM refractive indices are shown in Figure 6.21. In all cases the values are smaller than a single quantum well of similar total width and barrier composition. Although a single quantum well of width similar to that of one of the wells considered here would in general have a higher refractive index at both of the energies considered here, we find that the largest exciton oscillator strength in the case of the double quantum well is reduced in comparison to that in the case of the single well.

It can be seen from Figure 6.21 that the refractive index decreases with increasing thickness of the central barrier region, at both photon energies considered. In the particular case of TE polarisation this decrease is fairly linear over the range of calculated values. This is particularly useful for tailoring the refraction (and absorption) to a particular value. Although the precise values may differ in the case of a particular real quantum well sample, it is expected that this predicted theoretical trend will also exist in that case.

We find that broadly similar results are obtained in the case of a symmetric double quantum well structure with constant 'total' width $L_{tot} \approx 102$Å (36 monolayers), and with a similar range of central barrier thicknesses. The results for this structure are shown in Figure 6.22. In each case the refractive index is greater for TE polarisation. However, as the central barrier is increased in thickness, the difference in the values for TE and TM polarisation generally becomes less. The only exception to this is the TE-TM difference obtained for a central barrier thickness of 4 monolayers in the case of the first structure. If we assume that the effective-mass model is relevant at small thicknesses then the above result may be due to the fact that at a central barrier thickness of 4 monolayers the electronic dispersion is only slightly perturbed from that of a single quantum well. It is only in the case of thicker barriers that the electronic states may be considered as coupling between 'single well' states.

As the central barrier thickness increases the confined subbands are pushed to higher energies within each potential well. This also reduces the exciton oscillator strengths. The overall effect is a decrease in refractive index as seen in Figures 6.21 and 6.22.

The change in the refractive index due to the application of an external electric field is shown in Figure 6.23 for two different symmetric double quantum well structures, and for an electric field value F = 25kV/cm. In each case the 'total' width is 36 monolayers (≈102Å). The top graph shown

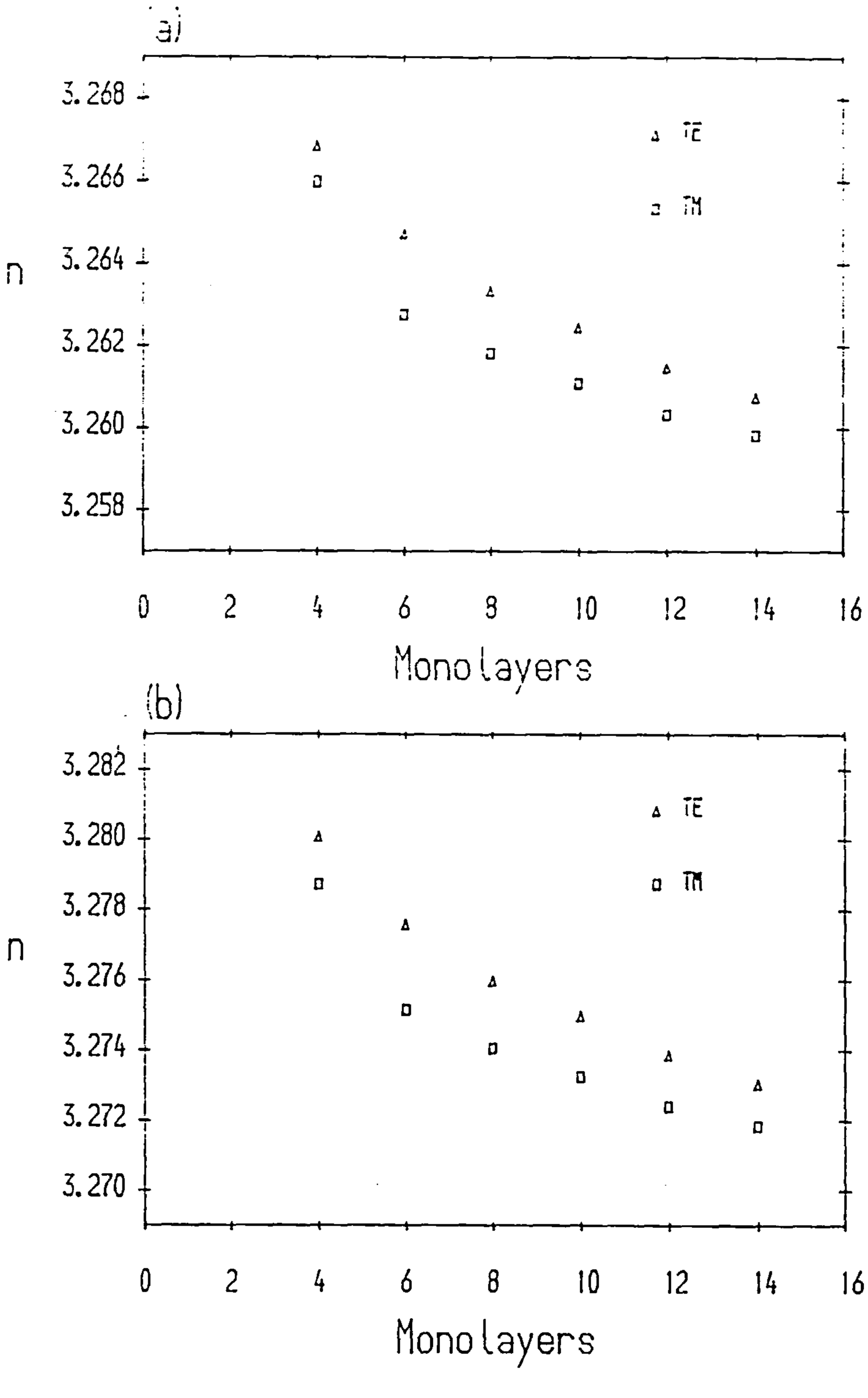

Figure 6.21 *Calculated refractive index of a symmetric double quantum well structure as a function of the central barrier thickness, at photon energies (a) 1.4 eV and (b) 1.42 eV. The 'total' width (the sum of the two wells and central barrier) is 32 monolayers and the central barrier is varied from 4 to 14 monolayers. The well regions are GaAs and each barrier region is* $Al_{0.25}Ga_{0.75}As$.

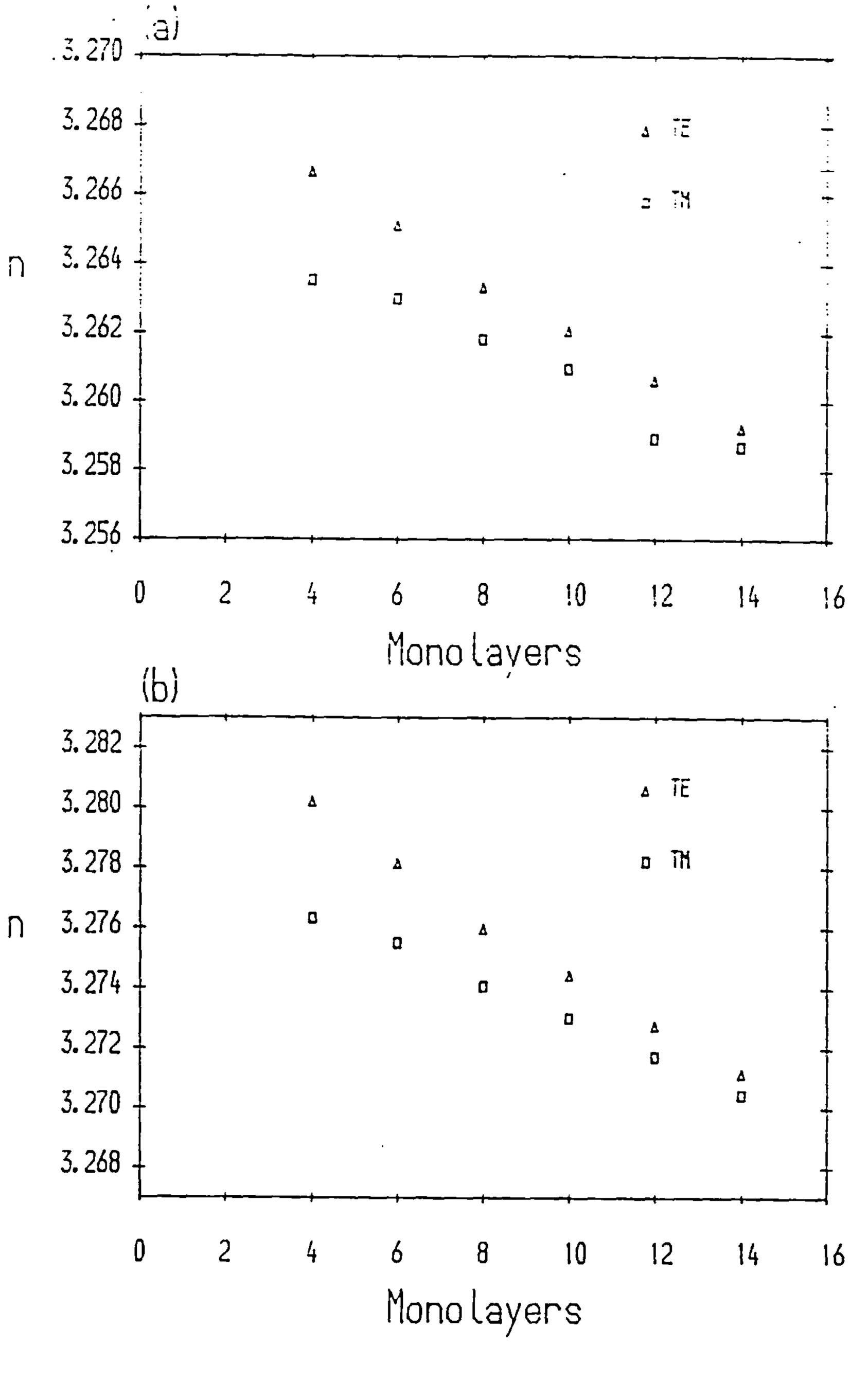

Figure 6.22 *Calculated refractive index of a symmetric double quantum well structure as a function of the central barrier thickness, at photon energies (a) 1.4 eV and (b) 1.42 eV. Each well width is 39.6Å (14 monolayers) and the central barrier is varied from 4 to 14 monolayers. The well regions are GaAs and each barrier region is* $Al_{0.25}Ga_{0.75}As$.

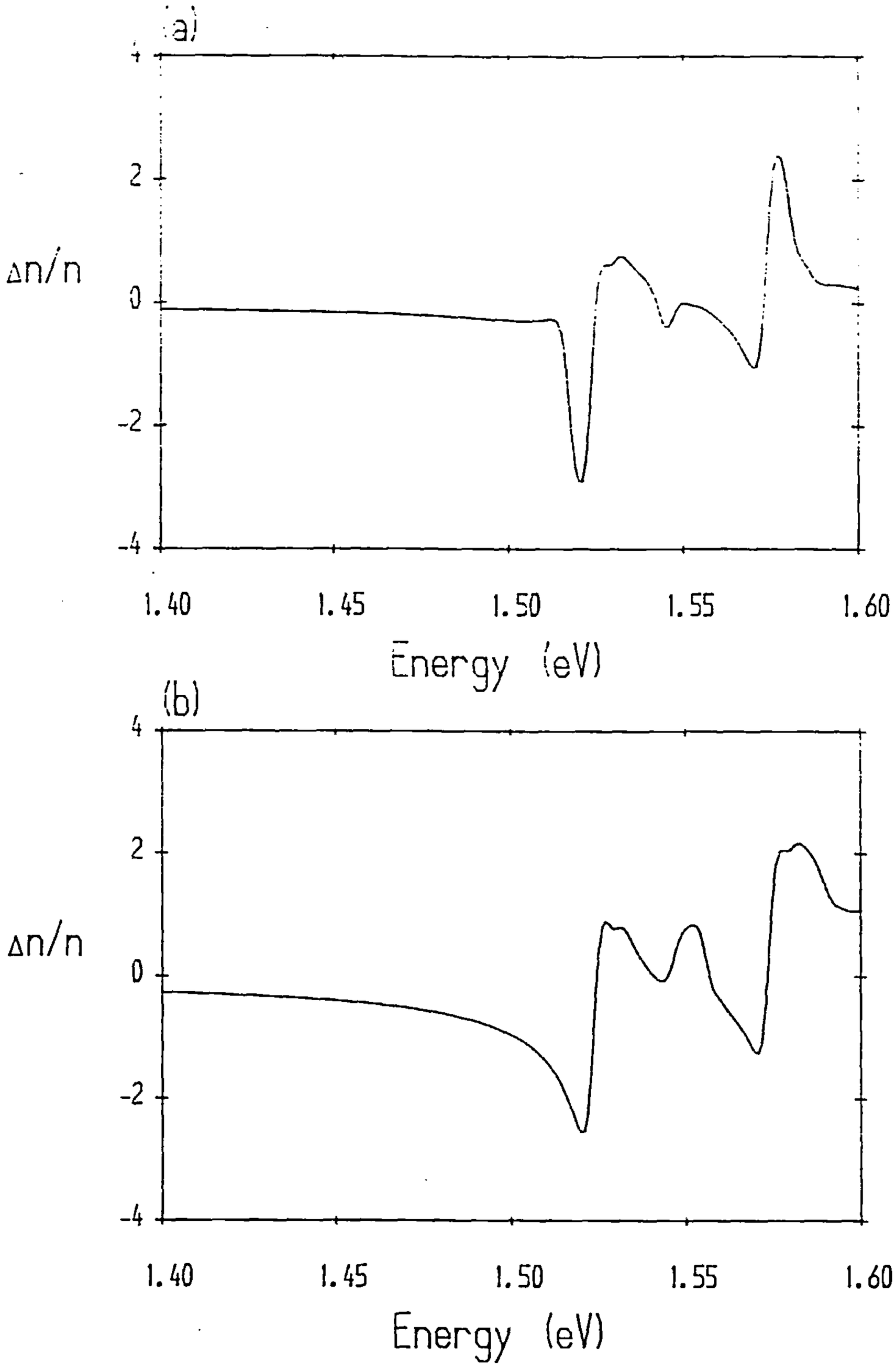

Figure 6.23 *Calculated electric field-induced change in the refractive index, Δn/n (percent), for two different double quantum well structures at field value F = 25kV/cm. Each structure has a 'total' length L_{tot} = 102Å (36 monolayers). Structure (a) is comprised of (15,6,15) monolayers and structure (b) is comprised of (12,12,12) monolayers. The well regions are GaAs and each barrier region is $Al_{0.25}Ga_{0.75}As$.*

in Figure 6.23 is for a structure with a central barrier width $L_B \approx 17$Å. The bottom graph shows the results with $L_B \approx 34$Å. The results in each case are broadly similar. The change in refraction in both cases is significantly larger than that of a single quantum well of width $L_Z \approx 102$Å. This results from the larger reduction in exciton absorption in the case of the double qūantum well structures, discussed in Chapter 5. It was seen in Chapter 5 that a double quantum well structure can offer a significantly enhanced modulation depth in comparison with a single quantum well. The reduction in refraction, however, may reduce waveguiding in an integrated modulation device. The inportance of this also depends on the interaction length (essentially the device length in this case), and may in practice prove to be of little concern.[23]

Consider now the case of asymmetric double quantum wells. In the specific examples which will be considered here, we have one wider well region of exactly twice the width of a narrower well region. As in the case of symmetric double quantum wells we examine two types of structural variations: (a) constant well widths with varying central barrier width and (b) constant 'total' width. For structures (a) the two well widths are taken as 18 monolayers and 9 monolayers of GaAs, with central barrier widths ranging from 4 to 14 monolayers of $Al_{0.25}Ga_{0.75}As$. For structures (b) the 'total' width is taken as 32 monolayers. The widths of the (well 1, barrier, well 2) combinations range from (18,5,9) monolayers to (12,14,6) monolayers.

The calculated TE and TM refractive indices at $\hbar\omega = 1.4$eV and $\hbar\omega = 1.42$eV are shown for structures (a) and (b) in Figures 6.24 and 6.25 respectively. In all cases the refractive index decreases as the central barrier thickness is increased. As the central barrier increases in thickness, this can be considered as effectively reducing the coupling between the 'single well' eigenstates. The interwell coupling effectively reduces the subband confinement energies and the zone-centre effective masses. This tends to increase the contribution to the index of refraction at a particular below-band gap energy from both the band-to-band and excitonic transitions. This applies to both symmetric and asymmetric double quantum wells.

For a given 'total' thickness and central barrier width, the asymmetric structure can have a different valence subband ordering and different subband confinement energies and dispersion from that of a symmetric structure. This leads to the two structures having different refractive indices at a particular energy. It is also seen from these Figures that the TE-TM anisotropy in the refractive index is enhanced in the asymmetric structure compared to the symmetric structure. For example, consider the symmetric well results of Figure 6.21 (both wells = 14 monloayers) and the asymmetric results of Figure 6.24 (wider well = 18 monolayers, narrower well = 9 monolayers). At $\hbar\omega = 1.4$eV and a central barrier thickness of 8 monolayers, the TE-TM anisotropy for the symmetric structure is less than 0.2% while that for the asymmetric structure is 0.5%. Increasing the central barrier thickness to 12 monolayers gives an anisotropy of 0.1% for the symmetric structure and still about 0.5% for the asymmetric structure. This comparison holds for all of the symmetric and asymmetric structures considered here. One important factor in this increased TE-TM anisotropy observed in the

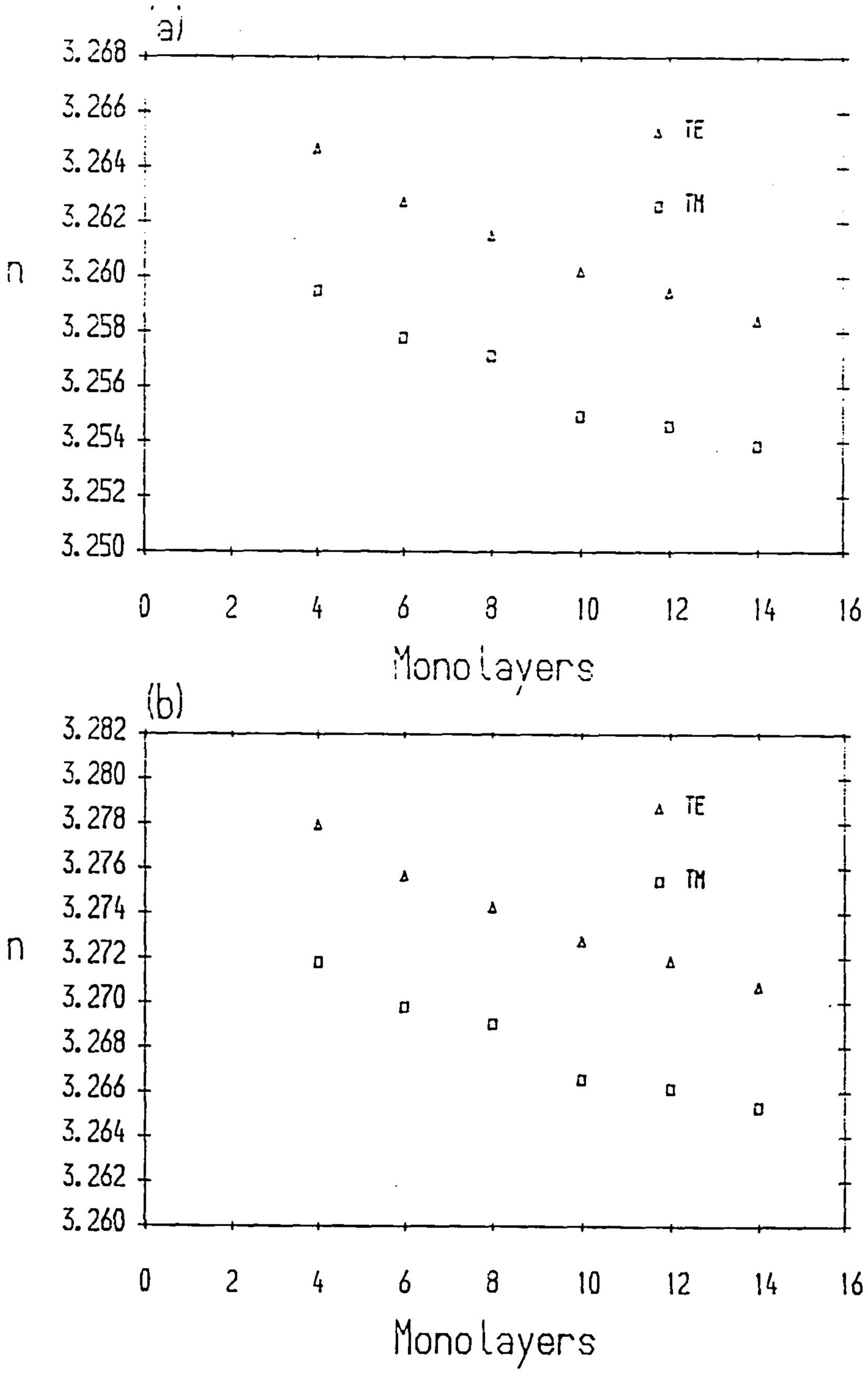

Figure 6.24 *Calculated TE and TM refractive indices of an asymmetric double quantum well structure as a function of the central barrier thickness, at photon energies (a) 1.4 eV and (b) 1.42 eV. The well widths are 18 monolayers (≈ 50.9Å) and 9 monolayers (≈ 25.4Å). The central barrier thickness is varied from 4 to 14 monolayers. Both of the well regions are GaAs and each of the barrier regions is* $Al_{0.25}Ga_{0.75}As$.

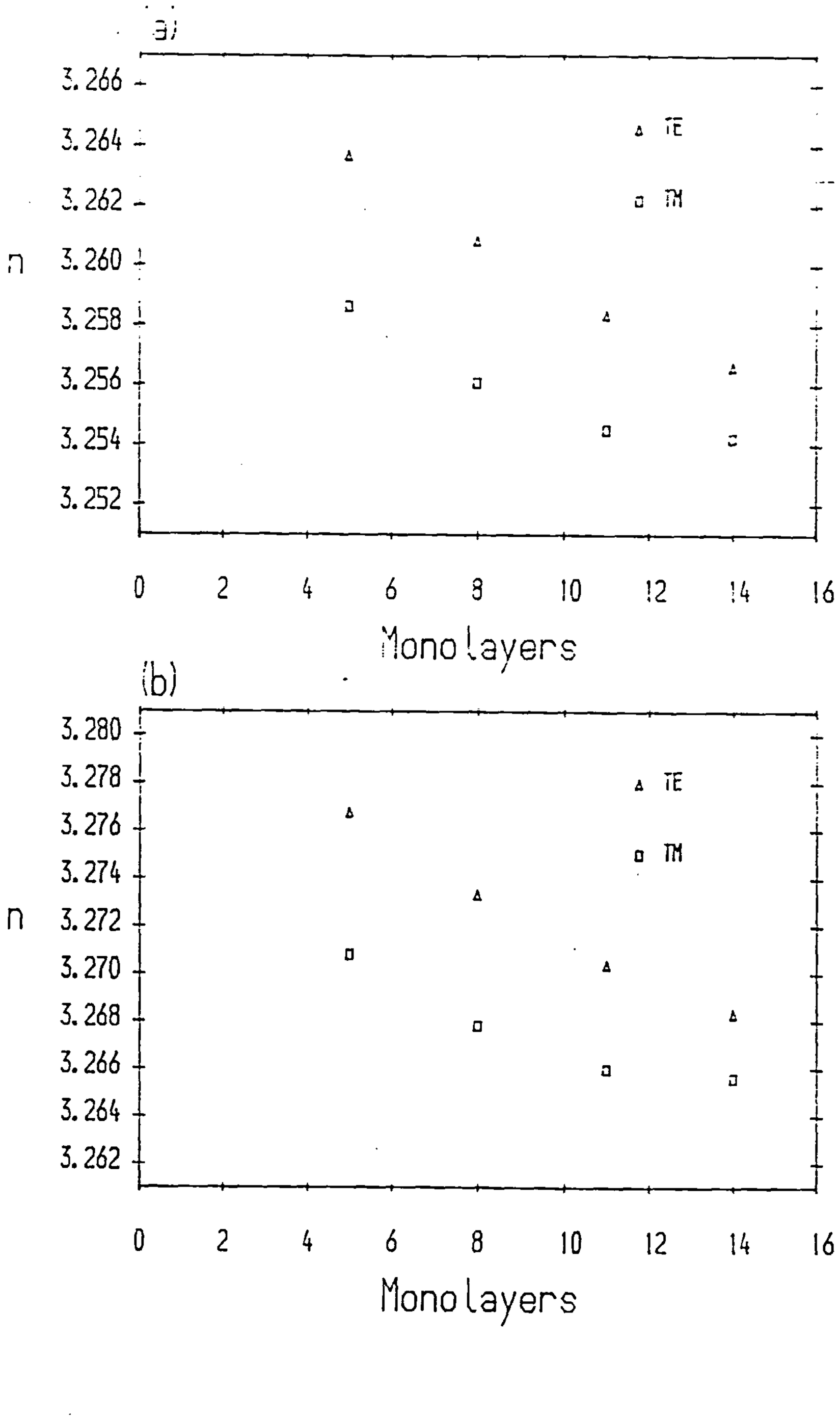

Figure 6.25 *Calculated TE and TM refractive indices of an asymmetric double quantum well structure as a function of the central barrier thickness, at photon energies (a) 1.4 eV and (b) 1.42 eV. The 'total' width is 32 monolayers (≈ 90.4Å). The width of the wider well is twice that of the narrower well. The central barrier thickness varies from 5 to 14 monolayers. Both of the well regions are GaAs and each of the barrier regions is* $Al_{0.25}Ga_{0.75}As$.

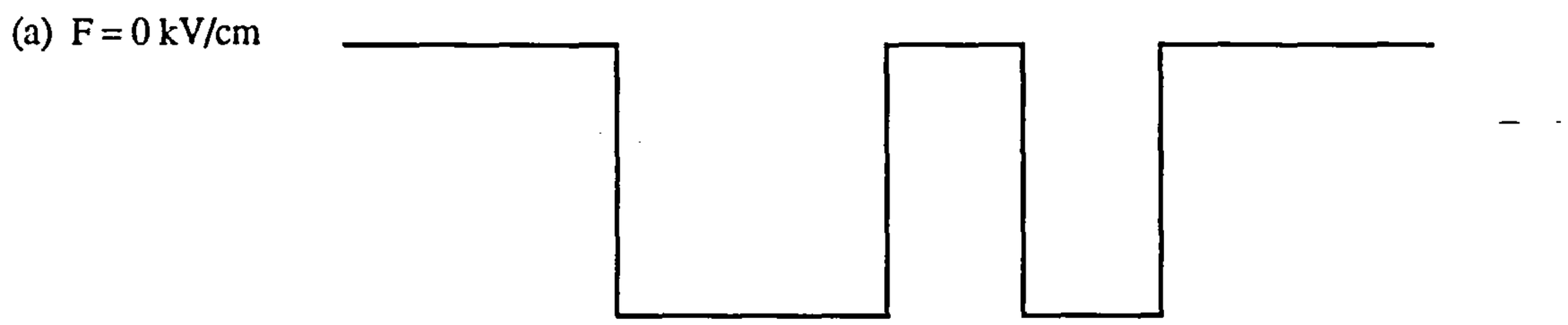

Figure 6.26 *Schematic illustration of the conduction band edge confinement potential of a (20,10,10)-monolayer asymmetric GaAs-$Al_{0.25}Ga_{0.75}As$ double quantum well structure in the presence of an external electric field applied along the growth axis (z-direction). Different electronic dispersion is obtained for the electric field values +25kV/cm and -25kV/cm, which leads to different field-induced refractive index changes. The calculated refractive index changes are shown in Figure 6.27. The different dispersion also results in different overlap integrals between the conduction subbands and valence subbands, which gives rise to different exciton oscillator strengths in each case.*

asymmetric structures is the fact that of the first four confined valence subbands only one has 'light-hole' character at the zone centre. In the symmetric structures considered two of these four subbands were 'light-hole' subbands. Since only a LH subband can lead to a (1s) exciton with non-zero TM oscillator strength this contributes to the larger TE-TM anisotropy seen in the case of the asymmetric double quantum well structures.

It was seen in Chapter 5 that the direction of electric field is important in the case of asymmetric quantum wells. The effect of an electric field of strength F = 25kV/cm on the conduction band edge confinement potential is illustrated schematically in Figure 6.26. The asymmetric structure considered consists of (20,10,10) monolayers. Two different directions of electric field are defined here as +ve and -ve. The change in refraction ($\Delta n/n$) with respect to the zero-field case, for each of these field directions is shown in Figures 6.27 (a) and (b) for the +ve and -ve field directions respectively. The structure here is different from that seen in the previous single well and symmetric double well results. The +ve field direction shows the smallest difference indicating that for this field direction the overlap integrals of the conduction and valence subbands are reduced less than for the -ve field direction.

It was noted in Chapter 5 that for small electric field values the exciton oscillator strengths of the normally parity-allowed excitons can actually increase for this field direction in asymmetric quantum well structures. This occurs since the position expectation value of each quantum well subband $\langle z_i \rangle = \langle \psi_i^* | z | \psi_i \rangle$ can differ for each subband in asymmetric structures (not only double quantum wells). The values of $\langle z_i \rangle$ for $k_{||} = 0$ are given below in Table 6.7 for the (20,10,10)-monolayer double well structure. The position z = 0 is set to the midpoint between the two outermost interfaces. Small values of electric field can increase the overlap integrals $\langle \psi_c^* | \psi_v \rangle$ resulting in an enhancement of the exciton oscillator strengths. In single symmetric quantum well structures the oscillator strength of each parity-allowed exciton generally decreases with increasing electric field, regardless of the electric field strength.

Table 6.7 *Quantum confined subband position expectation values* $\langle z_i \rangle = \langle \psi_i^* | z | \psi_i \rangle$ *in a (20,10,10) monolayer asymmetric GaAs-*$Al_{0.25}Ga_{0.75}As$ *double quantum well for several values of electric field, applied along the growth axis.*

Subband	0kV/cm	5kV/cm	10kV/cm	-5kV/cm	-10kV/cm
HH1	-28.04 Å	-27.62 Å	-27.20 Å	-28.45 Å	-28.85 Å
HH2	31.32	33.45	34.65	27.19	18.92
HH3	-22.91	-24.97	-26.10	-18.87	-10.69
LH1	-27.16	-26.69	-26.21	-27.63	-28.09
CB1	-27.19	-27.50	-27.80	-26.89	-26.58

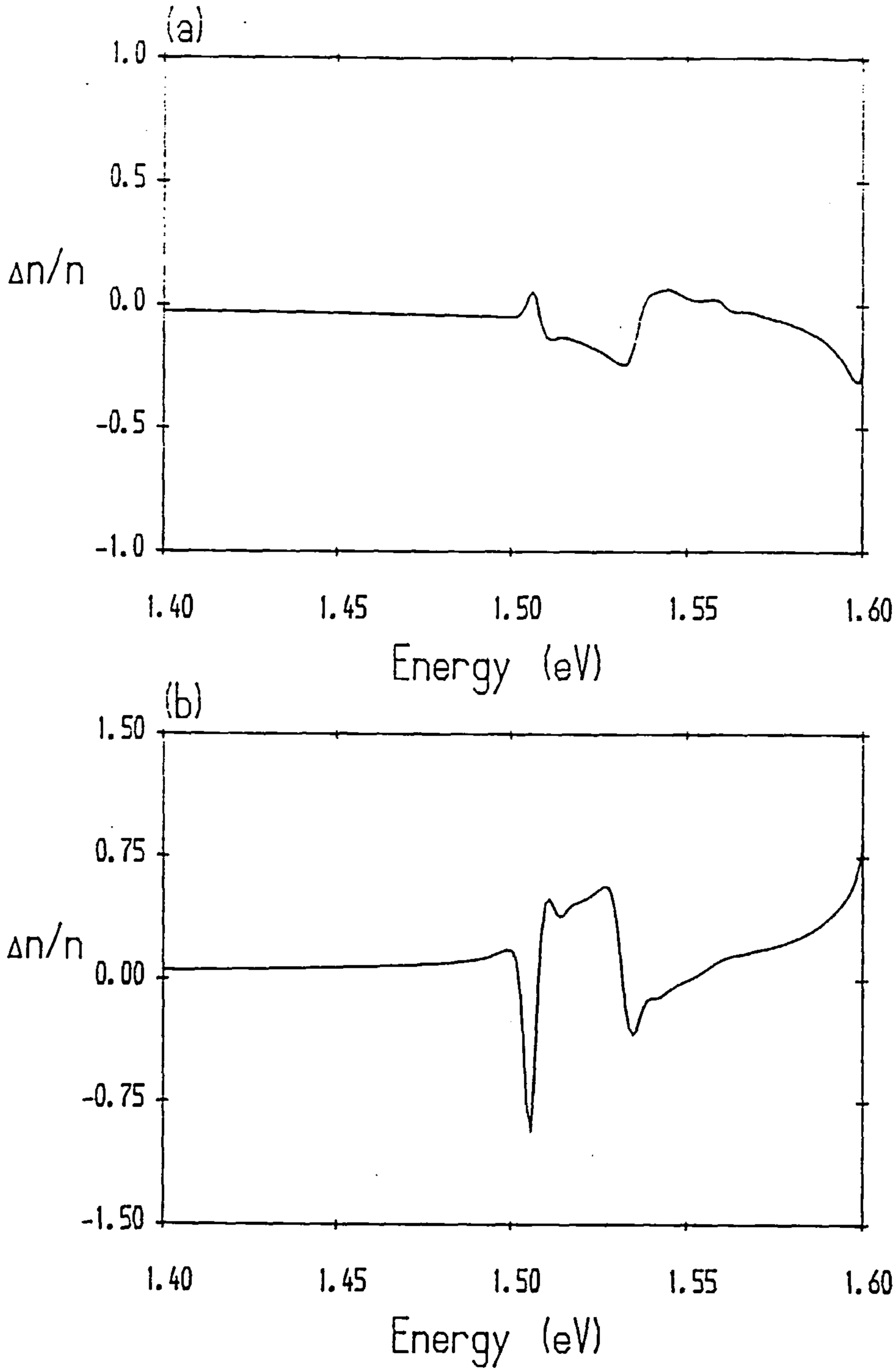

Figure 6.27 *Calculated electric field-induced change in the refractive index, Δn/n (percent), of a (20,10,10)-monolayer GaAs-AlGaAs asymmetric double quantum well structure. The values of the electric field are (a) +25kV/cm and (b) -25kV/cm. Both of the well regions are GaAs and each barrier region is* $Al_{0.25}Ga_{0.75}As$.

In general the values of refractive index obtained for single quantum well and double quantum well structures are lower than the values obtained for longer period multiple quantum well structures.[16] In the particular case of multiple quantum wells and superlattices the refraction is seen to be fairly similar to the averaged equivalent bulk alloy.

Experimental measurements of the refractive index in superlattice structures have recently been published.[24,25] The bulk-like values obtained are readily apparent. For the particular case of a GaAs-$Al_{0.25}Ga_{0.75}As$ single symmetric quantum well the refractive index at 1.4eV is seen to peak at a well width between 50Å and 75Å. The maximum value obtained in the vicinity of the HH1-CB1 exciton transition energies reaches a maximum of around $n = 3.56$ within this range of well widths. The experimental results[24,25] and theoretical results[16] obtained for multiple quantum well structures with well widths within the range 50Å to 75Å obtain a maximum value, within a similar spectral region, of around $n = 3.57$ to $n = 3.59$, which is slightly larger than the values obtained for single quantum well structures.

Intensity-dependent saturation

In this section we briefly consider the effect of saturation on the index of refraction. The structure considered is a 100Å GaAs-$Al_{0.25}Ga_{0.75}As$ single quantum well. The band-to-band contributions to the change in refraction can easily be obtained from the results given in Chapter 5, using the density-matrix theory which incorporates phase-space filling. In that case the change in absorption of the band-to-band transitions in the presence of an intense optical field was obtained using standard density-matrix theory. This model has been previously used to obtain the intensity-dependent changes in the refractive index in bulk semiconductors[26,27] with the assumption of completely parabolic conduction and valence band electronic dispersion.

To obtain the changes in the refraction due to the excitonic absorption we adopt a screening model similar to that discussed in Chapter 5. Justification for this approach has been given previously and need not be repeated here. The steady-state population due to band-to-band transitions is straightforward to obtain from the density-matrix equations. It is actually subsumed within the density-marix formalism. Note that this involves spectral integration and is not obtained from the simple formula $N = \alpha(\omega)I(\omega)T_1/\hbar\omega$. The spectral integration is transformed to a $k_{||}$-space integration as usual. The relaxation time T_1 is assumed to be 10nsec throughout, independent of carrier density and in-plane wavevector. The above simple expression for N is used however to estimate the additional free carrier density due to the exciton absorption. This assumes that the exciton states are rapidly thermalised, the process assisted by the existing unbound electrons and holes in the conduction and valence subbands. The above approach is therefore a reasonably simple

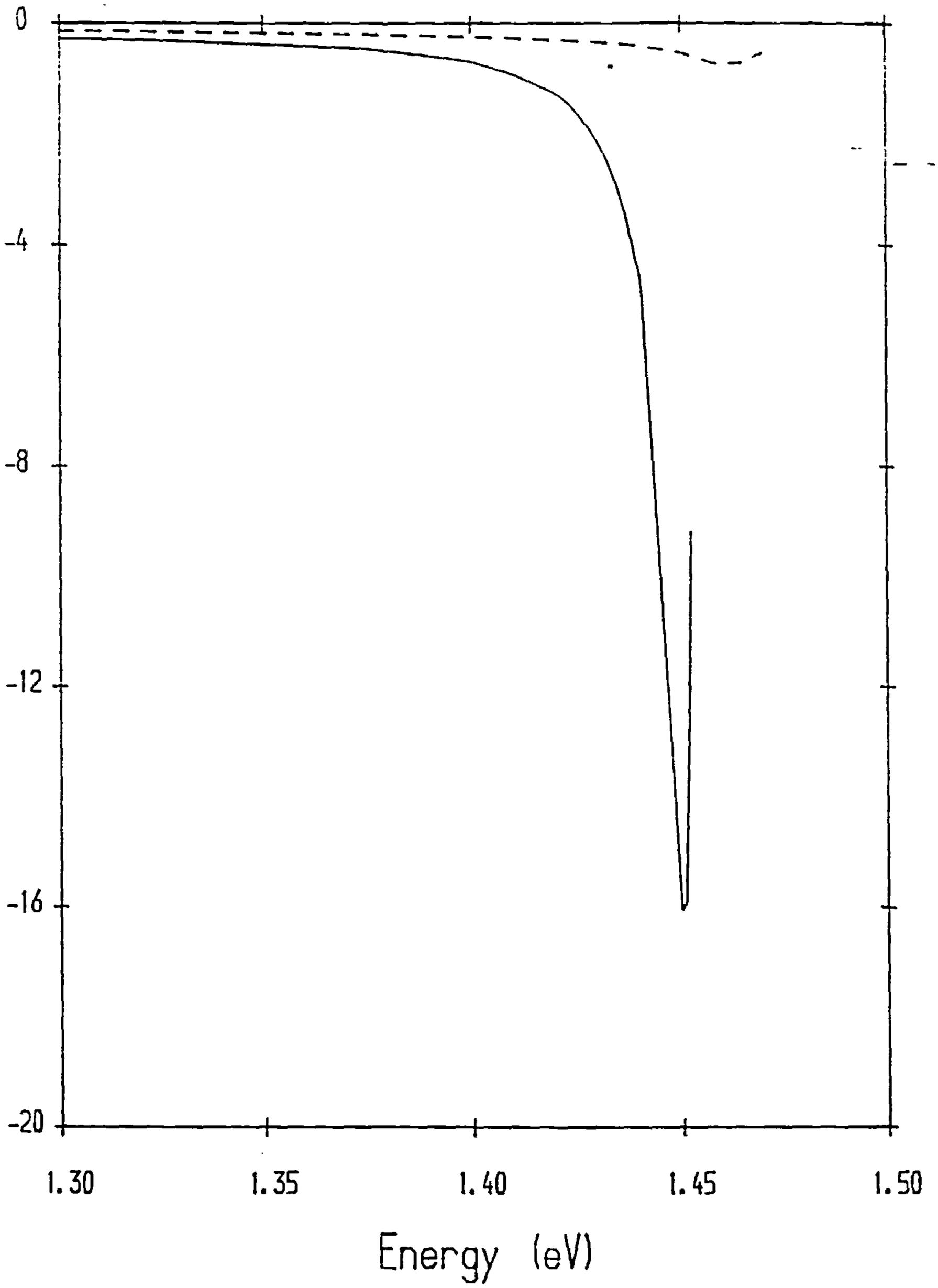

Figure 6.28 *Calculated intensity-dependent refractive index contribution $n_2(\omega)$ for a 100Å single GaAs-$Al_{0.25}Ga_{0.75}As$ quantum well structure for TE polarisation. The optical field intensity is 50W/cm^2 and the results are obtained for each value of photon energy in the range 1.3eV to 1.5eV. The relaxation time T_1 has been taken as 10nsec, independent of both carrier density and in-plane wavevector. The values of $n_2(\omega)$ obtained are within the range of values given in Ref. 28 (and references contained within).*

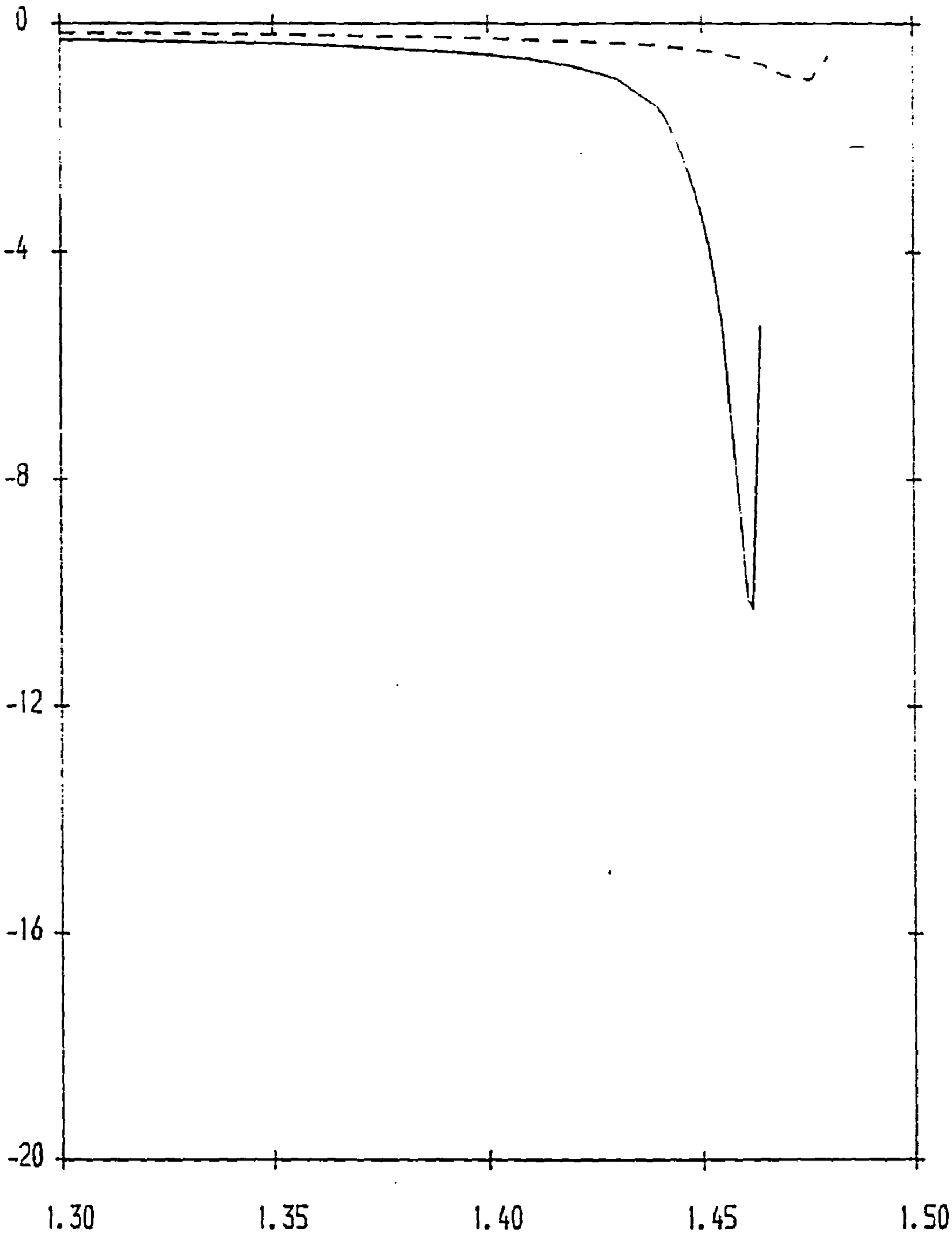

Figure 6.29 *Calculated intensity-dependent refractive index contribution $n_2(\omega)$ for a 100Å single GaAs-$Al_{0.25}Ga_{0.75}As$ quantum well structure for TM polarisation. The optical field intensity is 50W/cm^2 and the results are obtained for each value of photon energy in the range 1.3eV to 1.5eV. The relaxation time T_1 has been taken as 10nsec, independent of both carrier density and in-plane wavevector.*

approximation which neglects incorporation of finite exciton lifetimes. However, qualitative results are easily obtained within this approximate scheme since the technical details involved are fairly trivial. The results obtained for an optical field intensity of $50W/cm^2$ are shown in Figures 6.28 and 6.29 for TE and TM polarisation respectively. Also shown in these Figures is the separate band-to-band contribution to $n_2(\omega)$ when the exciton absorption is completely neglected. This contribution is not significantly greater than that obtained in bulk GaAs.[28]

In the particular case of TE polarisation (Figure 6.28) the maximum value of n_2 is obtained at a photon energy of 1.45eV and is $n_2 = -1.6x10^{-3}cm^2/W$. The band-to-band contribution at the same photon energy is only about 4% of this value. The results for TM polarisation are rather less and reach a maximum value of $n_2 = -1.1x10^{-3}cm^2/W$ at a photon energy of 1.47eV.

The results which we obtained during the course of this work were for a range of optical field intensities $I(\omega)$. From $I = 10W/cm^2$ to $I = 250W/cm^2$ (the range considered) broadly similar magnitudes for the maximum value of n_2 were obtained in all cases. The saturation is therefore roughly linear for optical intensities within this range of values.

References

1 K.B. KAHEN, J.B. LEBURTON and K. HESS, Superlattices and Microstructures **1**, 289 (1985)

2 J.P. LEBURTON and K. HESS, Journal of Vacuum Science and Technology **B1**, 415 (1983)

3 K.B. KAHEN and J.P. LEBURTON, Applied Physics Letters **47**, 508 (1985)

4 J.P. LEBURTON, K. HESS, N. HOLONYAK, J.J. COLEMAN and M. CAMRAS, Journal of Applied Physics **54**, 4230 (1983)

5 R. TSU and L. IORATTI, Superlattices and Microstructures **1**, 295 (1985)

6 B. JENSEN and A. TORABI, IEEE Journal of Quantum Electronics **QE-19**, 877 (1983)

7 B. JENSEN and A. TORABI, IEEE Journal of Quantum Electronics **QE-19**, 448 (1983)

8 B. JENSEN and A. TORABI, Journal of Applied Physics **54**, 2030 (1983)

9 H. YAMAMOTO, M. ASADA and Y. SUEMATSU, Journal of Lightwave Technology **6**, 1831 (1988)

10 Y. KAN, H. NAGAI, M. YAMANISHI and I. SUEMUNE, IEEE Journal of Quantum Electronics **QE-23**, 2167 (1987)

11 S.W. KOCH, S. SCHMITT-RINK and H. HAUG, Solid State Communications **38**, 1023 (1981)

12 S.W. KOCH, S. SCHMITT-RINK and H. HAUG, Physica Status Solidi **b106**, 133 (1981)

13 B. JENSEN and A. TORABI, Journal of the Optical Sociey of America **B2**, 1395 (1985)

14 D.E. ASPNES, S.M. KELSO, R.A. LOGAN and R. BHAT, Journal of Applied Physics **60**, 754 (1986)

15 D.S. CHEMLA, D.A.B. MILLER, P.W. SMITH, A.C. GOSSARD and W. WEIGMANN, IEEE Journal of Quantum Electronics **QE-20**, 265 (1984)

16 A.T. MENEY, Superlattices and Microstructures **11**, 47 (1992)

17 R. EPPENGA, M.F.H. SCHUURMANS and S. COLAK, Physical Review **B36**, 1554 (1987)

18 J.S. BLAKEMORE, Journal of Applied Physics **53**, R123 (1982)

19 M. CARDONA and D.L. GREENAWAY, Physical Review **125**, 1291 (1961)

20 J.M. LUTTINGER and W. KOHN, Physical Review **97**, 869 (1955)

21 *Numerical Data and Functional Relationships in Science and Technology*, Volume 17 of Landolt-Börnstein, edited by O. MADELUNG (Springer, Berlin, 1982)

22 R. ENDERLEIN and R. KEIPER, Physica Status Solidi **23**, 127 (1967)

23 T. WOLF, C.L. SHIEH, R. ENGELMANN, K. ALAVI and J. MANTZ, Applied Physics Letters **55**, 1412 (1989)

24 G.K. HUBLER, C.N. WADDELL, E.P. DONOVAN and J.M. ZAVADA, Optical and Quantum Electronics **23**, S883 (1991)

25 P. BLOOD, E.D. FLETCHER, C.T. FOXON, B.N. MURDIN and D.E. LACKLISON, Optical and Quantum Electronics **23**, S895 (1991)

26 B.S. WHERRETT and N.A. HIGGINS, Proceedings of the Royal Society of London **A379**, 67 (1982)

27 B.S. WHERRETT, Proceedings of the Royal Society of London **A390**, 373 (1983)

28 See for example: H.M. Gibbs, *Optical Bistability: Controlling Light with Light* (Academic Press, New York 1985)

MISSING

PAGE/PAGES

HAS NO

CONTENT

7 Conclusions and Future Work

In this thesis we have constructed a theoretical model for the refractive index in quantum well structures in the vicinity of the Γ_6-Γ_8 band gap. The model includes the Γ_{6c}, Γ_{5c} and Γ_{5v} states, and also allows for inclusion of the electronic states at the X and L points. Additionally, the ground state and excited state excitons have also been explicitly included within the theoretical model. The exciton model employed takes into account the Coulomb coupling between different exciton states. The results obtained are in good agreement with published experimental results.[1]

The effects of band filling and screening have both been incorporated, allowing the intensity-dependent index of refraction to be obtained. Additionally the effects of external perturbations and of different material parameters have also been examined. All of the necessary theoretical detail has been presented so that it may be accessible to those with no prior knowledge of this field. As such it should also be directly accessible to experimentalists.

By concentrating on a multi-band effective mass approach it should be possible to apply the model directly to the problem of layer-intermixing or disordering in quantum well structures with the

introduction of suitable position-dependent material parameters. This was considered to be an essential requirement for a 'follow-on'project. In actual fact this work has already started since the research for this thesis was completed.[2,3]

The ability to accurately calculate the frequency-dependent index of refraction in quantum well structures is important in the case of optoelectronic devices which contain a quantum well or multiple quantum well layer. In particular the refraction at near-band gap frequencies is strongly dependent on an accurate knowledge of the excitonic wave functions, which have been obtained in this thesis.

As mentioned above, one particular example of future work concerns the fabrication of optoelectronic devices with an imbedded quantum well or multiple quantum well layer. To obtain the polarisation within this layer, accurate knowledge of the quantum confined electronic dispersion is required. Additionally, at photon energies near the fundamental band gap it is also necessary to have an accurate description of the quantum well exciton states. It is intended that the theory presented in this thesis will be straightforwardly incorporated into the above work, which is in fact currently in progress. In this respect it is not necessary to restrict attention to the (Ga,Al)As system. Many III-V and II-VI binary, ternary and quaternary compounds are currently available which can be used to construct lattice-matched or strained-layer quantum well structures. New materials offer different optical properties by virtue of their different energy gaps and electronic dispersion. A wide range of quantum well and optoelectronic devices can therefore be fabricated with varying operating wavelengths. The application of the theory in this thesis to these systems should involve no more than altering the appropriate material parameters where necessary. The work involved in altering existing numerical codes for different material parameters is very little indeed.

Also mentioned above is the particular example of layer-intermixed structures. The intermixing can be viewed as a disordering process initiated by interdiffusion. This can be achieved by annealing or laser irradiation, with or without the presence of impurity implantation. This implantation can enhance the diffusion process[4-7] but is not strictly required to achieve the interdiffusion of, for example, gallium and aluminium in (Ga,Al)As heterostructures. Comparison of the published experimental work and the published theoretical work shows that the diffusion process can be considered as obeying a standard Fick-type law,[8] which leads to a variation in the material parameters.

Considerable research has already been carried out modelling the electronic and optical properties of layer-intermixed (Ga,Al)As quantum wells and multiple quantum wells by directly applying the theoretical models in this thesis.[2,3] These studies incorporate diffusion along the growth axis and lead to position-dependent parameters substituted into the Hamiltonians. Accurate diffusion coefficients have been calculated in agreement with published experimental results.[7] Additionally, the absorption edge shifts and changes in refraction can also be obtained in good agreement with published experimental studies. It is expected that this work will be continued and

applied to other material systems, in particular InGaAsP-based quantum well structures.

Throughout this thesis the method of calculation applied to each Hamiltonian has been the finite-difference method. In the case of decoupled conduction-valence Hamiltonians the method used was a relaxation method. In the case of the 8x8 **k·p** Hamiltonian, the block-diagonalised 4x4 Hamiltonians were written as explicit finite difference equations and solved by an eigenvalue method. During the early stages of this project several methods of solution were considered and fully implemented for the valence band dispersion. These included:

1 Analytic expressions for the eigenvalues and eigenvectors of the 4x4 Luttinger equation and block-diagonalised 3x3 versions of the 6x6 Luttinger-Kohn equation

2 Finite-difference methods - both relaxation and eigenvalue techniques

3 Transfer Matrix methods[9]

4 Bond-orbital model[10,11] - essentially a tight-binding method on an FCC lattice which is forced to agree with a **k·p** matrix to second order in a Taylor expansion

5 Expansion of the wave functions in terms of zone-centre solutions.

In method 1 the resulting 16x16 homogeneous matrix equation (i.e. we assume use of the 4x4 Luttinger Hamiltonian) which requires to be solved for the four-component envelope function solutions can be reduced to an 8x8 matrix by considering the reflection symmetry of a symmetric single well structure. The method is inappropriate in the case of layer-disordering and the application of an electric field. Methods 3 and 4 are comparable to the finite-difference techniques (method 2) in accessibility, but are rather more involved at a computational level. In method 5 the zone-centre solutions can be easily obtained since each spinor component is uncoupled at $k_{||} = 0$ for symmetric growth directions. However, it was found that to obtain accuracy comparable to finite-difference methods at a general non-zero $k_{||}$-value, a considerable number of zone-centre states (typically at least 15) must be included in the expansion.

The interest in layer-intermixed structures leads to the requirement of methods which can cope with arbitrary potential profiles and which therefore disregard any simplifications arising due to reflection symmetry in symmetric single quantum well structures. Further, the adoption of method 2 thus allows parabolic and triangular quantum wells to be considered in a manner analogous to rectangular quantum well profiles with no difference in the computational approach. Extension to graded barrier structures is similar and can also be easily incorporated. A disadvantage of finite-difference techniques is the large matrix size required for numerical accuracy. This can be avoided if only two or three eigenvalues are required, but this is generally not the case. Large matrices, however, do not imply any inherent computational difficulty. The only implication is a longer computation time.

Finite-difference methods are in general simple and can be easily implemented. The precise

details of these techniques are well known and can be found in most good introductory texts on numerical methods.

Throughout this thesis a constant intraband relaxation time has been incorporated within the density-matrix theory, and which assumes a Lorentzian broadening. A more accurate model could be obtained by considering the phase damping due to carrier-carrier and carrier-phonon scattering. Recent attempts to do this have resulted in widely different values of the dipole transition linewidth.[12,13] The intraband scattering time used in this thesis is about midway in value between the two theoretical estimates obtained in Refs. 12 and 13. Further work is required in this area in order to accurately model and calculate the non-Markov relaxation processes in low-dimensional semiconductor devices.

References

1 T. WOLF, C.L. SHIEH, R. ENGELMANN, K. ALAVI and J. MANTZ, Applied Physics Letters **55**, 1412 (1989)

2 A.T. MENEY, Superlattices and Microstructures **11**, 47 (1992);
See also: *Research Review 1991*, Department of Electronics and Electrical Engineering, University of Glasgow, page 62 (unacknowledged)

3 A.T. MENEY (to be published in Journal of Applied Physics)

4 M. RAZEGHI, O. ACHER and F. LAUNAY, Semiconductor Science and Technology **2**, 793 (1987)

5 K. NAKASHIMA, Y. KAWAGUCHI, Y. KAWAMURA and Y. IMAMURA, Applied Physics Letters **52**, 1383 (1988)

6 D.G. DEPPE and N. HOLONYAK, Journal of Applied Physics **64**, R93 (1988)

7 Y. HIRAYAMA, Y. SUZUKI and H. OKAMOTO, Japanese Journal of Applied Physics **24**, 1498 (1985)

8 First given by: A. FICK, Pogg. Ann. **94**, 59 (1855)
First applied to diffusion in solids by: H. BRAUNE, Z. Phys. Chem. **110**, 147 (1924)

9 J.N. SCHULMAN and Y.C. CHANG, Physical Review **B31**, 2056 (1985)

10 W.A. HARRISON, Physical Review **B8**, 4487 (1973)

11 Y.C. CHANG, Physical Review **B37**, 8215 (1988)

12 M. ASADA, IEEE Journal of Quantum Electronics **QE-25**, 2019 (1989)

13 T. OHTOSHI and M. YAMANISHI, Proceedings of the 12th IEEE Semiconductor Laser Conference, Davos, Switzerland (1990);
ibid, IEEE Journal of Quantum Electronics **QE-27**, 46 (1991)

Appendix A

The Density Matrix

The density-matrix formalism[1-3] has been commonly used to calculate the linear and nonlinear contributions to the optical gain and absorption. It has also been used in the case of semiconductor lasers. For the present case, the system under consideration is a semiconductor quantum well in the presence of multimode radiation. Let ρ be the one-particle density matrix and H_o be the unperturbed Hamiltonian with an asymmetric potential energy, E(t) be the electric field strength of the optical radiation with polarisation vector $\hat{\varepsilon}$, and M be the dipole operator. For multimode radiation, the optical field E(t) is the sum over all modes

$$\begin{aligned} E(t) &= \hat{\varepsilon} Re\left[\sum_m E_m^* e^{-i\omega_m t}\right] \\ &= \hat{\varepsilon}\sum_m (E_m e^{-i\omega_m t} + E_m^* e^{i\omega_m t}) \ . \end{aligned} \tag{A1}$$

The density matrix equation, with intraband relaxation becomes[2]

$$\frac{\partial}{\partial t}\rho = \frac{1}{i\hbar}\left[H_o - M\cdot \mathrm{E}(t),\rho\right] - \frac{1}{2}\left[\Gamma(\rho-\rho^o)+(\rho-\rho^o)\Gamma\right], \qquad \text{(A2)}$$

where ρ^o is the unperturbed density matrix and Γ is a phenomenological operator responsible for damping. More precise details of damping, which involve electron-phonon interactions and electron-electron collisions, will be given later.

It is sufficient to assume that Γ is a diagonal matrix and has elements γ_{nn} which represent the inverse relaxation time of state $|n\rangle$. For the present discussion it is adequate to consider a two-level system only. The generalisation to a multi-level system is completely straightforward. Consider two states $|\alpha\rangle$ and $|\beta\rangle$ where

$$\begin{aligned} |\alpha\rangle &= |k_{||},k_{\perp}\rangle \\ |\beta\rangle &= |q_{||},q_{\perp}\rangle\ , \end{aligned} \qquad \text{(A3)}$$

and where $k_{||}$, $q_{||}$ are the in-plane wavevectors and $k_{\perp}$, $q_{\perp}$ the z-component of the momentum. We consider $|\alpha\rangle$ and $|\beta\rangle$ to be the initial and final states respectively. The unperturbed Hamiltonian is diagonal, with energies E_α and E_β. The operator Γ has diagonal elements

$$\begin{aligned} \langle\alpha|\Gamma|\alpha\rangle &= \frac{1}{\tau_\alpha} \\ \langle\beta|\Gamma|\beta\rangle &= \frac{1}{\tau_\beta}\ , \end{aligned} \qquad \text{(A4)}$$

where τ_α and τ_β are the relaxation times for states $|\alpha\rangle$ and $|\beta\rangle$. Equation (A2) may be solved by expanding the density matrix ρ in powers of the optical field E giving

$$\rho = \sum_n(\rho^n)\ . \qquad \text{(A5)}$$

It is assumed that the unperturbed density matrix $\rho^{(0)}$ has diagonal elements[2] only. It is convenient to define

$$\begin{aligned} \rho^{(n)}_{\alpha\alpha} &= \langle\alpha|\rho^{(n)}|\alpha\rangle \\ \rho^{(n)}_{\alpha\beta} &= \langle\alpha|\rho^{(n)}|\beta\rangle \\ \rho^{(n)}_{\beta\alpha} &= \langle\beta|\rho^{(n)}|\alpha\rangle \\ \rho^{(n)}_{\beta\beta} &= \langle\beta|\rho^{(n)}|\beta\rangle\ . \end{aligned}$$

This gives $\rho_{\beta\alpha}(t) = \rho^*_{\alpha\beta}(t)$. The perturbation series for ρ are given by[4]

$$\rho_{\beta\beta} = \rho^{(0)}_{\beta\beta} + \rho^{(2)}_{\beta\beta}E^2 + \cdots$$
$$\rho_{\alpha\beta} = \rho^{(1)}_{\alpha\beta}E + \rho^{(3)}_{\alpha\beta}E^3 + \cdots , \qquad (A6)$$

where the diagonal elements of the density matrix heve been neglected. The term $\rho^{(0)}_{\alpha\alpha}$ indicates the electron distribution in the injected state. The linear term $\rho^{(1)}_{\alpha\beta}E$ rotates in phase with the existing field mode and can be expressed as

$$\rho^{(1)}_{\alpha\beta} = \sum_m \rho^{(1)}_{\alpha\beta}(m) , \qquad (A7)$$

where $\rho^{(1)}_{\alpha\beta}(m)$ is the component with phase rotation $\exp(j\omega_m t)$.

The second order terms $\rho^{(2)}_{\beta\beta}E^2$ give the number of electrons whose phase rotation is synchronised with the existing field, given by

$$\rho^{(2)}_{\beta\beta} = \sum_{m,k} \rho^{(2)}_{\beta\beta}(m,k) , \qquad (A8)$$

where $\rho^{(2)}_{\beta\beta}(m,k)$ is the component built by the m and k modes. The phase rotation is $\exp(j(\omega_m \pm \omega_k)t)$.

Note that $\rho^{(2)}_{\beta\beta}E^2$ has dc components (m=k), and also beat frequency components (m≠k). The synchronisation saturates the dipole moment, shown by the third-order term

$$\rho^{(3)}_{\alpha\beta} = \sum_{m,k,q} \rho^{(3)}_{\alpha\beta}(m,k,q) , \qquad (A9)$$

where $\rho^{(3)}_{\alpha\beta}(m,k,q)$ is the component built by the m,k and q modes with phase rotation $\exp(j(\pm\omega_m \pm \omega_k \pm \omega_q)t)$. If there is only a single mode, then the third order element is built by using $(\omega_m, -\omega_m, \omega_m)$ and $(-\omega_m, \omega_m, \omega_m)$ for the phase rotation $\exp(j\omega_m t)$. If there are two modes however, then the phase rotation $\exp(j\omega_m t)$ is built by the terms $(\omega_k, -\omega_k, \omega_m)$, $(-\omega_k, \omega_k, \omega_m)$, $(\omega_m, -\omega_k, \omega_k)$ and $(-\omega_k, \omega_m, \omega_k)$. This means that with two modes there are twice as many terms as there are with identical modes. The extra terms arise from the beat frequency terms of $\rho^{(2)}_{\beta\beta}E^2$ at $(\omega_m, -\omega_k)$ and $(-\omega_k, \omega_m)$.

Equations (A2) to (A5) give for the even and odd elements of ρ respectively

$$\frac{\partial}{\partial t}\rho_{\beta\beta}^{(2n)} = -\gamma_{\beta\beta}\rho_{\beta\beta}^{(2n)} - \frac{1}{i\hbar}\left(M_{\beta\alpha}\rho_{\alpha\beta}^{(2n-1)} - M_{\alpha\beta}\rho_{\beta\alpha}^{(2n-1)}\right)E(t) \tag{A10}$$

$$\frac{\partial}{\partial t}\rho_{\alpha\alpha}^{(2n)} = -\gamma_{\alpha\alpha}\rho_{\alpha\alpha}^{(2n)} - \frac{1}{i\hbar}\left(M_{\alpha\beta}\rho_{\beta\alpha}^{(2n-1)} - M_{\beta\alpha}\rho_{\alpha\beta}^{(2n-1)}\right)E(t) \tag{A11}$$

$$\frac{\partial}{\partial t}\rho_{\beta\alpha}^{(2n+1)} = \left[\frac{1}{i\hbar}\left(E_\beta - E_\alpha\right) - \gamma_{\alpha\beta}\right]\rho_{\beta\alpha}^{(2n+1)} - \frac{1}{i\hbar}\left(\rho_{\alpha\alpha}^{(2n)} - \rho_{\beta\beta}^{(2n)}\right)M_{\beta\alpha}E(t) \tag{A12}$$

$$\frac{\partial}{\partial t}\rho_{\alpha\beta}^{(2n+1)} = \left[\frac{1}{i\hbar}\left(E_\alpha - E_\beta\right) - \gamma_{\beta\alpha}\right]\rho_{\alpha\beta}^{(2n+1)} - \frac{1}{i\hbar}\left(\rho_{\beta\beta}^{(2n)} - \rho_{\alpha\alpha}^{(2n)}\right)M_{\alpha\beta}E(t)\ . \tag{A13}$$

The first-order term $\rho_{\alpha\beta}^{(1)}$ can be obtained in terms of a linear combination of the components for different modes as

$$\rho_{\alpha\beta}^{(1)} = \sum_m\left[\tilde{\rho}_{\alpha\beta}^{(1)}(-\omega_m)e^{i\omega_m t} + \tilde{\rho}_{\beta\alpha}^{(1)}(\omega_m)e^{-i\omega_m t}\right] \tag{A14}$$

where

$$\tilde{\rho}_{\alpha\beta}^{(1)}(-\omega_m) = -\frac{M_{\alpha\beta}E_m^*}{i\hbar}\frac{\left(\rho_{\beta\beta}^{(0)} - \rho_{\alpha\alpha}^{(0)}\right)}{\left[i\left(\omega_m - \omega_{\beta\alpha}\right) + \gamma_{\alpha\beta}\right]} \tag{A15}$$

and

$$\tilde{\rho}_{\beta\alpha}^{(1)}(\omega_m) = -\frac{M_{\alpha\beta}E_m}{i\hbar}\frac{\left(\rho_{\beta\beta}^{(0)} - \rho_{\alpha\alpha}^{(0)}\right)}{\left[-i\left(\omega_m + \omega_{\beta\alpha}\right) + \gamma_{\alpha\beta}\right]}\ . \tag{A16}$$

If these first-order terms are then substituted into (A10), the second-order element, induced by modes m and k is obtained as

$$\rho_{\beta\beta}^{(2)}(m,k) = -\frac{M_{\beta\alpha}M_{\alpha\beta}}{\hbar^2}\left(\rho_{\beta\beta}^{(0)} - \rho_{\alpha\alpha}^{(0)}\right) \times\left\{\frac{E_k E_m^* E^{i(\omega_m-\omega_k)t}}{\left[i(\omega_m-\omega_k)+\gamma_{\beta\beta}\right]\left[i\left(\omega_m-\omega_{\beta\alpha}\right)+\gamma_{\beta\alpha}\right]} + \frac{E_m E_k^* E^{-i(\omega_m-\omega_k)t}}{\left[i(\omega_k-\omega_m)+\gamma_{\beta\beta}\right]\left[i\left(\omega_{\beta\alpha}-\omega_m\right)+\gamma_{\beta\alpha}\right]}\right\}\ . \tag{A17}$$

If the second-order term is substituted into (A12) the third-order term, comprised of modes m, k and q, is obtained as

$$\rho_{\alpha\beta}^{(3)} = \sum_{m,k,q} \rho_{\alpha\beta}^{(3)}(m,k,q) \tag{A18}$$

where

$$\begin{aligned}
\rho_{\alpha\beta}^{(3)}(m,k,q) = {} & \frac{M_{\alpha\beta}^2 M_{\beta\alpha}}{i\hbar^3}\left(\rho_{\beta\beta}^{(0)} - \rho_{\alpha\alpha}^{(0)}\right) \\
& \times \left\{ \frac{E_m^* E_k E_q^* e^{i(\omega_m - \omega_k + \omega_q)t}}{\left[i\left(\omega_m - \omega_k + \omega_q - \omega_{\beta\alpha}\right) + \gamma_{\beta\alpha}\right]\left[i\left(\omega_m - \omega_{\beta\alpha}\right) + \gamma_{\alpha\beta}\right]} \right. \\
& \times \left[\frac{1}{i(\omega_m - \omega_k) + \gamma_{\beta\beta}} + \frac{1}{i(\omega_m - \omega_k) + \gamma_{\alpha\alpha}}\right] \\
& + \frac{E_k^* E_m E_q^* e^{i(\omega_k - \omega_m + \omega_q)t}}{\left[i\left(\omega_k - \omega_m + \omega_q - \omega_{\beta\alpha}\right) + \gamma_{\beta\alpha}\right]\left[i\left(\omega_{\beta\alpha} - \omega_m\right) + \gamma_{\alpha\beta}\right]} \\
& \left. \times \left[\frac{1}{i(\omega_k - \omega_m) + \gamma_{\beta\beta}} + \frac{1}{i(\omega_k - \omega_m) + \gamma_{\alpha\alpha}}\right] \right\} .
\end{aligned} \tag{A19}$$

The polarisation P(t) is given by

$$P(t) = \frac{1}{V} Tr(\rho M) . \tag{A20}$$

The Fourier components of the polarisation for mode m are denoted by P_m and the susceptibility $\chi^{(1)}(t)$ for mode m by $\chi^{(1)}(\omega_m)$. This gives

$$P_m = \varepsilon_o \chi^{(1)}(\omega_m) E_m^* e^{i\omega_m t} + \varepsilon_o \chi^{(1)}(-\omega_m) E_m e^{-i\omega_m t} . \tag{A21}$$

The susceptibility is then

$$\chi^{(1)}(\omega_m) = \frac{1}{\varepsilon_o V} \sum_{\alpha\beta} \frac{|M_{\alpha\beta}|^2}{\hbar} \frac{\rho_{\beta\beta}^{(0)} - \rho_{\alpha\alpha}^{(0)}}{\left(\omega_m - \omega_{\beta\alpha} + i\gamma_{\alpha\beta}\right)} . \tag{A22}$$

If we only keep the resonant term at ω_m, the third-order susceptibility $\chi_{m(k)}^{(3)}(\omega_m)$, corresponding to

the mode m in the presence of another mode k is given by

$$\chi^{(3)}_{m(k)}(\omega_m) = \frac{1}{\varepsilon_o V}\sum_{\alpha\beta}\frac{|M_{\alpha\beta}|^4}{\hbar^3}\cdot\frac{1}{1+\delta_{m,k}}\cdot\frac{\rho^{(0)}_{\beta\beta}-\rho^{(0)}_{\alpha\alpha}}{(\omega_m-\omega_{\beta\alpha}+i\gamma_{\alpha\beta})}$$
$$\times\left\{\left(\frac{1}{i(\omega_m-\omega_{\beta\alpha})+\gamma_{\beta\alpha}}+\frac{1}{i(\omega_{\beta\alpha}-\omega_k)+\gamma_{\alpha\beta}}\right)\right.$$
$$\times\left(\frac{1}{i(\omega_m-\omega_k)+\gamma_{\beta\beta}}+\frac{1}{i(\omega_m-\omega_k)+\gamma_{\alpha\alpha}}\right)$$
$$\left.+\frac{2(\gamma_{\alpha\alpha}+\gamma_{\beta\beta})}{\gamma_{\alpha\alpha}\gamma_{\beta\beta}}\cdot\frac{\gamma_{\alpha\beta}}{(\omega_{\beta\alpha}-\omega_k)^2+\gamma^2_{\alpha\beta}}\right\}. \qquad \text{(A23)}$$

The material gain at ω_m is given by

$$g_m = \frac{\omega}{cn_r}Im\left[\chi_m(\omega_m)\right]$$
$$= g^{(1)}_m - \Gamma\sum_k g^{(3)}_{m(k)}|E_k|^2\,, \qquad \text{(A24)}$$

where Γ is the optical confinement factor and

$$\chi_m(\omega_m) = \chi^{(1)}(\omega_m) + \sum_k \chi^{(3)}_{m(k)}(\omega_m)\,. \qquad \text{(A25)}$$

The modal gain $g_m(\omega_m)$ is then

$$g_m(\omega_m) = \Gamma\left[g^{(1)}_m - \Gamma\sum_k g^{(3)}_{m(k)}|E_k|^2\right]. \qquad \text{(A26)}$$

Equations (A22) to (A25) then give

$$g^{(1)}_m(\omega_m) = \omega_m\sqrt{\frac{\mu}{\varepsilon}}\frac{1}{V}\sum_{\alpha\beta}\frac{|M_{\alpha\beta}|^2\gamma_{\alpha\beta}}{\hbar}\frac{(\rho^{(o)}_{\beta\beta}-\rho^{(o)}_{\alpha\alpha})}{(\omega_m-\omega_{\beta\alpha})^2+\gamma^2_{\alpha\beta}} \qquad \text{(A27)}$$

and

$$g^{(3)}_{m(k)}(\omega_m) = -\omega_m \sqrt{\frac{\mu}{\varepsilon}} \frac{1}{V} \sum_{\alpha\beta k} \frac{|M_{\alpha\beta}|^4}{\hbar^3} \cdot \frac{1}{(1+\delta_{m,k})}$$
$$\times Re \left[\frac{\left(\rho^{(o)}_{\beta\beta} - \rho^{(o)}_{\alpha\alpha}\right)}{i\left(\omega_m - \omega_{\beta\alpha}\right) + \gamma_{\alpha\beta}} \right.$$
$$\times \left\{ \left(\frac{1}{i\left(\omega_m - \omega_{\beta\alpha}\right) + \gamma_{\beta\alpha}} + \frac{1}{i\left(\omega_{\beta\alpha} - \omega_k\right) + \gamma_{\alpha\beta}} \right) \right.$$
$$\times \left(\frac{1}{i(\omega_m - \omega_k) + \gamma_{\beta\beta}} + \frac{1}{i(\omega_m - \omega_k) + \gamma_{\alpha\alpha}} \right)$$
$$\left. \left. + \frac{2\left(\gamma_{\alpha\alpha} + \gamma_{\beta\beta}\right)}{\gamma_{\alpha\alpha}\gamma_{\beta\beta}} \cdot \frac{\gamma_{\alpha\beta}}{\left(\omega_{\beta\alpha} - \omega_k\right)^2 + \gamma^2_{\alpha\beta}} \right\} \right]. \qquad \text{(A28)}$$

References

1 M. SARGENT, M.O. SCULLY and W.E. LAMB, *Laser Physics* (Addison-Wesley, 1974)

2 N. BLOEMBERGEN, *Nonlinear Optics* (Benjamin, New York, 1965)

3 W.E. LAMB, Physical Review **134**, A1429 (1964)

4 M. YAMADA and Y. SUEMATSU, IEEE Journal of Quantum Electronics **QE-21**, 44 (1985)

MISSING

PAGE/PAGES

HAS NO

CONTENT

Appendix B

Excitons in Quantum Wells

Two-band model

To consider the excitonic states in quantum wells it is necessary to include the effects of valence-subband mixing in the calculation. Previous studies of excitons have mainly concentrated on real space variational methods,[1-4] usually neglecting the correct details of the subband dispersion. Some authors[5-8] have attempted to combine a real space variational calculation with the off-diagonal elements of the Luttinger-Kohn Hamiltonian included via perturbation theory. A full solution in k-space is, however, essential.

Only a handful of authors[9,10] have attempted this previously and their excellent studies do not seem to have influenced the large number of researchers who still continue with real space

variational calculations. An exciton state necessarily includes the effect of Coulomb forces between all crystalline states and to consider one hole and one electron at **k**=0 as the necessary ingredients to begin the calculation is incorrect. The method of calculating the band structure has been dealt with previously. It is assumed therefore that this calculation has been performed and that all electron states (i.e. wavefunctions) are known a *priori*. The valence band mixing has already been obtained using the Luttinger-Kohn 4x4 Hamiltonian for the J=3/2 valence bands. The conduction band wavefunctions are then taken as having been effectively decoupled from the valence bands and are given by

$$\psi^{n}_{\alpha q_{||}}(\mathbf{r}) = g^{n}_{s}(z)\, e^{iq_{||}\cdot\rho} u^{s}_{c}(\mathbf{r}) = |\, q_{||}, n > \tag{B1}$$

and the valence band wavefunctions by

$$\psi^{m}_{vk_{||}}(\mathbf{r}) = \sum_{j} g^{m}_{j}(z)\, e^{ik_{||}\cdot\rho} u^{j}_{v}(\mathbf{r}) = |\, k_{||}, m > \ . \tag{B2}$$

In the absence of Coulomb interactions, the energies are given by

$$H_{c}\,|\, q_{||}, n > = E^{n}_{c}\left(q_{||}\right)|\, q_{||}, n > \tag{B3}$$

$$H_{v}\,|\, k_{||}, m > = E^{m}_{v}\left(k_{||}\right)|\, k_{||}, m > \ . \tag{B4}$$

To obtain the equation for the excitons, simply include the Coulomb interaction term V

$$H = H_{c} + H_{v} + V$$
$$H\psi(\mathbf{r}) = E\psi(\mathbf{r}) \tag{B5}$$

where

$$V(\mathbf{r}) = \frac{-e^{2}}{4\pi\varepsilon\left[(z_{e}-z_{h})^{2}+(\rho_{e}-\rho_{v})^{2}\right]}\ . \tag{B6}$$

According to group theory (and not an approximation as some workers seem to believe) the exciton wavefunctions can be expressed in terms of the non-interacting states as

$$\psi(\mathbf{r}) = \sum_{n,m}\sum_{q_{||},k_{||}} C_{nm}\left(q_{||},k_{||}\right)|\, q_{||}, n > |k_{||}, m > \ . \tag{B7}$$

Substitute equation (B7) into (B5) and multiply on the left by $<q'_{||},n'|<k'_{||},m'|$, to give

$$\left[E_c^n\left(q_{||}\right) - E_v^m\left(k_{||}\right)\right]C_{nm}\left(q_{||},k_{||}\right) + \sum_{n'm'}\sum_{q'_{||}k'_{||}} < q_{||},n \mid < k_{||},m \mid V \mid q'_{||},n' > \mid k'_{||},m' > C_{n'm'}\left(q'_{||},k'_{||}\right) = EC_{nm}\left(q_{||},k_{||}\right) . \quad (B8)$$

For the case of excitons at rest, or for optical transitions, the centre-of-mass momentum $k_{||}+q_{||}$ is set to zero (conservation of momentum). This gives

$$C_{nm}\left(q_{||},k_{||}\right) = C_{nm}\left(-k_{||},k_{||}\right) \equiv C_{nm}\left(k_{||}\right) , \quad (B9)$$

which enables (B8) to be re-written as

$$\left[E_c^n\left(k_{||}\right) - E_v^m\left(k_{||}\right)\right]C_{nm}\left(k_{||}\right) + \sum_{n'm'}\sum_{k'_{||}} V_{n'm'}^{nm}\left(k_{||},k'_{||}\right)C_{n'm'}\left(k'_{||}\right) = EC_{nm}\left(k_{||}\right) , \quad (B10)$$

where the Coulomb term is given by

$$\begin{aligned} V_{n'm'}^{nm}\left(k_{||},k'_{||}\right) &\equiv < k_{||},n \mid < -k_{||}m \mid V \mid k'_{||},n' > \mid -k'_{||},m' > \\ &= \iint dz_e dz_h \sum_j g_j^{m^*}\left(k_{||},z_h\right) g_j^{m'}\left(k'_{||},z_h\right) g_s^{n^*}\left(k_{||},z_e\right) g_s^{n'}\left(k'_{||},z_e\right) \\ &\quad \times V(r) e^{-i(k_{||}-k'_{||})\cdot\rho} . \end{aligned} \quad (B11)$$

The only approximation to be used is to take a two-band model for the calculation of the Coulomb term (B11). However, the non-interacting dispersion of each band has been accurately obtained previously. A Gaussian-type function is assumed for the term C_{nm}, giving

$$\phi_{eh}\left(k_{||}\right) = (2\pi\lambda)^{1/2} e^{-\lambda k_{||}^2/4} . \quad (B12)$$

In real space this is

$$\phi_{eh}\left(\mathbf{r}\right) = \left(\frac{2}{\pi\lambda}\right)^{1/2} e^{-|\mathbf{r}|^2/\lambda} . \quad (B13)$$

Setting $C_{nm}(k_{||}) \equiv \phi_{eh}(k_{||})$ in (B10) gives

$$\left[E_c^n\left(k_{||}\right) - E_v^m\left(k_{||}\right)\right]\phi_{eh}\left(k_{||}\right) + \frac{1}{(2\pi)^2}\int dk'_{||}\,\phi_{eh}\left(k'_{||}\right)V_{nm}\left(k_{||},k'_{||}\right) = E\phi_{eh}\left(k_{||}\right), \quad \text{(B14)}$$

Multiply by $\phi^*_{eh}(k_{||})$ and integrating (with respect to $k_{||}$) leads to

$$E = \frac{1}{(2\pi)^2}\int dk_{||}\left[E_c^n\left(k_{||}\right) - E_v^m\left(k_{||}\right)\right]\left|\phi_{eh}\left(k_{||}\right)\right|^2$$
$$+ \frac{1}{(2\pi)^4}\iint dk_{||}\,dk'_{||}\,\phi^*_{eh}\left(k_{||}\right)\phi_{eh}\left(k'_{||}\right)V_{nm}\left(k_{||},k'_{||}\right). \quad \text{(B15)}$$

By varying the parameter λ, to give $\frac{\partial E}{\partial \lambda} = 0$, the exciton binding energy is obtained as

$$E_B = E_c^n(0) - E_v^m(0) - E\Big|_{\frac{\partial E}{\partial \lambda}=0}. \quad \text{(B16)}$$

By obtaining an equation integrated throughout **k**-space, it is evident that the full effects of the valence-band mixing (and any details of the bandstructure) are completely incorporated into the solution. Real space integration[1-4] would not achieve this. To calculate the excitonic optical absorption, the squared momentum matrix element is given by[11]

$$\left|P_{cv}^{ex}\right|^2 = \left|\frac{1}{2\pi}\int dk_{||}\,\phi_{eh}\left(k_{||}\right)P_{cv}\left(k_{||}\right)\right|^2. \quad \text{(B17)}$$

Expressions for $P_{cv}(k_{||})$ have been given previously. The optical absorption can be given in two different forms, depending on the linewidth broadening factor used. If a Gaussian lineshape is used, the absorption can be given as

$$\alpha(\omega) = \omega\sqrt{\frac{\mu}{\varepsilon}}\frac{2\pi}{L_z}\left|M_{cv}^{ex}\right|^2\left(\frac{1}{\sigma\pi}\right)^{1/2}e^{-(\hbar\omega - E_x)^2/\sigma}, \quad \text{(B18)}$$

where the linewidth $\Gamma = (\sigma \ln 2)^{1/2}$ and is about 5-7meV in quantum wells at room temperature. The above expression used the dipole matrix element, which is defined as

$$M_{cv}\left(k_{||}\right) = \left(\frac{-ie\hbar}{m_o E_{cv}\left(k_{||}\right)}\right)P_{cv}\left(k_{||}\right). \quad \text{(B19)}$$

If a Lorentzian linewidth is assumed, then a density matrix expression (see Appendix A) gives

$$\alpha(\omega) = \omega\sqrt{\frac{\mu}{\varepsilon}}\,\frac{1}{L_Z}\,\frac{|M_{cv}^{ex}|^2(\hbar/\tau_x)}{(E_{ex}-\hbar\omega)^2+(\hbar/\tau_x)^2}\,, \qquad \text{(B20)}$$

where $E_{ex} \equiv E_c(0)\text{-}E_v(0)\text{-}E_B$ and $\Gamma \equiv (\hbar/\tau_x)$ and we have included the summation over spin within the matrix element.

It is then completely straightforward to obtain the exciton oscillator strength (per unit area) which is given by

$$\begin{aligned} f_o &= \left(\frac{2}{\hbar\omega_{ex}m_o}\right)|P_{cv}^{ex}|^2 \\ &= \left(\frac{2}{\hbar\omega_{ex}m_o}\right)|<\Psi_{ex}|P_{cv}^{ex}|0>|^2\,. \end{aligned} \qquad \text{(B21)}$$

Coupled-exciton model

The exciton theory outlined in the previous section is expected to give good results for the ground state HH1-CB1 exciton. For most well widths considered here, both the HH1 and CB1 subbands are well confined for most states of interest. These are here the single-particle states coupled by the Coulomb interaction. Only states within approximately $10^6 cm^{-1}$ from the zone centre at Γ are considered here. For other excitons, including excited states of the excitons, it is best to consider a model which couples the excitons. The theoretical description of the Coulomb interaction has already been outlined above. This section will therefore be descriptive only.

To obtain a consistent theoretical description of each exciton, including excited states, we initially describe each exciton envelope function in terms the known solutions of the 2-D hydrogen atom.[12] These are given by

$$\begin{aligned} \Phi_{nm}(\rho,\phi) &= \frac{1}{\sqrt{2\pi}}\,\frac{2}{a\left(n+\frac{1}{2}\right)}\,\frac{1}{(2|m|!)}\left[\frac{(n+|m|)!}{(n-|m|)!(2n+1)}\right]^{1/2} \\ &\quad\times\left(\frac{2\rho}{a\left(n+\frac{1}{2}\right)}\right)^{|m|} e^{im\phi}e^{-\left(\frac{2\rho}{a(2n+1)}\right)}F(|m|-n,\,2|m|+1,\,\rho)\,, \end{aligned} \qquad \text{(B22)}$$

where (n,m) are the quantum numbers for the exciton and F(a,b,c) is the confluent hypergeometric function. The term *a* denotes the exciton Bohr radius (length parameter) which we denote as λ in the following discussion.

The complete wave function has a definite total angular momentum. Since the angular momentum of each spin component of the four-component hole wave function (using the Luttinger description) differs by ±1 for neighbouring components, then for the particular case of excitons, only one valence band envelope function component can be optically active. The total orbital angular momentum is therefore derived from this spin component. The form of each *k*-space envelope function is obtained from equation (B22) as

$$\psi_{nm}(k) = \int \rho \, d\rho \, \Phi_{nm}(\rho) J_m(k\rho) \, . \tag{B23}$$

which gives

$$\begin{aligned}
\psi_{1s}(k) &= \frac{\lambda}{(\lambda^2+k^2)^{3/2}} \, , \\
\psi_{2s}(k) &= \frac{\lambda(k^2-\lambda^2)}{(\lambda^2+k^2)^{5/2}} \, , \\
\psi_{2p}(k) &= \frac{k\lambda}{(\lambda^2+k^2)^{5/2}} \, , \\
\psi_{3d}(k) &= \frac{k^2\lambda}{(\lambda^2+k^2)^{7/2}} \, .
\end{aligned} \tag{B24}$$

The solutions obtained from each two-band calculation can then be combined to form the variational wave function $\Psi = \sum \Psi_i$. Due to the different spin indices of each hole component, including the relative motion orbital angular momentum, we find that only those excitons with similar spin values for each hole component are in fact coupled by the Coulomb interaction. For those exciton states of interest, the coupled excitons are given in detail in Chapter 6.

In general we have found that for the HH1-CB1 (1s) exciton there is little difference in the results using the two-band model and the more proper coupled-exciton model given above. For other excitons, in particular the excited states, this is not the case. For these states the use of the coupled-exciton model is essential to obtain correct binding energies and oscillator strengths.

References

1 G. BASTARD, Physical Review **B24**, 4714 (1981)

2 G. BASTARD, E.E. MENDEZ, L.L. CHANG and L. ESAKI, Physical Review **B26**, 1974 (1982)

3 J.A. BRUM and G. BASTARD, Journal of Physics **C18**, L789 (1985)

4 R.L. GREENE, Physical Review **B29**, 1807 (1984)

5 U. EKENBERG and M. ALTARELLI, Physical Review **B35**, 7865 (1987)

6 Y.C. LEE, W.N. MEI and K.C. LIU, Journal of Physics **C15**, L469 (1982)

7 K.S. CHAN, Journal of Physics **C19**, L125 (1986)

8 G.E.W. BAUER and T. ANDO, Physical Review **B38**, 6015 (1988)

9 G.D. SANDERS and Y.C. CHANG, Physical Review **B31**, 6892 (1985)

10 G.D. SANDERS and Y.C. CHANG, Physical Review **B35**, 1300 (1987)

11 D.F. BLOSSEY, Physical Review **B2**, 3976 (1970)

12 M. SHINADA and S. SHUGANO, Journal of the Physical Society of Japan **10**, 1936 (1966)

MISSING

PAGE/PAGES

HAS NO

CONTENT

Appendix C

Envelope-Function Continuity in Semiconductor Heterostructures

There has been a considerable amount of work published concerning the boundary conditions for envelope-functions in quantum well structures.[1-10] The effective-mass equations used in Chapter 4 for the conduction and valence subbands have subsumed all microscopic properties of the well and barrier materials. This includes the Bloch functions and momentum matrix elements between all bands of interest. It is therefore required to obtain the correct boundary conditions for continuity of probability current density, from the point of view that the effective-mass equations are correct.

Given a Hamiltonian, to construct boundary conditions within the envelope-function approximation, necessarily means ignoring any relevance due to the approximations mentioned above. That is, the simple Hamiltonian is taken at face value, as a true mathematical expression of the kinetic energy. Many of the published papers in this field, having performed the necessary

calculations, then add comment which seeks to describe correct physics in the final result. However, since the approximations cannot be neglected without mention, many of the conclusions drawn and insights offered by these authors apply only to the mathematical behaviour of the approximate Hamiltonian used. More correctly the problem should be considered without use of any type of $\mathbf{k}\cdot\mathbf{p}$ formalism whatever.

The present state-of-the-art bandstructure calculation methods are based on the density functional method, and do not use the widespread local density approximation (LDA). These methods, however, can not presently be applied to excited states. However, this method and other *ab initio* methods still rely on approximation techniques. Although an attempt is made to start from as basic a physical model as possible, solution of the resulting equations requires much ingenuity in the approximations required. This leads to the choice of either *ab initio* methods and difficulties in solution or an effective-mass method (including the invariant expansion Hamiltonians used in this thesis) which although contain initial approximations are straightforward to solve and can be done so with limited computational resources.

Due to the similarity of GaAs and $Al_xGa_{1-x}As$ it was decided to use an effective-mass Hamiltonian and the envelope-function method throughout this thesis. This was partly due to the simplicity of solution and partly due to the simplicity of analysis offered by this method. With regard to the valence subband-mixing for non-zero in-plane wavevectors, this is straightforward to obtain with this method. The conduction subband dispersion, including the effects of nonparabolicity, is similarly straightforward to obtain. A more proper treatment would include the Bloch functions explicitly in each material, as has been done by Smith and Mailhiot (Refs. 4 and 5). However, this was beyond the brief of this thesis.

The conduction band effective-mass Hamiltonian used here is given by[11]

$$E(\mathbf{k}) = \frac{\hbar^2\mathbf{k}^2}{2m} + \alpha_o\mathbf{k}^4 + \beta_o\left(k_x^2k_y^2 + k_y^2k_z^2 + k_z^2k_x^2\right) \pm\gamma_o\left[k^2\left(k_x^2k_y^2 + k_y^2k_z^2 + k_z^2k_x^2\right) - 9k_x^2k_y^2k_z^2\right]^{\frac{1}{2}} . \qquad \text{(C1)}$$

If we collect the k_z terms and ignore the spin-splitting term proportional to γ_o this can be re-written as

$$E(\mathbf{k}) = \alpha_o k_z^4 + \left[\frac{\hbar^2}{2m^*} + (2\alpha_o + \beta_o)\left(k_x^2 + k_y^2\right)\right]k_z^2 + \frac{\hbar^2}{2m^*}\left(k_x^2 + k_y^2\right) + (2\alpha_o + \beta_o)k_x^2k_y^2 + \alpha_o\left(k_x^4 + k_y^4\right) . \qquad \text{(C2)}$$

The basic prescription of effective-mass theory[12] is then to use this as the kinetic energy and we add

the confinement potential V(z). We replace k_z by the operator $-i\partial/\partial z$ which is taken to act on the z-dependent envelope function. The in-plane translational invariance leaves k_x and k_y as good quantum numbers. For the case of finite quantum wells it is not possible to decouple the in-plane and perpendicular motion, as is usually done. The value of m^* in equation (C1) is taken as m_1 (well material) or m_2 (barrier material) given by the bulk zone-centre effective mass in the [001] direction. The common method of obtaining the boundary conditions is to integrate the Schrödinger equation from $-\delta$ to $+\delta$ (taking the boundary at $z = 0$) and then letting $\delta \to 0$. The Hamiltonian can be written as (for $k_{||} = 0$)

$$H = -\frac{d}{dz}\frac{\hbar^2}{2m^*}\frac{d}{dz} + \frac{d^2}{dz^2}\alpha_o\frac{d^2}{dz^2} + V(z)\ . \tag{C3}$$

Integrating across the boundary gives continuity of

$$\frac{\hbar^2}{2m^*}\frac{dF}{dz} - \alpha_o\frac{d^3F}{dz^3} - \frac{d\alpha_o}{dz}\frac{d^2F}{dz^2}\ . \tag{C4}$$

where F denotes the z-dependent envelope function. If we set $\alpha_{o_1} = \alpha_{o_2}$, then the result given in Ref. 8 is obtained. This is then identical to the boundary conditions of continuity of the envelope function F divided by an energy dependent effective mass in the growth direction. Note that it is necessary to have $\delta = 0$ to eliminate the potential V(z). Also the derivative of the envelope function with respect to z has a discontinuity at the boundary.

If we consider the most general case ($k_{||} \neq 0$) then the coefficient of k_z has the form

$$A = \frac{\hbar^2}{2m^*} + (2\alpha_o + \beta_o)k_{||}^2\ . \tag{C5}$$

Current density is obtained from the continuity equation

$$\frac{d\rho}{dt} + \frac{dj}{dt} = 0\ , \tag{C6}$$

where $\rho = F^*F$ is the charge density of the postulated envelope function F. This gives

$$\frac{d\rho}{dt} = F^*\frac{dF}{dt} + F\frac{dF^*}{dt} = \frac{1}{i\hbar}(F^*HF - FHF^*)\ , \tag{C7}$$

from the time-dependent Schrödinger equation and gives

$$\frac{dj}{dt} = \frac{1}{i\hbar}\left(F^{*}A\frac{d^{2}F}{dz^{2}} - F^{*}\alpha_{o}\frac{d^{4}F}{dz^{4}} - c.c.\right), \tag{C8}$$

where c.c. denotes the complex conjugate of the preceding terms. It is seen that this equation is fulfilled if

$$j = \frac{1}{i\hbar}\left(F^{*}A\frac{dF}{dz} - F^{*}\alpha_{o}\frac{d^{3}F}{dz^{3}} + \frac{dF^{*}}{dz}\alpha_{o}\frac{d^{2}F}{dz^{2}} - c.c.\right). \tag{C9}$$

For quantum well structures the current density for bound states must be zero. Consider a potential step at z = 0 and incoming, reflected and transmitted waves

$$\begin{aligned} F(z) &= Ie^{ik_{1}z} + Re^{-ik_{1}z} && , z < 0 \\ F(z) &= Te^{ik_{2}z} && , z > 0 \end{aligned} \tag{C10}$$

Substitution in equation (C9) gives

$$\begin{aligned} j_{1} &= \frac{2k_{1}}{\hbar}\left(A_{1} + 2\alpha_{o_{1}}k_{1}^{2}\right)\left(|I|^{2} - |R|^{2}\right) && , z < 0 \\ j_{2} &= \frac{2k_{2}}{\hbar}\left(A_{2} + 2\alpha_{o_{2}}k_{2}^{2}\right)|T|^{2} && , z > 0 \end{aligned} \tag{C11}$$

where $k_{||}$ has been set to zero for convenience. Taking continuity of the envelope function and of equation (C4), neglecting the term ($d\alpha_{o}/dz$) leads to conservation of current if and only if

$$A\frac{dF}{dz} - 2\alpha_{o}\frac{d^{3}F}{dz^{3}} \tag{C12}$$

is continuous at the boundary. Extension to $k_{||} \neq 0$ gives the following boundary conditions at each interface

$$A_{1}\frac{dF_{1}}{dz} - \left(2\alpha_{o_{1}} + \beta_{o_{1}}k_{||}^{2}\right)\frac{d^{3}F_{1}}{dz^{3}} = A_{2}\frac{dF_{2}}{dz} - \left(2\alpha_{o_{2}} + \beta_{o_{2}}k_{||}^{2}\right)\frac{d^{3}F_{2}}{dz^{3}}. \tag{C13}$$

If we take the *ansatz* F = Bcos(Kz) in the quantum well region and F = Cexp(-λ|z|) in the barrier

regions equation (C13) gives the eigenvalues as solutions of the transcendental equation

$$\tan(KL) = \frac{\left[\frac{\hbar^2}{2m_2} + \left(2\alpha_{o_2} + \beta_{o_2}\right)k_{||}^2\right]\lambda - 2\alpha_{o_2}\lambda^3}{\left[\frac{\hbar^2}{2m_1} + \left(2\alpha_{o_1} + \beta_{o_1}\right)k_{||}^2\right]K + 2\alpha_{o_1}K^3} . \qquad \text{(C14)}$$

for the even-parity states and interfaces at z = ±L. The odd-parity states are obtained by replacing tan(KL) by -cotan(KL) in equation (C13) obtained by taking the envelope function of the form F=Bsin(Kz) in the well region. The wavenumbers K and λ are obtained from equation (C2) as

$$K = \left[A_1 - A_1\left(1 + \frac{B_1}{A_1^2}\right)^{1/2}\right]^{1/2} \qquad \text{(C15}a\text{)}$$

$$\lambda = \left[A_2\left(1 + \frac{B_2}{A_2^2}\right)^{1/2} - A_2\right]^{1/2} , \qquad \text{(C15}b\text{)}$$

where

$$A_1 = -\frac{\hbar^2}{4m_1\alpha_{o_1}} - \frac{\left(2\alpha_{o_1} + \beta_{o_1}\right)}{2\alpha_{o_1}}k_{||}^2 \qquad \text{(C16}a\text{)}$$

$$B_1 = \frac{E}{\alpha_{o_1}} - \frac{\hbar^2}{2m_1\alpha_{o_1}}k_{||}^2 - k_{||}^4 - \frac{\beta_{o_1}}{\alpha_{o_1}}k_x^2k_y^2 \qquad \text{(C16}b\text{)}$$

$$A_2 = -\frac{\hbar^2}{4m_2\alpha_{o_2}} - \frac{\left(2\alpha_{o_2} + \beta_{o_2}\right)}{2\alpha_{o_2}}k_{||}^2 \qquad \text{(C16}c\text{)}$$

$$B_2 = \frac{(E-V)}{\alpha_{o_2}} - \frac{\hbar^2}{2m_2\alpha_{o_2}}k_{||}^2 - k_{||}^4 - \frac{\beta_{o_2}}{\alpha_{o_2}}k_x^2k_y^2 . \qquad \text{(C16}d\text{)}$$

The boundary conditions for continuity of current density for the 4x4 Luttinger-Kohn Hamiltonian can be more simply obtained by integrating the Hamiltonian across the well-barrier interface.[13,14] The Hamiltonian can be written as

$$H = A\frac{d^2}{dz^2} + B\frac{d}{dz} + C , \qquad \text{(C17)}$$

where the A, B, C matrices are obtained from the 4x4 Hamiltonian given by equation (4.12) in Chapter 4. To ensure Hermiticity this can be re-written as

$$H = \frac{d}{dz}A\frac{d}{dz} + \frac{1}{2}\left(B\frac{d}{dz} + \frac{d}{dz}B\right) + C\,. \tag{C18}$$

Integration across the interfaces gives

$$\left[A_1\frac{d}{dz} + \frac{1}{2}B_1\right]F_1 = \left[A_2\frac{d}{dz} + \frac{1}{2}B_2\right]F_2 \tag{C19}$$

at each interface and where the subscript 1 (2) refers to the well (barrier) material. This leads to continuity at each interface of the four-component envelope function and of the vector

$$\begin{vmatrix} (\gamma_1 - 2\gamma_2)\frac{\partial}{\partial z} & \sqrt{3}\gamma_3(k_x - ik_y) & 0 & 0 \\ \sqrt{3}\gamma_3(k_x + ik_y) & (\gamma_1 + 2\gamma_2)\frac{\partial}{\partial z} & 0 & 0 \\ 0 & 0 & (\gamma_1 + 2\gamma_2)\frac{\partial}{\partial z} & -\sqrt{3}\gamma_3(k_x - ik_y) \\ 0 & 0 & -\sqrt{3}\gamma_3(k_x + ik_y) & (\gamma_1 - 2\gamma_2)\frac{\partial}{\partial z} \end{vmatrix} \begin{vmatrix} f_1 \\ f_2 \\ f_3 \\ f_4 \end{vmatrix} . \tag{C20}$$

References

1 D.J. BenDANIEL and C.B. DUKE, Physical Review **152**, 683 (1986)

2 G. BASTARD, Physical Review **B24**, 5693 (1981)
ibid, Physical Review **B25**, 7584 (1982)

3 M.F.H. SCHUURMANS and G.W. t'HOOFT, Physical Review **B31**, 8041 (1985)

4 D.L. SMITH and C. MAILHIOT, Physical Review **B33**, 8345 (1986)

5 C. MAILHIOT and D.L. SMITH, Physical Review **B33**, 8360 (1986)

6 U. EKENBERG, Physical Review **B36**, 6152 (1987)

7 M.G. BURT, Semiconductor Science and Technology **2**, 460 (1987); erratum **2**, 701 (1987)
ibid, **3**, 739 (1988)
ibid, **3**, 1224 (1988)

8 M. De DIOS LEYVA, J. LOPEZ GONDAR and J. SABIN Del VALLE, Physica Status Solidi **b142**, K151 (1987); erratum **b145**, K155(E), (1988)

9 U. EKENBERG, Physical Review **B40**, 7714 (1989)

10 A. PERSSON and R.M. COHEN, Physical Review **B38**, 5568 (1988)

11 M. BRAUN and U. RÖSSLER, Journal of Physics **C18**, 3365 (1985)

12 J.M. LUTTINGER and W. KOHN, Physical Review **97**, 869 (1955)

13 M. ALTARELLI in: *Heterojunctions and Semiconductor Superlattices*, ed. by G. ALLAN, G. BASTARD, N. BOCCARA, M. LANNOO and M. VOOS (Springer-Verlag, 1986)

14 L.C. ANDREANI, A. PASQUARELLO and F. BASSANI, Physical Review **B36**, 5887 (1987)

MISSING

PAGE/PAGES

HAS NO

CONTENT

Publications

A.T. MENEY and J.M. ARNOLD

"Nonlinear Gain and Saturation Effects in GaAs-AlGaAs Quantum Well Lasers"

9th International Quantum Electronics Conference, Oxford, July 18-22 (1989)

A.T. MENEY

"Orientation Dependence of Subband Structure and Optical Properties in GaAs-AlGaAs Quantum Wells: [001], [111], [110] and [310] Growth Directions"

Superlattices and Microstructures **11**, 31 (1992)

A.T. MENEY

"Effects of Impurity Induced Disorder on the Index of Refraction in GaAs-AlGaAs Quantum Wells"

Superlattices and Microstructures **11**, 47 (1992)

A.T. MENEY

"Excitons in GaAs-AlGaAs Quantum Wells: Effect of Substrate Orientation"

Solid State Communications **83**, 89 (1992)

A.T. MENEY

"Effects of Growth Direction on Lasing Performance in GaAs-AlGaAs Quantum Well Lasers"

to be published in Superlattices and Microstructures

MISSING

PAGE/PAGES

HAS NO

CONTENT

Abstract

Nonlinear Gain and Saturation Effects in GaAs/AlGaAs Quantum Well Lasers

A.T. Meney and J.M. Arnold

Department of Electronics and Electrical Engineering

University of Glasgow

Glasgow G12 8QQ

Many recent advances in the field of integrated optoelectronics have been due to the development of novel semiconductor devices, especially semiconductor diode lasers, which have proved to be of great potential in communication and telecommunication industries. Improvements in fabrication techniques have also led to the production of single quantum well and multiple quantum well devices, which have shown many new physical phenomena, as well as superior operating characteristics.

Apart from experimental work, much research has been devoted to modelling gain spectra and gain-current relations in semiconductor lasers. It is known, however, that the gain-current relation in quantum well lasers is nonlinear. In order to model gain in quantum well lasers, it is therefore necessary to consider the microscopic nonlinear polarisation within the multi-level quasi-2-dimensional structure, and without resort to a phenomenologically introduced gain coefficient [1]. In addition, widely-used assumptions modelling gain saturation and refractive index changes (carrier dependent) may lead to an inaccurate description [2] of laser operation.

We present model calculations based on an undoped GaAs/AlGaAs single quantum well laser which incorporates nonlinear gain and saturation effects, using calculated nonlinear susceptibilities within the reduced dimensionality of the quantum well layer. Of particular interest are the lasing transitions between different quantum well subbands and the gain saturation of the higher wavelength transitions (n=1 transitions) at high injection current densities, and also the observed carrier-dependent dispersion of the real refractive index in the active layer.

In our future work, this analysis will be extended to incorporate the effects of an additional waveguide structure and will permit accurate calculation of the optical confinement within the quantum well active layer.

References

[1] B.Thedrez et al, **IEEE J.Quant.Elect.** 24, p1499, 1988.
[2] W.W.Chow et al, **Optics Letters** 12, p25, 1987.

MISSING

PAGE/PAGES

HAS NO

CONTENT

ORIENTATION DEPENDENCE OF SUBBAND STRUCTURE AND OPTICAL PROPERTIES IN GaAs-AlGaAs QUANTUM WELLS: [001], [111], [110] AND [310] GROWTH DIRECTIONS.

Alistair T. Meney

Laser and Optical Systems Engineering Group
Department of Mechanical Engineering
University of Glasgow
Glasgow G12 8QQ
Scotland U.K.

(Received 13 May 1991)

We calculate the valence subband dispersion in GaAs-$Al_xGa_{1-x}As$ quantum wells, with growth axes along the [001], [111], [110] and [310] directions, by solving the multiband effective mass equations for the four-component envelope function. Boundary conditions for conservation of probability current are given for each growth direction. The conduction band dispersion is obtained from an accurate expression for the bulk dispersion which includes the effects of anisotropy and nonparabolicity. We use the calculated dispersion to examine the dependence of optical interband transitions on both polarization and valence-subband mixing.

1. Introduction.

Semiconductor heterostructures have received much attention in recent years, due to their novel electronic properties, and also due to their possible use in electronic and optoelectronic devices such as tunneling diodes, high-electron-mobility transistors[1] (HEMT), quantum well lasers[2], optical waveguides, modulators and switches.

Many different methods have been employed to study the electronic properties of these heterostructures. These include the multiband effective mass theory[3-6], tight-binding method[7], bond-orbital model[8], density-functional method[9] and pseudopotentials.[10,11]

The envelope-function method, based on the effective mass theory of the Luttinger-Kohn Hamiltonian[12], is especially easy to apply, and gives a reasonable description of valence band dispersion near the Brillouin zone centre. It is particularly well suited to the inclusion of the effects of external perturbation such as uniaxial stress, external magnetic field, or a built-in quantum well potential.

Possibly one of the most important results of the application of this method is the significant subband mixing for in-plane wavevectors away from the zone centre at k_t=0. This mixing arises due to the off-diagonal terms in the Luttinger-Kohn Hamiltonian, and also due to the application of boundary conditions for the conservation of probability current density[3] at each interface in the well growth direction.

In this paper we adopt the four-component envelope function scheme to study the Γ_8 subband structure in $GaAs/Al_xGa_{1-x}As$ quantum wells, with the growth direction (z-axis) along the [001], [111], [110] or [310] directions. Quantum wells in the [001] direction have been the subject of most studies to date. However, wells grown in the [111] and [110] directions[13-16] have recently attracted interest. Experimental studies have recently been reported on wells grown along the [111] and [310] directions.[17]

The method of calculation is outlined in section 2. The 4x4 Luttinger-Kohn Hamiltonian for each growth direction, along with explicit expressions for the current-conserving boundary conditions in each case, are also presented. It has recently been suggested that the lower in-plane effective masses of [001]-grown strained-layer quantum wells may be present also in unstrained material[16] grown in different crystal directions. The threshold current required for population inversion in quantum well lasers depends on the density of states, and therefore the effective masses, of the valence- and conduction-subbands. Recent experimental results[14], for [111]-grown GaAs/AlGaAs quantum well lasers, indicate a significant reduction in

0749–6036/92/010031+10 $02.00/0

threshold current compared to those grown along [001]. More recently, theoretical results[16] have confirmed this, but used only a simplified model, with parabolic conduction bands (regardless of growth direction), and the assumption of axially symmetric valence band dispersion. We have therefore retained the off-diagonal terms in the Luttinger-Kohn Hamiltonian which give rise to warping of the valence band dispersion in the plane of the well, and we include the effects of anisotropy and nonparabolicity on the conduction band dispersion to fourth order in **k**.

2. Method of calculation.

(a) [001]-growth valence band dispersion.

We consider an isolated quantum well with the GaAs well region extending from z=-L to z=+L, where z is the growth direction. The Luttinger-Kohn Hamiltonian[18] for the Γ_8 valence band is given by the 4x4 matrix

$$H = -\begin{vmatrix} P+Q & L & M & 0 \\ L^* & P-Q & 0 & M \\ M^* & 0 & P-Q & -L \\ 0 & M^* & -L^* & P+Q \end{vmatrix} + V(z), \quad (1)$$

where

$$P = \frac{1}{2}\gamma_1\left(k_x^2+k_y^2+k_z^2\right) \quad (2a)$$

$$Q = \frac{1}{2}\gamma_2\left(k_x^2+k_y^2-2k_z^2\right) \quad (2b)$$

$$L = -\sqrt{3}\gamma_3\left(k_y+ik_x\right)k_z \quad (2c)$$

$$M = \frac{\sqrt{3}}{2}\gamma_2\left(k_x^2-k_y^2\right)-\sqrt{3}i\gamma_3 k_x k_y. \quad (2d)$$

V(z) represents the potential due to the valence band edge discontinuity. We assume that the zone centre Bloch functions are similar in both the well and barrier materials, restricting the method to materials of similar chemical composition. Equation (1) can then be taken as acting on a four-component envelope function $\underline{F}=(f_1,f_2,f_3,f_4)$ and we take the wave functions to be of the form

$$\Psi(r) = f_1(r)\left|\tfrac{3}{2},\tfrac{3}{2}\right> + f_2(r)\left|\tfrac{3}{2},\tfrac{1}{2}\right> + f_3(r)\left|\tfrac{3}{2},-\tfrac{1}{2}\right> + f_4(r)\left|\tfrac{3}{2},-\tfrac{3}{2}\right>. \quad (3)$$

Analytic expressions for the eigenvalues and eigenvectors of equation (1) in bulk (V(z)=0) have been given by Andreani et al (Ref. 19). The in-plane components of Bloch vector **k** are still good quantum numbers in the case of quantum wells, and the envelope functions have the form

$$\underline{F} = (f_1,f_2,f_3,f_4)\cdot e^{i\mathbf{k}\cdot\mathbf{r}}, \quad (4)$$

where (f_1,f_2,f_3,f_4) is an eigenvector of equation (1). The energy eigenvalues are given by

$$E = -P \pm \left(Q^2+LL^*+MM^*\right)^{\frac{1}{2}}, \quad (5)$$

where the +(-) sign refers to heavy(light) holes. In the barrier we must replace E by $(E-V_0)$, where V_0 is the valence band discontinuity in V(z). In the well V_0=0.

Continuity of the envelope function, and continuity of probability current density (see below) at the interfaces z=+/-L leads to a system of linear homogeneous equations with 16 unknown coefficients. The energy eigenvalues of the subbands are given by the zeros of the associated determinantal equation, for each value of in-plane wavevector.

To obtain the boundary condition for current conservation, we decompose the Hamiltonian (1) as

$$H = A\frac{\partial^2}{\partial z^2}+B\frac{\partial}{\partial z}+C, \quad (6)$$

where A,B and C are matrices with components obtained using equations (2), and $k_z \rightarrow -i(\partial/\partial z)$. To ensure Hermiticity, this is re-written as

$$H = \frac{\partial}{\partial z}A\frac{\partial}{\partial z}+\frac{1}{2}\left(B\frac{\partial}{\partial z}+\frac{\partial}{\partial z}B\right)+C. \quad (7)$$

Integrating across the interfaces leads to

$$\left[A^{(1)}\frac{\partial}{\partial z}+\frac{1}{2}B^{(1)}\right]F^{(1)} = \left[A^{(2)}\frac{\partial}{\partial z}+\frac{1}{2}B^{(2)}\right]F^{(2)}, \quad (8)$$

at each interface.

For the [001]-growth Hamiltonian, this leads to continuity of the following vector at each interface

$$\begin{bmatrix} (\gamma_1-2\gamma_2)\frac{\partial}{\partial z} & \sqrt{3}\gamma_3(k_x-ik_y) & 0 & 0 \\ \sqrt{3}\gamma_3(k_x+ik_y) & (\gamma_1+2\gamma_2)\frac{\partial}{\partial z} & 0 & 0 \\ 0 & 0 & (\gamma_1+2\gamma_2)\frac{\partial}{\partial z} & -\sqrt{3}\gamma_3(k_x-ik_y) \\ 0 & 0 & -\sqrt{3}\gamma_3(k_x+ik_y) & (\gamma_1-2\gamma_2)\frac{\partial}{\partial z} \end{bmatrix} \begin{bmatrix} f_1 \\ f_2 \\ f_3 \\ f_4 \end{bmatrix} . \qquad (9)$$

(b) [001]-growth conduction band dispersion.

The conduction bands in zincblende semiconductors are known to exhibit anisotropic[20] and nonparabolic dispersion. Spin-splitting[21] within each subband is also present due to the lack of inversion symmetry. To obtain an accurate description of the conduction bands, it is necessary to include the effects of the higher p-antibonding conduction band. Braun and Rössler (Ref 22) have obtained an accurate expression for the conduction band dispersion to fourth order in **k**, which is obtained by an invariant expansion of the two-fold lowest conduction band states, with weighting factors obtained using standard **k·p** theory. The 14x14 Hamiltonian consists of the states Γ_{6c}, $\Gamma_{7v}+\Gamma_{8v}$ and $\Gamma_{7c}+\Gamma_{8c}$. To fourth order in **k**, the dispersion may be written as[22]

$$E(k) = \frac{\hbar^2 k^2}{2m} + \alpha_o k^4 + \beta_o\left(k_x^2k_y^2 + k_y^2k_z^2 + k_z^2k_x^2\right) \pm \gamma_o\left[k^2\left(k_x^2k_y^2 + k_y^2k_z^2 + k_z^2k_x^2\right) - 9k_x^2k_y^2k_z^2\right]^{\frac{1}{2}} . \qquad ..(10)$$

The coefficients α_o, β_o and γ_o describe isotropic nonparabolicity, anisotropic nonparabolicity and spin-splitting respectively. The explicit expressions for these coefficients may be found in Ref. 22. They can be expressed in terms of standard band parameters such as energy gaps and momentum matrix elements. We choose to ignore the spin-splitting term γ_o since it is small. We assume similar momentum matrix elements in GaAs and AlGaAs (x<0.4), and for consistency calculate the Γ_{6c} zone centre effective mass using a five-level **k·p** scheme. (All the parameters used in the calculations are given in Table 1). The effective mass is therefore given by[23]

$$\frac{m}{m^*} = 1 + \frac{E_P}{3}\left[\frac{2}{E_o} + \frac{1}{E_o+\Delta_o}\right] - \frac{E_P'}{3}\left[\frac{1}{E_o'-E_o} + \frac{2}{E_o'+\Delta_o'-E_o}\right] + C , \qquad (11)$$

where C is a constant chosen to give m*=0.0665 for x=0. This includes coupling to remote bands not explicitly included in equation (11). The parameters α_o and β_o also depend on the Γ_{5v}-Γ_{5c} interband matrix elements (see Table 1).

Following Ekenberg (Ref. 24) we re-write equation (10) as

$$k_z^4 + \left[\frac{\hbar^2}{2m\alpha_o} + \frac{(2\alpha_o+\beta_o)}{\alpha_o}k_{||}^2\right]k_z^2 + \frac{\hbar^2}{2m\alpha_o}k_{||}^2 + k_{||}^4 + \frac{\beta_o}{\alpha_o}k_x^2k_y^2 - \frac{E}{\alpha_o} = 0 , \qquad (12)$$

where $k_{||}=(k_x^2+k_y^2)^{1/2}$. If we put $K=k_z$ in the well and $\lambda=ik_z$ in the barrier, where $E\rightarrow(E-V_o)$, we easily obtain

$$K = \left[A_1 - A_1\left(1+\frac{B_1}{A_1^2}\right)^{\frac{1}{2}}\right]^{\frac{1}{2}} \qquad (13a)$$

$$\lambda = \left[A_2\left(1+\frac{B_2}{A_2^2}\right)^{\frac{1}{2}} - A_2\right]^{\frac{1}{2}} , \qquad (13b)$$

where

$$A_1 = -\frac{\hbar^2}{4m_1\alpha_{o1}} - \frac{(2\alpha_{o1}+\beta_{o1})}{2\alpha_{o1}}k_{||}^2 \qquad (14a)$$

$$B_1 = \frac{E}{\alpha_{o1}} - \frac{\hbar^2}{2m_1\alpha_{o1}}k_{||}^2 - k_{||}^4 - \frac{\beta_{o1}}{\alpha_{o1}}k_x^2k_y^2 \qquad (14b)$$

$$A_2 = -\frac{\hbar^2}{4m_2\alpha_{o2}} - \frac{(2\alpha_{o2}+\beta_{o2})}{2\alpha_{o2}}k_{||}^2 \qquad (14c)$$

$$B_2 = \frac{(E-V)}{\alpha_{o2}} - \frac{\hbar^2}{2m_2\alpha_{o2}}k_{||}^2 - k_{||}^4 - \frac{\beta_{o2}}{\alpha_{o2}}k_x^2k_y^2 . \qquad (14d)$$

In equations (13) and (14) the subscript 1(2) refers to the well(barrier) material.

Boundary conditions for conservation of current density have been discussed in detail by Ekenberg.[24] It is

straightforward to show that for the dispersion of equation (10), the appropriate current-conserving boundary condition leads to a simple transcendental equation for the well eigenstates given by

$$\tan(KL) = \frac{\frac{\hbar^2\lambda}{2m_2} - 2\alpha_{o2}\lambda^3}{\frac{\hbar^2 K}{2m_1} + 2\alpha_{o1}K^3}, \qquad (15)$$

for even-parity solutions at $k_{\|}$=0. For odd-parity solutions we replace tan(KL) by -cotan(KL). For non-zero in-plane wavevectors equation (15) is easily generalised to

$$\tan(KL) = \frac{\left[\frac{\hbar^2}{2m_2} + (2\alpha_{o2} + \beta_{o2})k_{||}^2\right]\lambda - 2\alpha_{o2}\lambda^3}{\left[\frac{\hbar^2}{2m_1} + (2\alpha_{o1} + \beta_{o1})k_{||}^2\right]K + 2\alpha_{o1}K^3}. \qquad (16)$$

(c) Dispersion for other growth directions.

For the [111]-growth direction we take wavevector components k_1,k_2,k_3 along the (1,1,-2), (-1,1,0) and (1,1,1) directions respectively. The natural direction for angular momentum quantization is now [111]. The elements of the Luttinger-Kohn Hamiltonian[18] now take the form

$$P = \frac{1}{2}\gamma_1\left(k_1^2 + k_2^2 + k_3^2\right) \qquad (17a)$$

$$Q = \frac{1}{2}\gamma_3\left(k_1^2 + k_2^2 - 2k_3^2\right) \qquad (17b)$$

$$L = \frac{i}{\sqrt{6}}(\gamma_2 - \gamma_3)(k_1 + ik_2)^2 - \frac{i}{\sqrt{3}}(2\gamma_2 + \gamma_3)(k_1 - ik_2)k_3 \qquad (17c)$$

$$M = \frac{1}{2\sqrt{3}}(\gamma_2 + 2\gamma_3)(k_1 - ik_2)^2 + \frac{2}{\sqrt{6}}(\gamma_3 - \gamma_2)(k_1 + ik_2)k_3. \qquad (17d)$$

From (8) conservation of current at each interface is now given by continuity of the vector

$$\begin{bmatrix} (\gamma_1 - 2\gamma_3)\frac{\partial}{\partial z} & \frac{1}{\sqrt{3}}(2\gamma_2 + \gamma_3)(k_1 - ik_2) & -\frac{2}{\sqrt{6}}(\gamma_2 - \gamma_3)(k_2 - ik_1) & 0 \\ \frac{1}{\sqrt{3}}(2\gamma_2 + \gamma_3)(k_1 + ik_2) & (\gamma_1 + 2\gamma_3)\frac{\partial}{\partial z} & 0 & -\frac{2}{\sqrt{6}}(\gamma_2 - \gamma_3)(k_2 - ik_1) \\ -\frac{2}{\sqrt{6}}(\gamma_2 - \gamma_3)(k_2 + ik_1) & 0 & (\gamma_1 + 2\gamma_3)\frac{\partial}{\partial z} & -\frac{1}{\sqrt{3}}(2\gamma_2 + \gamma_3)(k_1 - ik_2) \\ 0 & -\frac{2}{\sqrt{6}}(\gamma_2 - \gamma_3)(k_2 + ik_1) & -\frac{1}{\sqrt{3}}(2\gamma_2 + \gamma_3)(k_1 + ik_2) & (\gamma_1 - 2\gamma_3)\frac{\partial}{\partial z} \end{bmatrix} \begin{bmatrix} f_1 \\ f_2 \\ f_3 \\ f_4 \end{bmatrix}. \qquad (18)$$

For the [110]-growth direction, k_1,k_2 and k_3 are now along the (0,0,-1), (-1,1,0) and (1,1,0) directions respectively. The Luttinger-Kohn Hamiltonian now has elements

$$P = \frac{1}{2}\gamma_1\left(k_1^2 + k_2^2 + k_3^2\right) \qquad (19a)$$

$$Q = \frac{1}{2}\gamma_2\left(k_1^2 - \frac{1}{2}k_2^2 - \frac{1}{2}k_3^2\right) + \frac{3}{4}\gamma_3\left(k_2^2 - k_3^2\right) \qquad (19b)$$

$$L = -\sqrt{3}\gamma_2 k_2 k_3 - \sqrt{3}i\gamma_3 k_1 k_3 \qquad (19c)$$

$$M = -\frac{\sqrt{3}}{4}\left[(\gamma_2 + \gamma_3)k_2^2 + (\gamma_2 - \gamma_3)k_3^2\right] + \frac{\sqrt{3}}{2}(\gamma_2 k_1 - 2i\gamma_3 k_2)k_1. \qquad (19d)$$

Continuity of current at each interface is now given by continuity of

$$\begin{bmatrix} (\gamma_1 - \frac{1}{2}\gamma_2 - \frac{3}{2}\gamma_3)\frac{\partial}{\partial z} & -\sqrt{3}i\gamma_2 k_2 + \sqrt{3}\gamma_3 k_1 & -\frac{\sqrt{3}}{2}(\gamma_2 - \gamma_3)\frac{\partial}{\partial z} & 0 \\ \sqrt{3}i\gamma_2 k_2 + \sqrt{3}\gamma_3 k_1 & (\gamma_1 + \frac{1}{2}\gamma_2 + \frac{3}{2}\gamma_3)\frac{\partial}{\partial z} & 0 & -\frac{\sqrt{3}}{2}(\gamma_2 - \gamma_3)\frac{\partial}{\partial z} \\ -\frac{\sqrt{3}}{2}(\gamma_2 - \gamma_3)\frac{\partial}{\partial z} & 0 & (\gamma_1 + \frac{1}{2}\gamma_2 + \frac{3}{2}\gamma_3)\frac{\partial}{\partial z} & \sqrt{3}i\gamma_2 k_2 - \sqrt{3}\gamma_3 k_1 \\ 0 & -\frac{\sqrt{3}}{2}(\gamma_2 - \gamma_3)\frac{\partial}{\partial z} & -\sqrt{3}i\gamma_2 k_2 - \sqrt{3}\gamma_3 k_1 & (\gamma_1 - \frac{1}{2}\gamma_2 - \frac{3}{2}\gamma_3)\frac{\partial}{\partial z} \end{bmatrix} \begin{bmatrix} f_1 \\ f_2 \\ f_3 \\ f_4 \end{bmatrix}. \qquad (20)$$

For [310]-grown quantum wells, we take k_1,k_2,k_3 along (0,0,-1), (-1,3,0) and (3,1,0) respectively. For the valence bands we now have

$$P = \frac{1}{2}\gamma_1\left(k_1^2+k_2^2+k_3^2\right) \qquad (21a)$$

$$Q = \frac{1}{2}\gamma_2 k_1^2+\frac{1}{4}(\gamma_2+\gamma_3)k_2^2 - \frac{1}{4}(3\gamma_2+\gamma_3)k_3^2 \qquad (21b)$$

$$L = -\sqrt{3}i\gamma_3 k_1 k_3 - \frac{\sqrt{3}}{5}(2\gamma_2+3\gamma_3)k_2 k_3 \qquad (21c)$$

$$M = \frac{\sqrt{3}}{2}\gamma_2 k_1^2-\frac{\sqrt{3}}{10}(4\gamma_2+\gamma_3)k_2^2 - \sqrt{3}i\gamma_3 k_1 k_2 . \qquad (21d)$$

Continuity of current is now given by continuity of

$$\begin{bmatrix} \left(\gamma_1-\frac{3}{2}\gamma_2-\frac{1}{2}\gamma_3\right)\frac{\partial}{\partial z} & \sqrt{3}\gamma_3 k_1-\frac{\sqrt{3}}{5}i(2\gamma_2+3\gamma_3)k_2 & 0 & 0 \\ \sqrt{3}\gamma_3 k_1+\frac{\sqrt{3}}{5}i(2\gamma_2+3\gamma_3)k_2 & \left(\gamma_1+\frac{3}{2}\gamma_2+\frac{1}{2}\gamma_3\right)\frac{\partial}{\partial z} & 0 & 0 \\ 0 & 0 & \left(\gamma_1+\frac{3}{2}\gamma_2+\frac{1}{2}\gamma_3\right)\frac{\partial}{\partial z} & -\sqrt{3}\gamma_3 k_1+\frac{\sqrt{3}}{5}i(2\gamma_2+3\gamma_3)k_2 \\ 0 & 0 & -\sqrt{3}\gamma_3 k_1-\frac{\sqrt{3}}{5}i(2\gamma_2+3\gamma_3)k_2 & \left(\gamma_1-\frac{3}{2}\gamma_2-\frac{1}{2}\gamma_3\right)\frac{\partial}{\partial z} \end{bmatrix}\begin{bmatrix} f_1 \\ f_2 \\ f_3 \\ f_4 \end{bmatrix} . \qquad (22)$$

The quantum well conduction subbands for each growth direction are obtained by rotating the Hamiltonian (10) for each new direction, and replacing E by (E-V_c) in the barrier, where V_c is the conduction band discontinuity in V(z). The resulting equations are solved by the standard finite-difference method, and we set the conduction band envelope function $\psi(z)\rightarrow 0$, at $z=\pm 2L_z$ where L_z is the well width.

3. Results.

In this section we present the results of the calculated conduction and valence subband dispersion, and also the linear gain spectra, for for each growth direction under consideration. We take the barrier Aluminium concentration x=0.2, and consider well widths of 50Å and 100Å.

TABLE 1
Parameters used in the calculations

	GaAs	$Al_{0.2}Ga_{0.8}As$
γ_1 [a]	6.78	5.64
γ_2	1.92	1.46
γ_3	2.70	2.20
m_c^*	0.0665	0.082 [b]
α_o (eV Å^4)	-2088 [c]	-1305
β_o (eV Å^4)	-2271	-1734
E_o (meV)	1425 [d]	1671
Δ_o (meV)	341	328
E_o' (meV)	4488	4508
Δ_o' (meV)	171	163
E_P (eV)	28.9	28.9
$E_{P'}$ (eV)	6.0	6.0
E_Q (eV)	17.5	17.5
ΔE_o (meV)	—	246

a. GaAs values are from Ref. 25. AlGaAs values are obtained by linear interpolation of the hole masses in the [001] and [111] directions.
b. Calculated using equation (11).
c. α_o and β_o are calculated from Ref. 22.
d. Energy band gaps are taken from Refs. 26 and 27.

Figures 1 and 2 show the n=1 conduction subband dispersion along [100] (to right) and [110] (to left) for [001]-grown wells and along the equivalent in-plane directions for the [111]- and [110]-grown wells. The dispersion for [310]-grown wells is close to that of [001] and is not shown for clarity. It is clear that the confinement energies E($k_{\parallel}$=0) are not the same for any growth direction. This would not be the case had the simple isotropic parabolic effective mass model been used instead. The

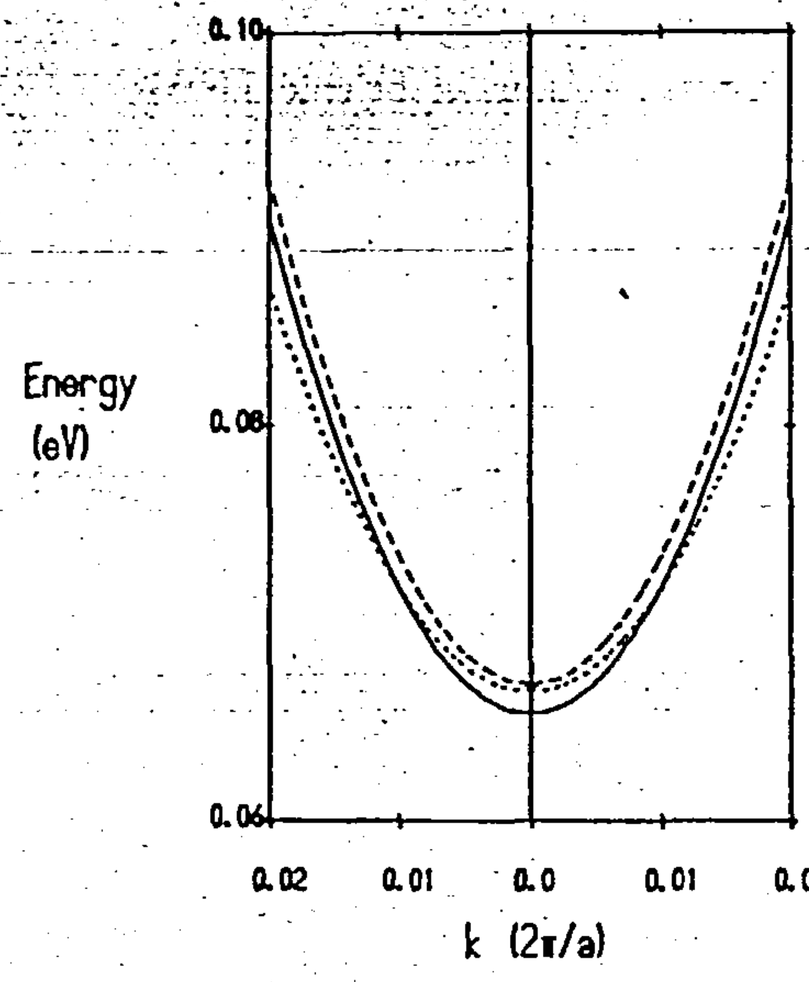

Figure 1. n=1 conduction subband dispersion for a 50Å GaAs-$Al_{0.2}Ga_{0.8}As$ quantum well for the growth axes oriented along the [001] (solid line), [111] (dashed line) and [110] (dotted line) growth directions. For [001] growth, the wavevectors are along [100] (to right) and [110] (to left). The wavevectors are along equivalent in-plane directions for the other growth axes.

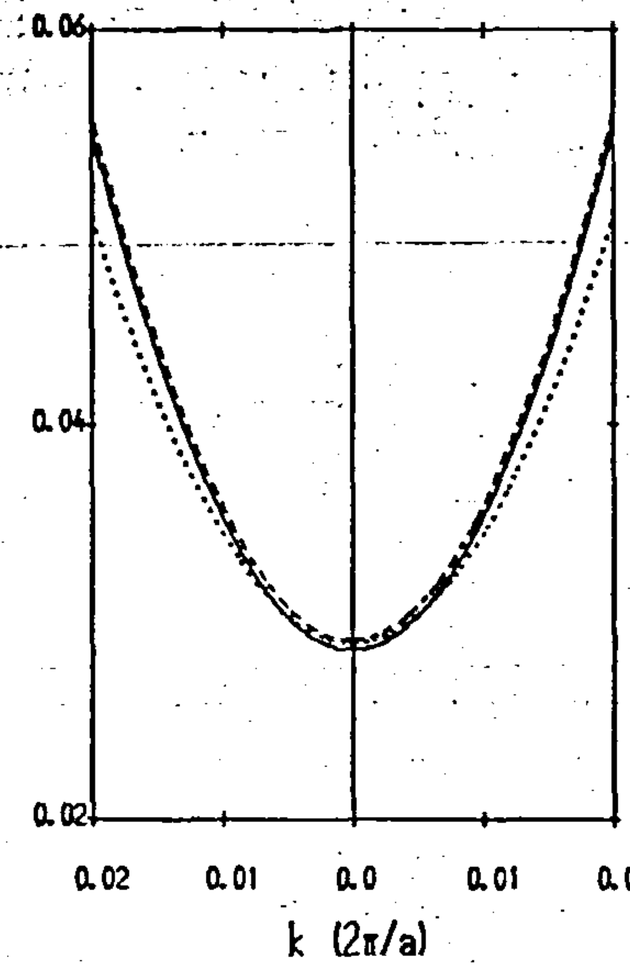

Figure 2. n=1 conduction subband dispersion for a 100Å GaAs-$Al_{0.2}Ga_{0.8}As$ quantum well for the growth axes oriented along the [001] (solid line), [111] (dashed line) and [110] (dotted line) growth directions.

average in-plane zone-centre effective mass is given for each growth direction in Table 2. The most significant departure from the simple parabolic model is the conduction subband effective mass of the [110]-grown wells. This leads to a greater conduction band density of states for this growth direction, the other growth directions having broadly similar effective masses and density of states. The valence subband dispersion is shown in figure 3 (L_z=50Å) and figure 4 (L_z=100Å), for all four growth directions. The subbands are labelled according to their character at $k_{\parallel}$=0. Note that the order of the subbands is not the same for all directions, due to the different quantisation masses, which can be obtained from the diagonal elements of the Luttinger-Kohn Hamiltonian for each direction. For well widths of 50Å, the [111] growth direction HH1 subband has a pronounced 'light-hole' character extending to $k_{\parallel}>0.025(2\pi/a)$ giving a smaller density of states for this subband than in the other growth directions. Also noticeable is the separation in energy between the first and second confined subbands which is greatest for the [111]-grown wells. For both [111] and [110] the second subband is HH2, therefore it is expected that the TM mode laser gain will be less than the TE mode gain for these orientations, and the TM modes will be effectively suppressed.

TABLE 2

Calculated average zone-centre effective masses

Well width	Growth direction	m_{CB1}	m_{HH1}	m_{LH1}	m_{HH2}
50Å	[001]	0.072	0.172	-1.872	0.110
	[111]	0.073	0.133	0.045	-0.078
	[110]	0.0904	0.173	0.060	-0.111
	[310]	0.0735	0.172	-0.552	0.106
100Å	[001]	0.0696	0.159	-0.254	0.079
	[111]	0.0687	0.127	0.104	1.381
	[110]	0.0865	0.157	0.038	-0.053
	[310]	0.0707	0.158	-0.101	0.053

It is seen from figures 3 and 4 that an axial approximation for the valence subband dispersion (i.e. neglect of in-plane subband warping) would be reasonable for the [001], [111] and [310] oriented wells, but would not be good for the [110] orientation. The anisotropy of the dispersion in this case is quite apparent, and is it unlikely that an axial approximation would be satisfactory. Nevertheless, it is expected that our results for the gain spectra using the non-axial model considered here will still differ noticeably from an axial model.

The calculated TE mode gain spectra, using standard density matrix theory,[28] and assuming a constant intra-band relaxation time of 100 fsec, are shown in figures 5 and 6, for well widths of 50Å and 100Å respectively. The

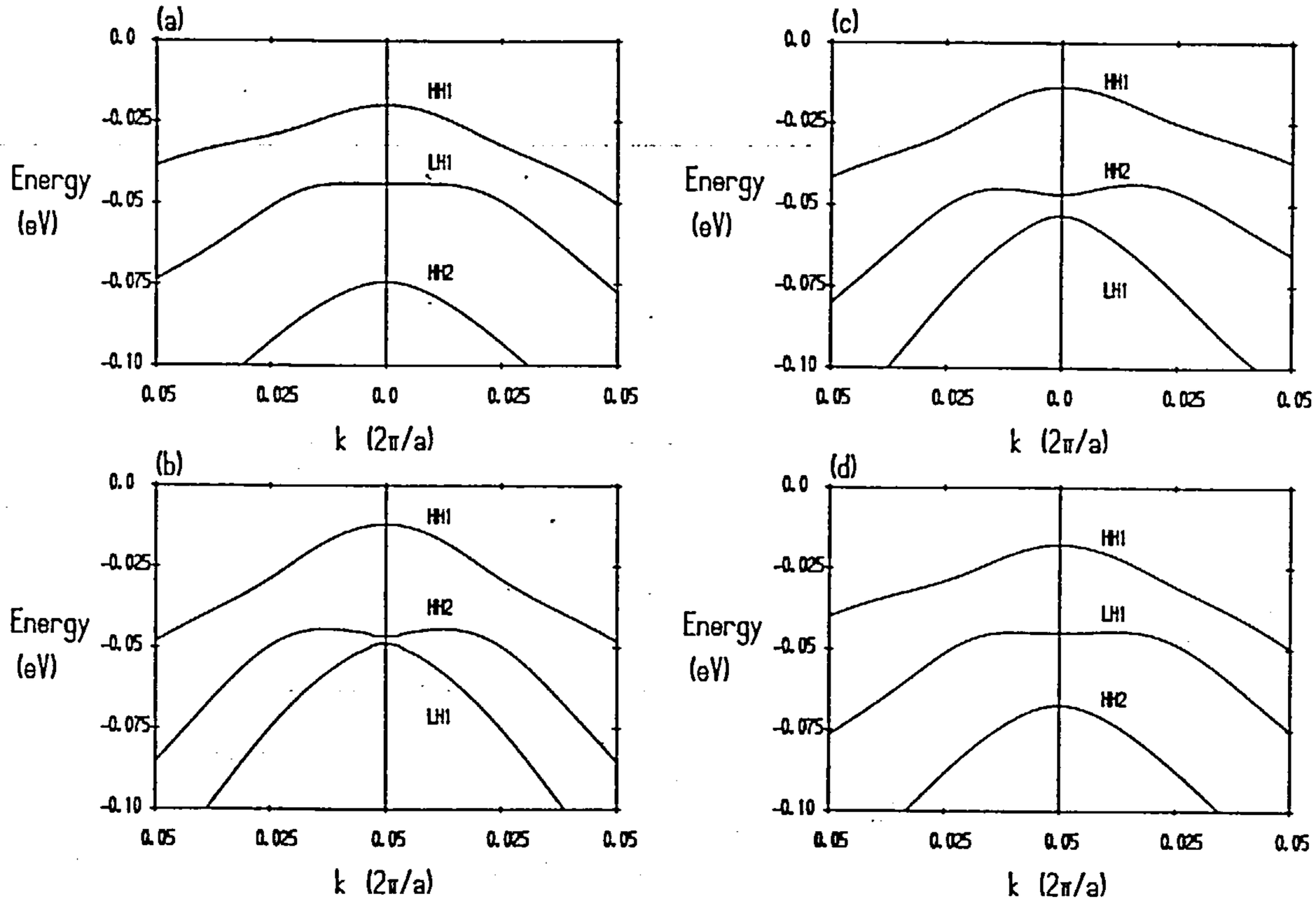

Figure 3. Valence subband dispersion for a 50Å GaAs-$Al_{0.2}Ga_{0.8}As$ quantum well for the growth directions (a) [001], (b) [111], (c) [110] and (d) [310].

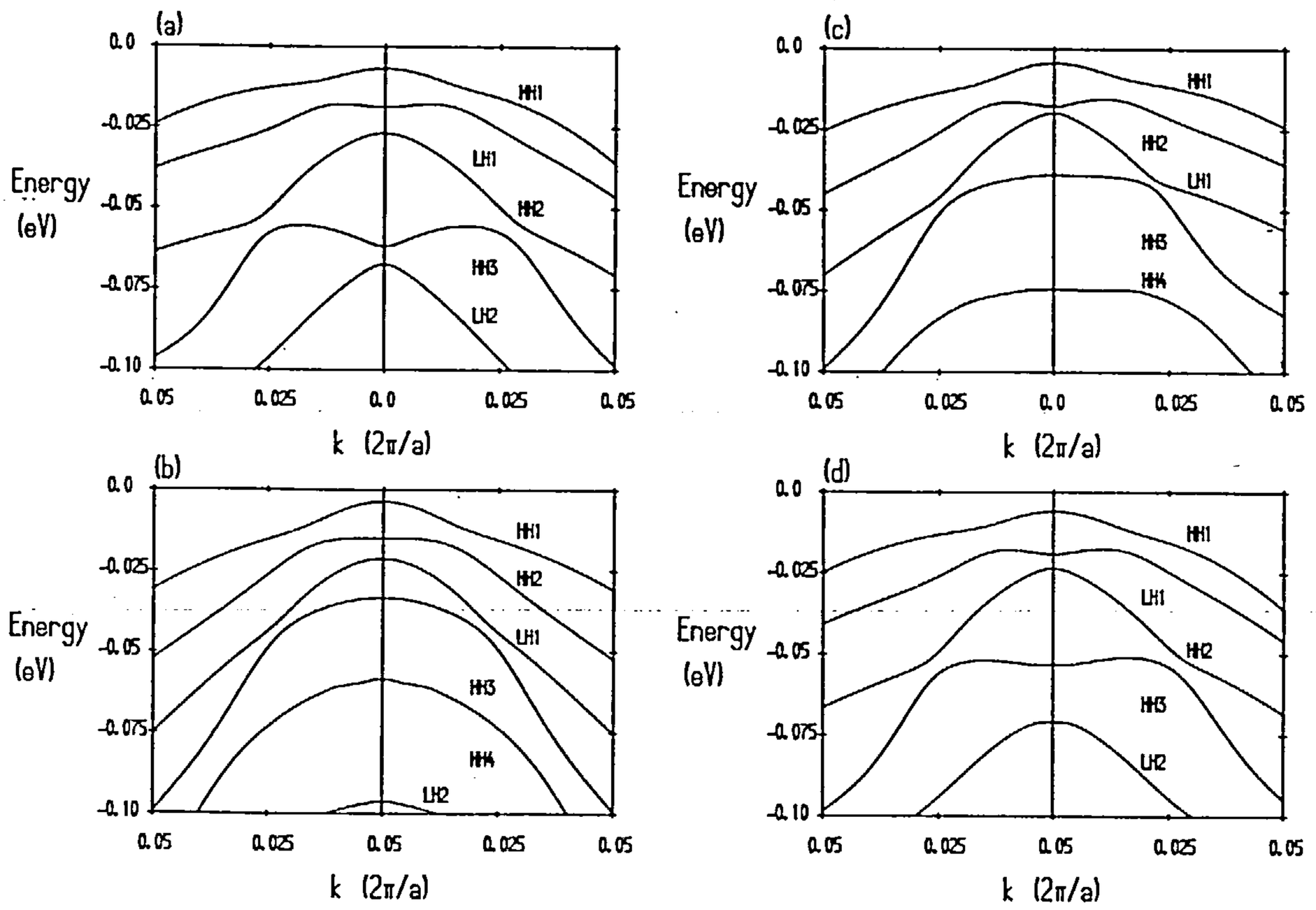

Figure 4. Valence subband dispersion for a 100Å GaAs-$Al_{0.2}Ga_{0.8}As$ quantum well for the growth directions (a) [001], (b) [111], (c) [110] and (d) [310].

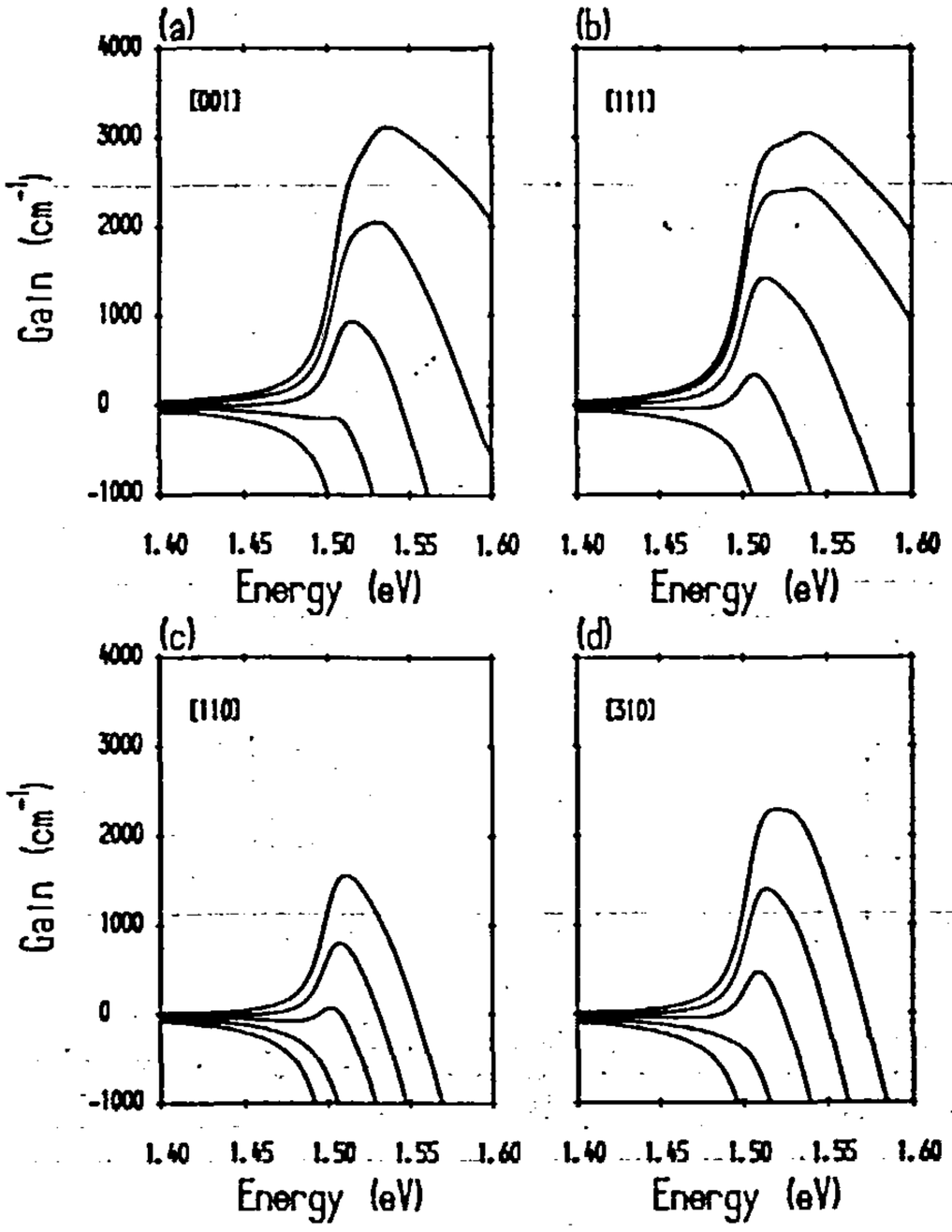

Figure 5. Linear gain spectra of the 50Å quantum wells for TE mode polarisation, and for injected carrier densities of 2-6x10^{18}cm^{-3}.

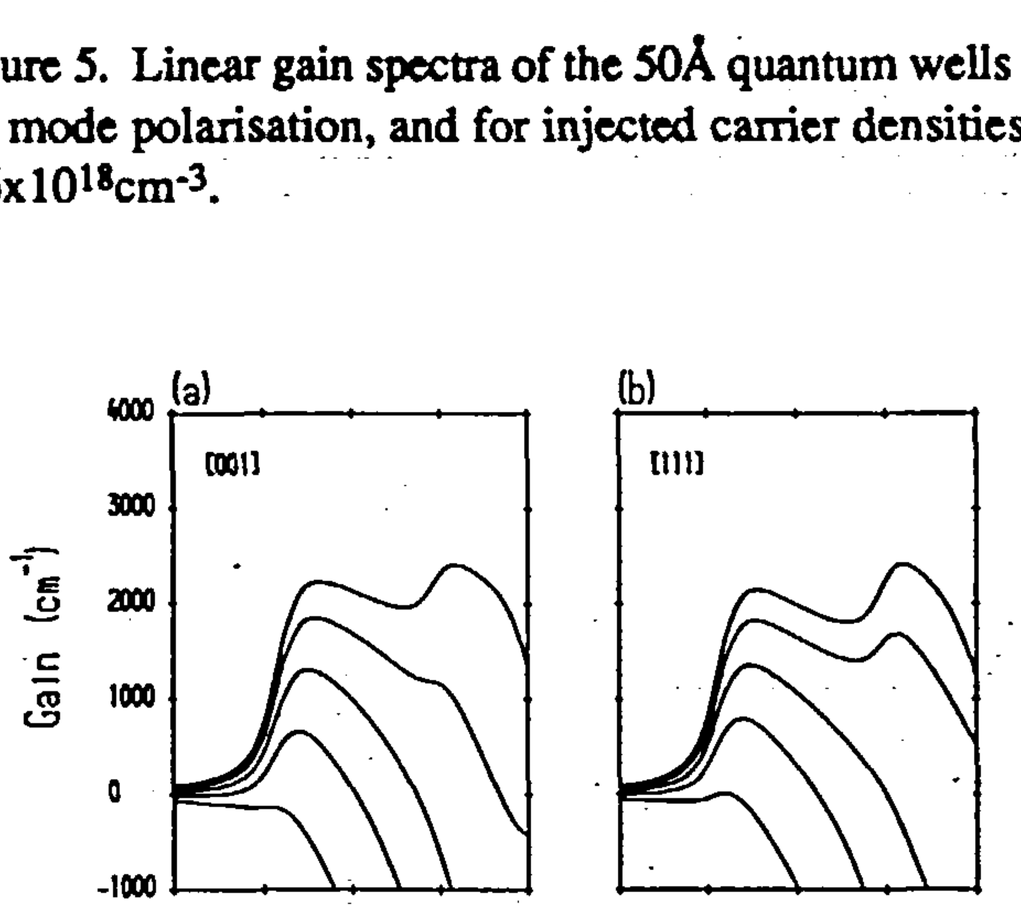

Figure 6. Linear gain spectra of the 100Å quantum wells for TE mode polarisation, and for injected carrier densities of 2-6x10^{18}cm^{-3}.

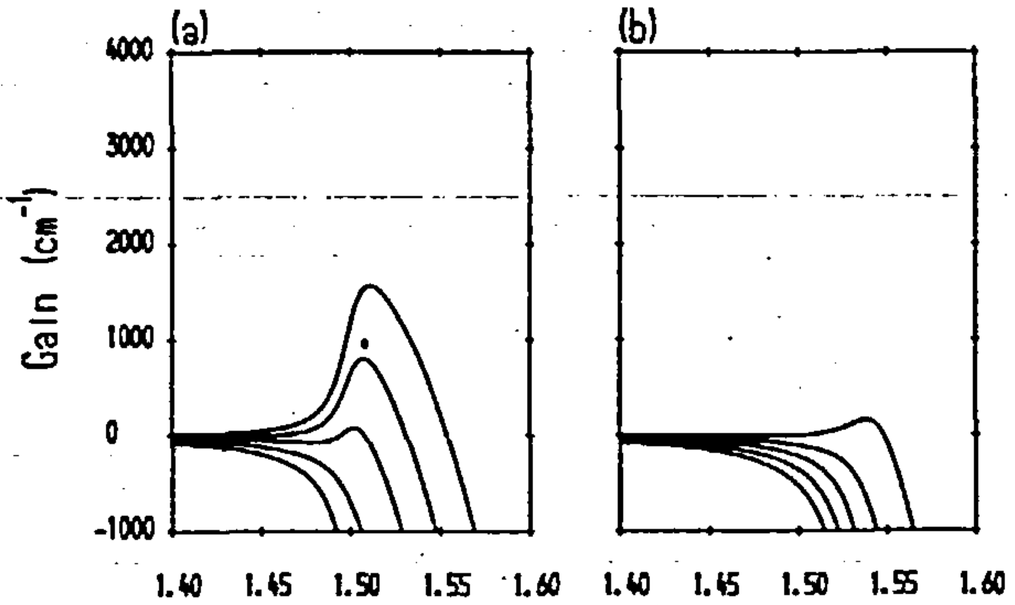

Figure 7. Linear gain spectra of 50Å [110]-oriented quantum well for (a) TE mode polarisation and (b) TM mode polarisation for injected carrier densities of 2-6x10^{18}cm^{-3}.

effect of the above-mentioned 'light-hole' nature of the [111] HH1 subband clearly reduces the threshold for TE mode gain compared to all the other orientations. Note that the results for [001] and [310] are broadly similar, and it is seen from figures 3 and 4 that the valence subband dispersion for these orientations is also similar. In the case of [110]-grown wells, the gain is the lowest of all the systems considered here, and the gain is in general a function of the subband dispersion, the separation between the subbands and the confinement ordering of the 'light' and 'heavy' subbands. It is also interesting to note that for 50Å [110]-oriented wells the TE mode gain far exceeds that for the TM mode. This can be seen more clearly in figure 7, where the TE mode gain and TM mode gain for 50Å [110]-oriented wells is shown. The reduction in TM mode gain is quite remarkable.

TABLE 3

Calculated threshold current densities

Well width	Orientation	TE (A/cm^2)	TM (A/cm^2)
50 Å	[001]	147	181
	[111]	119	176
	[110]	236	407
	[310]	183	253
100 Å	[001]	147	158
	[111]	134	140
	[110]	203	223
	[310]	146	160

For 100Å wells, the possibility of n=2 state lasing (TE modes only) is shown in figure 6, where the n=2 gain peak becomes larger than the n=1 peak at injected carrier

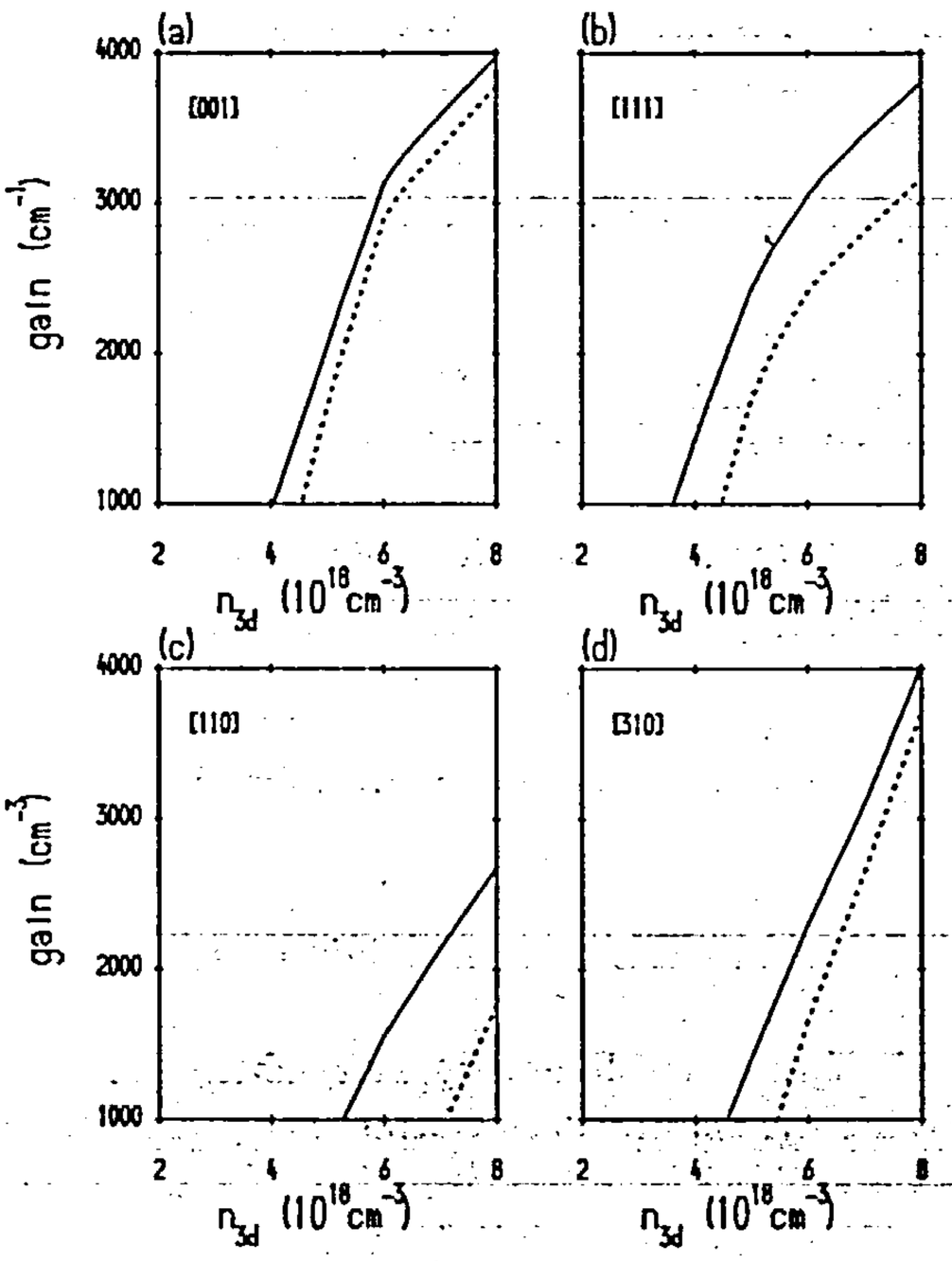

Figure 8. Peak gain versus carrier density for TE (solid line) and TM (dashed line) for 50Å wells.

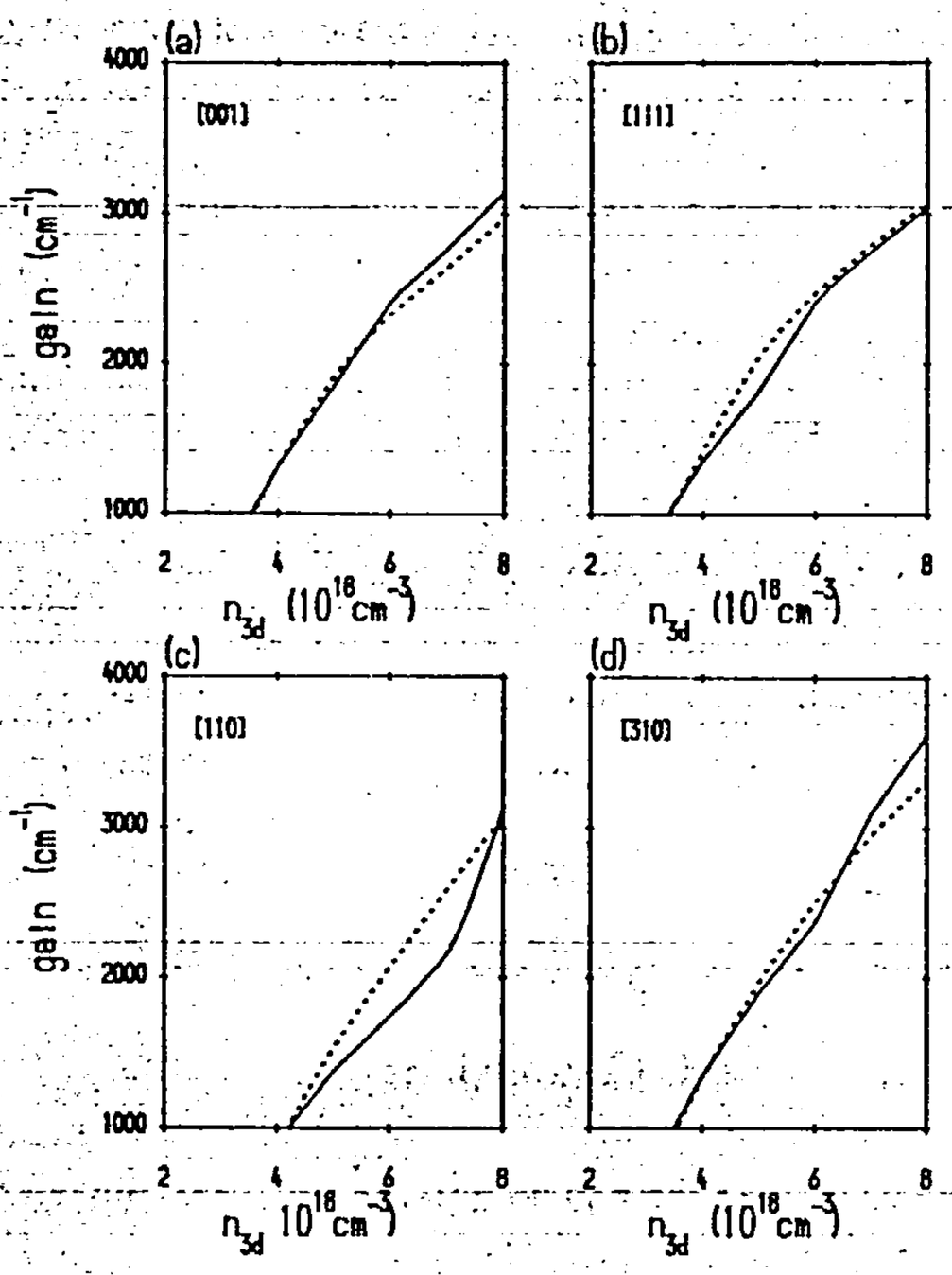

Figure 9. Peak gain versus carrier density for TE (solid line) and TM (dashed line) for 100Å wells.

densities around $6x10^{18}cm^{-3}$. The peak gain versus carrier density is shown in figure 8 (L_z=50Å) and figure 9 (L_z=100Å). The threshold for TE modes is less than that of TM in all cases. However, at higher carrier densities, TM gain is often higher, resulting in the possibility of TE-TM mode-hopping. For the range of injected carrier densities considered here ($2\text{-}6x10^{18}cm^{-3}$), the TE gain in 50Å wells is always higher than TM. However in 100Å wells this is not the case, and the TM gain will always exceed the TE gain at higher injection curents. Further increase of injection current can lead to n=2 TE mode lasing. In the case of [110] wells, for L_z=100Å, TM modes are favoured with respect to TE modes over almost the entire range of carrier densities considered, in stark contrast to the situation for 50Å wells.

We calculate the threshold current density from the condition that the modal gain balances the internal losses at threshold, giving $\Gamma g=\alpha+(1/L)\ln(1/R)$. We take a cavity length L=500μm, $\alpha=10cm^{-1}$ for the internal losses and mirror reflectivity R=0.32. For GaAs-AlGaAs a typical value of the optical confinement factor is given by $\Gamma=2.5x10^{-4}L_z$, where L_z is the well width in Angstroms. The threshold current density may be given as[29]

$$J = eN_w L_z\left(\frac{n_{thr}}{t_s}\right), \qquad (23)$$

where t_s is the electron recombination lifetime with the value $t_s=2.6x10^6(n_{thr})^{-0.81}$ in bulk GaAs. Using this value of t_s and equation (23), and estimating n_{thr} from the results given in figures 5 and 6, the threshold current densities are calculated as in Table 3. The TE mode threshold current density for each orientation with respect to that for [001]-grown wells is given in Table 4. Note that the [111]-grown wells have a lower threshold than any other orientation, and the [110]-grown wells have a much higher threshold. The values for the reduction in J_{thr} for [111] with respect to [001] agree with the experimental values obtained in Reference 14.

TABLE 4

Threshold current density with respect to [001]-orientation

Orientation	L_z=50Å	L_z=100Å
[111]	-19%	-10%
[110]	+60%	+38%
[310]	+24%	0%

The comparison between the threshold current for TM mode lasing with respect to that for TE mode lasing is given below in Table 5, for all the systems considered. Note that the decrease for [111] in comparison with [001] is larger

for narrow wells (L_z=50Å) and decreases with increasing well width. The reduction for L_z=50Å is estimated to be 19%, and for L_z=100Å is only 10%. This trend is in agreement with those of Ref 16, which used a simpler theoretical model, but the calculated values of the reduction differ slightly, as expected.

TABLE 5
Comparison of the TM mode threshold current with respect to the TE mode threshold current

Orientation	L_z=50Å	L_z=100Å
[001]	+23%	+8%
[111]	+48%	+5%
[110]	+73%	+10%
[310]	+38%	+10%

4. Conclusions

We have calculated the conduction- and valence-subband dispersion for 50Å and 100Å GaAs-$Al_{0.2}Ga_{0.8}As$ quantum wells, with the growth axes along the [001], [111], [110] and [310] directions.

We have shown that for thin wells (L_z=50Å) the TE laser modes predominate, efficiently suppressing TM laser operation and reducing the possibility of TE-TM mode-hopping. The threshold current density for the [111]-oriented wells is lower than that for any other growth direction considered, in agreement with earlier experimental results.[14] For [110]-grown wells, with L_z=50Å, lasing takes place for TE modes only, while for larger well widths (L_z>100Å) TM modes are favoured over a wide range of operating currents.

References

1 T. Mimura, S. Hiyamizu, T. Fujii and K. Nanbu, Japanese Journal of Applied Physics **19**, L225 (1980).

2 L. Esaki and R. Tsu, IBM J. Res. Dev. **14**, 61 (1970).

3 M Altarelli, in *Heterojunctions and Semiconductor Superlattices*, edited by G. Allan, G. Bastard, N Boccara, M. Lannoo and M. Voos (Springer, Berlin, 1986).

4 D.A. Broido and L.J. Sham, Physical Review B **31**, 888 (1985).

5 G. Bastard, Physical Review B **24**, 5693 (1981).

6 G. Bastard and J.A. Brum, IEEE Journal of Quantum Electronics, **QE-22**, 1625 (1986).

7 J.N. Schulman and Y.C. Chang, Physical Review B **31**, 2056 (1985).

8 Y.C. Chang, Physical Review B **37**, 8215 (1988).

9 G.E.W. Bauer and T. Ando, Physical Review B **34**, 1300 (1986).

10 M. Jaros, K.B. Wong and M.A. Gell, Physical Review B **31**, 1205 (1985).

11 D. Ninno, M.A. Gell and M. Jaros, Journal of Physics C **19**, 3845 (1986).

12 J.M. Luttinger and W. Kohn, Physical Review **97**, 869 (1955).

13 H. Kroemer, K.J. Polasko and S.C. Wright, Applied Physics Letters **36**, 763 (1980).

14 T. Hayakawa et al, Journal of Applied Physics **64**, 297 (1988);
ibid, Applied Physics Letters **52**, 339 (1988).

15 R. Eppenga and M.F.H. Schuurmans, Physical Review B **37**, 10923 (1988).

16 W. Batty, U. Ekenberg, A. Ghiti and E.P. O'Reilly, Semiconductor Science and Technology **4**, 904 (1989):
A. Ghiti, W. Batty, E.P. O'Reilly, Superlattices and Microstructures **7**, 353 (1990).

17 L.W. Molenkamp et al, Physical Review B **38**, 4314 (1988).

18 J.M. Luttinger, Physical Review **102**, 1030 (1956).

19 L.C. Andreani, A. Pasquarello and F. Bassani, Physical Review B **36**, 5887 (1987).

20 M. Dobrowolska, Y. Chen, J.K. Furdyna and S. Rodriguez, Physical Review Letters **51**, 134 (1983).

21 D. Stein, K.v. Klitzing and G. Weimann, Physical Review Letters **51**, 130 (1983).

22 M. Braun and U. Rössler, Journal of Physics C **18**, 3365 (1985).

23 C. Hermann and C. Weisbuch, Physical Review B **15**, 823 (1977).

24 U. Ekenberg, Physical Review B **40**, 7714 (1989)

25 B.V. Shanabrook, O.J. Glenbocki and D.A. Broido, Superlattices and Microstructures **5**, 503 (1989).

26 *Numerical Data and Functional Relationships in Science and Technology*, vol. 17 of Landolt-Börnstein, ed. by O. Madelung (Springer, Berlin, 1982)

27 S. Adachi, Journal of Applied Physics **58**, R1 (1985).

28 See for example: A. Yariv, *Quantum Electronics* (Wiley, New York, 1975)

29 M. Yamada, S. Ogita, M. Yamagishi and K. Tabata, IEEE Journal of Quantum Electronics **21**, 640 (1985)

EFFECTS OF IMPURITY INDUCED DISORDER ON THE INDEX OF REFRACTION IN GaAs-AlGaAs QUANTUM WELLS

Alistair T. Meney

Laser and Optical Systems Engineering Group
Department of Mechanical Engineering
University of Glasgow
Glasgow G12 8QQ
Scotland U.K.

(Received 3 July 1991)

A theoretical model for the refractive index in impurity induced disordered (IID) GaAs-AlGaAs quantum wells is presented. The electron and hole dispersion is obtained from the Luttinger-Kohn Hamiltonian and a bulk conduction band Hamiltonian which includes the effects of nonparabolicity. We solve the Hamiltonians using a finite difference method which is flexible enough to accommodate the potential profile in disordered quantum wells. Both TE and TM refractive indices are calculated, and our results are in excellent agreement with the published experimental data available. The inter-diffusion coefficient of Al and Ga is obtained by comparing our calculated subband level results, including the effects of excitons, to the published experimental data. The theoretical model allows accurate calculation of the index of refraction, allowing the refractive properties of impurity induced disordered wells to be accurately tailored experimentally.

1. Introduction.

The process of impurity induced disordering (IID) or layer intermixing in semiconductor quantum well structures has been the subject of much research effort since its discovery in 1980.[1] Several experimental reports have been concerned with the shift in the fundamental absorption edge in IID material[2,3], while, others[4] have concentrated on the reduced absorption due to the intermixing process.

The change in absorption in these intermixed quantum wells leads to a change in the refractive index. Recently, experimental results have been reported[5] which demonstrate the reduction in the index of refraction in a GaAs-AlGaAs quantum well structure. The experiments were performed using the electrically neutral donor species boron and fluorine, which should have little effect on the absorption coefficient at photon energies near the bandgap.

It is the aim of this paper to obtain a theoretical model of the TE and TM mode refractive indices in impurity induced disordered quantum wells, and to compare the results of our model calculations with the experimental results.

2. Method of Calculation.

We calculate the potential profile after disordering by considering the interdiffusion of the aluminium from the barrier regions into the wells, along with the out-diffusion of gallium from the wells into the barriers. The excess concentration of gallium in the well regions is assumed to obey a standard Fick's law diffusion process when annealed in the presence of the neutral donor species, with the inter-diffusion coefficient depending on both donor species concentration and annealing temperature.

The experimental results obtained in Ref. 5 were obtained with a 2-D doping concentration of fluorine at $10^{14}cm^{-2}$ and an annealing temperature of 890°C for 90 minutes, and the multiple quantum well structure had an initial barrier aluminium concentration of x=0.26. The

0749-6036/92/010047+07 $02.00/0

surplus of gallium in each well is then taken as y=0.26. The diffused profile g(z) of gallium is therefore given by

$$g(z) = (1-y) + \frac{y}{2}\sum_{n=-m}^{n=+m}\left\{\operatorname{erf}\frac{L_z+2n\left(\frac{L_z}{2}+\frac{L_B}{2}\right)-z}{2\sqrt{Dt}} + \operatorname{erf}\frac{L_z-2n\left(\frac{L_z}{2}+\frac{L_B}{2}\right)+z}{2\sqrt{Dt}}\right\}, \quad (1)$$

where the origin z=0 is at the centre of the middle well region, L_B is the barrier width, L_z is the well width and the sum is over the (2m+1) well and barrier regions.

We further assume that the local conduction/valence band offset remains in the ratio 65:35 and that the local bandgap shift is given by $\Delta E=1.247x(z)$, where x(z) is the aluminium concentration along the z (growth) direction. The aluminium concentration profile x(z) is obtained from equation (1) as x(z)=1-g(z). To simplify the calculations we set the conduction band confinement potential to zero at the centre of each well and similarly for the valence band. This 'shifts' the energy gap at z=0 to $E_g+\Delta E(z=0)$.

We consider an MQW structure composed of five well regions, surrounded by thick substrate layers of $Al_{0.26}Ga_{0.74}As$. The MQW structure is composed of alternating regions of GaAs and $Al_{0.26}Ga_{0.74}As$, the well widths are L_z=60Å and the barrier widths are L_B=60Å. This limits the sum in equation (1) to 5 terms only. The structure is taken to be grown along the [001] direction and we calculate the quantised hole subbands using the Luttinger-Kohn Hamiltonian given by[6]

$$H = -\begin{vmatrix} P+Q & L & M & 0 \\ L^* & P-Q & 0 & M \\ M^* & 0 & P-Q & M \\ 0 & M^* & -L^* & P+Q \end{vmatrix} + V(z), \quad (2)$$

where

$$P = \frac{1}{2}\gamma_1\left(k_x^2+k_y^2+k_z^2\right)$$
$$Q = \frac{1}{2}\gamma_2\left(k_x^2+k_y^2-2k_z^2\right)$$
$$L = -\sqrt{3}\gamma_3\left(k_y+ik_x\right)k_z$$
$$M = \frac{\sqrt{3}}{2}\gamma_2\left(k_x^2-k_y^2\right)-\sqrt{3}i\gamma_3 k_x k_y\,. \quad (3)$$

In equation (2) V(z) represents the confinement potential due to the material composition and is obtained from equation (1). We average the effective masses in the well and barrier regions, which gives the averaged Luttinger parameters as γ_1=5.98, γ_2=1.60, γ_3=2.35 and the averaged conduction band mass as $m_c=0.0774m_0$. Values of the bulk masses are obtained from Ref. 7. We calculate the quantised conduction band levels from the Hamiltonian of Braun and Rössler (Ref. 8), neglecting the spin-splitting term, which gives the bulk conduction band energy as

$$E = \frac{\hbar^2k^2}{2m^*}+\alpha_o k^4+\beta_o\left(k_x^2k_y^2+k_y^2k_z^2+k_z^2k_x^2\right)+V(z), \quad (4)$$

where the nonparabolicity parameters α_o and β_o are defined in Ref. 8, and where we have added the confinement potential V(z). As well as averaging the zone-centre conduction band effective mass, we have also averaged the α_o and β_o nonparabolicity parameters which then have the values α_o=-1699 eVÅ^4 and β_o=-1984 eVÅ^4.

Equations (2) and (4) are solved using the standard finite difference method, with the potentials V(z) in the conduction and valence bands obtained from equation (1) and the boundary condition that the wavefunctions vanish inside each substrate region. The error introduced by using average effective masses rather than considering position-dependent effective masses is expected to be small. This method can therefore accommodate an arbitrary potential profile V(z) and is extremely useful when considering the confinement potentials arising due to the inter-diffusion process.

To model the continuum states, we ignore the anisotropy in the conduction band dispersion and use the dispersion relation given by[9]

$$\frac{\hbar^2k^2}{2m^*} = E(1+\alpha E), \quad (5)$$

where

$$\alpha = \frac{1}{E_g}\left(1-\frac{m^*}{m_o}\right)^2. \quad (6)$$

For simplicity we take parabolic continuum heavy- and light-hole dispersion, with averaged effective masses

$m_{hh}=0.49m_o$ and $m_h=0.091m_o$. We also include the HH1-CB1 and LH1-CB1 exciton states in our calculation by performing a variational calculation in **k**-space[10] with a Gaussian-type trial function given by

$$\Phi_{eh}(k_{||}) = (2\pi\lambda)^{1/2} e^{-\lambda k_{||}^2/4}, \qquad (7)$$

for each exciton state, which incorporates the effects of the nonparabolic subband dispersion, and where λ is the variational parameter.

To determine the imaginary part of the dielectric function we consider three separate contributions, which sum as

$$\varepsilon_i(\hbar\omega) = \varepsilon_i^{ex}(\hbar\omega) + \varepsilon_i^{QW}(\hbar\omega) + \varepsilon_i^{bulk}(\hbar\omega), \quad (8)$$

where ε_i^{ex} is the contribution due to the exciton states, ε_i^{QW} is the band-to-band quantised level contribution and ε_i^{bulk} is the contribution due to the continuum states. Each term is given by

$$\varepsilon_i^{QW}(E) = \frac{1}{\pi\varepsilon_o L_Z}\frac{e^2\hbar^2}{m^2E^2}\sum_{nn'}\int dk_{||}|\hat{\varepsilon}\cdot p_{nn'}|\delta(E_n^c - E_{n'}^v - E)$$

$$\varepsilon_i^{bulk}(E) = \frac{1}{\pi\varepsilon_o}\frac{e^2\hbar^2}{m^2E^2}\sum_{v=l,h}\int dk|\hat{\varepsilon}\cdot p_{nn'}|\delta(E^c - E^v - E)$$

$$\varepsilon_i^{ex}(E) = \frac{1}{\pi\varepsilon_o L_Z}\frac{e^2\hbar^2}{m^2E^2}\sum_{v=l,h}\left|\frac{1}{2\pi}\int dk_{||}\Phi_{eh}^{c,v}p_{nn'}\right|^2\delta(E_{ex} - E) \quad \ldots (9)$$

where L_Z is the total length of the multiple quantum well structure, $p_{nn'}$ is the momentum matrix element between a conduction band state and a valence band state, E_{ex} is the exciton transition energy and $\Phi_{eh}(k_{||})$ are the Fourier components of the exciton envelope function given by equation (7).

We replace the delta functions in equation (9) with Lorentzian lineshape functions, with linewidths of 10meV for the band-to-band contributions and 5meV for the exciton contributions respectively. We have taken these as realistic values to model the experimental conditions.

The real part of the dielectric function is then obtained from the imaginary part via the Kramers-Kronig relation

$$\varepsilon_r(\omega) = 1 + \frac{2}{\pi}P\int_0^\infty \frac{\omega'\varepsilon_i(\omega')}{(\omega')^2 - \omega^2}\,d\omega'. \qquad (10)$$

The total dielectric function can then be given as

$$\varepsilon_r^{total} = \varepsilon_r^B - \varepsilon_r^B(\Gamma) + \varepsilon_r(\Gamma), \qquad (11)$$

where $\varepsilon_r^B(\Gamma)$ is the bulk contribution to ε_r^B from the states in the vicinity of the Γ-point, and $\varepsilon_r(\Gamma)$ is our calculated contribution from equations (8), (9) and (10). Note that since in our case the barrier widths and the well widths are equal, then the average over the bulk materials in ε_r^B contains no length factors.

The optical matrix elements for the bound subband transitions are different for TE and TM polarisation since the natural direction for angular momentum quantisation is the growth axis along z. The TE mode matrix elements can be given as

$$|\hat{\varepsilon}\cdot p|^2 = \langle P\rangle^2 \left\{ \tfrac{3}{2}\langle\phi_c|\varphi^{(1)}\rangle^2 + \tfrac{1}{2}\langle\phi_c|\varphi^{(2)}\rangle^2 + \tfrac{1}{2}\langle\phi_c|\varphi^{(3)}\rangle^2 + \tfrac{3}{2}\langle\phi_c|\varphi^{(4)}\rangle^2 \right\}, \qquad (12)$$

and the TM mode matrix elements as

$$|\hat{\varepsilon}\cdot p|^2 = \langle P\rangle^2 \left\{ 2\langle\phi_c|\varphi^{(2)}\rangle^2 + 2\langle\phi_c|\varphi^{(3)}\rangle^2 \right\}, \qquad (13)$$

where ϕ_c is the conduction subband envelope function, the $\varphi^{(i)}$ are the elements of the four-component hole envelope function solutions of the Luttinger-Kohn Hamiltonian, and $\langle P\rangle^2$ is the bulk-averaged momentum matrix element.

3. Results.

In Figure 1 we show the calculated HH1-CB1 exciton transition energy shifts as a function of the diffusion length $L=\sqrt{Dt}$, where D is the diffusion coefficient and t is the diffusing time. For a known experimental transition energy shift and diffusing time, it is

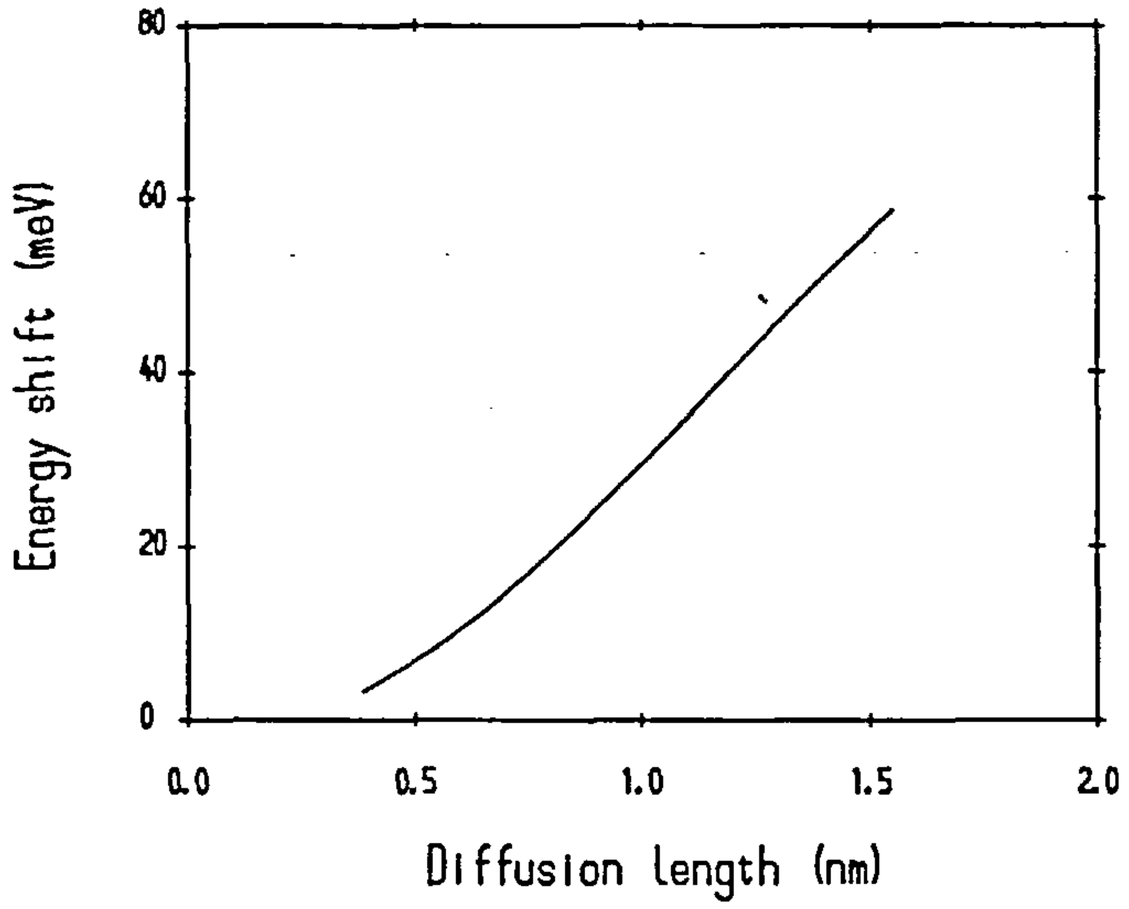

Figure 1. Calculated shift in the lowest quantum well transition energy (in meV) as a function of the diffusion length $L=\sqrt{Dt}$ (nm).

straightforward to estimate the inter-diffusion coefficient for the experimental conditions from the results given in this Figure.

In Ref. 5, the values quoted are a HH1-CB1 exciton peak shift of 40meV, after an annealing time of 90 minutes. Therefore from Figure 1 we estimate the inter-diffusion coefficient to be $D=2.5\times10^{-18}cm^2/sec$, for the given experimental conditions. This value compares well with that estimated experimentally in Ref. 11, where the inter-diffusion coefficient with fluorine doping and annealed at 800°C is estimated to be $3\times10^{-18}cm^2/sec$.

Using equation (1) the confinement potentials at t=0 minutes and t=90 minutes are as shown in Figure 2. There is still little reduction in the peak value of this potential (which occurs at the middle of each barrier region) but the shape of the potential after 90 minutes has completely changed from the original step-like potential. This indicates that the most significant factor in the transition energy shift at small diffusion lengths is the change in the quantised subband energy levels due to the change in the potential profile, and is not simply due to the amount of aluminium which has diffused to the well centres, as has previously been suggested.[12] At higher values of diffusion length, however, the indiffused aluminium concentration at the well centres will make an increasingly important contribution to the total energy shift.

At photon energies below the HH1-CB1 exciton peak, both the TE and TM mode absorption decreases with

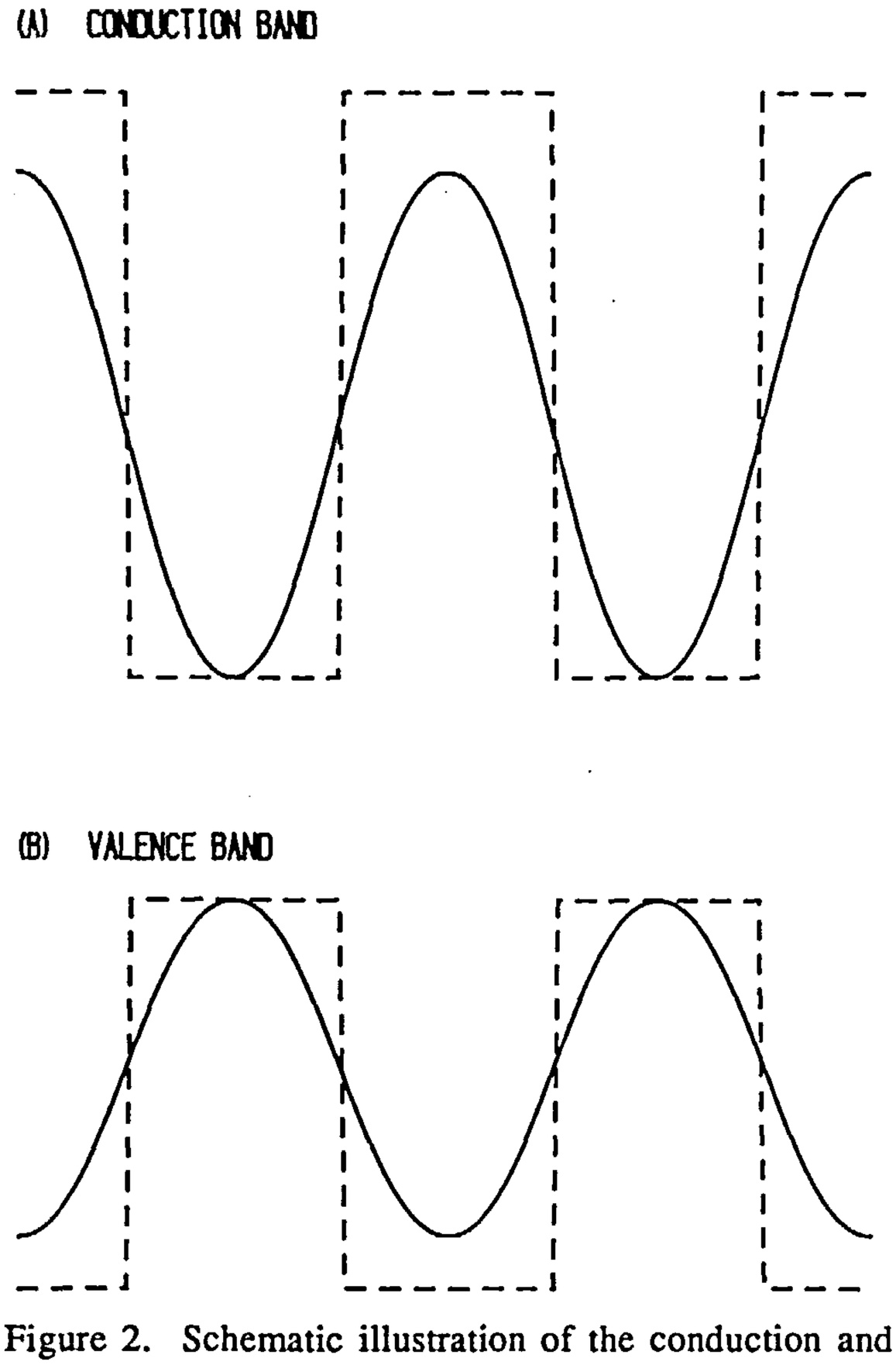

Figure 2. Schematic illustration of the conduction and valence band confinement potentials along the growth axis at t=0 minutes (broken line) and t=90 minutes (solid line) with a diffusion coefficient of $D=2.5\times10^{-18}cm^2/sec$, for two well regions. The potential at the centre of the wells has been set to zero.

the diffusion time. In Figures 3 and 4 we give the calculated TE and TM absorption results at several wavelengths. The λ=835nm line is just below the HH1-CB1 exciton peak at t=0 minutes, which we obtain as 1.49eV. We have normalised this value to 1, and normalised all the other results in Figures 3 and 4 with respect to this. The absorption is seen to decrease very rapidly initially, with the TE mode absolute values greater than the TM mode at each wavelength considered. However, as the absorption decrease tails off, after around 60 to 90 minutes, all results start to approach each other in magnitude. After this point there is little difference between the TE and TM absorption and the TE-TM anisotropy, characteristic of bound quantum well states, decreases. The

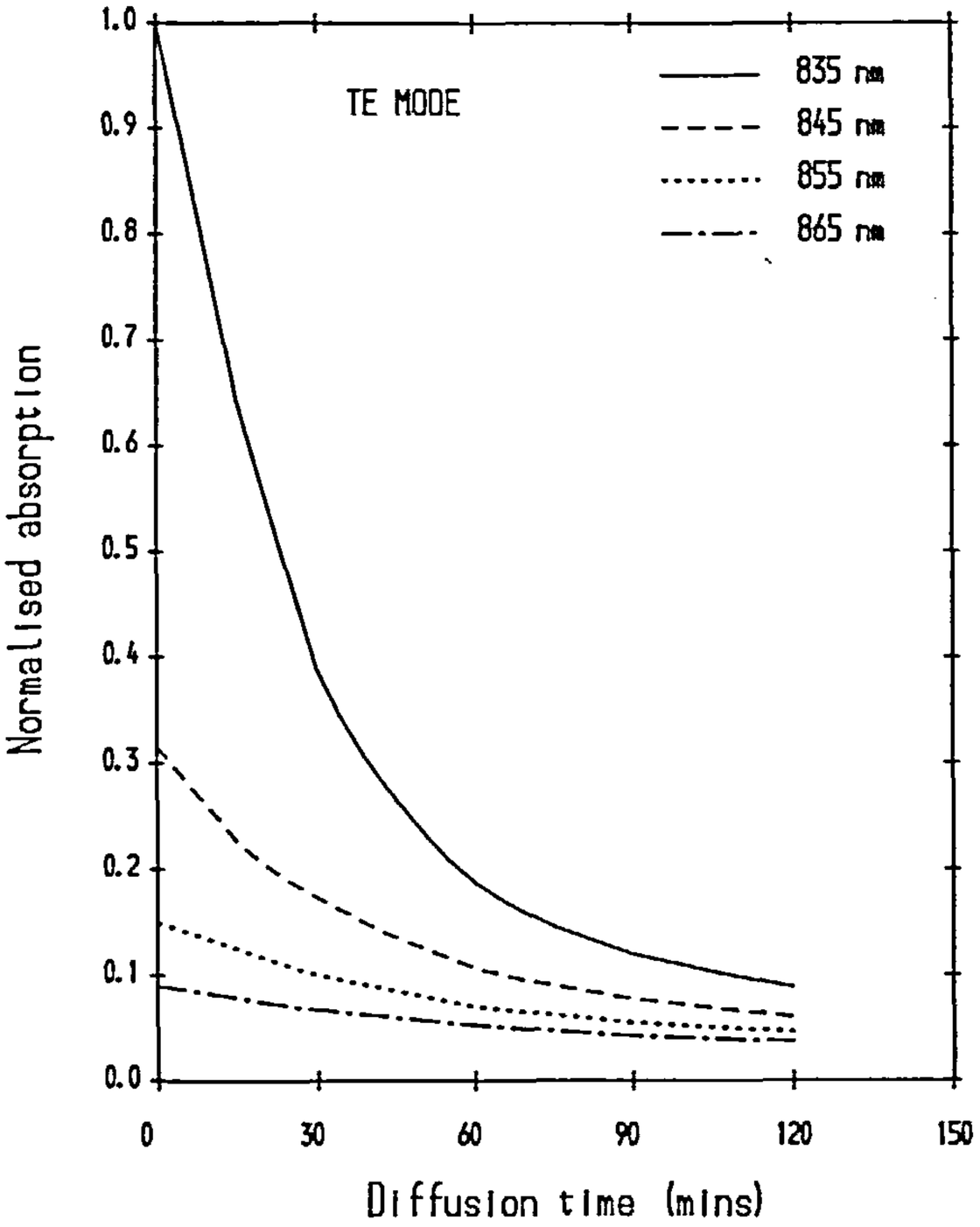

Figure 3. Relative TE mode absorption coefficient as a function of the disordering time at four different wavelengths for energies below the HH1-CB1 exciton transition energy.

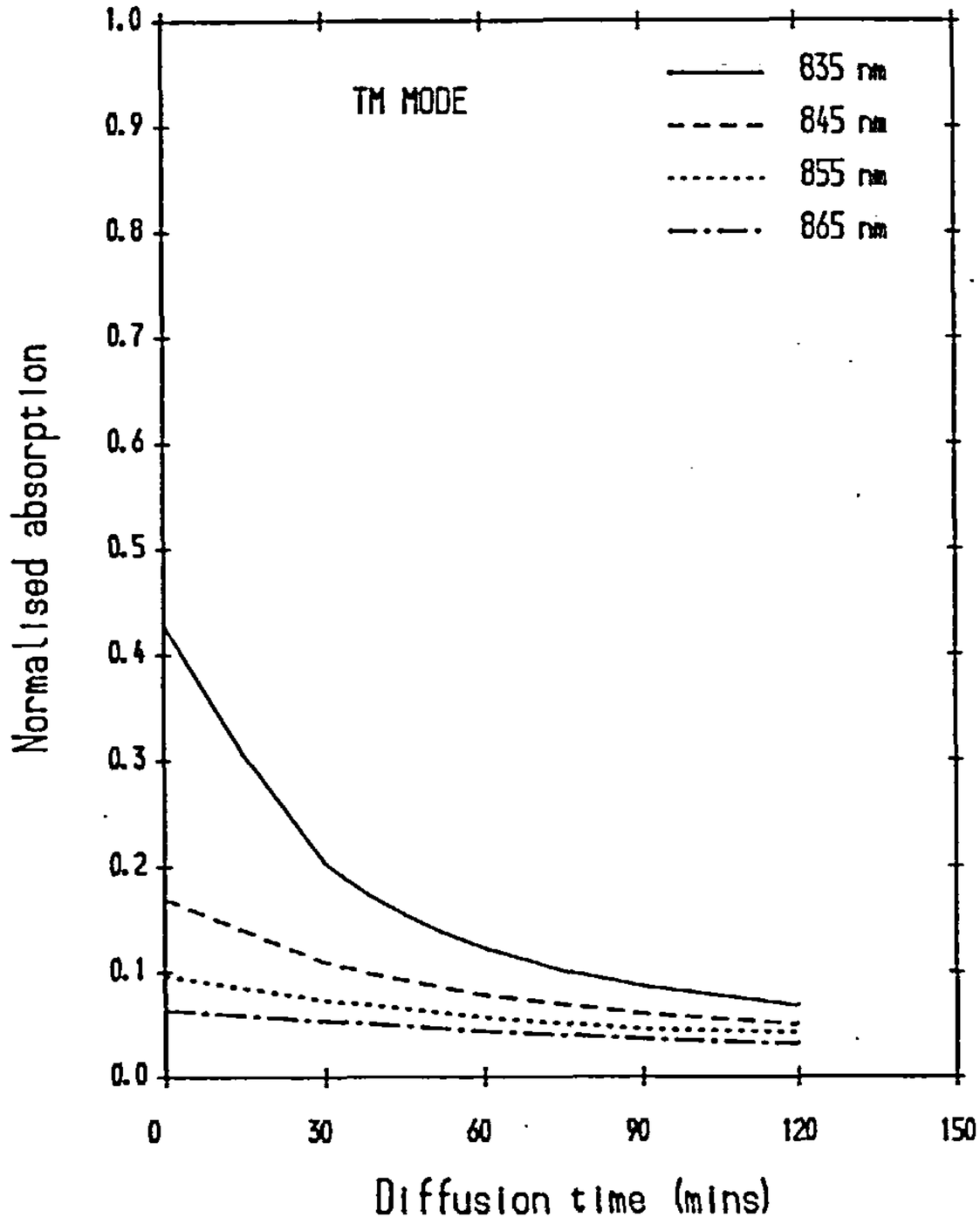

Figure 4. Relative TM mode absorption coefficient as a function of the disordering time at four different wavelengths for energies below the HH1-CB1 exciton transition energy.

contribution of the continuum states increases with diffusion time, along with the bound states being squeezed out of the wells. With diffusion times longer than about three hours, the well and barrier regions will be essentially totally intermixed and the absorption become isotropic with respect to polarisation similar to bulk AlGaAs alloy.

The results of our calculations of the TE and TM refractive indices are shown in Figures 5 and 6. The solid lines are the theoretical results and the plotted symbols are the experimental results of Ref. 5. For t=0 minutes, there is a clear difference between the TE and TM polarisation, but at t=90 minutes both TE and TM approach similar values. Although there is excellent agreement between the theoretical and experimental results, there is an overestimate of the refractive index at energies below 1.4eV. For most of the results shown however, the agreement is very good.

The experimental results for the TM mode index at t=90 minutes appear to show some structure which is not present in the calculated values. There is little difference, however, in the absolute values.

We have found that in considering only the quantum well states it is not possible to obtain results in agreement with the experimental values. In practice it was found necessary to include states exceeding 1eV into the conduction band before the calculated values converged towards the measured values. These higher energy transitions are extremely important therefore in contributing to the index of refraction even for photon energies well below the first excitonic transition peak. Proper modelling of the index of refraction in quantum well structures must therefore include the contribution from remote states if the results are to be favourably compared with known experimental values.

However, it should be noted that all the theoretical results were obtained from the dispersion calculated using averaged effective mass parameters. This was done in order to simplify the calculations. It is known, however, that this has the effect of producing slightly lower energies for all states. This then tends to increase the contribution to the refractive index from all energy transitions considered.

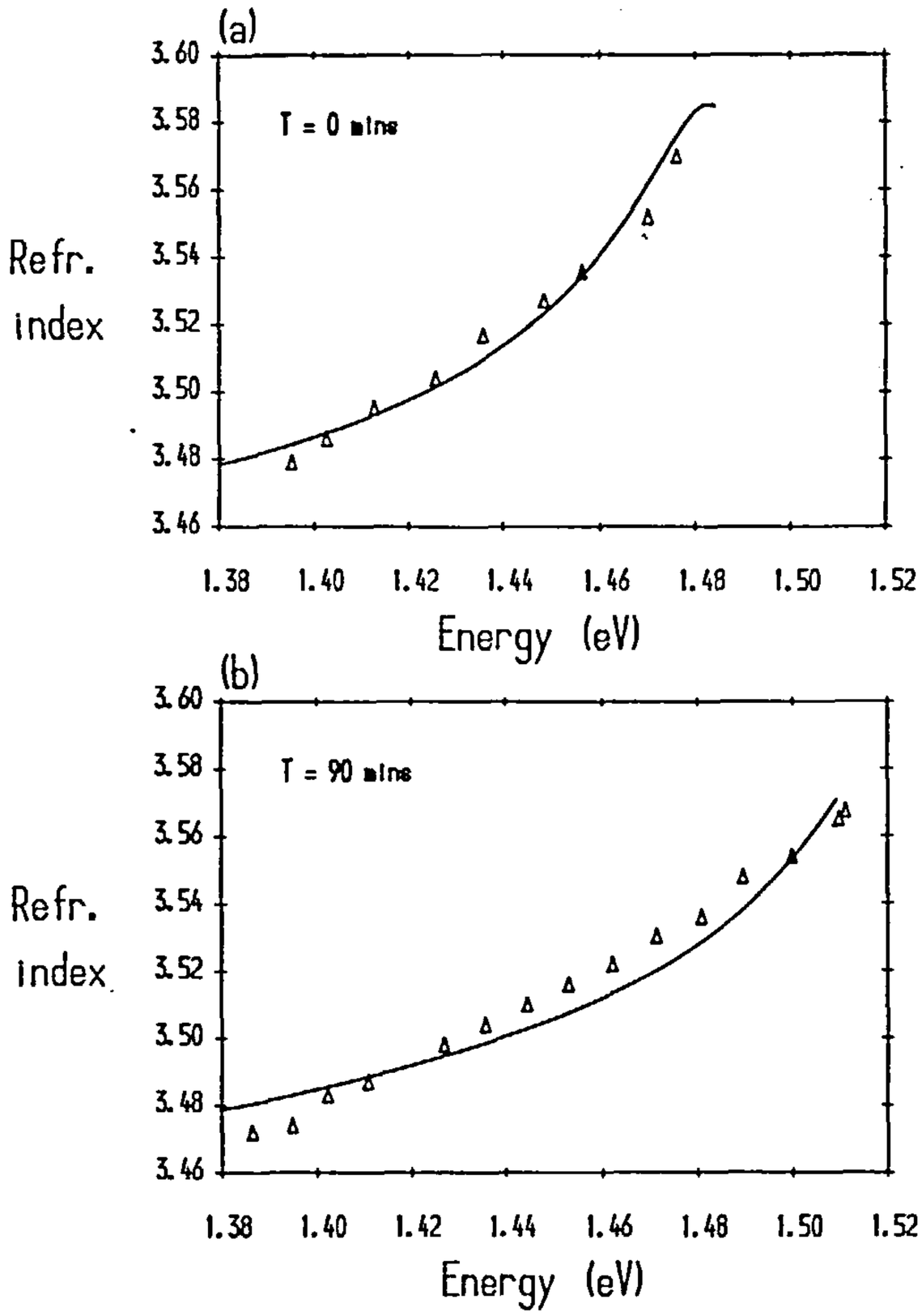

Figure 5. TE mode refractive index for (a) t=0 minutes and (b) t=90 minutes and D=2.5x10^{-18}cm^2/sec (equivalent to a diffusion length of 1.16nm).

The use of position-dependent effective mass parameters, which is more correct, would therefore give a reduction in the calculated values of both the TE and TM refractive indices.

4. Conclusions.

We have calculated the TE and TM mode refractive indices in an impurity induced disordered GaAs-AlGaAs quantum well structure. We have shown that the theoretical results are in excellent agreement with published experimental data. However it was found necessary to include the contribution from higher conduction band states in order to achieve good agreement.

By comparing our theoretical results with the experimentally obtained transition energy shifts, we estimate the inter-diffusion coefficient, for fluorine doping at 10^{14}cm^{-2} and for an annealing temperature of 890°C, to

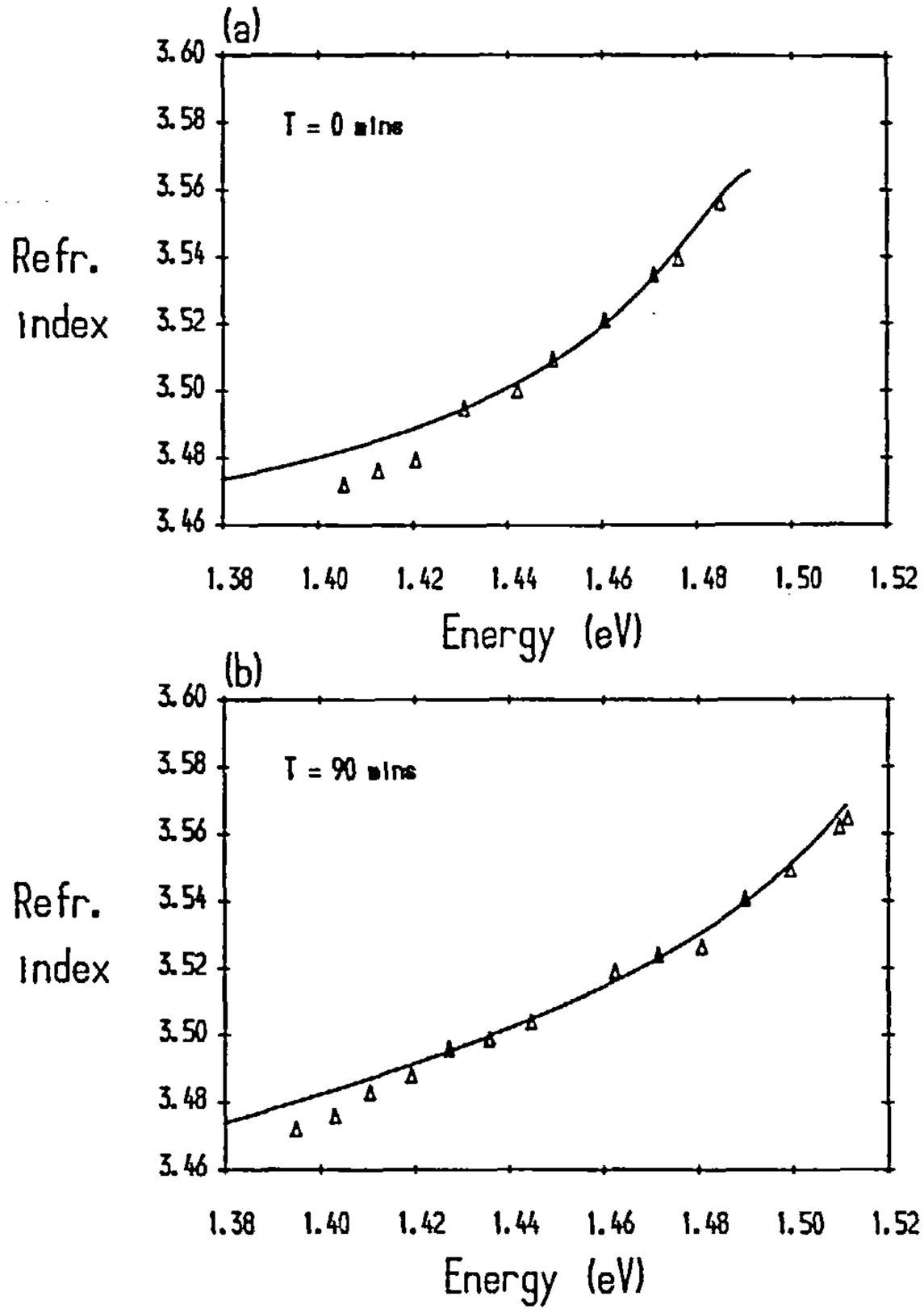

Figure 6. TM mode refractive index for (a) t=0 minutes and (b) t=90 minutes and D=2.5x10^{-18}cm^2/sec.

be 2.5x10^{-18}cm^2/sec. The results presented here could be used to accurately tailor the index of refraction and absorption coefficient in impurity induced disordered GaAs-AlGaAs quantum well structures.

Acknowledgement - The author would like to thank Dr. J.H. Marsh for communicating his results prior to publication and for permission to quote the experimental results in Reference 5.

References.

1 W D Laidlig *et al*, Applied Physics Letters **35**, 776 (1981)
2 M O'3eill *et al*, Applied Physics Letters **55**, 1371 (1989)
3 K Kash *et al*, Journal of Applied Physics **63**, 190 (1988)
4 J D Ralston, W J Schaff, D P Bour and C F Eastman, Aplied Physics Letters **54**, 1536 (1989)

5 J H Marsh, S I Hansen, A C Bryce and R M DeLaRue, to be published in Optical and Quantum Electronics

6 J M Luttinger, Physical Review **102**, 1030 (1956)

7 *Numerical Data and Functional Relationships in Science and Technology*, vol. 17 of Landolt-Börnstein, ed by O Madelung (Springer, Berlin, 1982)

8 M Braun and H Rössler, Journal of Physics **C18**, 3365 (1985)

9 J Wang and J P Leburton, Superlattices and Microstructures **8**, 191 (1990)

10 G D Sanders and Y C Chang, Physical Review **B32**, 5517 (1985)

11 Y Hirayama, Y Suzuki and H Okamoto, Japanese Journal of Applied Physics **24**, 1498 (1985)

12 T E Schlesinger and T Kuech, Applied Physics Letters **49**, 519 (1986)

Excitons in GaAs-AlGaAs Quantum Wells: Effects of Substrate Orientation

Alistair T. Meney

Laser and Optical Systems Engineering Group

Department of Mechanical Engineering

University of Glasgow

Glasgow G12 8QQ

Scotland UK

The binding energies of excitons in GaAs-AlGaAs quantum wells are studied theoretically as a function of the crystallographic growth direction. The electronic dispersion is obtained using the 4x4 Luttinger Hamiltonian for the valence bands, and an accurate expression for the conduction band dispersion which includes the effects of non-parabolicity and warping to fourth order in k. The exciton binding energies are obtained for six growth directions. The different subband mixing for each orientation is seen to strongly influence the exciton properties. The coupling of different exciton states is also dependent on the subband order and energy level spacing, which differ for each quantum well orientation.

Semiconductor quantum wells have attracted considerable interest in recent years due to their novel electronic and optical properties. High-quality heterostructures have been grown almost exclusively along the [001] crystallographic direction. However, several investigations of quantum wells grown along other crystallographic directions have recently been reported.[1-6] Investigations of exciton binding energies and oscillator strengths for growth directions other than [001] have also been reported. Bauer and Ando[7] have considered the [111] and [110] growth directions in GaAs-AlGaAs quantum wells while others[8] have extended this model to include [310]-grown quantum wells. Since the exciton states only sample a small number of states around Γ (typically wave vectors less than $10^6 cm^{-1}$) the conduction band and valence bands can be effectively decoupled within the theoretical model. This simplifies the calculations, and allows the nonparabolicity of the conduction band to be more easily incorporated.

Previous studies of excitons in quantum wells with non-[001] orientations[7,8] have ignored the orbital angular momentum nature of each exciton. This leads to incorrect selection rules and incorrect calculation of the TE and TM mode oscillator strengths.[9,10] Only by considering the proper angular momentum character of each exciton can the coupling between the exciton states be correctly included, This may also lead to incorrect assignment of exciton peaks in absorption and photoluminescence results.[10]

We take the conduction band and valence band as being decoupled, and neglect the split-off spin-orbit Γ_7 valence band. The Hamiltonian for the conduction band is given by[11]

$$E = \frac{\hbar^2 k^2}{2m_c} + \alpha_o k^4 + \beta_o \left(k_x^2 k_y^2 + k_y^2 k_z^2 + k_z^2 k_x^2 \right) + V(z) , \tag{1}$$

where the nonparabolicity parameters α_o and β_o are defined in Ref. 11, and we have included the confinement potential V(z). The Luttinger Hamiltonian (in atomic units) with the additional confinement potential is given by[12]

$$H = -\begin{vmatrix} P+Q & L & M & 0 \\ L^\dagger & P-Q & 0 & M \\ M^\dagger & 0 & P-Q & -L \\ 0 & M^\dagger & -L^\dagger & P+Q \end{vmatrix} + V(z) , \tag{2}$$

where

$$
\begin{aligned}
P &= \tfrac{1}{2}\gamma_1\left(k_x^2 + k_y^2 + k_z^2\right) \\
Q &= \tfrac{1}{2}\gamma_2\left(k_x^2 + k_y^2 - 2k_z^2\right) \\
L &= -\sqrt{3}\gamma_3\left(k_y + ik_x\right)k_z \\
M &= \tfrac{\sqrt{3}}{2}\gamma_2\left(k_x^2 - k_y^2\right) - \sqrt{3}i\gamma_3 k_x k_y \ .
\end{aligned}
\tag{3}
$$

In equation (2) we have neglected k-linear terms since they are small.

Equations (1) and (2) are solved by the standard finite-difference method, with the replacement $k_z \rightarrow -i\frac{\partial}{\partial z}$. The method is well suited to dealing with an arbitrary potential profile, such as in layer-disordered quantum wells and graded barrier structures. We rotate to our new basis for each growth direction, with the direction of angular momentum quantisation taken along the growth axis in each case. We assume a single GaAs-$Al_{0.25}Ga_{0.75}As$ quantum well structure. All the parameters used in the calculations are given in Table 1, and are obtained from Ref. 13.

Table 1. Parameters used in the calculations

	GaAs	$Al_{0.25}Ga_{0.75}As$
E_o	1.4240 eV	1.7259 eV
Δ_o	0.3410 eV	0.3248 eV
m_c	0.0665	0.0874
$m_{hh}(001)$	0.3774	0.4027
$m_{lh}(001)$	0.0905	0.1199
$m_{hh}(111)$	0.9524	1.0017
ε_r	12.5	12.5
ΔE_v	0	0.1208 eV

It is not strictly possible to have similar well widths for each different growth direction. However, since the interatomic spacings are not explicitly included in the effective mass equations (unlike tight-binding or effective bond-orbital models) we assume a free choice of well widths in our calculations. The single-particle wave functions resulting from the solutions to equations (1) and (2) are input to the exciton problem. The effects of nonparabolicity in the conduction band dispersion, and those of valence band-mixing, are therefore fully incorporated into the calculation of the single-particle states.

The envelope function for the (n,m)-state exciton (n,m are 2D hydrogen-like quantum numbers) is taken to be of the form

$$\Psi_{nm}(k) = \int \rho \, d\rho \, \Phi_{nm}(\rho) \, J_m(k\rho) \tag{4}$$

where Φ_{nm} is the 2D hydrogenic radial wave function.[14] This gives the form of the k-space envelope functions used here as[10]

$$\begin{aligned}
\Psi_{1s}(k) &= \lambda\left(\lambda^2 + k^2\right)^{-3/2} \\
\Psi_{2s}(k) &= \lambda\left(k^2 - \lambda^2\right)\left(\lambda^2 + k^2\right)^{-5/2} \\
\Psi_{2p}(k) &= k\lambda\left(\lambda^2 + k^2\right)^{-5/2} \\
\Psi_{3d}(k) &= k^2\lambda\left(\lambda^2 + k^2\right)^{-7/2}
\end{aligned} \tag{5}$$

The term λ is taken as a variational parameter. The energy can be divided between a Coulomb term and a kinetic term, for the variational calculation, giving

$$\begin{aligned}
E_{Coul} + E_{kin} = &\frac{\langle \Psi_{ex} | V_{Coul} | \Psi_{ex} \rangle}{\langle \Psi_{ex} | \Psi_{ex} \rangle} \\
&+ \frac{\langle \Psi_{ex} | H_e + H_h | \Psi_{ex} \rangle}{\langle \Psi_{ex} | \Psi_{ex} \rangle}
\end{aligned} \tag{6}$$

By considering which excitons Ψ_i are coupled by the Coulomb interaction we can then form the variational wave function $\Psi = \sum c_i \Psi_i$. For the HH1-CB1 (1s,2s) excitons we use a two-band model only. For the LH1-CB1 (1s) exciton we include coupling to the HH1-CB1 ($3d_+$), HH3-CB1 ($3d_+$) and HH2-CB1 ($2p_-$) excitons.

Table 2. Calculated exciton binding energies (meV) for 100Å quantum well (x=0.25 in barrier).

Growth Direction	H1-C1 (1s)	H1-C1 (2s)	L1-C1 (1s)
[001]	8.46	1.48	10.50
[111]	8.18	1.45	11.84
[110]	8.02	1.44	10.85
[310]	8.38	1.47	10.60
[311]	8.32	1.46	10.69
[211]	8.26	1.46	11.72

The calculated exciton binding energies for each growth direction are given in Table 2. It is seen that in the case of the HH1-CB1 excitons there is little difference between the results obtained for each orientation. In each case, there is no great difference in the overall HH1 subband dispersion (apart from the precise value of the zone-centre effective mass) for wavevectors less than $10^6 cm^{-1}$. The confinement energies are also similar for this valence subband in each case. We conclude that this leads to the similar results for the HH1-CB1 binding energies (both 1s and 2s) for each orientation.

In the case of the LH1-CB1 exciton, the differences in the calculated binding energies are slightly larger. It is possible to group the results into two distinct classes. This can be done according to the order of the valence subbands, obtained from Table 3 which gives the calculated confinement energies of the first four valence subbands for each orientation.

Table 3. Calculated valence subband confinement energies (meV) for 100Å quantum well.

Growth Direction	HH1	LH1	HH2	HH3
[001]	7.02	20.48	27.77	61.21
[111]	3.60	22.54	14.33	31.99
[110]	4.50	22.03	17.90	39.86
[310]	6.14	21.04	24.35	53.90
[311]	5.47	21.46	21.70	48.18
[211]	4.50	22.03	17.90	39.86

For the [001], [310] and [311] growth directions, the LH1 subband is the second confined valence subband. These three growth directions are seen to have the smallest LH1-CB1 (1s) exciton binding energy. The other three growth directions, for which the LH1 subband is the third confined subband, have the largest LH1-CB1 (1s) exciton binding energy. (This grouping also holds for the HH1-CB1 binding energies, but with the first three directions now having the largest binding energies, although the differences here are smaller).

It is also important to consider the mixing between different subbands. This can be simply estimated by the difference in confinement energy between each of the subbands considered. For the [111] growth direction the LH1 subband is closest to both the HH2 and HH3 subbands than any of the other growth directions. The reversed order of the LH1 and HH2 subbands, compared with the [001] growth direction for example, tends to increase the (hole) effective mass of the LH1

subband. This increase in the effective mass then tends to increase the LH1-CB1 binding energy. A similar situation also arises for the [110] and [211] growth directions although to a lesser degree.

In general, therefore, it can be seen that the proximity of valence subbands contributing to exciton states coupled via the Coulomb interaction is an important factor in determining the exciton binding energy. The order of these subbands is also important. Interaction with lower bands tends to reduce the (electron) effective mass, which is seen to result in a reduction of the exciton binding energy. Interaction with higher-lying bands will tend to increase the (electron) effective mass, resulting in an increase in the exciton binding energy. Both of these effects are important in determining the binding energy of excitons in quantum wells.

REFERENCES

1. S.L. Wright. H. Kroemer and M. Inada, Journal of Applied Physics **55**, 2916 (1983)
2. W.A. Harrison, E.A. Kraut, J.R. Waldrop and R.W. Grant, Physical Review **B18**, 4402 (1978)
3. L. Vina and W.I. Wang, Applied Physics Letters **48**, 36 (1986)
4. C.A. Chang, Applied Physics Letters 40, 1037 (1982)
5. K. Tsutsui, H. Mizukami, O. Ishiyama, S. Nakamura and S. Kurukawa, Japanese Journal of Applied Physics **29**, 468 (1990)
6. M. Lopez, T. Ikei, Y. Takano, K. Pak and H. Yonezu, Japanese Journal of Applied Physics **29**, 551 (1990)
7. G.E.W. Bauer and T. Ando, Physical Review **B38**, 6015 (1988)
8. L.W. Molenkamp, G.E.W. Bauer and R. Eppenga, Physical Review **B38**, 6147 (1988)
9. L.C. Andreani and A. Pasquarello, Europhysics Letters **6**, 259 (1988)
10. B. Zhu, Physical Review **B37**, 4689 (1988)
11. M. Braub and U. Rossler, Journal of Physics **C18**, 3365 (1985)
12. J.M. Luttinger, Physical Review **102**, 1030 (1956)
13. "Numerical Data and Functional Relationships in Science and Technology", Volume 17 of Landolt-Bornstein, Ed. by O. Madelung (Springer, Berlin, 1982)
14. M. Shinada and S. Sugano, Journal of the Physical Society of Japan **21**, 1936 (1966)

EFFECTS OF GROWTH DIRECTION ON LASING PERFORMANCE IN GaAs-$Al_xGa_{1-x}As$ QUANTUM WELLS

Alistair T. Meney
Laser and Optical Systems Engineering Group
Department of Mechanical Engineering
University of Glasgow
Glasgow G12 8QQ
Scotland UK

The properties of GaAs-$Al_xGa_{1-x}As$ quantum well lasers are studied theoretically as a function of the crystallographic growth direction. The growth directions considered are [001], [111], [110], [310], [311] and [211]. The electronic dispersion is obtained using an 8x8 **k·p** Hamiltonian which couples the electron, heavy-hole, light-hole and spin-orbit split-off bands. We calculate the threshold current for single quantum well lasers and determine the lowest threshold current for the growth directions considered. It is seen that for some growth directions the threshold current can be less than that previously calculated for a strained-layer quantum well laser. The results also differ from a previous model which completely decoupled the valence and conduction bands.

1. Introduction

Semiconductor quantum wells have attracted considerable attention in recent years due to their novel electronic and optical properties. High-quality heterostructures have been grown almost exclusively along the [001] crystallographic direction. Several investigations of growth along other crystallographic directions have recently been reported.[1-6] Experimental results[7,8] have indicated reduced current thresholds for [111]-grown GaAs-AlGaAs quantum well lasers, also confirmed by several theoretical studies.[9,10] This reduction in threshold current is with respect to quantum well lasers grown along the [001] direction. It has also been shown recently that [111]-grown quantum well lasers also have reduced current threshold compared to both [110]- and [310]-grown quantum well lasers.[9] In Ref. 11 it was shown that the [110] growth direction is preferred for zincblende-on-diamond MBE growth, which includes GaAs on silicon. It was argued that the [110] interface leads to defect-free heteroepitaxy. This is in contrast to other crystallographic growth directions. Ref. 12 investigated the crystal orientation dependence of n- and p-type Si doping in GaAs-AlGaAs heterostructures, for several high index planes, including [211] and [311]. Reduced in-plane effective masses have also been reported for [111]-oriented substrates. This offers a significant enhancement over [001]-oriented devices.

In this paper we extend our previous calculations[9] to include the [311] and [211] growth directions. Not all of the growth directions considered here have been the subject of experimental investigation regarding the lasing performance of quantum well structures. Previously we considered the conduction and valence bands to be efectively decoupled. The nonparabolic conduction band dispersion was obtained using the Hamiltonian of Braun and Rossler.[13] The valence bands were then described by the 4x4 Luttinger-Kohn Hamiltonian,[14] in the limit of infinite spin-orbit energy. In this paper, however, we use an 8x8 **k·p** Hamiltonian which couples the electron, heavy-hole, light-hole and spin-orbit split-off bands. In addition to the different parameters employed in this model, this gives results which differ slightly from our previous results, although the trends in each case are the same.

2. Subband Dispersion

To obtain the quantum well subband dispersion we use the 8x8 **k·p** model of Cohen and Marques.[15] This model includes the second-order contribution to the conduction band (Γ_6) effective mass which has often been neglected in previous **k·p** models.[16,17] Full details of the **k·p** Hamiltonian can be obtained from Ref. 15. For convenience they are not repeated here. The parameters used in the calculations are given in Table 1. The values of F (Γ_6 second-order Kane parameter) and $2m_oP^2/\hbar^2$ are obtained self-consistently from the experimental energy gaps and effective masses at Γ.

Table 1. Parameters used in the calculations.

	GaAs	$Al_{0.2}Ga_{0.8}As$
E_0	1.4240 eV	1.6734 eV
Δ_0	0.3410 eV	0.3280 eV
mc	0.0665	0.0832
$m_{hh}(001)$	0.3774	0.3976
$m_{lh}(001)$	0.0905	0.1140
$m_{hh}(111)$	0.9524	0.9918
$m_{so}(001)$	0.1735	0.2058
$2m_oP^2/\hbar^2$	24.01 eV	24.01 eV
2F	-1.7350	-2.5450
ΔE_v	0	99.8 meV

For each orientation we take the direction of angular momentum quantisation to be the growth axis. It is straightforward to rotate the **k·p** Hamiltonian for each new growth direction considered. Since we neglect the inversion asymmetry terms it is simple to block-diagonalise the Hamiltonian as in Ref. 15. Retaining only the off-diagonal terms which give rise to in-plane warping of the subbands, then following the method outlined in Ref. 15, we find that these terms are not completely diagonalised. However, since the effect of this is only apparent at large values of in-plane momentum $k_{||}$ we choose to ignore this small error

introduced. We solve each block in the Hamiltonian by using the standard finite-difference method for eigenvalue equations. Continuity of current is obtained by integrating the Hamiltonian across each interface in the growth direction, and we also take the envelope functions $\phi \rightarrow 0$ at $z=\pm 5\bar{L}_z$, where z is the growth direction and L_z is the width of the quantum well region.

Table 2. Directions of the wavevectors k_1, k_2 and k_3 for each growth direction.

Growth	k_1	k_2	k_3
[001]	(1,0,0)	(0,1,0)	(0,0,1)
[111]	(1,1,-2)	(-1,1,0)	(1,1,1)
[110]	(0,0,-1)	(-1,1,0)	(1,1,0)
[310]	(0,0,-1)	(-1,3,0)	(3,1,0)
[311]	(3,1,10)	(-1,3,0)	(3,1,1)
[211]	(0,1,-1)	(-1,1,1)	(2,1,1)

In Figures 1 and 2 we show the lowest confined valence subbands for each growth direction and for well widths of 50Å and 100Å respectively. In each case we have taken the barrier Aluminium fraction to be $x = 0.2$. The direction of $k_{||}$ is along (100) for the [001]-oriented wells and along the equivalent in-plane direction for each of the other growth directions. In Table 2 this direction is denoted as k_1. Compared with our previous calculations it is seen that the lowest subbands are less affected by the finite spin-orbit energy than the higher-lying subbands. This indicates that at higher pumping levels in quantum well lasers (typical in thin quantum wells) this may lead to noticeable differences in the calculated linear gain when compared to the widely-used model with infinite spin-orbit energy. For each orientation we have calculated the zone-centre effective mass for several confined subbands (averaged over the in-plane direction). These are given in Table 3 for both 50Å and 100Å well widths.

Table 3. Calculated zone-centre CB1 and HH1 masses (in-plane averages).

Growth axis	CB1 50Å	CB1 100Å	HH1 50Å	HH1 100Å
[001]	0.0733	0.0697	0.1736	0.1616
[111]	0.0721	0.0689	0.1323	0.1269
[110]	0.0908	0.0854	0.1416	0.1350
[310]	0.0733	0.0698	0.1592	0.1491
[311]	0.0703	0.0676	0.1446	0.1378
[211]	0.0683	0.0677	0.1402	0.1336

3. Linear Gain and Threshold Current

To obtain the linear gain spectra we use the density-matrix formalism[18] with a constant intraband relaxation time τ_{in} = 100 fsec. This gives the linear gain as

$$g(\omega)=\omega\sqrt{\frac{\mu}{\varepsilon}}\sum_{\sigma}\sum_{k}\sum_{c,v}\frac{[f_c(k)-f_v(k)]\left[\hat{\varepsilon}\cdot M_{cv}(k)\right]^2\left(\hbar/\tau_{in}\right)}{\left(E_c(k)-E_v(k)-\hbar\omega\right)^2+\left(\hbar/\tau_{in}\right)^2}, \qquad (1)$$

where f_c (f_v) are the electron (hole) Fermi functions, $\hat{\varepsilon}\cdot M_{cv}(k)$ is the optical dipole matrix element between conduction subband c and valence subband v which depends on the photon polarisation ($\hat{\varepsilon}$) and the envelope function for each subband. The sum over σ includes both blocks of the diagonalised Hamiltonian. The intraband relaxation time is not here considered to be a function of the orientation. The effect of the subband dispersion on the scattering rates in quantum wells, as a function of the growth direction, will be the subject of a future study.

The highly nonparabolic valence subband dispersion, arising due to the strong valence band mixing, indicates that the optical matrix elements are now a strong function of the in-plane momentum $k_{\|}$ and the selection rules are no longer strictly given by $\Delta n = 0$. Therefore the normally parity-forbidden transitions are now possible. The

nonparabolicity in the valence subband dispersion is enhanced by the inclusion of finite spin-orbit energy.

It has been shown that only in the case of thin quantum wells (Lz≈50Å) is there a significant reduction in lasing threshold current for [111]-growth in comparison to [001]-growth.[9,10] If we assume that at threshold all the injected current is converted into spontaneous emission then the current density at threshold can be obtained. The spontaneous emission rate is given by

$$R_{sp} = \int \frac{4e^2 n_r \hbar\omega}{3m_o^2 c^3 \hbar^2} d(\hbar\omega) \sum_{c,v} \int dk \sum_{s} \left| P_{cv}^{\sigma}(k) \right|^2 \times f_c(k)\left[1 - f_v(k)\right] \delta\left(E_c(k) - E_v(k) - \hbar\omega\right) \ . \tag{2}$$

The current density is given by $J = eR_{sp}$. The material gain at threshold is obtained by equating the modal gain and the internal loss α. This gives

$$\Gamma g = \frac{1}{L} \ln\left(\frac{1}{R}\right) + \alpha \ . \tag{3}$$

We take the mirror reflectivity R=0.32, L=500μm and α=10 cm-1. We further assume that the optical confinement factor $\Gamma = 2.5 \times 10^{-4} Å^{-1}$. Equation (3) then gives $\Gamma g = 33 cm^{-1}$ for the above parameters. In the following we consider only the TE-mode polarisation.

The calculated linear gain spectra are shown in Figures 3 and 4. The numbers after each gain curve indicate the 3D carrier density in units of $10^{18} cm^{-3}$. The calculated threshold current density for each orientation is given in Table 4. It is clear that the most pronounced result is the reduction in the threshold current for the [211]-oriented quantum well, better than that of the [111] result. In the case of the 50Å wells, this is 24% less than the [001]-oriented well. Even at 100Å the reduction is 21%, about the same reduction as in the 50Å [111] result. The results for the other growth directions differ slightly from our previous results,[9] due to the different theoretical model and slightly different parameters employed. It is expected that for high injection levels the coupled eight-band **k·p** model will lead to more accurate results than our previous calculations.

It is interesting to note also that for several growth directions, the threshold current is less than that previously calculated for 40Å strained $Ga_{0.35}In_{0.67}As$-$Ga_{0.71}In_{0.29}As$ quantum well lasers.[19] The reduction in threshold current without the need to incorporate strain within the epitaxial layers may be beneficial for long-term operation of quantum well lasers, if good-quality heterostructure devices can be grown with these orientations.

Table 4. Calculated threshold current densities (A/cm^2) for 50Å and 100Å wells.

L_z	[001]	[111]	[110]	[310]	[311]	[211]
50Å	168.0	138.2	187.7	147.6	141.0	127.1
100Å	158.1	142.6	174.5	139.9	124.3	124.8

The reduction in threshold current can not be viewed as simply due to the reduced in-plane zone-centre effective mass of the HH1 valence subband. The averaged zone-centre HH1 masses are given in Table 3. It is seen that the [111] quantum well has the lowest HH1 subband effective mass. The gain is therefore a complicated function of the density-of-states (via the effective masses), the separation in energy between the subband energy levels, and the overlap between the electron and hole wave functions. All of the above are dependent on both the quantum well width, orientation and barrier composition. Note also that the reduction in current density for the [311] quantum well is more for L_z=100Å than for L_z=50Å. In this case (contrary to [111] therefore) thin quantum wells, around 50Å, may not be required for significant reductions in threshold current. We have tacitly assumed that α=10cm^{-1} for each orientation considered. This will of course vary with the quality of interfaces and layer structure. However, for the particular case of [211]-grown quantum wells, increasing α by a factor of 3 still results in a lower threshold current than the [001]-grown quantum well.

4. Conclusions

We have studied the lasing performance of GaAs-AlGaAs quantum well lasers for six different substrate orientations. It has been shown that three orientations offer a significant reduction in the threshold current required for TE mode lasing with respect to [001]-oriented lasers. In the particular case of [311]- and [211]-grown quantum wells, is is seen that it is not necessary to have thin active regions ($L_z \approx 50$Å) in order to achieve significant reduction in threshold current. The possiblity of reduction in threshold current without the necessity for incorporating strain in the epitaxial layers may offer benefit for long-term operation of heterostructure lasers. We would welcome further experimental studies of non-[001]-oriented quantum well lasers, for comparison with the theoretical results presented here.

References

1. S.L. Wright, H. Kroemer and M. Inada, Journal of Applied Physics **55**, 2916 (1983)
2. W.A. Harrison, E.A. Kraut, J.R. Waldrop and R.W. Grant, Physical Review **B18**, 4402 (1978)
3. L. Vina and W.I. Wang, Applied Physics Letters **48**, 36 (1986)
4. C.A. Chang, Applied Physics Letters **40**, 1037 (1982)
5. K. Tsutsui, H. Mizukami, O. Ishiyama, S. Nakamura and S. Furukawa, Japanese Journal of Applied Physics **29**, 468 (1990)
6. M. Lopez, T. Ikei, Y. Takano, K. Pak and H. Yonezu, Japanese Journal of Applied Physics **29**, 551 (1990)
7. T. Hakayawa, T. Suyama, K. Takahashi, M. Kondo, S. Yamamoto and T. Hijikata, Applied Physics Letters **52**, 339 (1988)
8. T. Hakayawa, T. Suyama, K. Takahashi, M. Kondo, S. Yamamoto and T. Hijikata, Journal of Applied Physics **64**, 297 (1988)
9. A.T. Meney, Superlattices and Microstructures (in press)

10. A. Ghiti, W. Bhatty and E.P. O'Reilly, Superlattices and Microstructures **7**, 353 (1990)
11. H. Kroemer, K.J. Polasko and S.C. Wright, Applied Physics Letters **36**, 763 (1980)
12. W.I. Wang, E.E. Mendez, T.S. Kuan and L. Esaki, Applied Physics Letters **47**, 826 (1985)
13. M. Braun and U. Rossler, Journal of Physics C18, 3365 (1985)
14. J.M. Luttinger, Physical Review **102**, 1030 (1956)
15. A.M. Cohen and G.E. Marques, Physical Review **B41**, 10608 (1990)
16. M.F.H. Schuurmans and G.W. 't Hooft, Physical Review **B31**, 8041 (1985)
17. R. Eppenga, M.F.H. Schuurmans and S. Colak, Physical Review **B36**, 1554 (1987)
18. See for example: A. Yariv, "Quantum Electronics" (Wiley, New York, 1975)
19. E.P. O'Reilly, K.C. Heasman, A.R. Adams and G.P. Witchlow, Superlattices and Microstructures **3**, 99 (1987)

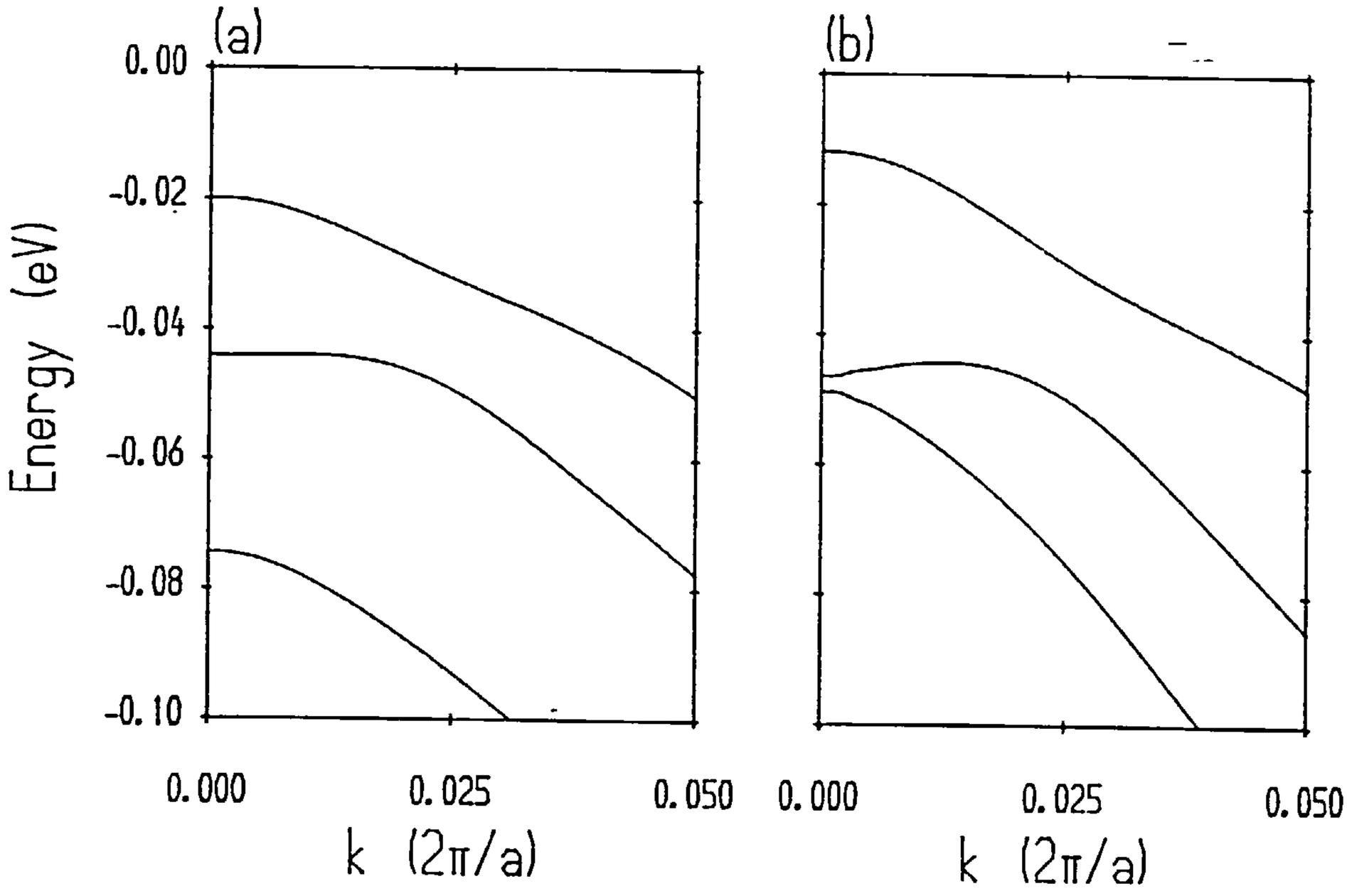

Figure 1

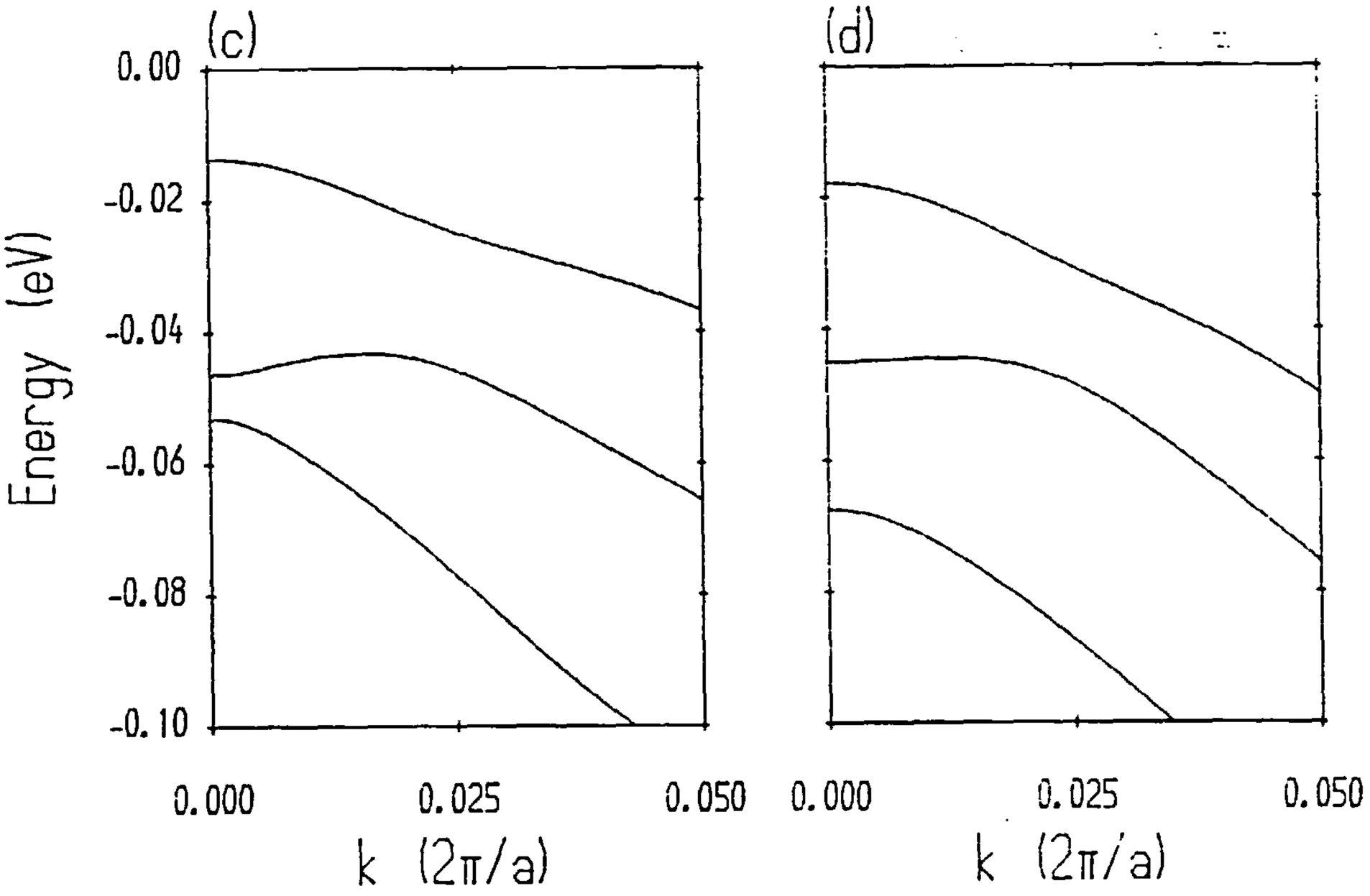

Figure 1 (contd)

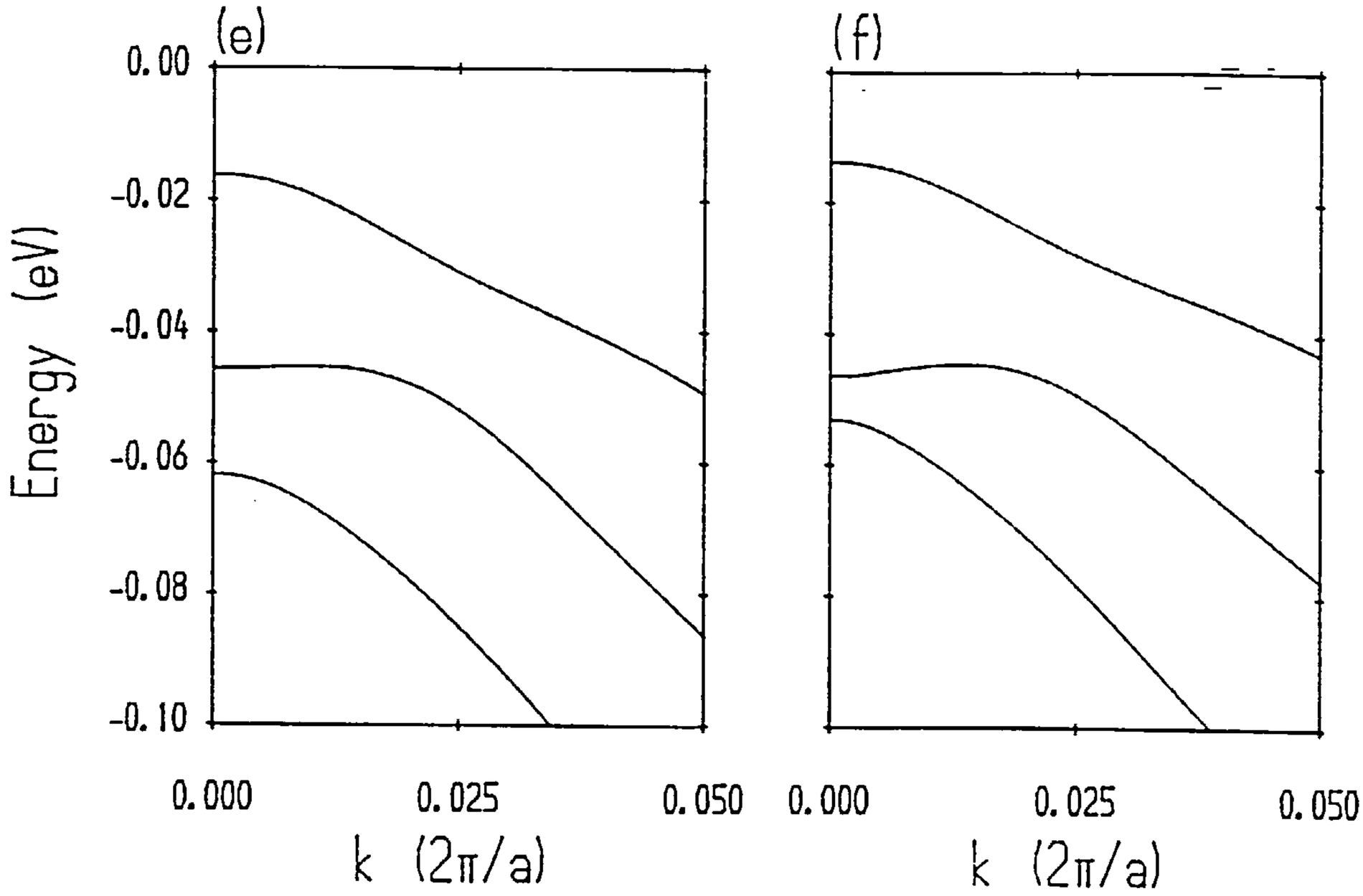

Figure 1 (contd)

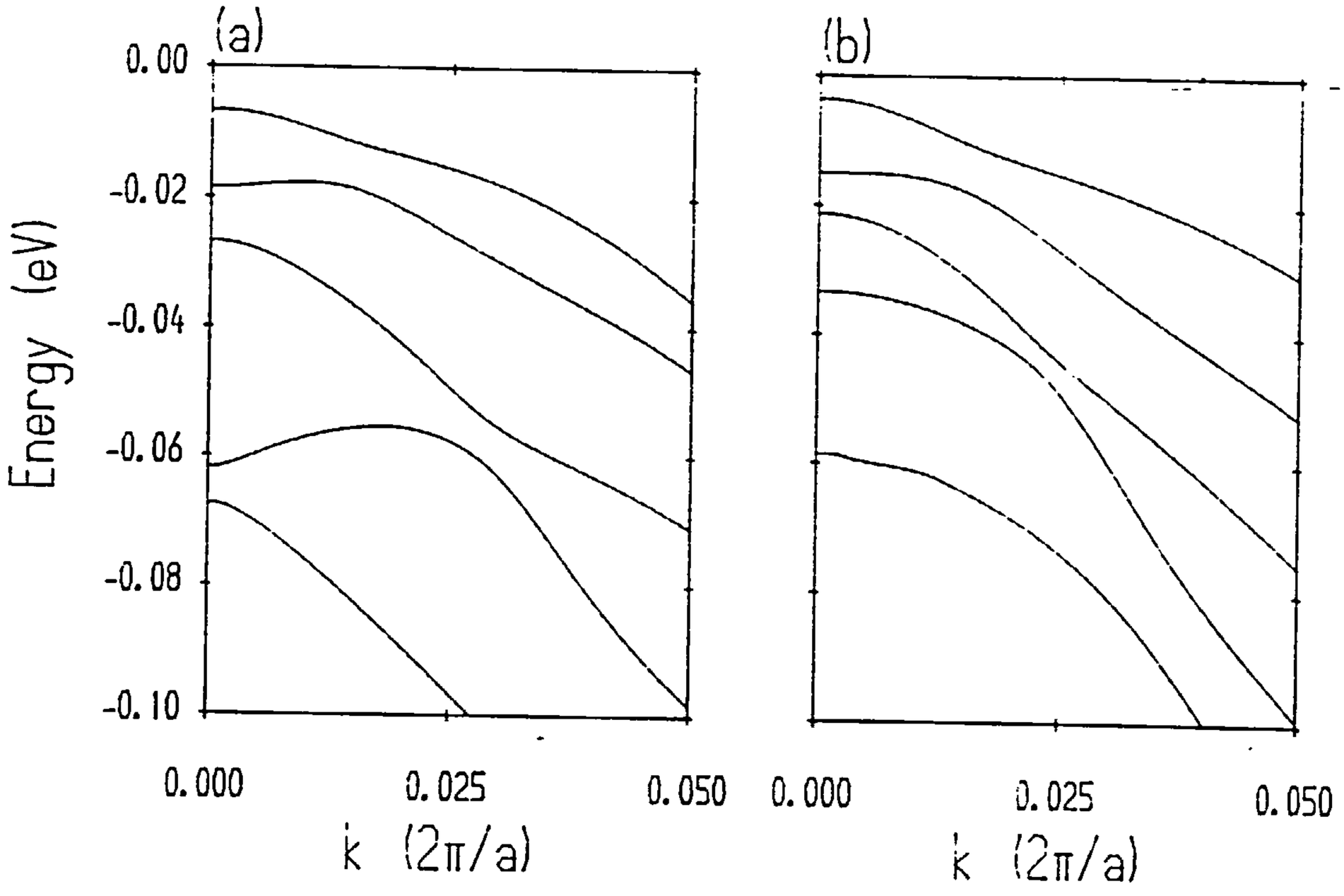

Figure 2

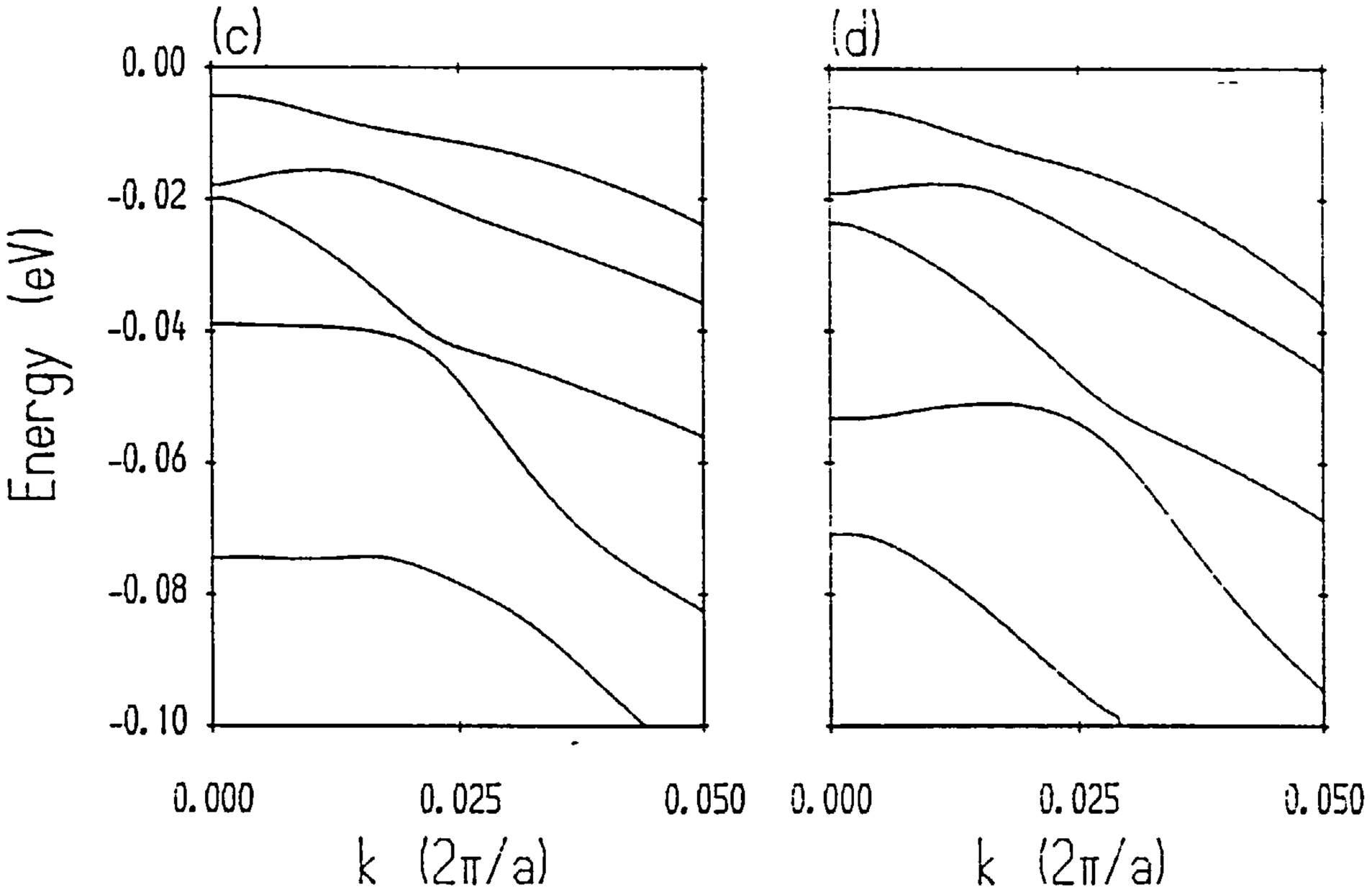

Figure 2 (contd)

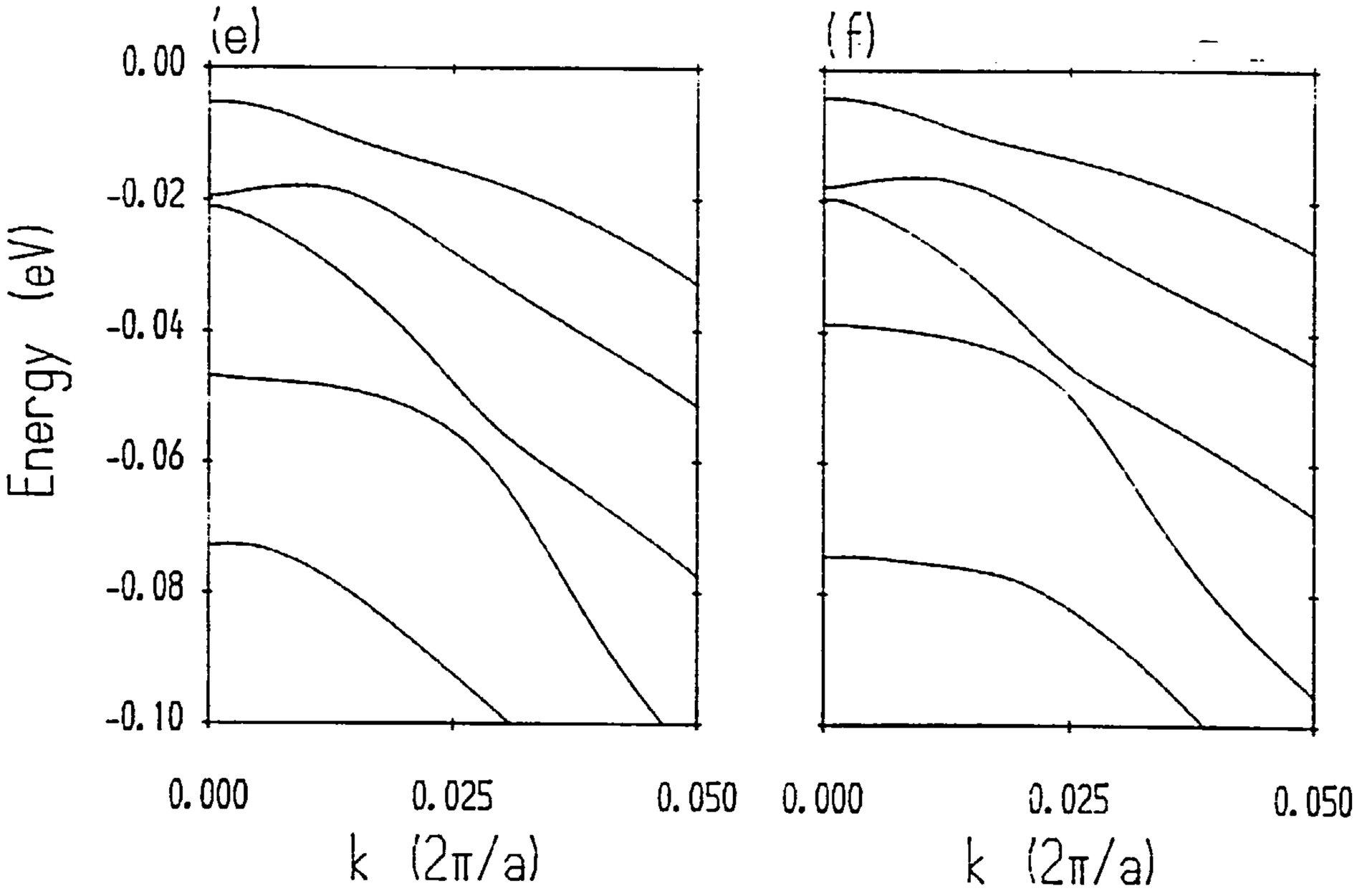

Figure 2 (contd)

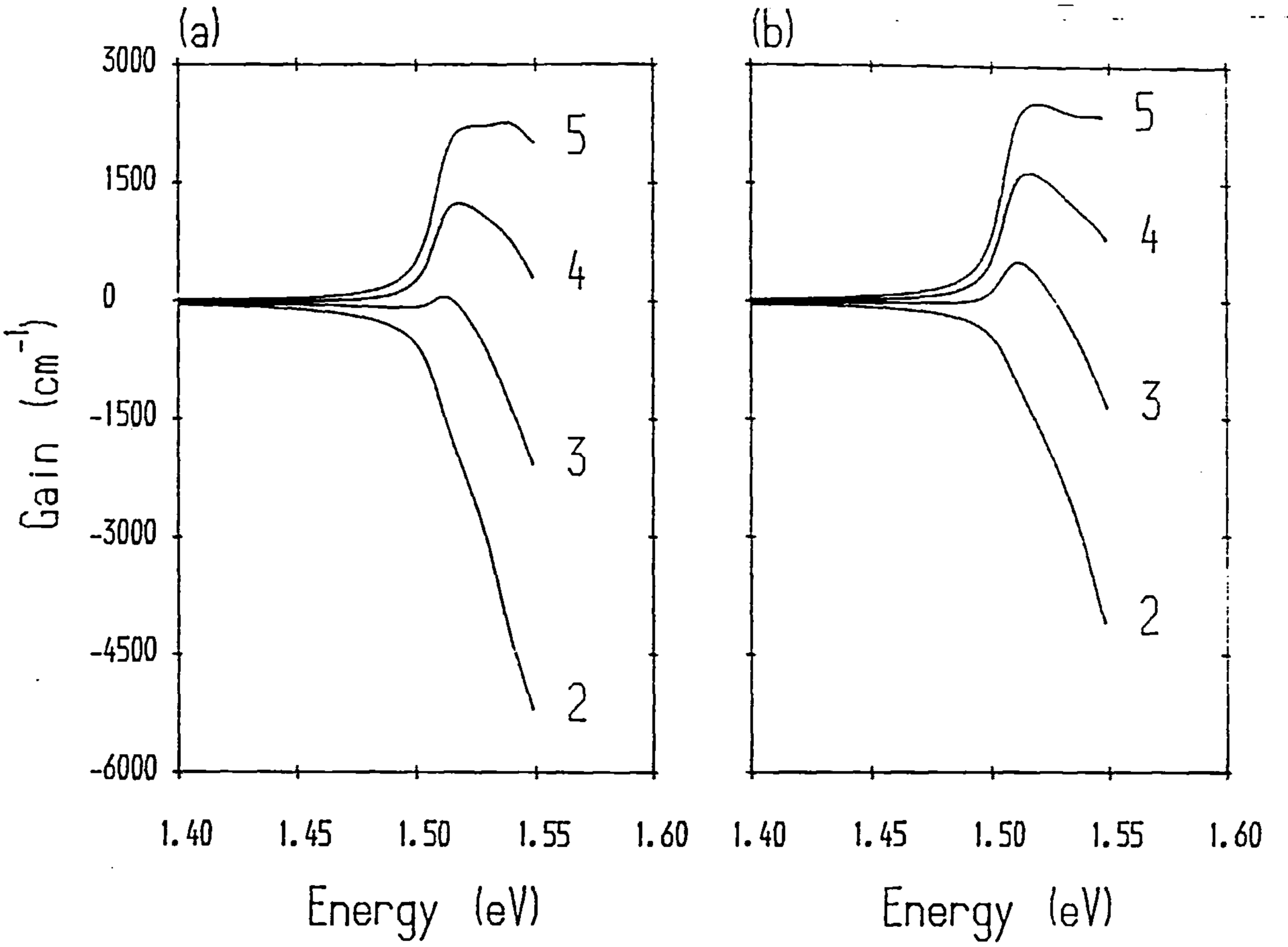
(a)
(b)
3000
1500
0
-1500
-3000
-4500
-6000
Gain (cm^{-1})
5
4
3
2
1.40
1.45
1.50
1.55
1.60
Energy (eV)

Figure 3

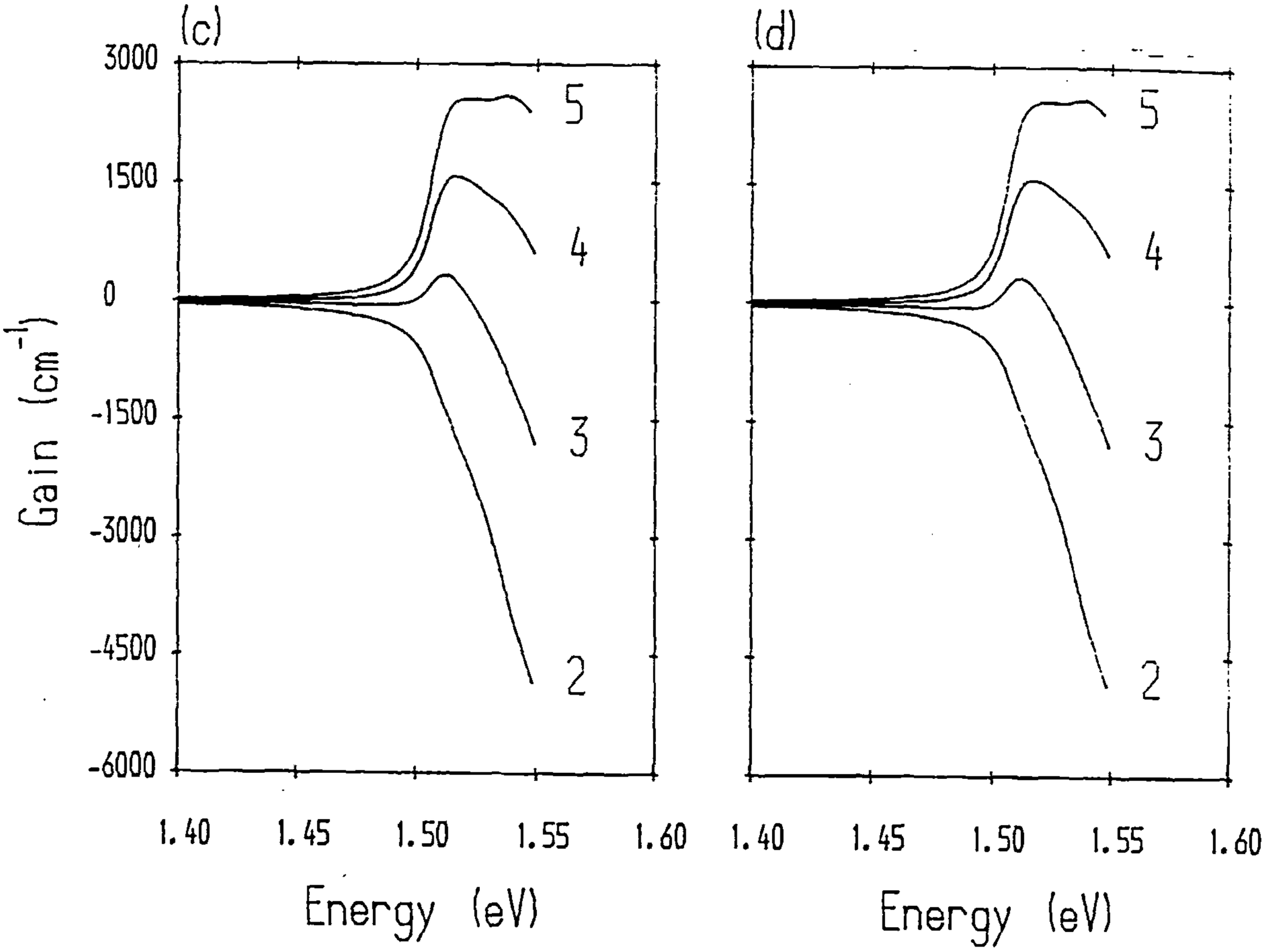

Figure 3 (contd)

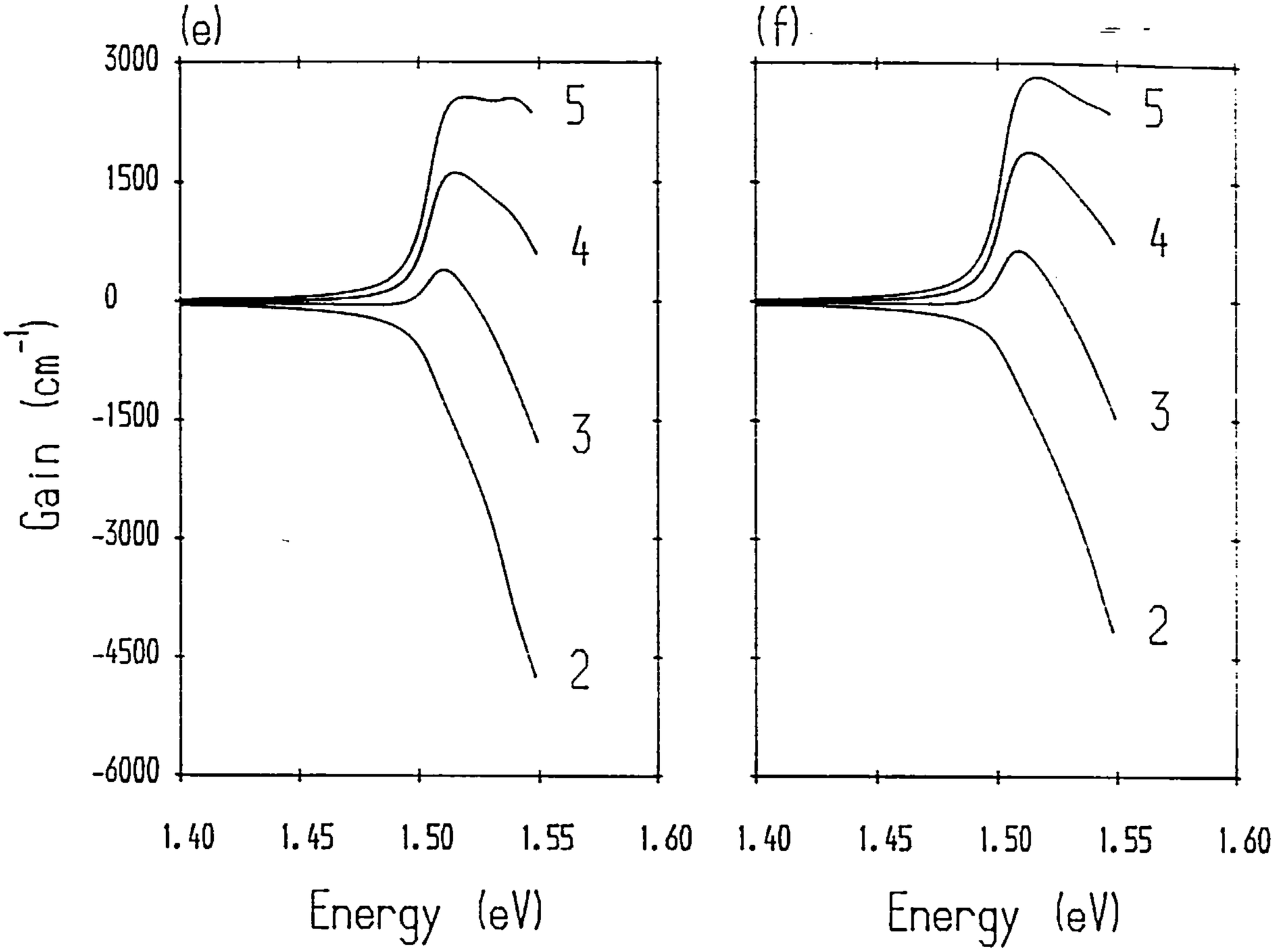

Figure 3 (contd)

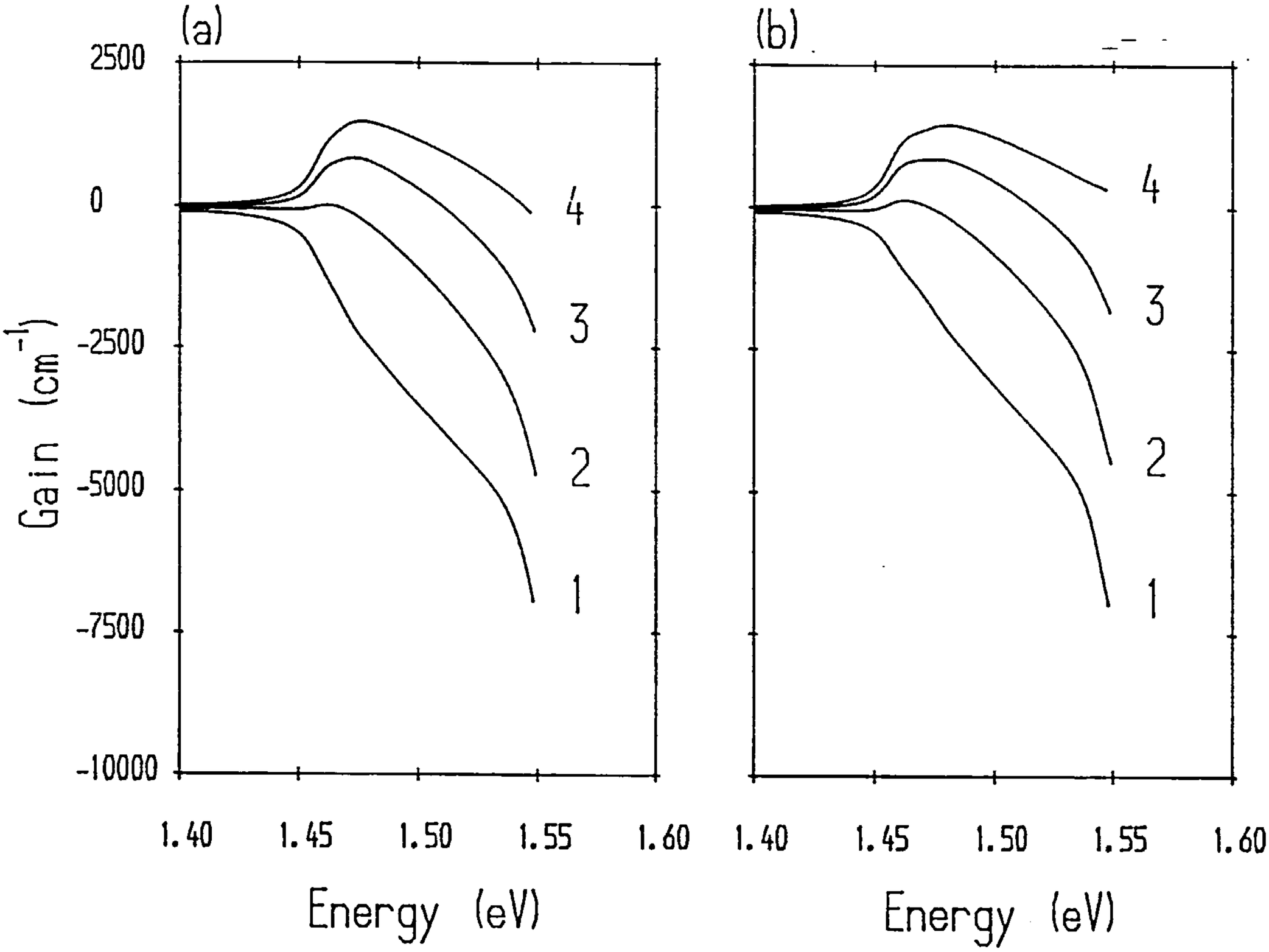
(a)
(b)
2500
0
-2500
-5000
-7500
-10000
Gain (cm^{-1})
1
2
3
4
1.40
1.45
1.50
1.55
1.60
Energy (eV)
Energy (eV)

Figure 4

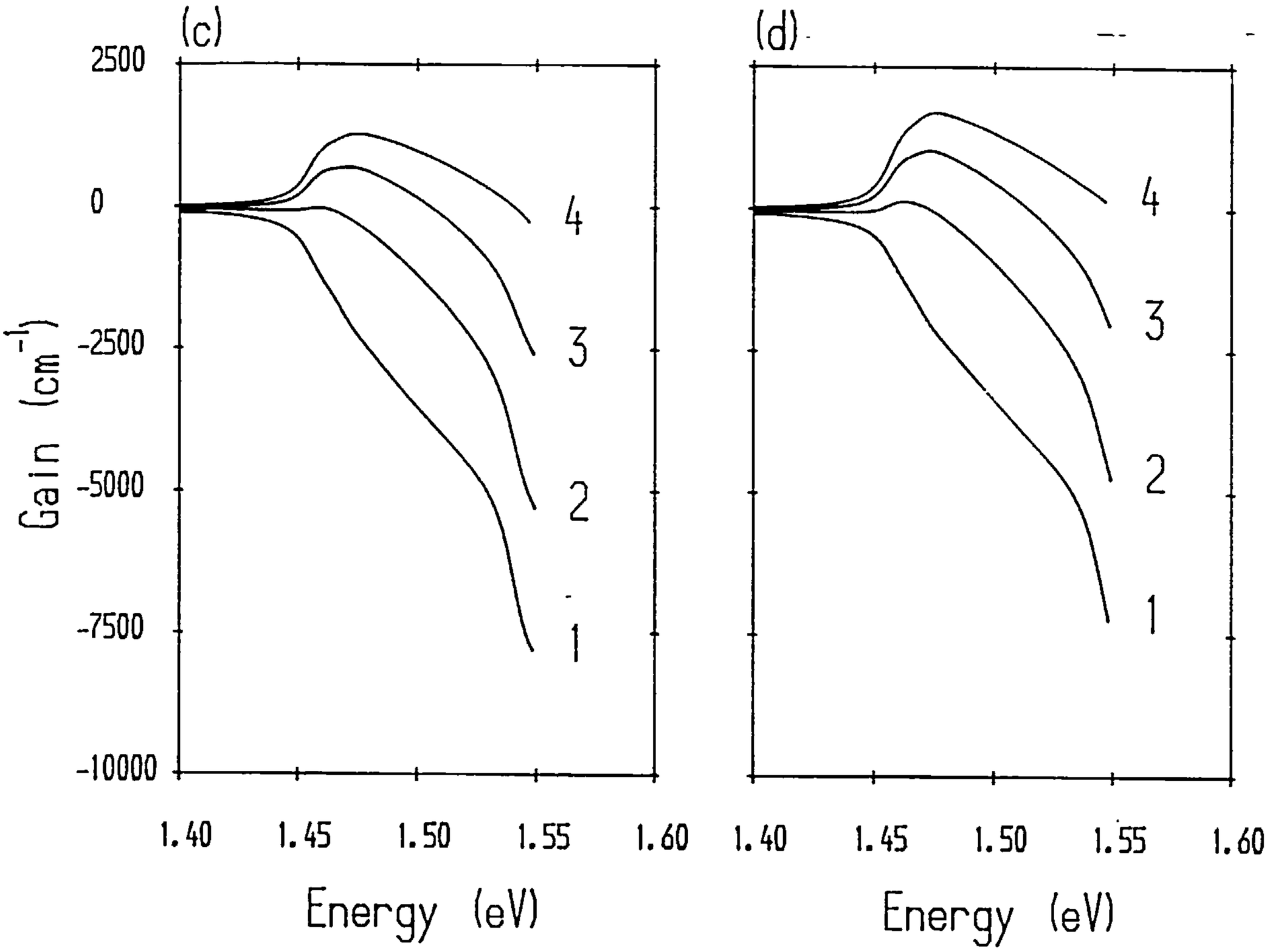

Figure 4 (contd)

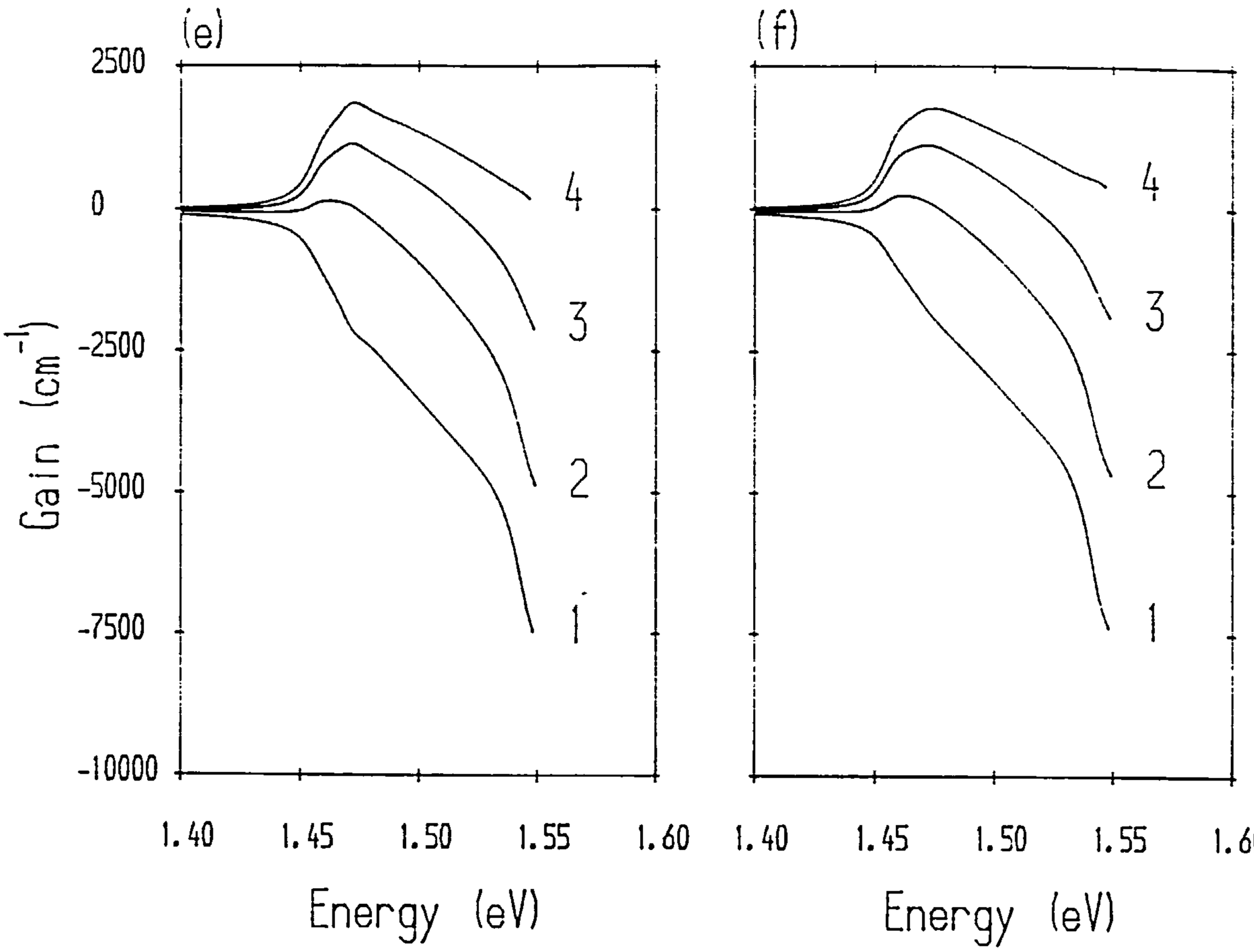

Figure 4 (contd)